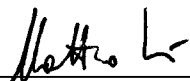RICE UNIVERSITY

Electrochemistry and Self-Assembly of Complex Single-Walled Carbon Nanotube (SWNT) Nanostructures

by

Juan G. Duque

A THESIS SUBMITTED
IN PARTIAL FULFILLMENT OF THE
REQUIREMENTS FOR THE DEGREE

Doctor of Philosophy

APPROVED, THESIS COMMITTEE:

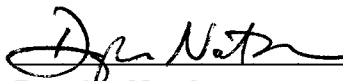_Matteo Pasquali_, Chair
Professor of Chemical and Biomolecular
Engineering and of Chemistry

Clarence A. Miller
Louis Calder Professor Emeritus of
Chemical and Biomolecular Engineering
Research Professor

Douglas Natelson
Associate Professor of Physics and
Astronomy and in Electrical and
Computer Engineering

Howard K. Schmidt
Senior Research Fellow of Chemical and
Biomolecular Engineering

Laurent Cognet
CNRS Research Associate, University of
Bordeaux, France

Houston, Texas

December, 2008

UMI Number: 3362218

Copyright 2009 by
Duque, Juan G.

INFORMATION TO USERS

The quality of this reproduction is dependent upon the quality of the copy
submitted.   Broken or indistinct print, colored or poor quality illustrations
and photographs, print bleed-through, substandard margins, and improper
alignment can adversely affect reproduction.
In the unlikely event that the author did not send a complete manuscript
and there are missing pages, these will be noted.   Also, if unauthorized
copyright material had to be removed, a note will indicate the deletion.

UMI®

ABSTRACT

Electrochemistry and Self–Assembly of Complex Single–Walled Carbon Nanotube (SWNT) Nanostructures

by

JUAN G. DUQUE

This dissertation explores the optical and electrochemical properties of surfactant stabilized and individually–suspended SWNTs in aqueous media via application of various external stimuli. Resulting effects such as nanostructure formation, photocurrent generation, and inherent nanotube electronic and optical properties are then analyzed. The goal is to engineer SWNT systems which can be tuned by understanding the mechanism of the electrochemical and environmental reactions so that applications in nanophotonics, photovoltaics, and electronics can be effectively exploited.

A strategy to obtain a surfactant–polymer protective "shell" that improves the stability and luminescence signal of individual SWNTs is presented. We used literature evidence of emission shifts to understand the interactions between polymers and surfactants and show how morphological changes induced by extrinsic factors distort the SWNT luminescence. We developed an in–situ polymerization which creates an outer shell around the SWNT micelle that resulted in suspensions with stable luminescence at all pH, in saline buffers, and on the surface of living cells.

Single molecule imaging and time resolved spectroscopy of individual (6,5) SWNTs demonstrated that SWNT luminescence depends strongly on intrinsic and extrinsic factors such as sample preparation, sample inhomogeneities, defects, and tube synthesis conditions. Moreover, we found compelling spectroscopic evidence of

substantial differences in chirality distribution and luminescence properties within HiPco batches.

Nanoparticle-nanotube Structures (nanoPaNTs) were fabricated by exploiting the electrochemical properties of SWNTs upon activation with alternating electromagnetic fields. The incident field polarizes the SWNTs at the ends, antenna-like-behavior, which readily drives electrochemical reactions. This process is shown to activate redox reactions preferentially with metallic SWNT and proceed at or near diffusion-limited rates.

Electrochemical photocathodes with optical rectifying antennae were developed from an array of vertically grown CNT forests. We demonstrated rectification of AC signals by associating anionic surfactant molecules around the CNT and charge separation in the optical regime that generates measurable, wavelength dependent, electrical current. We show that charge separation drives redox reactions with transition metal salts in SWNT suspensions.

The results of this research provide key information on the interaction between SWNTs and electromagnetic fields and insight into the extrinsic and intrinsic factors that affect the optical properties.

Acknowledgements

First of all, I would like to thank my advisor Matteo Pasquali and co-advisor Howard K. Schmidt for their guidance and support during my Ph.D., not only professionally, but personally as well. I would like to especially thank them for their trust and confidence in me by opening their laboratory up to me and giving me the tools to do the best work possible in the middle of my doctorate after my previous advisor departed from Rice.

I will always be grateful to Laurent Cognet (Université de Bordeaux) for his support and trust during his sabbatical year at Rice. Also, I would like to thank L. Cognet and Prof. Brahim Lounis for inviting me to their Nanophotonics Laboratory at the Centre de Physique Moléculaire Optique et Hertzienne (CPMOH), Université de Bordeaux and CNRS, France. They introduced me to single molecular detection and made my stay in their laboratory a success. Thanks to Dr. Jean-Baptiste Trebbia, Vivien Octeau, and all of the staff and support group at CPMOH for their experimental help and welcoming atmosphere.

I thank all the members of the Pasquali group; they contributed significantly to my growth and development as a researcher with the exchanging of ideas; Nikta Fakhri, Oscar Coronado, Natnael Behabtu, Chloe Liu, Micah Green, Mainak Majumder, and Colin Young. Special thanks to Nicholas Parra-Vasquez for invaluable research discussions, critical comments on all my work and experimental help, Cary Pint for providing samples, and Alex Eukel for his experimental help.

I thank everyone from the Richard E. Smalley Institute for Nanoscale Science and Technology: Wade Adams, Carlos Garcia, Addy Saenz, and Steven Ripley, and the staff of the Department of Chemical and Biomolecular Engineering at Rice, especially Hazel Cole, for their daily help in administrative matters and making my stay at Rice a more enjoyable experience.

I thank Prof. Bruce Weisman for access to his laboratory and Dmitri A. Tsy-

boulski for experimental help, also Prof. James Tour and Dr. Robert H. Hauge for helpful discussions.

I thank Prof. Alexander Couzis (City College of New York) for introducing me to academic research, believing in me, showing me that graduate school was an option and helping me obtained a scholarship from the Grove Foundation. Also thanks to Silvia Arredondo for her friendship and support during my undergraduate and graduate years.

I thank all my 2003 Rice classmates, colleagues and friends who encouraged me during the good and bad times. From Rice everyone I know, especially: Grace Rojas, Laura Peña, Milton Esteva, Sergio Iadevaia, and Stephanie Portle, and from City College: all of my dear friends from "La mesa de los Colombianos", especially: Uriel Bohorquez, Cesar Gomez, and Alejandro Cano.

I thank mi segunda familia: Amanda L. Higginbotham, Nicholas Parra-Vasquez, Corinne M. Allen and Nate Pettigrew for their love and encouragement, la familia Sanchez and my baby boy Victor.

I thank my whole family in New York, Ohio, Houston, and Medellín for their love and support.

I dedicate this thesis to mis cuatro muñes for their unquestioned love, understanding, and for bringing balance into my life; and to my father, who taught me the value of an integral education and whose love, dedication, and perseverance has shown me that one can only be great by loving those around you and everything we do, **Gracias Pa.**

Contents

3 Environment and Synthesis Related Luminescence Properties of Ensembles and Individual Single-Walled Carbon Nanotubes   49

4 Antenna Chemistry with Metallic Single-Walled Carbon Nanotubes

Illustrations

Thesis Contents

This thesis has seven main sections. Chapter 1 is an overall introduction to SWNT properties (Sec. 1.1) and characterization techniques (Sec. 1.2). Chapters 2 and 3 deal with the optical properties of individual SWNTs in bulk (2) and at the single molecular level (3). These two sections examine how extrinsic and intrinsic factors affect the spectroscopic properties of SWNTs; such factors include the immediate surroundings, surfactant wrapping, surface-tube and tube-tube interactions, sample quality, structural defects and tube type. More precisely, Chapter 2 shows a new strategy to obtain suspensions of highly luminescent SWNTs using a combination of surfactant (SDBS) and a biocompatible polymer (PVP) or by polymerizing in-situ its monomer vinyl pyrrolidone (ISPVP). This results in nanotube suspensions with optimal luminescent properties at any pH value between 1 and 11, in biocompatible environments like phosphate buffered saline (PBS), and in the presence of living cells. Chapter 3 utilizes a combination of continuous wave (cw) and time resolved spectroscopy to investigate several extrinsic factors which deeply influence the SWNT luminescence properties, mainly the synthesis, dispersion, and environment.

Chapters 4 and 5 discuss the interactions between incident electromagnetic fields and carbon nanotubes. These interactions cause the development of an apparent electric field enhancement at the SWNT tips which generates sufficient current densities to induce redox reaction with transition metal salts (4) and/or inject electrons in solution that can be later collected in the form of current (5). Chapter 4 utilizes radio frequencies, microwaves and optical irradiation to induce redox reactions preferentially at the end of SWNTs. Atomic Force Microscopy (AFM) images show formation of novel SWNT Nanoparticles-Nanotube Structures (nanoPaNTs) including dumbells, SWNTs partially or completely encapsulated by metal, rings and straight SWNT "threaded" through rings to form shish-kebab structures. Chapter 5 shows that anionic surfactant molecules around carbon nanotube photocathodes

behave as a rectifying barrier (diode) for current generation under incident light illumination. Finally, Chapter 6 summarizes separate but relevant SWNT experimental work and Chapter 7 presents a set of conclusions.

Chapter 1

Introduction and Background

1.1 Optical and Electronic Properties of Single-Walled Carbon Nanotubes

Single-Wall Carbon Nanotubes (SWNTs) comprise a large family of cylindrical all-carbon polymers with a high aspect ratio ($\sim$1000) and remarkable mechanical, optical, and electrical properties; the specific structure of individual SWNT can be uniquely described by an (n,m) vector (type) that defines its diameter and chirality [Saito et al., 1992]. Roughly two-thirds SWNT species are direct band-gap semiconductors that fluoresce in the near-infrared (near-IR) [O'Connell et al., 2002]. About two percent are 'true' metals with a finite density of states at the Fermi level, while the rest are semi-metals.

A striking example of a SWNT chirality-dependent property is the near-IR luminescence of surfactant-stabilized semiconducting species. The spectroscopic signatures of SWNTs depend on their environment [Ohno et al., 2006; O'Connell et al., 2002; Zhang et al., 2006]. For example, changes in the surroundings, such as acidification, can induce bleaching of their UV-vis absorption, quenching of their fluorescence, and shifting of their spectra. These manifestations can be used to monitor electron transfer, protonation, and charge transfer reactions [Zhang et al., 2006; Strano et al., 2003; O'Connell et al., 2005; Lee et al., 2006], and even individual molecular reactions [Cognet et al., 2007]. However, the pronounced sensitivity of SWNT optical and electronic properties to their environment is not always desirable; it might restrict or

prevent altogether their use in some of the most promising applications, especially in biological systems including drug delivery, biosensors, biomedical devices, and cell biology [Sinnott and Andrews, 2001; Dai, 2002; Palwai et al., 2007]. Viable cells and tissues require specific environmental conditions such as temperature, salt concentration, and pH; these variables influence to various degrees the spectral properties of SWNT suspensions [Strano et al., 2003; Nish and Nicholas, 2006; Niyogi et al., 2007]. None of the SWNT wrapping strategies proposed to date provides highly luminescent tubes across these conditions.

Individual metallic SWNT are essentially ballistic conductors that support DC current densities approaching 10^9 A/cm^2 [McEuen et al., 2002]. As a consequence, metallic SWNT have a high axial dielectric constant [Benedict et al., 1995] and rapidly polarize in response to externally applied electric fields, with expected axial resonance in the THz regime [Hao and Hanson, 2006]. Therefore, metallic SWNT can be considered nano-scale antennae and this polarization-based 'antenna effect' has several interesting and useful manifestations [Wang et al., 2004a; Dresselhaus, 2004]. For example, radio frequency (RF) dielectrophoresis [Krupke et al., 2003] can be employed to manipulate and type-separate suspensions of individualized SWNT [O'Connell et al., 2002], while SWNT networks have been shown to efficiently convert electromagnetic radiation into heat across the RF [Gannon et al., 2007], microwave (MW) [Imholt et al., 2003], and optical [Ajayan et al., 2002] frequency regimes. Their high aspect ratio, $\beta \equiv L/D \sim 1000$, provides a localized apparent field amplification factor (equal to the aspect ratio) at their tips, which enables substantial field emission currents in vacuo at nominal field strengths around 10^6 V/m [Bonard et al., 1998]. There are a few reports of similar effects in aqueous solution using supported multi-wall carbon nanotube electrodes in DC or quasi-static fields, including production of solvated electrons [Krivenko et al., 2006] and electrodeposition on the ends of bundles [Bradley et al., 2005].

1.2 Single-Walled Carbon Nanotube Characterization Techniques

1.2.1 Microscopy

Atomic Force Microscopy (AFM)

The atomic force microscope (AFM) is a high-resolution scanning probe microscope with demonstrated resolution of fractions of a nanometer (x and y resolution is limited by tip dimensions), more than 1000 times better than the optical diffraction limit. The AFM consists of a microscale cantilever with a sharp tip (probe, $\sim$20 nm) at its end that is used to scan the specimen surface. The cantilever is typically silicon or silicon nitride with a tip radius of curvature on the order of nanometers. When the tip is brought into proximity of a sample surface, forces between the tip and the sample lead to a deflection of the cantilever according to Hooke's law. Depending on the situation, forces that are measured in AFM include mechanical contact force, Van der Waals forces, capillary forces, chemical bonding, electrostatic forces, magnetic forces etc. Typically, the deflection is measured using a laser spot reflected from the top of the cantilever onto an array of photodiodes. A feedback mechanism is employed to adjust the tip-to-sample distance to maintain a constant force between the tip and the sample. Traditionally, the sample is mounted on a piezoelectric tube that can move the sample in the z direction for maintaining a constant force, and the x and y directions for scanning the sample. Alternatively a 'tripod' configuration of three piezo crystals may be employed, with each responsible for scanning in the x, y, and z directions. The resulting map of the area s = f(x,y) represents the topography of the sample.

From AFM, images can be used to visualize SWNT samples and extract diameter and length distribution information [Islam et al., 2003; Zaric et al., 2004].

AFM sample preparation of SWNTs requires special care because the SWNTs are suspended in surfactants which need to be removed so that reliable information can be obtained; however, surfactant removal can also induce reaggregation of the sample.
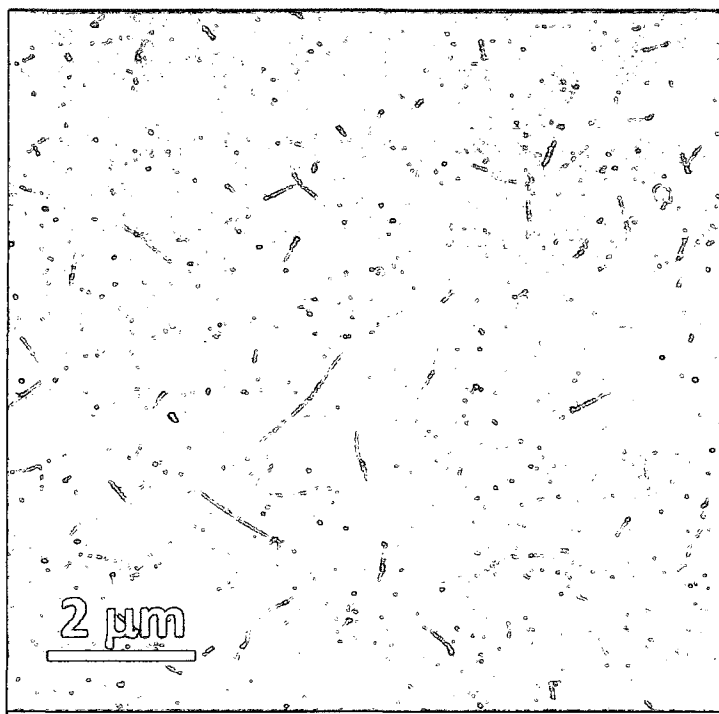
Figure 1.1 : AFM images were obtained with a Nanoscope IIIa, operating in tapping mode, using 1 – 10 Ohm–cm phosphorus (n) doped Si tips at a scan rate of 2 Hz and 512 × 512 resolution. Samples for AFM analysis were prepared with 20 μL of SWNT suspensions spin coated at 3000 RPM onto a roughly 0.25 cm^2 freshly cleaved mica surfaces. To remove the excess of surfactant, the deposited SWNT suspension was immediately rinsed with 2 mL of 2-isopropanol, followed by 5 μL of N-methyl-pyrrolidone (NMP), and then again with 2 mL of 2-isopropanol after which the sample was spun for 10 min.

Transmission electron microscopy (TEM)

Transmission electron microscopy (TEM) is a technique whereby a beam of electrons is transmitted through an ultra thin specimen, interacting with the specimen as it

passes through it. An image is formed from the electrons transmitted through the specimen, magnified, and focused by an objective lens. The image then appears on an imaging screen, a fluorescent screen in most TEMs, plus a monitor, or is detected by a sensor such as a CCD camera.

TEM images enable the direct observation of SWNT samples from which sample composition (diameter distribution), quality (structural defects), and state (individual vs. aggregate) information can be extracted [Sloan et al., 2000; Chiang et al., 2001].
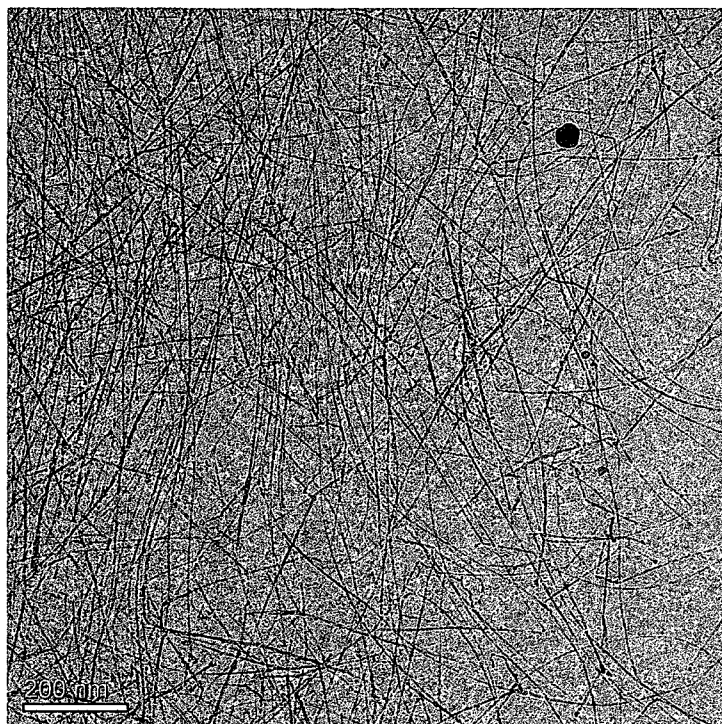
Figure 1.2 : cryo-TEM images were obtained using a JEM FasTEM 2010 at 200 kV. Samples were prepared by adding 5 μL of SWNT suspension onto a lacy carbon grid and frozen using a Vitrobot automated system (FEI Company).

1.2.2 Spectroscopy

Optical Transitions

The optical properties of SWNTs are derived from electronic transitions within 1-D density of states. The major difference between 1-D nanotubes and 3-D materials is the presence of sharp van Hove singularities which result in remarkable optical properties for SWNTs [Dresselhaus et al., 2007b,a; Weisman et al., 2004; O'Connell et al., 2002; Bachilo et al., 2002]. Figure 1.3 shows the density of states of metallic and semiconducting SWNTs. Metallic SWNTs have one electron picture with only band to band transitions. Semiconducting tubes, on the other hand, have a series of inter-band transitions with band gaps inversely proportional to the diameter of the tube (large diameter → small band gaps). In the presence of light, both types of tubes absorb photons, M_{11} in the case of metallic and E_{11} and E_{22} in the semiconducting, as depicted by the black arrows (Fig. 1.3). These transitions can be probed using ultraviolet-visible absorbance spectroscopy (Sec. 1.2.2) as shown in Figure 1.4. After light is absorbed, an electron in excited from the valence to the conduction band (V_1 to C_1 or V_2 to C_2) creating an electron-hole pair (exciton). In the case of semiconducting tubes, both electrons and holes rapidly relax (via phonon-assisted processes) from C_2 to C_1 (red arrow) and from V_2 to V_1 states, respectively. They then recombine through a $C_1 \rightarrow V_1$ (green arrow) transition resulting in light emission. No excitonic luminescence can be produced in metallic tubes because the hole is immediately filled by another electron since the valence band resides at the same energy level as the conduction band. The emission of semiconducting SWNTs can be measured using fluorescence spectroscopy for ensembles (Fig. 1.6), or for single tubes (Fig. 1.10) using an InGaAs spectrometer (Sec. 1.2.2); each peak has been assigned to a different type of semiconducting tube [Bachilo et al., 2002]. Also, their emission can be directly visualized using a liquid nitrogen-cooled camera equipped with a near-infrared detector (Fig. 1.10). Optical transitions for metallic and semiconducting

tubes can also be probed using Raman spectroscopy (Sec. 1.2.2).
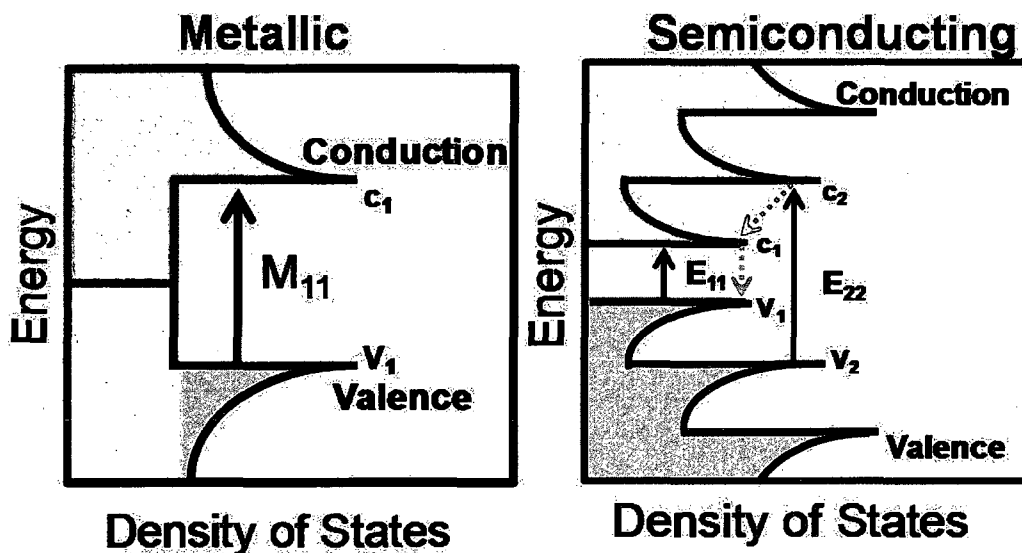
Figure 1.3 : Electronic transitions of metallic and semiconducting SWNTs. Metallic: photon is absorbed via M_{11} which excites an electron from V_1 to C_1, leaving an empty hole. The hole is immediately filled by another electron, therefore, no emission is observed. Semiconducting: photon is absorbed via E_{11} and E_{22}; both electrons and holes rapidly relax from C_2 to C_1 (red arrow) and from V_2 to V_1, respectively. They then recombine through C_1 to V_1 (green arrow), a transition which results in light emission.

Ultraviolet-Visible Absorbance Spectroscopy (UV-vis)

Ultraviolet-visible spectroscopy (UV-vis) is a technique which measures how much light of a particular wavelength is absorbed by a sample and involves the spectroscopy of photons in the UV-visible region. It uses light in the visible and adjacent near ultraviolet (UV) and near-infrared (NIR) ranges. In this region of the electromagnetic spectrum, molecules undergo electronic transitions. Absorption measures transitions from the ground state to the excited state. UV-vis is most often used to determine quantitative concentrations of an absorbing species in solution [Attal et al., 2006; Rai et al., 2006] using the Beer-Lambert law:

$$A = -log\left(\frac{I}{I_0}\right) = \epsilon c L \qquad (1.1)$$

where A is the measured absorbance, I_0 is the intensity of the incident light at a given wavelength, I is the transmitted intensity, L the pathlength through the sample, c is the concentration of the absorbing species, and ϵ is a constant (*log* is the base 10 *log*). The concentration (in mg/L) of surfactant-stabilized HiPco SWNTs suspension can be determinate by dividing the optical absorbance value at 763 nm by 0.043. When the absorbing species are SWNTs, UV-vis gives information on the sample composition of both metallic and semiconductors. The optical absorption spectrum shows a series of relatively sharp interband transitions associated with the first van Hove transitions. The first transition (E_{11}) of the direct band gap semiconducting tubes falls in the 800 to 1600 nm wavelength range (Fig. 1.4, red), slightly overlapping the 550 to 900 nm region of the E_{22} transitions (Fig. 1.4, blue). The lowest energy van Hove transitions of the metallic tubes appear between $\sim$400 and 600 nm (M_{11}, Fig. 1.4, yellow) [O'Connell et al., 2002].

Raman Spectroscopy

Raman spectroscopy is a technique used to study vibrational, rotational, and other low-frequency modes in a system. It relies on inelastic scattering, usually from a laser. The laser light interacts with phonons or other excited species in the system, resulting in a shift in the energy of the laser photons, either up or down. The shift in energy gives information about the phonon modes in the system. SWNTs, due to their size and elemental composition, have unique Raman signatures which in turns gives information on the sample composition (metallic or semiconductor), diameter distribution, and sample quality (side-wall defects). The most important Raman signatures are [Dresselhaus et al., 2005, 2007a; Doorn et al., 2004]:

- **G-band ($\sim$1592 cm^{-1})**: arises from the optical vibration of two adjacent carbon atoms on the wall of the tube. The vibrations are lengthwise and its the
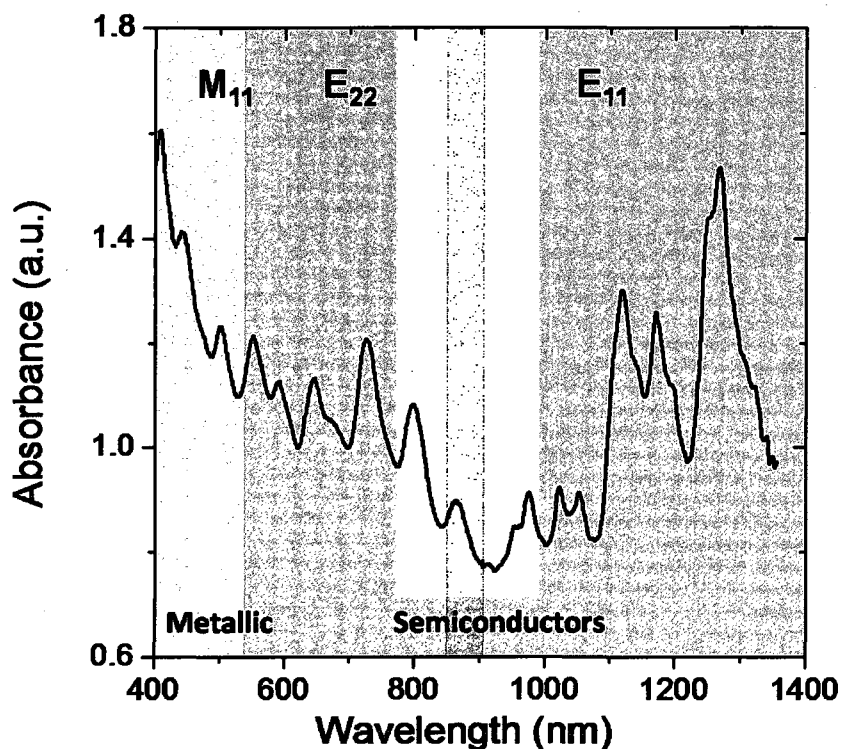
Figure 1.4 : Ultraviolet-visible spectrum obtained with 1 mL of SWNT-surfactant mixture in a sterile 1.5 mL polymethylmethacrylate (PMMA) cuvette with a Nanospectralyzer Model NS1, Version 1.95. The spectrum was obtained in the visible and near infrared regions (400 to 1400 nm) using integration times of 500 ms and 10 accumulations.

carbon nanotube fingerprint.

- **Radial Breathing Modes (RBM, between 100 and 300 cm^{-1})):** low frequencies associated with vibration in the radial direction in an asymmetric totally symmetric breathing pattern, unique to SWNTs. These frequencies are proportional to the diameter of the tubes. Thus, depending on the excitation wavelength, one can extract information on the sample chirality (metallic vs. semiconductor) and diameter by examining the RBM.

- **D-band (~1332 cm⁻¹):** arises from highly second order resonance processes from which order and disorder (sidewall defects or moieties) information can be obtained.

- **G'-band (between 2500 and 2700 cm⁻¹):** is a second order resonance process from which sample composition information can be extracted, such as tube diameter. The frequency of the G'-band is close to twice the D-band frequency.
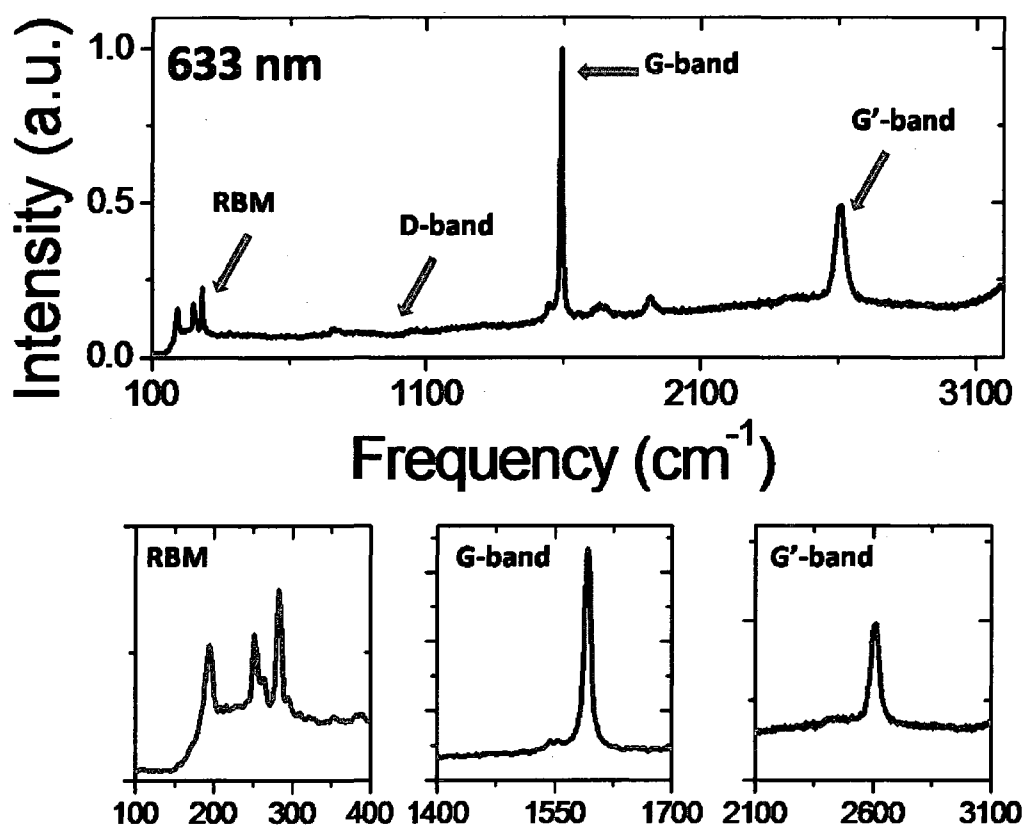
Figure 1.5 : Raman measurement was obtained using 633 nm laser excitation with an inVia micro-Raman spectrometer (laser wavelengths of 785 and 514 nm are also available for exciting different populations of tubes). Liquid samples were held in a Renishaw Raman Macro Sampling Set in a 2 mL glass vial. Raman spectra were collected from 100 to 3200 cm⁻¹ with Wire2 data acquisition software, using 20 sec exposure times and 1 accumulation.

Fluorescence Spectroscopy

Fluorescence is an optical phenomenon in which the molecular absorption of a photon triggers the emission of another photon with a longer wavelength. The energy difference between the absorbed and emitted photons ends up as molecular vibrations or heat. In fluorescence spectroscopy, the species is excited by absorbing a photon, and moves from its ground electronic state to one of the various vibrational states within the excited electronic state. Collisions with other molecules cause the excited molecule to lose vibrational energy until it reaches the lowest vibrational state of the excited electronic state. Only semiconducting SWNTs fluoresce due to their unique bandgap structure in the near-infrared [Ohno et al., 2006; O'Connell et al., 2002; Zhang et al., 2006]. Figure 1.6 shows the fluorescence spectrum of a suspension of SWNTs in SDBS using a 660 nm excitation wavelength. Each peak can be uniquely assigned to a different diameter semiconducting tube with increasing diameter as the wavelength increases [Bachilo et al., 2002].

Importantly, the E_{11} absorbance peaks can be correlated with the fluorescence peaks (Fig. 1.6) for better interpretation of the data and more qualitative and quantitative assessment of the suspension quality as shown in Figure 1.7.

Figure 1.8 shows a 2-D map of the emission as a function of excitation of surfactant dispersed SWNTs. This figure gives a map of the emission profile of each of the semiconductors present in the suspension.

Figure 1.10 shows the luminescence and fluorescence spectrum of an individual (6,5) SWNT, which has one narrow, well-defined peak.
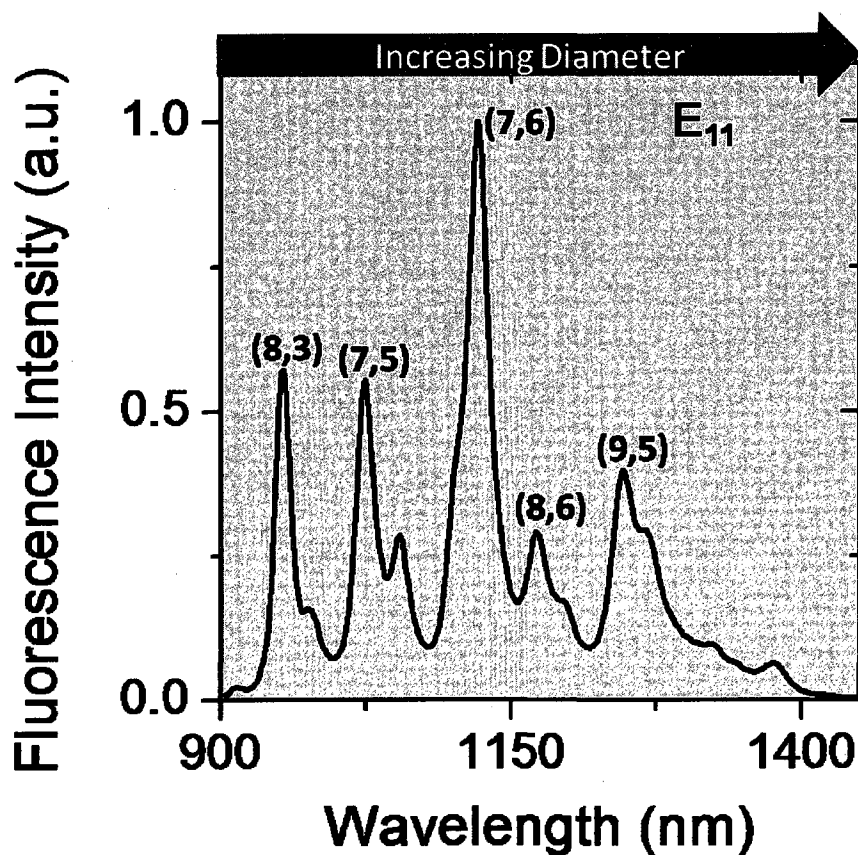
Figure 1.6 : Fluorescence spectrum was obtained with 1 mL of SWNT-surfactant mixture in a sterile 1.5 mL polymethylmethacrylate (PMMA) cuvette with a Nanospectralyzer Model NS1, Version 1.95. The SWNT fluorescence was excited at 660 and/or 785 nm and emission spectra were obtained between 900 and 1400 nm using 500 ms integration times and 10 accumulations.

Photothermal Heterodyne Imaging (PHI)

Photothermal heterodyne imaging (PHI) combines a time-modulated heating beam and a nonresonant probe beam that overlap on the sample. The probe beam produces a frequency-shifted scattered field as it interacts with the time-modulated variations of the refractive index around the absorbing nanoparticle. The scattered field is then detected by a photodiode through its interference with the probe field, which acts
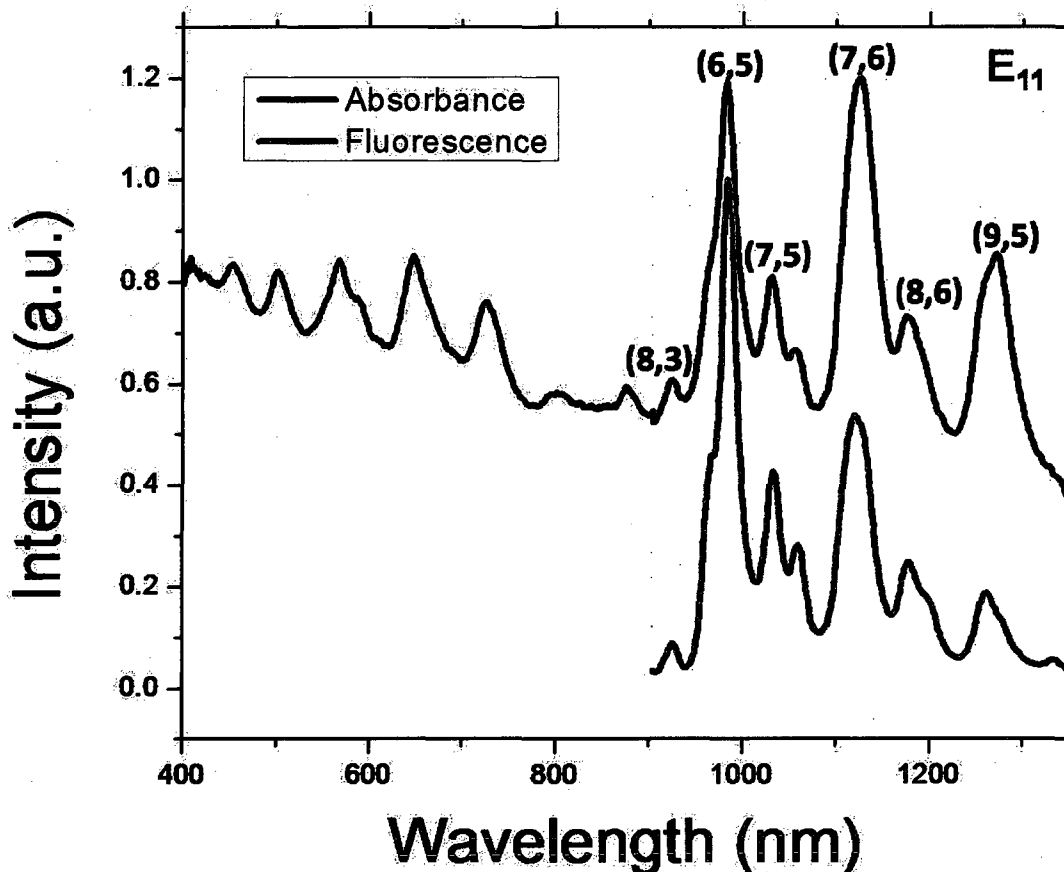
Figure 1.7 : Absorbance (black trace) and fluorescence (blue trace) spectra correlating the E_{11} peaks.

like a local oscillator as in any heterodyne technique. This signal is extracted from the beat note at the modulation frequency by lock-in detection [Berciaud et al., 2004, 2006; Cognet et al., 2008a; Berciaud et al., 2007]. Since it only relies on light absorption and changes in refractive index, PHI is an important technique to directly visualize both semiconducting and metallic SWNTs [Berciaud et al., 2007], in contrast to near-IR images which only probe semiconducting species. This technique is very powerful because it does not suffer from blinking and photobleaching and is immune to the effects of fluorescing and scattering backgrounds.
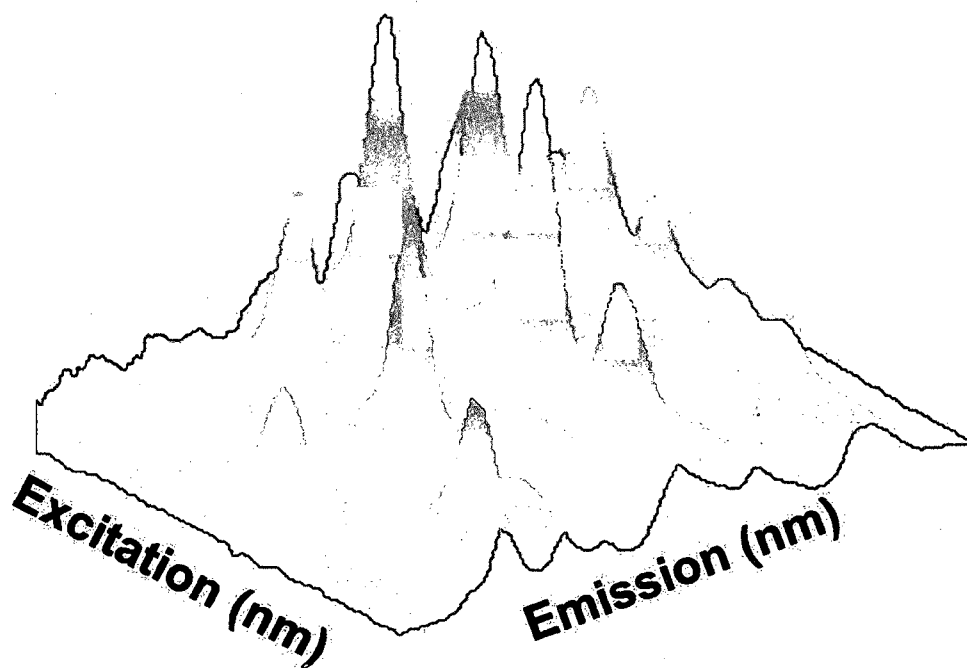
Figure 1.8 : Representative 2-D spectrum of fluorescence emission as a function of excitation. 2-D spectrum was obtained with 1 mL of SWNT-surfactant mixture in a sterile 1.5 mL polymethylmethacrylate (PMMA) cuvette with a Spectrolog system. Excitation was from 550 to 900 nm in 3 nm intervals. Emission was collected from 900 to 1400 nm.
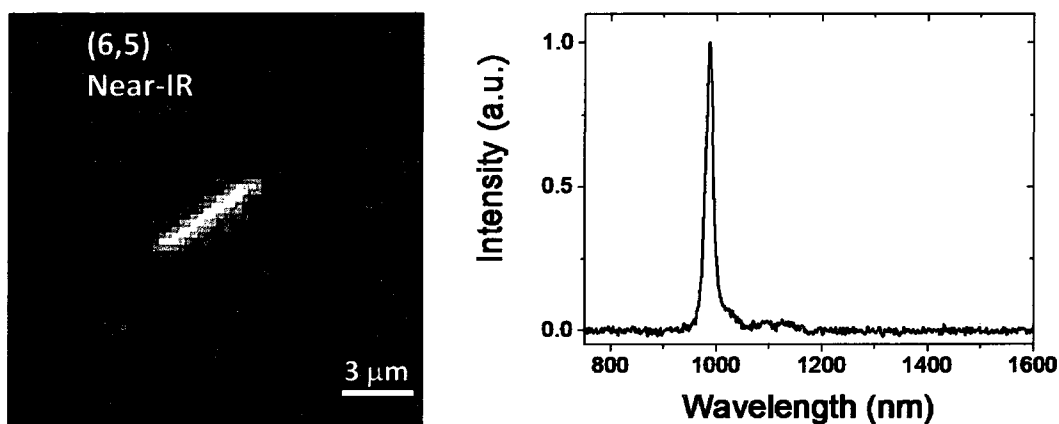
Figure 1.9 : Luminescence and fluorescence spectrum of an individual (6,5) SWNT. SWNTs were visualized by near-infrared fluorescence microscopy by adding a 5 μL drop of nanotube suspension between a glass slide and a microscope coverslip sealed with silicon grease to prevent drying. SWNT samples were mounted onto an inverted epifluorescence microscope equipped with a 60× oil emersion objective. Samples were continuously excited by a circularly polarized beam of a 567 nm diode laser. The infrared photoluminescence emitted by the SWNTs passed through long-pass infrared filters and was detected by a liquid nitrogen-cooled camera. Single frame acquisition images of the SWNT luminescence were recorded with an integration time of 50 ms.
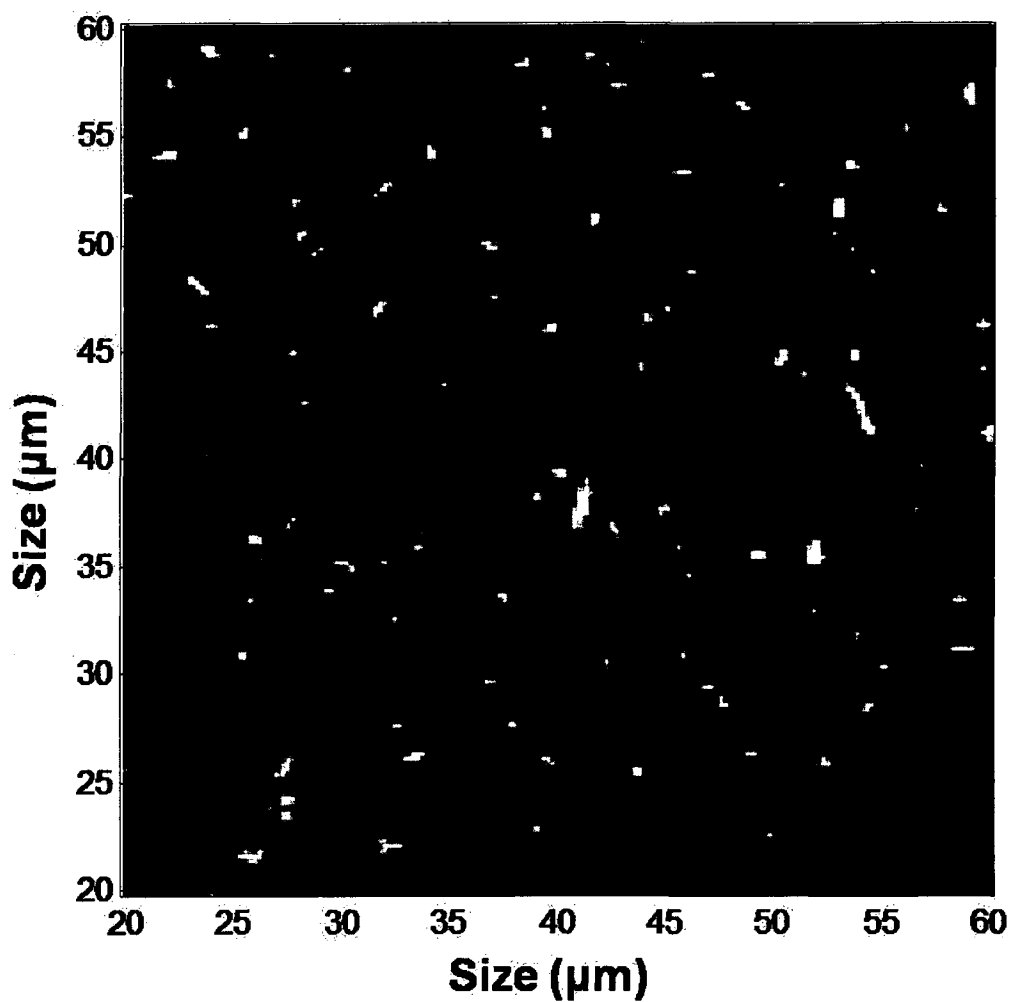
Figure 1.10 : Photothermal images were obtained by spin-coating a 5 μL drop of nanotube suspension on a microscope coverslip. The probe beam at 633 nm was overlaid with a modulated cw absorption beam at 532 nm. The absorption and probe beams were both focused onto the sample using a high NA objective. The intensity of the heating beam is modulated at a predetermined frequency by an acousto-optic modulator.

Chapter 2

Stable Luminescence from Individual Carbon Nanotubes in Acidic, Basic and Biological Environments

2.1 Objective

The aim of the work described in this chapter is to obtain suspensions of single-wall carbon nanotubes (SWNTs) with stable luminescence properties in different environmental conditions. Toward this, we developed a mixture of surfactants and polymers which protect the optical properties of the tubes at all pHs ranging from 1 to 11, and in biological fluids like phosphate buffer saline (PBS). Moreover, the SWNTs were stable and highly luminescent below the critical micelle concentration of the stabilizing surfactant, in the presence of living cells, and retained their fluorescence after lyophilization and resuspension in deionized water. Not only were we able to protect the optical properties of the tubes with polymers, but also conduct an in-situ-polymerization around the tube to better isolate and protect the SWNTs from its immediate surroundings. The characterization of the samples was conducted using atomic force microscopy (AFM), cryo-transmission electron microscopy (cryo-TEM), ultraviolet-visible absorbance (UV-vis), Raman spectroscopy, and near-infrared fluorescence.

2.2 Background

Single-wall carbon nanotubes (SWNTs) are one of the most interesting classes of nano-objects due to their unique thermal, physical, optical, and electronic proper-

ties [Sinnott and Andrews, 2001; Khan and Husain, 2005; Setton, 1995; Dai, 2002; Baughman et al., 2002; Banks, 2006]. The unique characteristics of the carbon nanotubes is due to the chirality angle of the tube and its diameter which gives rise to varying electronic state densities which in turn leads to its unique electrical characteristics. SWNTs can exhibit metallic–, semimetallic–, or semiconductor-type behavior depending on their chirality angle, conceptualized by the twist angle of a graphene sheet rolled to form a tube.

Surfactants are routinely used to suspend and isolate SWNTs in aqueous environments, enabling examination of the optical and electronic properties of the semiconducting and metallic species [O'Connell et al., 2002; Bachilo et al., 2002; Dresselhaus et al., 2005]. Anionic surfactants are the most widely employed to examine the optical properties of semiconducting SWNTs, and SDBS is generally preferred because it gives the most blueshifted resonances and high luminescent yields from the suspended SWNTs. Although surfactant wrapped SWNTs are stable in aqueous suspensions, slight changes in the pH of the solution (especially toward acidity) decreases the photoluminescence of the SWNTs and can even destabilize the suspension and cause flocculation [Strano et al., 2003; Cognet et al., 2007; Wang and Chen, 2007]. The bleaching of the fluorescence of sodium dodecyl sulfate (SDS) or sodium dodecylbenzene sulfonate (SDBS) suspended nanotubes in acidic media was attributed to the selective protonation of pre-adsorbed oxygen at the SWNT sidewalls; the protonation could be reversed by readjusting the solution pH from acidic to alkaline. Interestingly, a partial restoration of the absorption and fluorescence spectrum was observed after addition of PVP; this was attributed to strong interaction between the interface of the SDS micelles and PVP that had been documented previously [Strano et al., 2003; Atkin et al., 2005; Zhai et al., 2004; Brackman and Engberts, 1993; Zanette et al., 1997]. The luminescence properties of nanotube suspensions are also strongly dependent on the surfactant concentration [McDonald et al., 2006]. Below the crit-

ical micelle concentration (CMC), substantial redshifts, fluorescence reduction, and eventual flocculation are observed in the suspension [Strano et al., 2003]. An additional drawback of the use of surfactants alone is that they are not biocompatible. To overcome this limitation, biocompatible SWNT suspensions have been recently obtained and thought to result from the non-specific replacement of Pluronics polymer wrapping by unidentified proteins in biological sera. This strategy, however, is not universal and produces weakly luminescent SWNTs [Cherukuri et al., 2006].

2.3 Overall Findings

Here we report a new strategy to obtain suspensions of highly luminescent SWNTs using a combination of surfactant (SDBS) and a biocompatible polymer (PVP) or by polymerizing in-situ its monomer vinyl pyrrolidone (ISPVP). This results in nanotube suspensions with the optimal luminescent properties of SDBS-SWNT suspensions at any pH value between 1 and 11. We combine literature evidence of the strong PVP-SDBS micelle surface interaction together with SWNT spectroscopic signatures and different types of single molecule images to propose a model explaining the behavior of PVP-SDBS-SWNT at neutral and low pH. The suspensions remain stable (weeks) at all pH as well as in saline buffers. Importantly, they are also stable after extended dialysis (below the CMC of SDBS), and retain fluorescence after lyophilization and resuspension in deionized water (DI). This should open many applications in biology because the nanotubes can be suspended in a biocompatible environment. Using individual SWNT near-infrared photoluminescence microscopy, we show that ISPVP-SDBS-SWNTs suspensions are stable and strongly luminescent in living cell cultures, where they interact efficiently on cell membranes and do not display any sign of aggregation.

2.4 Experimental Methods

2.4.1 Suspensions Preparation

Suspensions of HiPco tubes were dispersed in one weight percent (wt%) anionic (SDBS, $C_{18}H_{29}O_3SNa$; SDS, $C_{12}H_{25}O_4SNa$), neutral (Pluronics (F88, $(C_5H_{10}O_2)_n$)) or cationic (cetyl trimethyl ammonium bromide (CTAB, $C_{19}H_{42}NBr$)) surfactants as well as in polymers (PVP, $(C_6H_8ON)_n$) alone using homogenization, ultrasonication, and ultracentrifugation following standard literature methods [O'Connell et al., 2002]. All suspensions were characterized spectroscopically and by atomic force microscopy (AFM) to ensure that the SWNT were predominantly suspended as individuals. Suspensions in SDBS, SDS, pluronic, and CTAB were also added to 1 wt% PVP or 1 wt% VP to obtain suspensions of mixed wrapping agents. The surfactant-polymer molar ratio was maintained above the critical micelle concentration (CMC) for all surfactants used (SDBS, CMC = 1.6 mM, SDS, CMC = 8.35 mM, F88, CMC = 1.6 mM, and CTAB, CMC = 1.3 mM). Suspensions of mixed wrapping agents were prepared using one part SWNT-surfactant and three parts PVP to result in a final concentration of 10 mg/L SWNT, 0.25 wt% surfactant and 0.75 wt% PVP or VP. All spectroscopy measurements were performed on 1 mL samples in a sterile cuvette.

2.4.2 Optical Ensemble Measurements

Fluorescence, absorbance, and liquid-phase Raman measurements were first performed on solutions at neutral pH. Successive additions of 1 μL aliquots of 1 N hydrochloric acid (HCl) or 1 M KOH were then added until the desired pH was reached. Bulk fluorescence and absorbance measurements were measured with a Nanospectralyzer Model NS1, Version 1.97 (Applied Nanofluorescence, Houston, Texas, USA). The SWNT fluorescence was excited at 660 nm and emission was detected between 900 and 1400 nm. Absorbance was measured in the visible and near infrared (400 to 1400 nm); integration times of 500 ms and 10 accumulations were used in both cases.

Absorbance at 763 nm was used to normalize the fluorescence spectra. Liquid phase Raman was performed using a 785 nm laser excitation in a Renishaw system fitted with a microscope. Spectra were collected with a Renishaw Raman Macro Sampling Set (Wire 2 software) between 100 to 3200 cm^{-1} with 10 sec exposure time and 1 sec accumulation. Time dependent luminescence spectra of SWNT suspensions in SDBS, PVP, or PVP-SDBS were taken every 0.5 sec (50 msec exposure time and 6 accumulations) using a 660 nm laser excitation. Successive measurements began immediately after a SWNT suspension at neutral pH was injected into 10 μL of 1 M HCl.

2.4.3 Near-Infrared Fluorescence Microscopy of Individual SWNT

Individual semiconducting SWNTs were visualized by near-infrared fluorescence microscopy. Prior to imaging, a 5 μL drop of nanotube suspension was placed between a glass slide and a microscope coverslip sealed with silicon grease to prevent drying. SWNT samples were mounted onto an inverted epifluorescence microscope (Nikon TE-2000) equipped with a 60× oil emersion objective (NA = 1.4, Nikon). Samples were continuously excited by a circularly polarized beam of a 658 nm diode laser. The infrared photoluminescence emitted by the SWNTs passed through long-pass infrared filters (LP950, Thorlabs) and was detected by a liquid nitrogen-cooled camera (16-bit InGaAs 2-D array, OMA-V 2-D, Princeton Instruments). Single frame acquisition images of the SWNT luminescence were recorded with an integration time of 50 ms [Tsyboulski et al., 2005].

2.4.4 Cell Culture and Preparation for Microscopy

HEK293 cells were cultured on microscope cover slips in DMEM medium supplemented with streptomycin (100 g/ml), penicillin (100 U/mL), and 10% bovine serum in a humidified atmosphere (95%) at 5% CO_2 and 37 ^oC. Cells were used for 12–14 passages and were transferred every 4–6 days. Cells were exposed to 50 μl of VP-

SDBS-SWNTs suspension (of 1 μg/mL added to 1.5 mL of culture medium) for either 5 min at room temperature or 12 hrs at 37 °C. The cells were then washed with fresh medium. The cover slips were mounted in a custom chamber with culture medium and all data were taken at room temperature. Atomic force microscopy images were taken using a Nanoscope IIIa system (Veeco/Digital Instruments) in tapping mode at a scan rate of 2 Hz and scan size of 10 μm. 20 μL of SWNT suspension was spin coated at 3000 RPM onto a freshly cleaved mica surface (Ted Pella, Inc.) and rinsed with DI water.

2.4.5 Lyophilization and Re-Suspension of ISPVP-SDBS-SWNT

Lyophilization was done using a Freezemobile 3+SL (The Virtis Company). 1 mL of ISPVP-SDBS-SWNT was freeze-dried at -40 °C for 12 hrs. Resuspension was accomplished by addition of 1 mL DI water and mild shaking.

2.5 Results and Discussion

2.5.1 Ensemble Spectroscopic Measurements of PVP-SDBS-SWNT in Neutral and Acidic Conditions

The PVP-SDBS-SWNT suspensions studied here are prepared in two steps. First, raw HiPco SWNTs are dispersed in SDBS (1 weight percent (wt%)) through a standard decant procedure (see Experimental Methods). Second, a fraction of the suspension is mixed with a 1 wt% solution of PVP (55 kDa, unless otherwise stated) to obtain a surfactant-polymer complex. The variations of the luminescent properties of PVP-SDBS-SWNT suspensions with pH are presented in Figure 2.1. Figure 2.1.a–b show the 2D-contour plots of the fluorescence intensity vs. excitation and emission wavelength before (Fig 2.1.a) and after (Fig 2.1.b) addition of HCl (1N) to reach a final pH of 2. Strikingly, the addition of acid enhanced the luminescence intensity at every wavelength. For a simpler quantitative analysis, the emission spectra of the

semiconducting SWNT obtained from excitation at 660 nm are displayed (Fig 2.1.c). The spectra were normalized to the maximum intensity peak at 1120 nm of the initial suspension, which can be assigned to the (7,6) tube [Weisman et al., 2004]. Upon acidification, the fluorescence intensity was enhanced approximately by a factor of two. Interestingly, this enhancement was accompanied by a narrowing and blueshift ($\sim$25 nm) of every peak (see section 2.7.1, Figure 2.11). To complement these observations, the liquid-phase Raman spectra of the suspensions were also measured. Using 785 nm excitation, which selectively excites semiconducting nanotubes with diameters near 1 nm [Strano et al., 2003; Dresselhaus et al., 2007a], we studied the radial breathing modes (RBM, 100 – 300 cm^{-1}) [Heller et al., 2004] as well as fluorescence in the 1620 – 3200 cm^{-1} range. The fluorescence obtained by liquid-phase Raman confirmed the previous observations (Fig 2.1.c-d). The degree of bundling could be monitored by comparing the area under the RBM of individual semiconducting SWNTs (150 to 250 cm^{-1}) with that of SWNT that are brought into resonance with the laser due to the presence of SWNT bundles* (250 – 300 cm^{-1}) [Heller et al., 2004; Doorn et al., 2004; Dyke et al., 2005]. The RBM area of the individual SWNTs increased after acidification (Fig 2.1.e), suggesting that a subtle change in the SWNT immediate environment had occurred. The degree of bundling, however, was unchanged because the bundling peak remained constant. Moreover, the location and amplitude of the G-peak remained constant after acidification, indicating that the SWNTs were not protonated (see section 2.7.2, Figure 2.12) [Strano et al., 2003]. A variety of acids besides HCl (phosphoric, nitric, and sulfuric) were surveyed and similar fluorescence enhancements and spectral shifts were observed with each. Analogous effects were obtained using SDS instead of SDBS. Altogether, these observations support the notion that at low pH, PVP-SDBS-SWNTs remain individual and that a change must

---

*The RBM of the bundles or bundling peak is the excitation of metallic (11,0) and semiconducting (10,2) tubes with the 780 nm laser that are redshifted into resonance due to the presence of bundles in the bulk solution

occur in the close environment of the SWNTs.

2.5.2 Comparison of SDBS-SWNT, PVP-SWNT and PVP-SDBS-SWNT Fluorescence Ensemble Properties

To elucidate further the mechanism of PVP-SDBS-SWNT luminescence enhancement upon acidification, we compared the behavior of SDBS-SWNT, PVP-SWNT and PVP-SDBS-SWNT suspensions. Figure 2.2.a–b display the fluorescence spectra of SDBS-SWNT (black curve) and PVP-SDBS-SWNT (red curve) recorded at pH 7 (a) and pH 2 (b) after normalization to the (7,6) SWNT for SDBS at pH 7. The spectra in Figure 2.2.a indicate that when PVP is added to SDBS-SWNTs, the fluorescence peaks decrease in intensity, redshift and broaden [O'Connell et al., 2002]. Thus, the addition of PVP at pH 7 strongly affects the luminescence properties of SDBS-SWNTs. When acidified to pH 2, SDBS-SWNT solutions bleach partially, in analogy with previously reported data for SDS [Strano et al., 2003], to an extent that is dependent on the tube diameter (Figure 2.2.b). As discussed above, PVP-SDBS-SWNT suspension displayed the opposite trend when acidified down to pH 2, because the fluorescence is enhanced to about 80% of the level of SDBS-SWNTs at neutral conditions (pH 7). It is important to note that if PVP is added to a SDBS-SWNT suspension that was previously acidified, only a partial luminescence recovery is observed (∼10%) in accordance with previous reports [Strano et al., 2003]. Therefore, PVP must be present in the SDBS-SWNT solution before the addition of acid to obtain a suspension that is highly fluorescent at low pH.

Figure 2.2.c shows the kinetic time course of the (7,6) fluorescence peak intensity for the three different SWNT suspensions following the addition of acid. The fluorescence intensities were normalized to the initial condition at pH 7. For the first 200 seconds, the luminescence intensity of the SDBS-SWNT suspension does not evolve noticeably (black dots). It then decreases substantially (with faster rates for the small
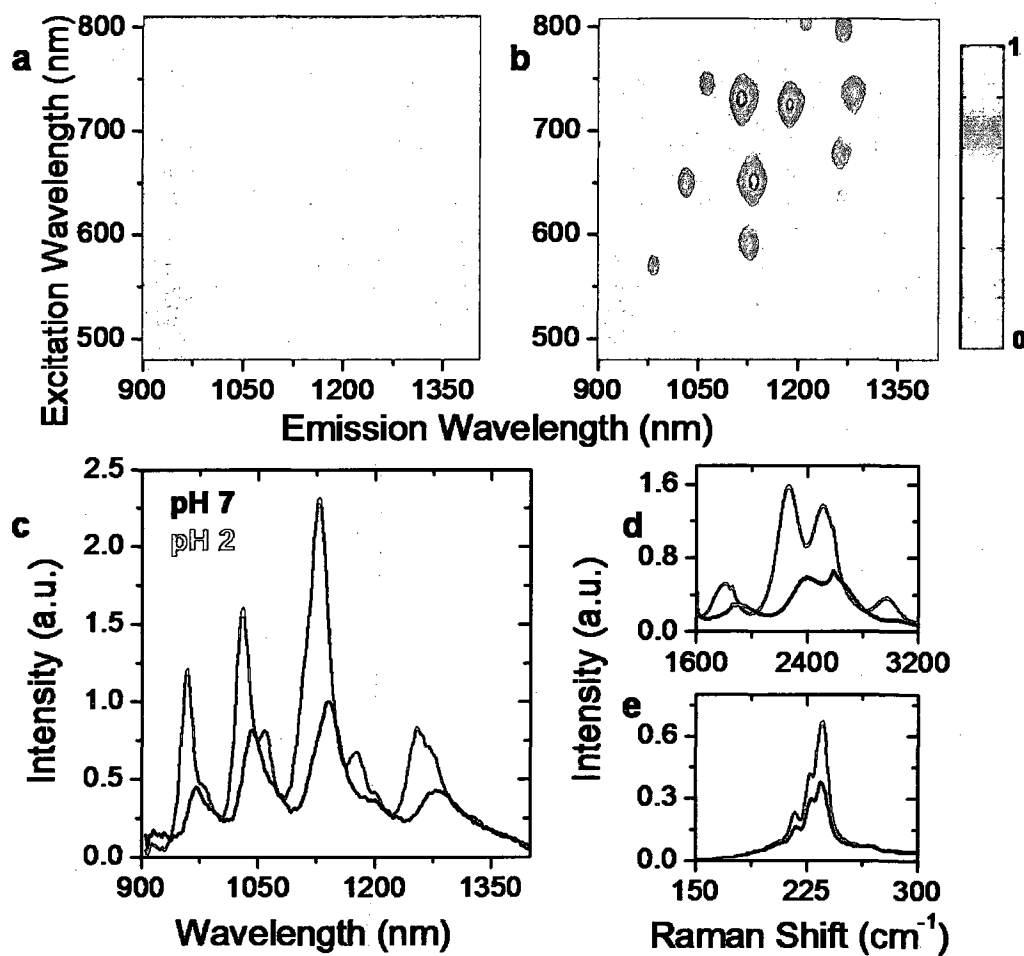
Figure 2.1 : Ensemble spectroscopic measurements of PVP-SDBS-SWNT in neutral and acidic conditions. (a–b.) Contour plots of fluorescence intensity vs. excitation and emission wavelength of PVP-SDBS-SWNT at pH 7 (a) and 2 (b). Identical intensity scales are used in (a) and (b). (c.) Fluorescence spectra obtained from excitation at 660 nm from PVP-SDBS-SWNT at pH 7 (black) and 2 (red). (d–e.) Liquid phase Raman spectroscopy using excitation at 785 nm (see text). Fluorescence (d) and RBM (e) spectra obtained at pH 7 (black) and 2 (red).

band-gap tubes, i.e., large diameters, section 2.7.3, Figure 2.13) before we eventually observed that the nanotubes flock out of the solution. We tentatively attribute this behavior to a slight destabilization of the SDBS micelle in acidic conditions which creates openings through which acid can contact SWNTs and consequently quench fluorescence [Strano et al., 2003; Dukovic et al., 2004]; the result at low pH is complete destabilization of the micelles and flocculation of the SWNTs. The flocculation onset time (depicted by the triangle on Figure 2.2.c) can vary from minutes to hours depending on the amount of acid and concentration of surfactant (section 2.7.4, Figure 2.14). Notably, the fluorescence of a neat PVP-SWNT suspension (no SDBS) is considerably weaker than that of SDBS suspended tubes (only ~3% of that of SDBS-SWNTs at equal concentrations)[†]. Nevertheless, the same acidification procedure can be performed and indicates that PVP-SWNT luminescence is barely affected by acidification: luminescence drops only by 5% drop over 24 hours (blue dots in Figure 2.2.c). In clear contrast to the two preceding suspensions, PVP-SDBS-SWNTs exhibit a very different kinetic behavior upon acidification. The fluorescence peak intensity increased rapidly until it stabilized at about twice the initial fluorescence level (red dots in Figure 2.2.c). This rapid increase suggests an entirely different mechanism than for SDBS-SWNT suspensions.

The steady fluorescence intensity levels of the (7,6) peak are presented for SDBS-SWNT (in black) and PVP-SDBS-SWNT (in red) as a function of pH (Figure 2.2.d). Both curves were normalized to SDBS-SWNTs at neutral pH. In both nanotube suspensions, the fluorescence remained constant between pH 11 and 7. In acidic conditions, the relative intensity of SDBS-SWNT suspensions decreased gradually as the pH was lowered to 1 with subsequent flocculation, whereas that of PVP-SDBS-

---

[†]Obtaining a stable and highly luminescence suspension of SWNTs in PVP alone is very difficult to accomplish without the aid of previously suspended tubes in surfactants like SDS or SDBS. The fluorescence yield of PVP wrapped tubes is only 3 percent of that of SDBS.

SWNT increased continuously to reach 80% of the luminescence level of the benchmark SDBS-SWNT suspension at pH 7. The luminescence of PVP-SDBS-SWNT remained stable for weeks over the entire pH range studied.

Finally, we tested the influence of the charge of the surfactant. When PVP is added to SWNTs initially suspended in cationic or neutral surfactants (CTAB and Pluronics), no spectral changes are observed, in stark contrast to anionic surfactants. This can be related to previous reports that showed no interactions between PVP and cationic micelles, while strong interactions between PVP and anionic micelles were observed [Zhai et al., 2004]. In addition, when various types of acids were added to SWNTs suspended in cationic surfactants, efficient fluorescence bleaching was observed comparable with previous observations [Strano et al., 2003] regardless of the presence of PVP. Altogether, our data suggest that in PVP-SDBS-SWNT suspensions, SDBS remains around the SWNTs after the addition of PVP and is not replaced by PVP. Instead, a surfactant-polymer complex is formed that wraps the SWNTs and apparently provides an efficient and stable barrier between the SWNTs and their local environment. This amounts to a bi-layer assembly of complementary polymers, reminiscent of the chemistry underlying fuzzy nanoassemblies [Decher, 1997] and nanotube/polyelectrolyte composites [Mamedov et al., 2002] and suggests a perhaps general approach for engineering a variety of specialized SWNT bio-platforms.

We believe that the conformation of PVP together with its strong affinity to SDBS are at the origin of the redshift and partial quenching of luminescence that follows the addition of PVP to SDBS-SWNTs at neutral and basic pH (Figure 2.2.a). PVP contains both hydrophobic and hydrophilic moieties; thus, it adopts a coiled conformation in neutral and basic solutions [Khanal et al., 2004]. The strong interaction of PVP with the outer surface (due to the charge transfer between the sulfate molecule from SDBS and the nitrogen group from PVP [Zhai et al., 2004]) of

the SDBS micelles surrounding the SWNTs is therefore likely to destabilize slightly the micelle structures and subsequently disturb the SWNT luminescent properties. Upon acidification, PVP is known to protonate and swell [Atkin et al., 2005]. This conformational change (Figure 2.2.c) allows SDBS to reform its ideal micelle structure around the SWNT, rewrapping it completely. This seems to occur before the incoming acid could destabilize the micelle and quench the SWNT luminescence, because this would happen at a longer time scale (Figure 2.2.c). In this model, the stabilizing layer (PVP) prevents any disruption of the micelles and the luminescence that is obtained in acidic environment is comparable to that of SDBS-SWNTs at basic conditions.

2.5.3 AFM and Near-IR Study of Individual PVP-SDBS-SWNT

The model presented above was deduced from spectroscopic measurements of bulk suspensions. To test it, we used several imaging techniques that can probe the environmental and photophysical properties of individual nanotubes. Figures 2.3.a–b show AFM images of nanotubes prepared under basic and acidic conditions. In order to allow a statistical analysis on a large number of tubes, AFM images were primarily acquired on samples that were cleaned to remove the excess of PVP and SDBS (see methods). It should be noted that it was more difficult to obtain clean surfaces at neutral conditions at which the excess of surfactant could not be fully removed, compared to acidic conditions (Figure 2.3.a–b). Close examination of these images indicates that the vast majority of the tubes are individual. This conclusion was also confirmed by cryo-TEM (see Figure 2.4.1). The quantifications of the apparent nanotube height at pH 7 (3.9 ± 0.1 nm, ± standard error of the mean (s.e.m), n = 102) and at pH 2 (1.3 ± 0.04 nm, n = 102) indicate that nanotubes are surrounded by a bulkier structure at pH 7 than at pH 2 (Figure 2.3.c–d). To rule out the effect of the cleaning procedure, and obtain a more precise picture of the PVP-SDBS structure around the nanotubes, we obtained AFM images using samples that had not been pre-cleaned. Examples of tubes isolated from the excess of surfactant/polymer mixture
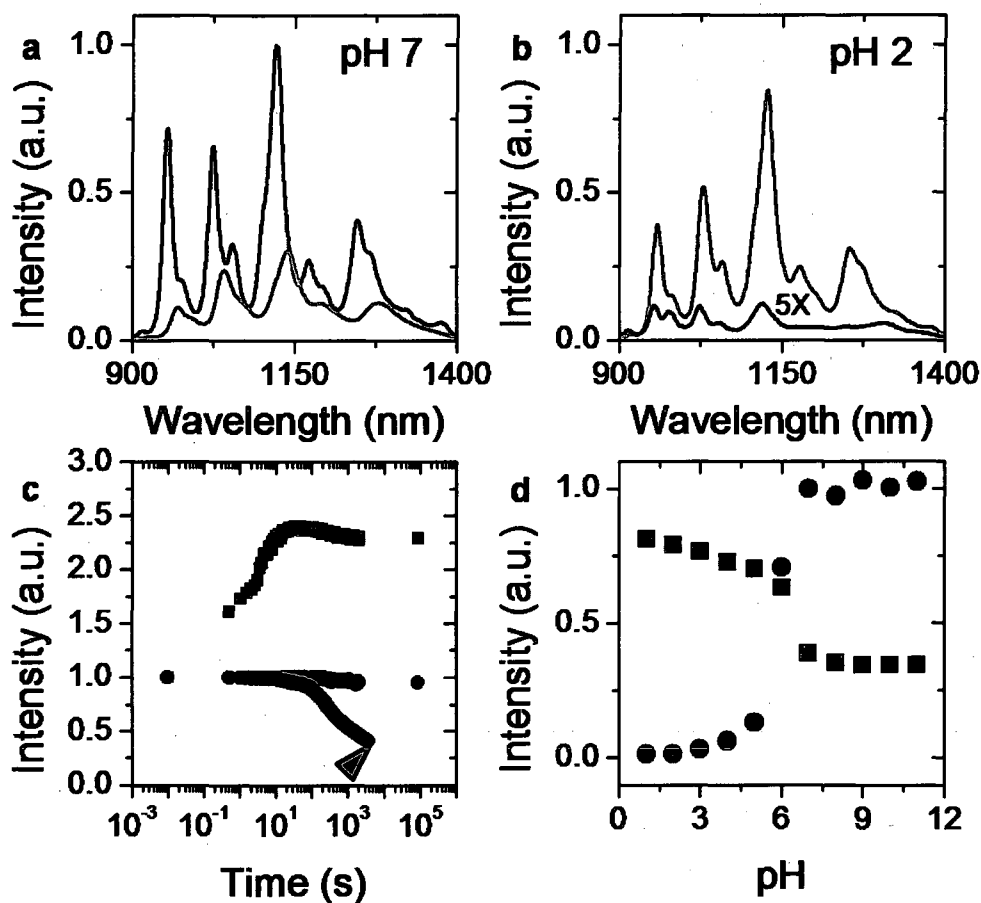
Figure 2.2 : Comparison of SDBS-SWNT, PVP-SWNT, and PVP-SDBS-SWNT fluorescence ensemble properties. (a–b) Comparative fluorescence spectra recorded at pH 7 (a) and 2 (b) from SDBS-SWNT (black curves) and PVP-SDBS-SWNT (red curves). All spectra were normalized to absorbance at 763 nm. (c.) Kinetic time course of the (7,6) fluorescence peak intensity (1120 nm) for the three different SWNT suspensions following the addition of acid. SDBS-SWNT in black, PVP-SWNT in blue, and PVP-SDBS-SWNT in red. The triangle indicates occurrence of flocculation of the SDBS-SWNT suspension. (d.) Steady state fluorescence intensity of the (7,6) peak of SDBS-SWNT (black) and PVP-SDBS-SWNT (red) as a function of pH. All steady state values were normalized to SDBS-SWNT at pH 7.

are presented in Figure 2.3.e–f. The different conformations of PVP-SDBS presented in our model are now evident: at pH 7, large agglomerates (~10 nm) are present on the SWNTs whereas at pH 2, a more uniform and thinner coverage is observed (6 nm).

The photoluminescence of the SWNT suspensions was investigated further by direct visualization in a near-IR microscope [Tsyboulski et al., 2005]. Figure 2.3.g–h show movie snapshots obtained from dilute PVP-SDBS-SWNT suspensions in neutral and acidic conditions. The majority of the luminescence spots are likely to originate from individual SWNT [Tsyboulski et al., 2005] and are diffraction limited (2 pixels correspond to 670 nm in Figures 2.3.g–h) which indicates that most of them have a length shorter than 670 nm. In these images, the luminescence spots appear brighter in the acid suspension than in the neutral suspension. This observation is quantified by computing and comparing the cumulative distributions of the individual fluorescent spot signal amplitudes obtained in the two conditions (Figure 2.3.i) [Schmidt et al., 1995]. The signals were obtained from the statistical fit of each spot spatial distribution by a 2-D Gaussian function [Schmidt et al., 1996]. The widths of the distributions are identical and broad. This dispersion in signal amplitudes is likely due to the heterogeneity in length and electronic structure of the SWNTs present in the sample. The distribution of the acidic suspension (shown in red) is however shifted toward higher luminescence signals compared to the neutral condition (shown in black). This indicates that the luminescence of each individual PVP-SDBS-SWNT is enhanced in acidic conditions. More precisely, the ratio of the median value of the two distributions is equal to 1.9, in good agreement with the fluorescence enhancement observed in bulk using the same excitation 660 nm wavelength (Figure 2.1.c).

Figure 2.4 shows cryo-TEM images of SWNTs initially prepared in basic and acidic conditions. Close examination of these images indicates that the vast majority of the SWNT are individuals; this corroborates the spectroscopic and microscopic ob-
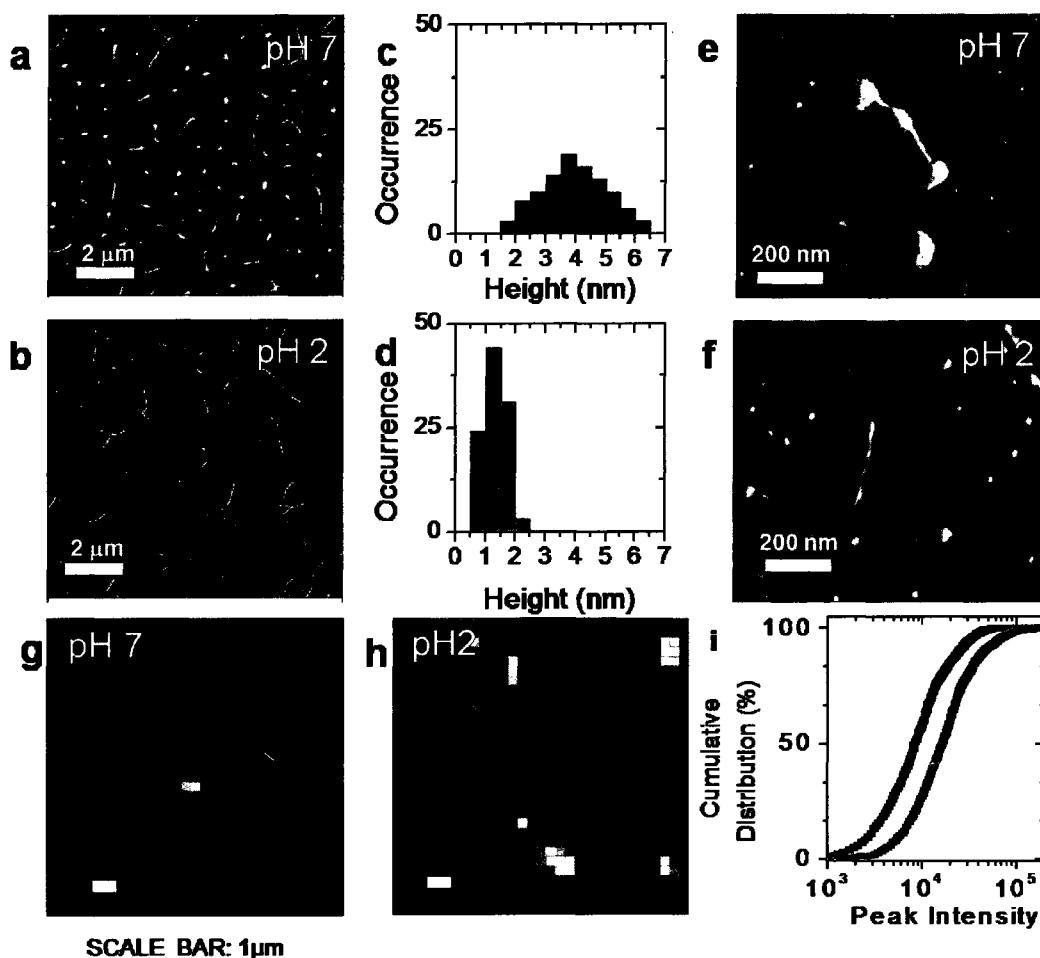
Figure 2.3 : (a–b.) Representative AFM images of PVP-SDBS-SWNT at pH 7 (a) and 2 (b) after surface cleaning. (c–d.) Distributions of the SWNT heights measured on several similar AFM images at pH 7 (c) and 2 (d). (e–f.) same as in (a–b) but without surface cleaning. (g–h.) Near-infrared luminescence images of individual PVP-SDBS-SWNT at pH 7 (g) and 2 (h). Scale bars are 1 μm. (i.) Cumulative distribution of the luminescence signal amplitudes of the peaks detected in 400 similar images as (g–h), at pH 7 (black) and 2 (red).

servations that indicate the suspensions are stable and the SWNTs remain individual at all pH.
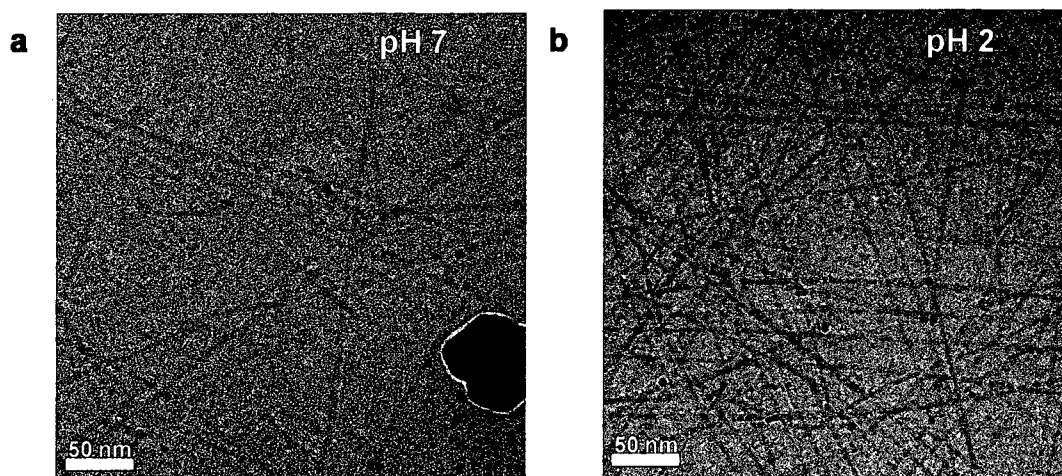
Figure 2.4 : Cryo-transmission electron microscopy (cryo-TEM) images were obtained using a JEM FasTEM 2010. Samples were prepared using a Vitrobot automated system (FEI Company) and a supporting lacy carbon grid (330M, Ted Pella, Inc.)

2.5.4 Fluorescence Properties and AFM Images of VP-SDBS-SWNT

To examine the hypothesis that coiled-PVP disrupts the SDBS micelle conformation at pH 7, causing the SWNT luminescence peaks to redshift, broaden, and decrease in intensity compared to SDBS tubes alone, we examined the influence of PVP molecular weight (MW). Figure 2.5.a shows the ratio of the integrated area of PVP-SDBS-SWNT to SDBS-SWNT fluorescence (excited at 660 nm) measured at pH 7 as a function of the PVP MW (from the monomer VP to 1 MDa). This ratio decreased with the MW in the range of the monomer to polymers of about 55 kDa. This spectroscopic dependence on MW indicates that the size, and certainly the conformation, of PVP have a significant effect on the optical properties of the SWNTs. Moreover, we found that the arrangement of PVP on the SDBS-SWNT complex could be controlled by polymerizing the monomer VP directly on the micelle. VP is known to undergo cationic polymerization [Stevens, 1999]; this process is slow at pH 7, but progresses rapidly at low pH (see Fig 2.6 and section 2.5.4 for polymerization procedure and characterization). Therefore we made in-situ polymerized PVP (ISPVP) by intro-

ducing VP at pH 7, allowing sufficient time for the diffusion of VP to the micelles, and subsequently acidifying the solution, causing complete polymerization of the VP and entrapping the SDBS-SWNT complex (complete polymerization of VP is also important because VP monomer is carcinogenic, whereas PVP is harmless) [Stevens, 1999]. Importantly, once the VP was polymerized in-situ under acidic conditions, the fluorescence intensity remained constant when the solution was returned to basic conditions (see Figure 2.7 and section 2.5.4 for ISPVP-SDBS-SWNT fluorescence stability).

Based on the behavior at neutral pH, ISPVP or very small PVP chains should yield encapsulated PVP-SDBS-SWNTs with ideal spectroscopic properties. This is indeed the case. First, the fluorescence intensity of VP-SDBS-SWNT suspensions is almost constant (red triangles) from alkaline (pH 11) to acidic (pH 1) conditions (Figure 2.5.d). This contrasts with the behavior of SDBS-SWNTs (black circle) and PVP-SDBS-SWNTs (red squares) as previously discussed in Figure 2.2.d. Second, VP-SDBS-SWNTs display essentially the optimal luminescence properties of SDBS-SWNTs suspensions (narrow and almost identical peak positions) but in the whole pH range investigated (Figure 2.5.b). The residual small redshifts ($\sim$10 nm) together with the absence of effect of pH suggest that ISPVP interacts strongly with the SDBS micelles but without disrupting the SDBS micelle conformation (see more details about ISPVP in Section 2.5.4). AFM images support this picture, since individual ISPVP-SDBS-SWNTs are found with a uniform thin coating (typically 5 nm) along their surface (Figure 2.5.c). ISPVP can serve as an alternative method for producing non-covalent encapsulated SWNTs whose intrinsic properties are retained in different environments [Kang and Taton, 2003; Wang et al., 2007]. Control experiments with pyrrolidone molecules that do not polymerize under acidic conditions (i.e., 1-methyl-2-pyrrolidone (NMP) and N-ethyl-2-pyrrolidone) did not show protection at low pH. To further examine the stability of the polymer wrapped SDBS-SWNTs system, we
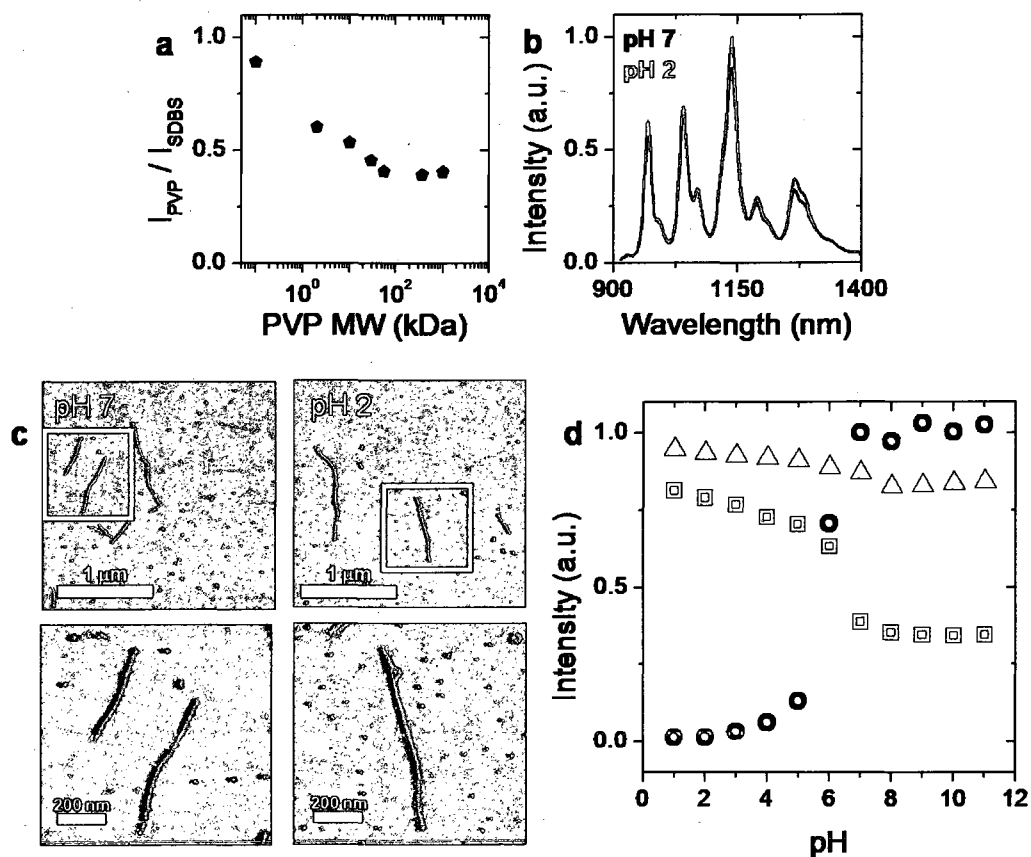
Figure 2.5 : Fluorescence properties and AFM images of VP-SDBS-SWNT. (a.) The ratio of the integrated areas of the fluorescence of PVP at different molecular weight to SDBS at 660 nm excitation and pH 7. (b.) The fluorescence of VP-SDBS-SWNT at neutral (in black) and acidic (in red) conditions. (c.) AFM images of covered SWNT with VP. (d.) The effect of pH to the relative intensity of the (7,6) peak of VP-SDBS-SWNT suspensions (red triangles; open symbols are previously shown data Figure 2.2.d).

freeze-dried the ISPVP-SDBS-SWNT suspensions (see section 2.5.5) at neutral pH and resuspended them in deionized water.

In-Situ-Polymerization of Vinyl Pyrrolidone (ISPVP)

Polymerization of vinyl pyrrolidone (VP) was conducted under acidic conditions. The polymerization was monitored using Raman spectroscopy while tracking the depletion of the stretching vibrational mode of the monomer carbon-carbon double bond (C=C) at 1638 cm^{-1} [Miyazaki et al., 2003]. Liquid phase Raman was performed using a 660 nm laser excitation wavelength in a sterile glass vial (1 mL mixture of 1:1 v/v VP and sodium dodecylbenzene sulfonate (SDBS, 1 wt% in H$_2$O)). Spectra were collected between 1550 to 1850 cm^{-1} with 10 sec exposure time and 1 accumulation in a Renishaw macro sampling set (Wire 2 software) system. Figure 2.6.a shows the Raman peak of the C=C bond from VP at pH 7 (in black), VP at pH 2 (green) and the polymer vinyl pyrrolidone (55 kDa molecular weight, Aldrich) at pH 7 (in blue). It is important to notice that the PVP signal did not change at any pH. Upon acidification, the Raman signal for the C=C peak (1638 cm^{-1}) decreases to that of PVP which indicates that the C=C double bond is no longer present and polymerization has occurred. Figure 2.6.b shows the intensity of the C=C signal at pH 7 and 2 as a function of time. At neutral conditions (pH 7), the intensity did not exhibit any noticeable changes within the first 20 minutes of preparing the 1:1 VP:SDBS mixture. When 20 μL of 1 N HCl was added to the solution, the intensity of the C=C peak decreased rapidly to the PVP base line (red dotted line). In order to eliminate the possibility of the SDBS contributing to the polymerization of the monomer, VP was diluted in DI water only and the rate of polymerization was compared to that of the VP:SDBS mixture. Figure 2.6.b shows that the rate of polymerization of VP in SDBS (black squares) is comparable with the rates found in DI water (green triangle and red dots). Moreover, the intensity of the C=C decay was fitted with a first order polynomial decay further indicating the polymerization of VP was induced by acidification reaching completion after 10 min.
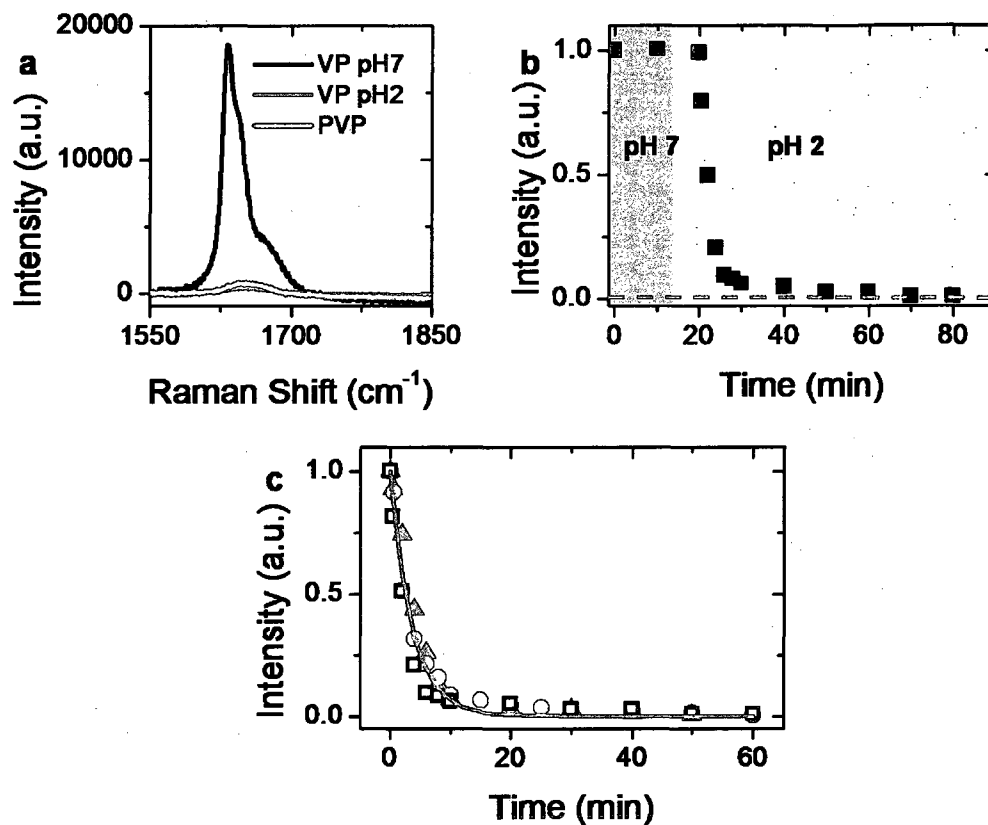
Figure 2.6 : In-situ polymerization of VP to PVP. (a.) Raman signal for the C=C peak (b.) Polymerization of VP. (c.)Rates of polymerization

ISPVP-SDBS-SWNT Fluorescence Stability

It was demonstrated in SDBS-SWNT systems that after VP is polymerized via acidification, the fluorescence intensity of the SWNT mixture remains unchanged. We carried out a set of experiments in which VP-SDBS-SWNT suspensions at neutral conditions (pH 7, Fig. 2.7.A) were brought to pH 2 (Fig. 2.7.B) (fluorescence was taken 45 minutes after acid injection to allow for complete polymerization of VP) and then taken back to basic conditions (pH 11, Fig. 2.7.C). This procedure allows for the

in-situ polymerization of the VP to take place arround the SWNTs without changing the spectroscopic characteristics of the ISPVP-SDBS-SWNT system. SDBS-SWNT suspensions were also subjected to this procedure as a negative control. Figure 2.7 shows the fluorescence intensity of the (7,6) tube (1120 nm) ISPVP-SDBS-SWNT (red dots) and SDBS-SWNTs (black squares); all intensities were normalized to SDBS-SWNT at pH 7. The intensity of SDBS-SWNT follows the previously reported trend of rapid bleaching in acidic conditions (pH 2) and a complete recovery of the fluorescence when the suspension is brought back to basic conditions [O'Connell et al., 2005; Cognet et al., 2007] (black squares). In contrast, VP-SDBS-SWNT suspensions did not exhibit any major changes in the fluorescence intensity at any pH corroborating our hypothesis that ISPVP does not alter the fluorescence properties of the SWNT suspensions.

2.5.5   Lyophilized ISPVP-SDBS-SWNT Suspension

Figure 2.8.a–c shows that ISPVP-SDBS-SWNT suspensions can be lyophilized to dryness and then readily resuspended in water by mild shaking. The positions of the spectroscopic peaks (absorbance, liquid-phase Raman, and fluorescence) remain unchanged; their relative fluorescence intensities after resuspension is approximately 75% of the initial intensity (Figure 2.8.d). Such small loss in intensity after resuspension may be due to the formation of small flocs of few polymer wrapped SWNTs during the freeze-drying process; however, inspection by brightfield optical microscopy (63×) did not reveal any structures. The retention of nearly all of the NIR fluorescence after resuspension confirms that ISPVP encapsulates the SDBS-SWNTs effectively without affecting the pristine electronic structure of the SWNT. In contrast, resuspension of SDBS-SWNTs after freeze-drying is not feasible.
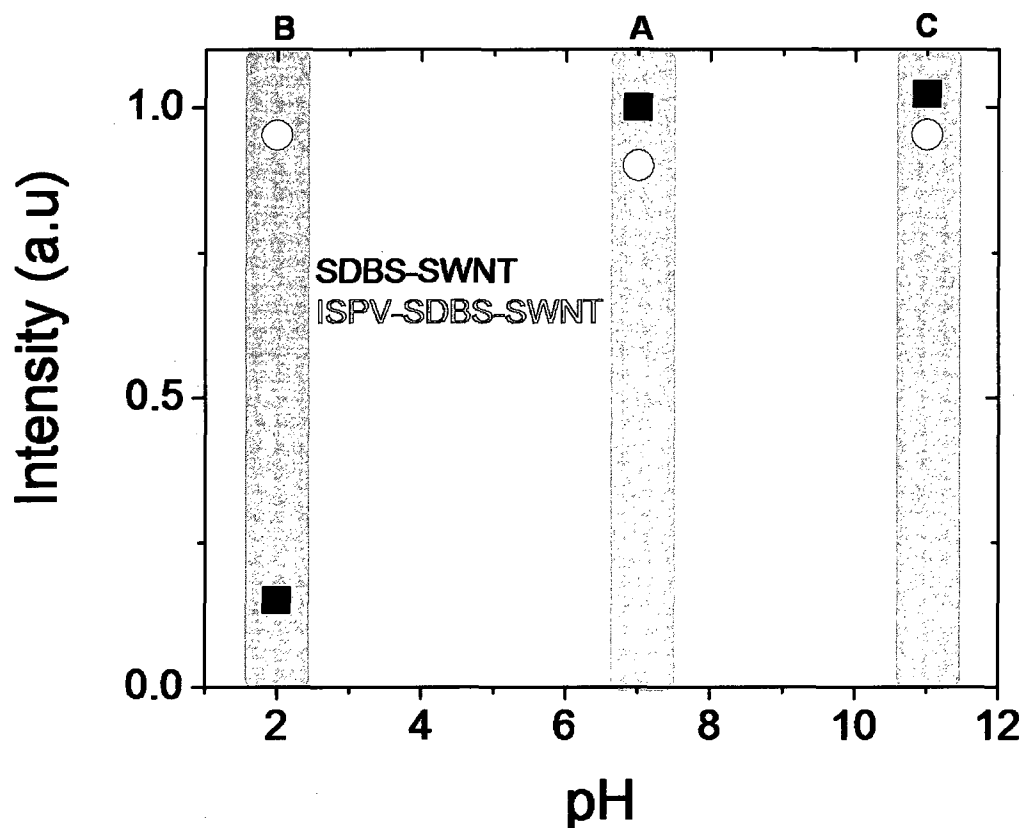
Figure 2.7 : ISPVP-SDBS-SWNT fluorescence stability, red dots ISPVP-SDBS-SWNT, and black squares SDBS-SWNT. Fluorescence of the two suspensions were first obtained at pH 7 (A) brought to pH 2 and a second fluorescence measurement was obtained (B), and finally taken to basic conditions at pH 11 (C).

2.5.6 Schematic Model

A schematic of the model proposed in this work is presented in Figure 2.9. This model shows that PVP or VP adsorbs strongly to the external surface of the SDBS micelle due to charge transfer between the sulfate group of SDBS and the nitrogen of PVP and/or VP. At neutral pH, the conformational state of PVP slightly disrupts the micelle conformation of SDBS and subsequently disturbs the SWNT luminescent properties while the monomer does not, as previously discussed. In acidic conditions,
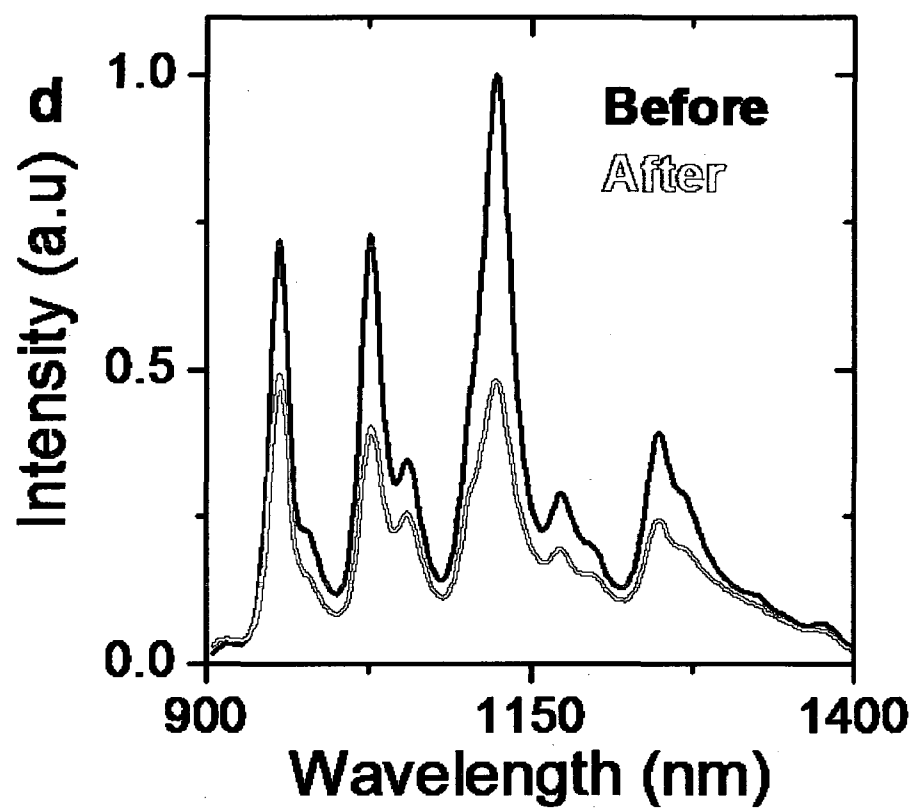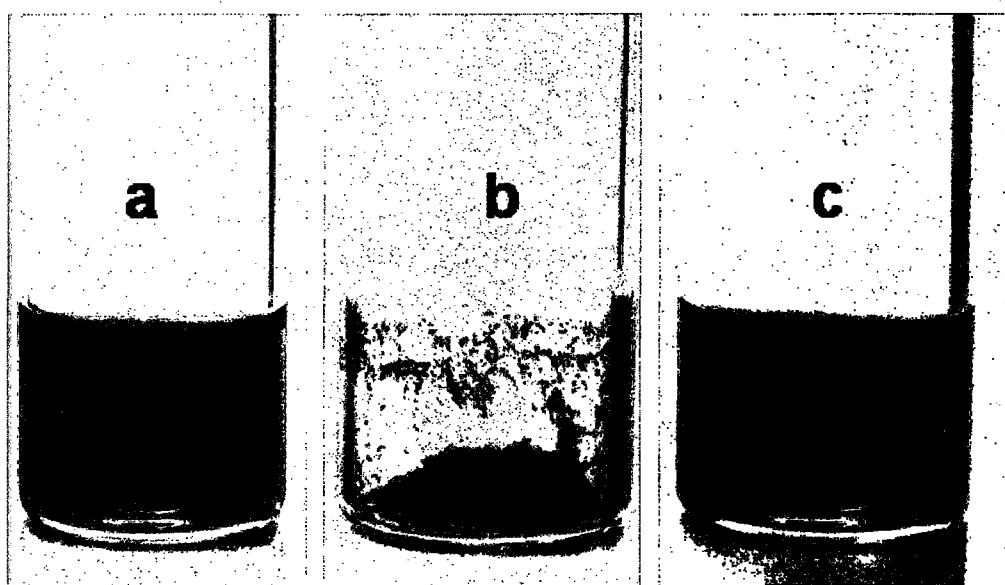
Figure 2.8 : Lyophilized ISPVP-SDBS-SWNT suspension. (a.) ISPVP-SDBS-SWNT suspension. (b.) Lyphilized ISPVP-SDBS-SWNT suspension. (c.) Resuspended ISPVP-SDBS-SWNT suspension. (d.) Fluorescence spectra before and after lyophilization.
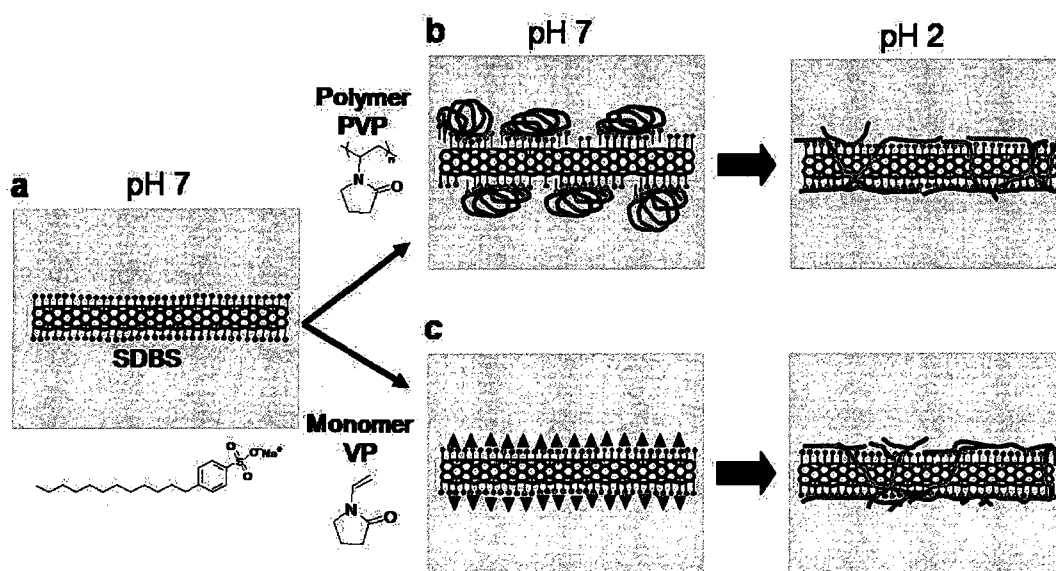
Figure 2.9 : Schematic illustration of the model. (a.) SDBS-SWNT at pH 7. (b.) PVP-SDBS-SWNT at pH 7 and 2. (c.) VP-SDBS-SWNT at pH 7 and 2 for which cationic polymerization occurred.

conformational changes of PVP and VP polymerization make both VP and PVP efficient wrappers of the SDBS-SWNTs, without displacing the SDBS micelle. The resulting surfactant-polymer complex that surrounds the SWNTs efficiently provides a stable barrier between the SWNTs and their local environment. Interestingly, this model implies that the ISPVP-SDBS interactions strengthen the micellar structure and therefore should protect the tube luminescence properties from different types of environmental factors, which would benefit important applications. Along this line, we first tested the luminescence stability of the ISPVP-SDBS-SWNT suspension far below the CMC of SDBS ($\sim$0.25 wt%). The suspensions remain stable and luminescent upon dilutions down to 1.25×10^{-4} wt% of SDBS, after which any further dilution prevented accurate fluorescence measurement (not shown). The model with characteristic spectrum is shown in section 2.7.5, Figure 2.15.

2.5.7 VP-SDBS-SWNT in Biological Environments

We then tested the effect of salinity on the stability of the suspensions: ISPVP-SDBS-SWNTs were diluted at a final concentration of 1 mg/L in 10 × phosphate buffer saline (PBS). Neither the suspension stability nor the luminescence was affected by this treatment (Figure 2.10.a). The combination of the above experimental findings suggests that ISPVP-SDBS-SWNTs suspensions should be a highly effective material in cellular environments. To this end, we exposed live cultured HEK293 cells to ISPVP-SDBS-SWNTs suspensions, either for 5 min at room temperature or overnight at 37 °C. Figures 2.10.b–c show the examples of near-IR luminescence images of a cell recorded at two different foci after 5 min SWNT incubation. The images were acquired in the presence of white light to identify the outline of cell. Highly luminescent and diffraction limited spots that likely originate from individualized SWNTs interacting with the surface of the cells are found, as expected because of the positive charge carried by PVP. In order to assess whether the luminescent spots originated from individual tubes, we first checked that the spots displayed a polarized absorption as evidence by using a rotating linearly polarized excitation [Tsyboulski et al., 2005] (not shown). Second, the narrow spectra originating from luminescent spots found at the surface of the cells (Figure 2.10.d) further support the presence of individual SWNT [Tsyboulski et al., 2005]. Comparable results were obtained after the 12 hour incubation procedure at 37 °C, indicating that ISPVP-SDBS-SWNTs remain perfectly suspended in biological environments. Further studies will be needed to address the question of cytotoxicity of such materials, but we can envision from our results, together with the known biocompatibility of PVP [Guowei et al., 2007], that ISPVP-SDBS-SWNTs should be advantageous in biological applications.

2.6 Conclusions

By studying the spectroscopic and structural behavior of mixtures of anionic surfactant and PVP polymers at various pH, we have identified a mixture (ISPVP-SDBS)
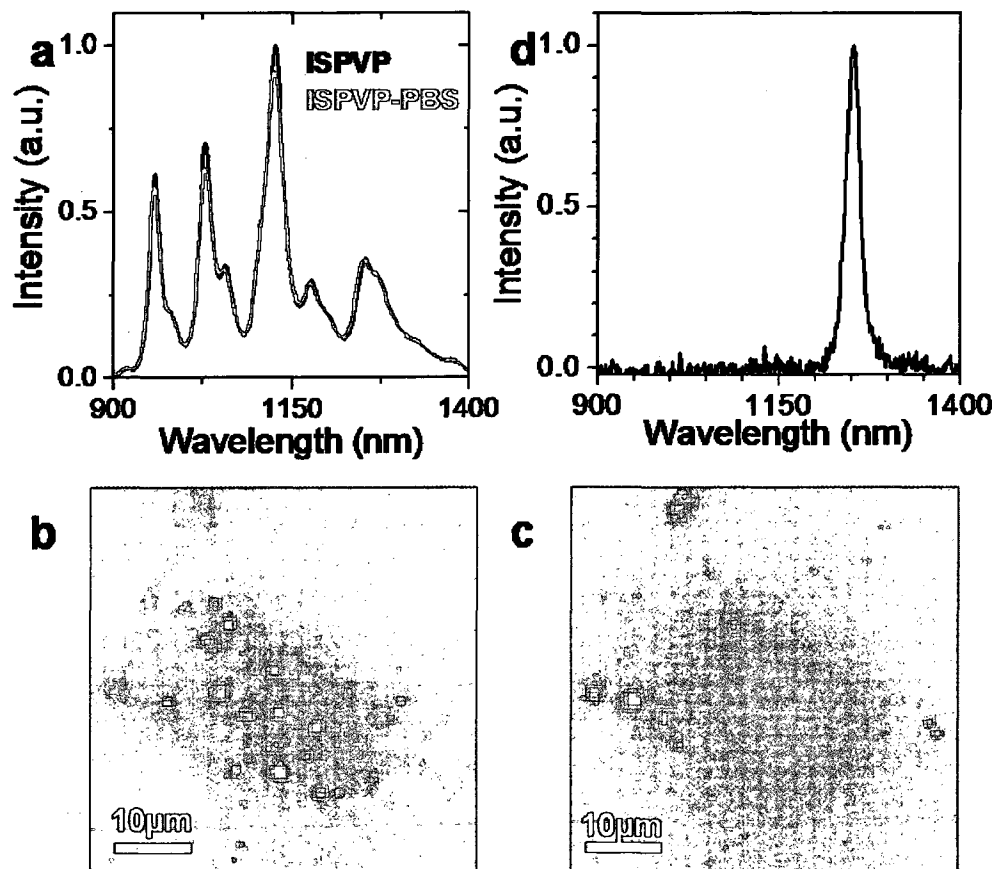
Figure 2.10 : VP-SDBS-SWNT in biological environments. (a.) Comparative fluorescence spectra of VP-SDBS-SWNT recorded in water at pH 7 (in black) and in 10 PBS (in red) at identical concentrations. (b–c.) Near-infrared luminescence images of the same cell incubated 5 min with ISPVP-SDBS-SWNT at different foci: at the apical membrane (b.) and at the surface of the coverslip (c). The luminescence images were acquired in the presence of white light to identify the outline of the cell. Scale bars are 10μm. (d.) Narrow spectrum measured from a luminescence spot identified at the surface of a cell, a signature of individual ISPVP-SDBS-SWNTs. Images taken from Duque et al. [2008a].

that might serve as a universal wrapping agent of individual SWNTs. Due to its effectiveness at all pH, in high saline environments as well as in physiological media, we foresee an extensive use of ISPVP-SDBS-SWNTs in fields as varied as chemistry,

physics, and biology for fundamental research as well as more applied technologies.

2.7 Appendix 2

2.7.1 2-D Luminescence Shifting

Figure 2.11 shows that SDBS-SWNT fluorescence decreases without any shifting of its peaks. On the other hand, PVP-SDBS-SWNT fluorescence increases after addition of HCl. Also, we were able to capture the narrowing and blueshifting of the fluorescence peaks after acidification for PVP-SDBS-SWNTs (bottom right, (7,6) tube).
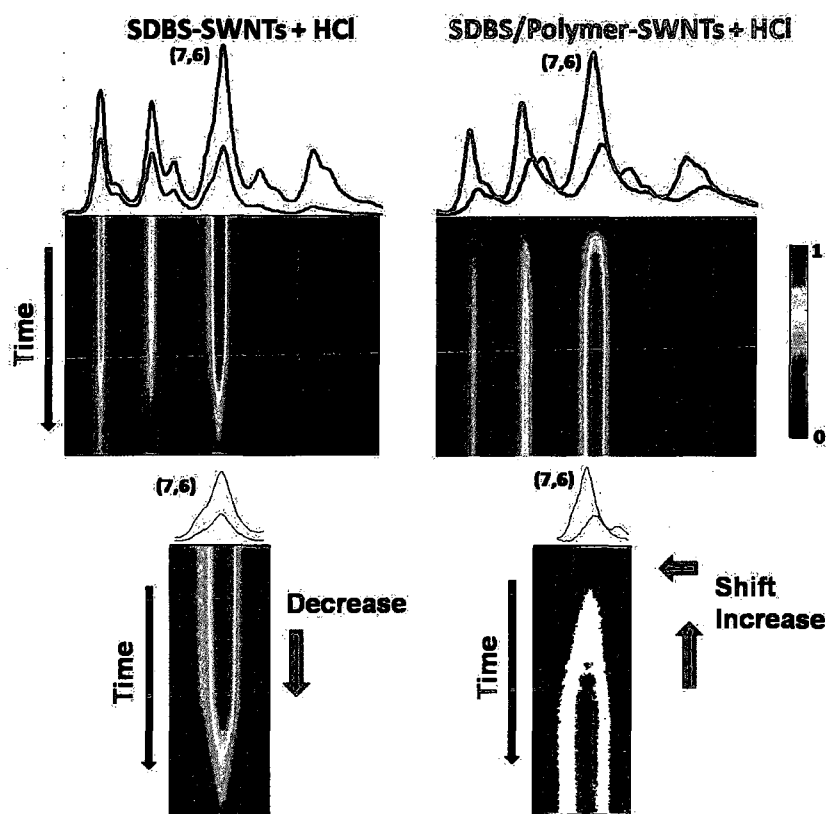
Figure 2.11 : Kinetic time course for SDBS-SWNTs and PVP-SDBS-SWNTs after addition of acid.

2.7.2 Liquid-Phase Raman

Liquid-phase Raman using 785 nm excitation of PVP-SDBS-SWNTs in acid (red) and at basic (black) conditions. The insert shows the G-band before and after acidification with no shift indicating that the sidewall of the tubes was not protonated by the acid.
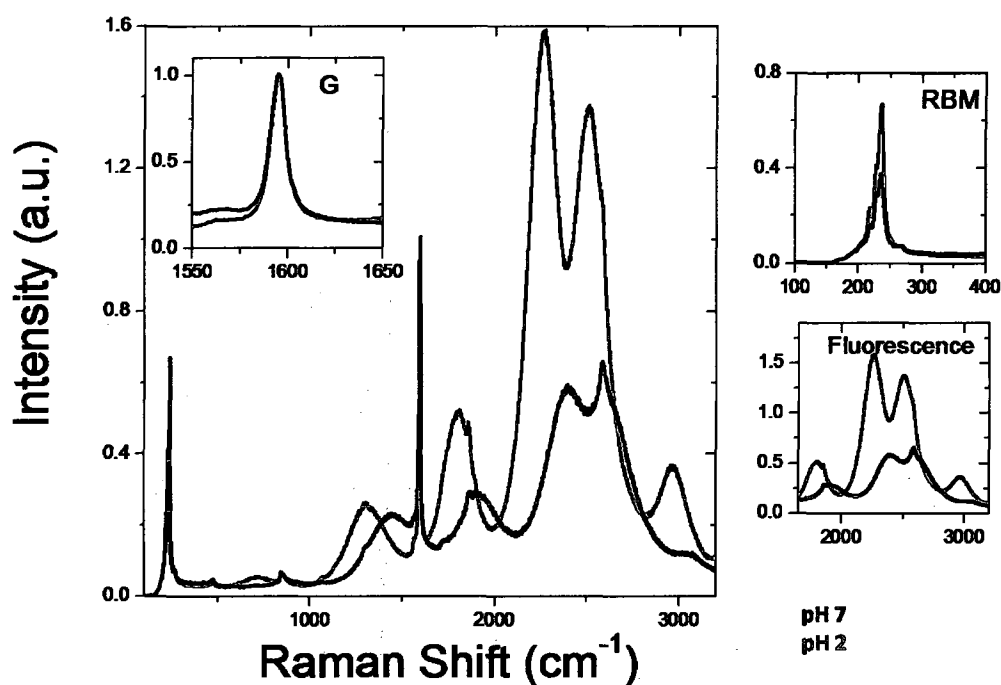
Figure 2.12 : Liquid-phase Raman with 785 nm excitation wavelength.

2.7.3 Diameter Dependence Fluorescence Quenching

Figure 2.13 shows that the large diameter tubes have a faster quenching rate than small diameter tubes after addition of HCl.
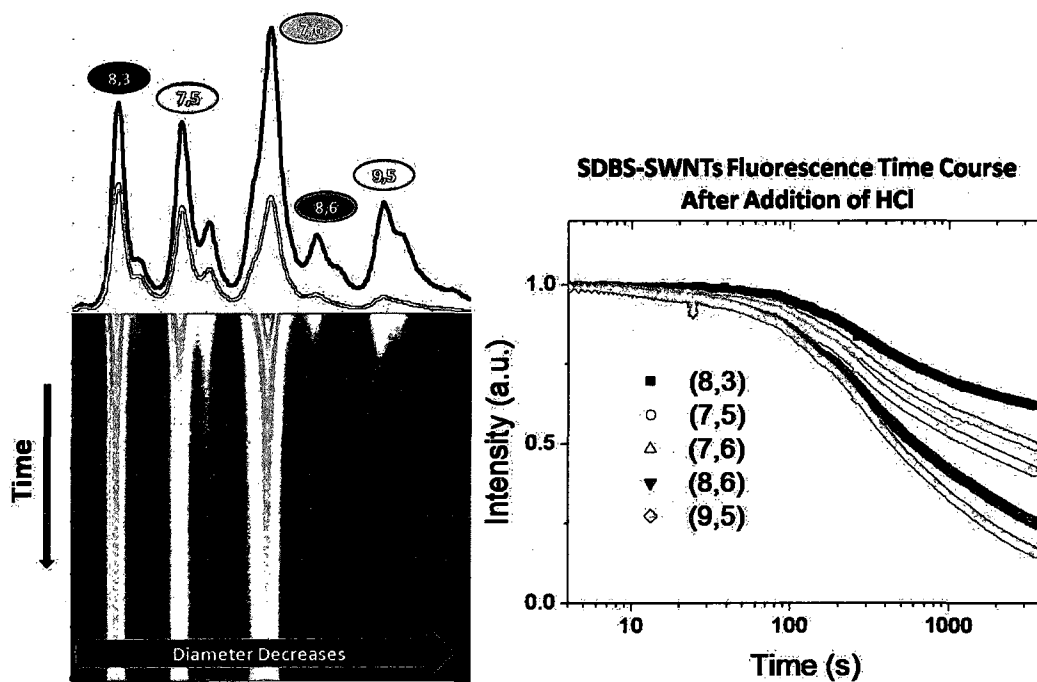
Figure 2.13 : Photoluminescence quenching after addition of HCl.

2.7.4 Surfactant Dependence Fluorescence Stability

Figure 2.14 shows the fluorescence quenching of the (7,6) tube as a function of time for SWNT suspensions prepared at different surfactant concentrations (1 wt%, 1.5 wt%, and 2.0 wt%) after addition of HCl. We observed that as the concentration of surfactant increases, the time before the suspension flocculates increases. Also shown ia a representative image of SWNT flocculation after acidification.

2.7.5 Model and Characteristic Spectrum

Figure 2.15 shows the model explained in section 2.5.6 with the representative fluorescence spectrum at each step.
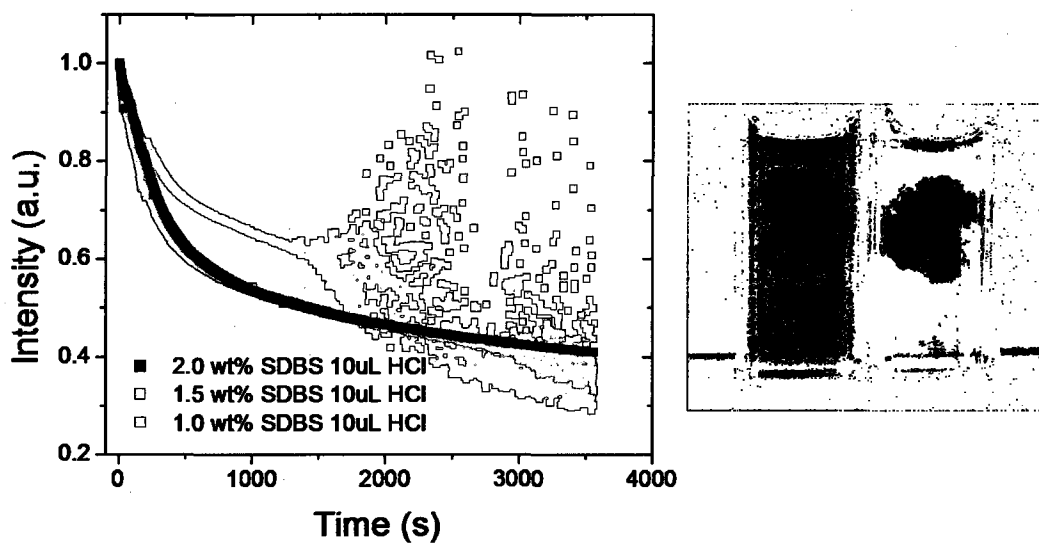
Figure 2.14 : Surfactant dependent fluorescence stability.

2.7.6   VP Polymerization Raw Data

Figure 2.16 shows the polymerization of VP upon acidification monitored via Raman spectroscopy. It is the raw data used to obtain Figure 2.6 (see section 2.5.4).
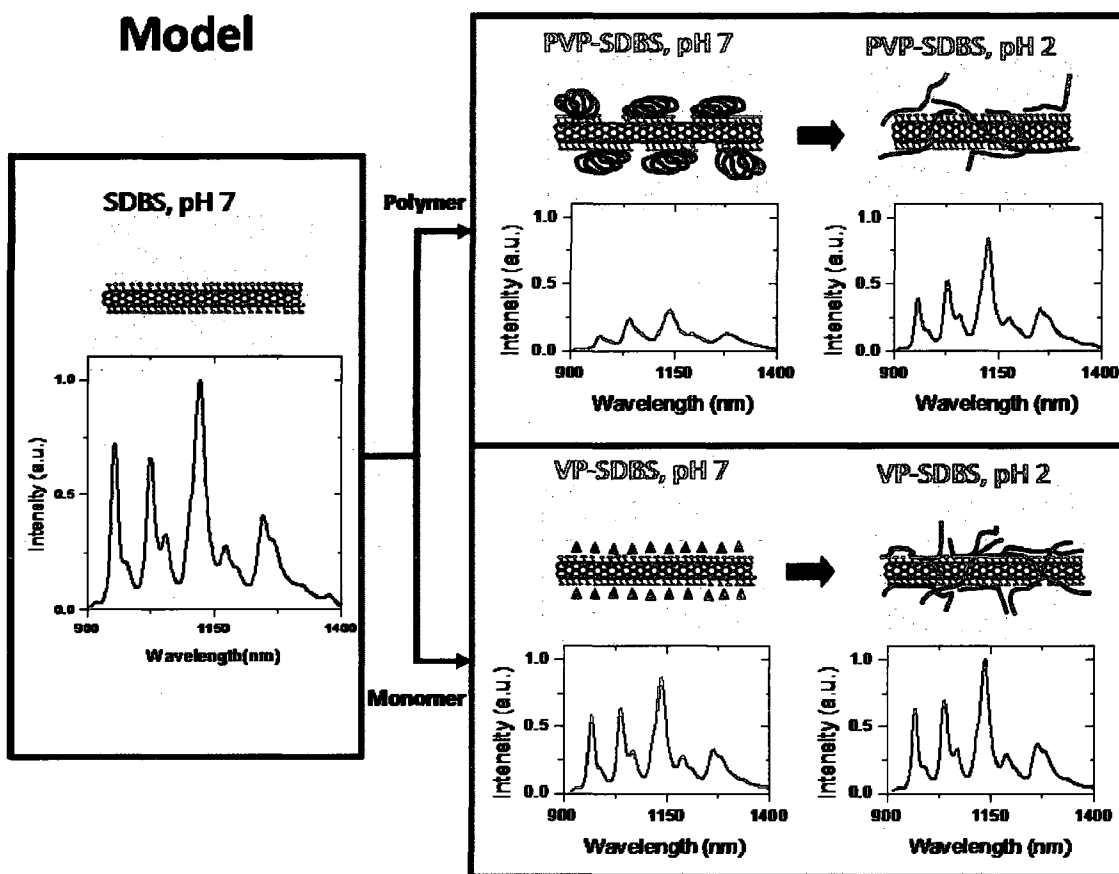
Figure 2.15 : Model with representative luminescence spectrum
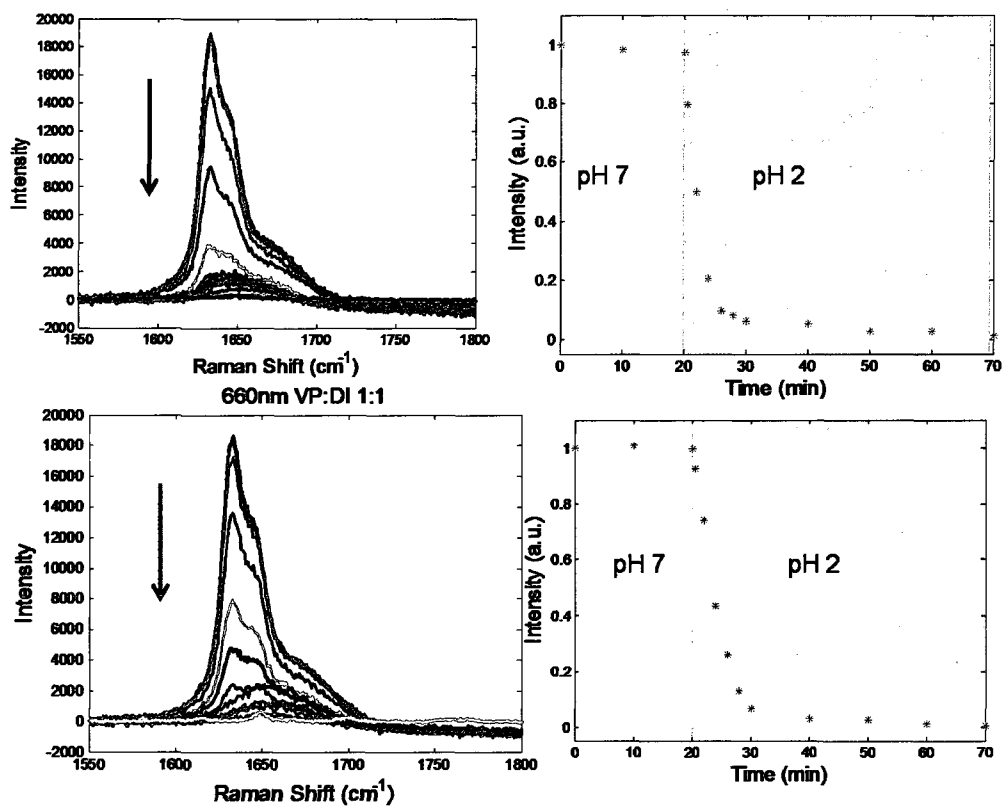
Figure 2.16 : The polymerization of VP to PVP was monitored using Raman spectroscopy by tracking the depletion of the stretching vibrational mode of the monomer carbon-carbon double bond (C=C) at 1638cm^{-1} of a 1 mL mixture of 1:1 v/v VP and SDBS before and after the addition of HCl, Section 2.5.4.

Chapter 3

Environment and Synthesis Related Luminescence Properties of Ensembles and Individual Single-Walled Carbon Nanotubes

3.1 Objective

The aim of this chapter is to explore the synthesis and environmental dependence of the luminescence properties of individual SWNTs in ensembles and at the single molecular level. The single molecular detection experiments were done in collaboration with the Nanophotonics laboratory at the Centre de Physique Moléculaire Optique et Hertzienne (CPMOH), Université de Bordeaux and CNRS, France, under the supervision of Professor Brahim Lounis and Professor Laurent Cognet. The study was performed during a 5 month stay at CPMOH. The ensemble characterization was conducted at Rice University.

The luminescence properties were studied using individual SWNTs in agarose gels, in solution, and after spin-coating onto a glass slide. The tubes were from two different synthesis procedures (HiPco and CoMoCat) and suspended in different anionic surfactants (sodium dodecylbenzenesulfonate (SDBS) or sodium deoxycholate (DOC)). We were able to demonstrate the strong dependence of the luminescence of the tubes on intrinsic and extrinsic factors such as sample preparation, sample inhomogeneities, defects, and tube synthesis.

3.2 Background

Single-wall carbon nanotubes (SWNTs) offer great potential in a number of photonics applications, ranging from quantum optics to biology, owing to their excellent properties including intrinsic near-infrared luminescence, quantum emittance, and excellent photostability. On a fundamental point of view, SWNTs constitute model systems for the study of the spatio-temporal dynamics of excited states in 1-D systems. Experimental and theoretical work has shown that SWNT optical properties are excitonic in nature with strong coupling between the dark and bright excitonic states [Dresselhaus et al., 2007b; Berciaud et al., 2008; Shaver et al., 2007; Wang et al., 2005; Cognet et al., 2007; Perebeinos et al., 2004; Zhao and Mazumdar, 2004].

Multiple efforts have been made to understand these excitonic states and how they affect the optical properties of SWNTs; however both fundamental and applied developments are still hindered by poor control over the synthesis and processing methods which affect the structure, sidewall quality, and environment of SWNTs. The intrinsic luminescence properties of the nanotubes are often masked by uncontrolled extrinsic factors that make comparison between studies difficult. For example, fluorescence quantum yield (QY%) measured from ensembles or single nanotubes range between 10^{-3} to 7 % [Hogele et al., 2008; Carlson et al., 2007; Crochet et al., 2007; Huang et al., 2004; O'Connell et al., 2002; Lefebvre et al., 2006] in literature. Accordingly, measurements of the luminescence lifetime of nanotubes have been reported from 5 to 200 psec with excitonic dynamics that exhibit monoexponential or bioexponential decays depending on the report [Berciaud et al., 2008; Huang et al., 2004; Berger et al., 2007; Gokus et al., 2008; Hagen et al., 2005; Hirori et al., 2006; Wang et al., 2004a].

The large heterogeneity of results is often attributed to extrinsic factors such as sample inhomogeneities (different tube types and manufacturers) [Huang et al., 2004],

environmental interactions (i.e., surfactants, molecules and/or tube–tube, tube–substrate) [Duque et al., 2008a], and structural defects during the dispersion process [Tsyboulski et al., 2007]. Spectroscopy performed on individual nanotubes lift part of this heterogeneity, but comparisons between different synthetic methods, suspension agents, and nanotube environments are still lacking.

3.3 Overall Findings

Here we combined continuous wave (cw) and time resolved spectroscopy performed on individual nanotubes to investigate several extrinsic factors which deeply influence their luminescence properties, namely the synthesis, dispersion, and environment of the nanotubes produced by the HiPco and CoMoCat processes. We report histograms of fluorescence intensity, full width at half maximum intensity (FWHM), fluorescence peak location, and exciton lifetime measurements of more than 1000 SWNTs, all performed by exciting the (6,5) SWNTs to their second order excitonic resonance ($E_{22} = 567$ nm). Using the same preparation procedure, we concluded that (6,5) HiPco SWNTs have $\sim 2\times$ brighter near-IR luminescence than CoMoCat SWNTs with narrower FWHM fluorescence intensities and longer excitonic lifetimes. Also, DOC appears to be a better wrapping agent than SDBS because DOC-SWNTs are more stable (less blinking), brighter, and exhibit narrower distributions than SDBS-SWNTs. Moreover, we showed that different batches of HiPco-produced SWNTs display substantial differences in their chirality distribution and luminescence properties.

3.4 Experimental Methods For Single Molecular Study

3.4.1 Sample Preparation

HiPco and CoMoCat SWNT samples were prepared using brief tip ultrasonication (~ 10 sec) in aqueous suspensions of the anionic surfactants sodium deoxycholate

(DOC) and sodium dodecylbenzenesulfonate (SDBS) at a concentration of 1 weight percent (wt%). The SWNT suspensions were then immobilized using 5 wt% agarose gels sandwiched between a glass cover slip and a glass slide.
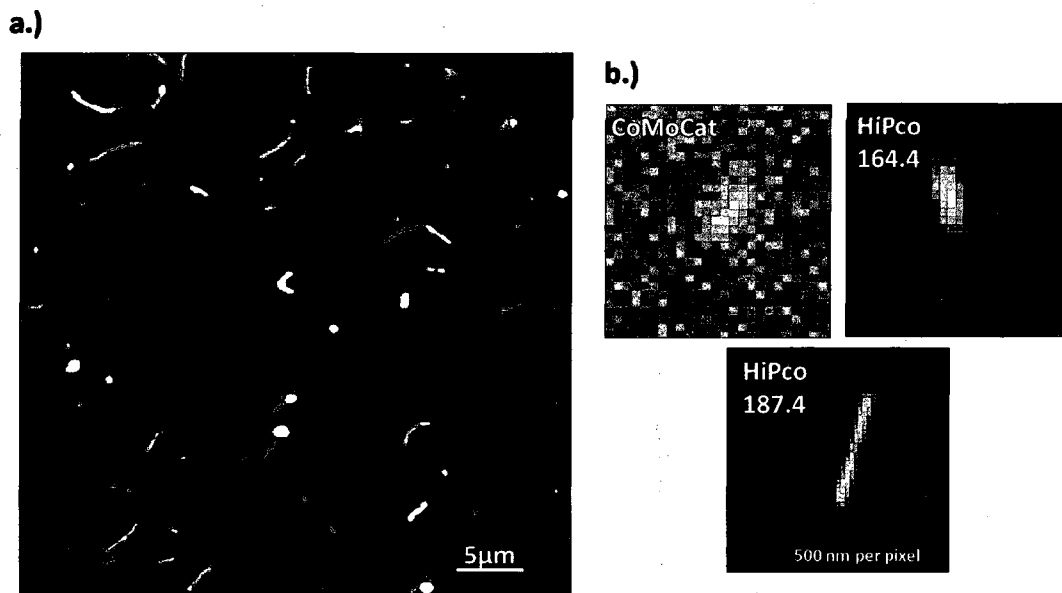
Figure 3.1 : Sample composition of SWNTs with photothermal (a) and near-IR (b) images

Photothermal Images

Photothermal Heterodyne Imaging (PHI) is a very important technique in SWNT characterization because it has the unique ability to probe all tube types and optical absorption transitions of individual SWNTs (Sec. 1.2.2) in contrast to near-IR images which only probe semiconducting species.

3.4.2 Setup

All measurements were performed using (6,5) SWNTs (peak emission at 975 nm) excited at their second order excitonic resonance (E_{22} = 567 nm) with a continuous

wave (cw) dye laser (rhodamine) pumped with an Argon ion laser or an optical parametric oscillator (OPO) system (~150 fsec pulse, 76 MHz repetition rate or every 12.5 ns) coupled into a fiber optic. Near-IR luminescence was detected using cw excitation wavelength in an inverted microscope with a high numerical aperture (NA) immersion objective (NA = 1.4×) in wide field or confocal configuration using a CCD camera or a silicon avalanche photodiode, respectively. To switch from wide field to confocal imaging, a removable lens was placed between the fiber optic and a dichroic mirror. Near-IR emission spectra were detected using a 1-D nitrogen-cooled Si-CCD camera on a silicone avalanche photodiode. Exciton lifetime measurements were performed using the pulsed beam and a single photon counting Picoharp 300 (Fig 3.2). In confocal mode, cw or pulsed beams were focused at 430 ± 50 nm (FWHM). All laser beams were circular polarized and the experiments were carried out at room temperature.

3.4.3   Criteria for Choosing Tubes

Our criteria for choosing which tubes to study were that they be of type (6,5), be longer than the diffraction limit of our system (~3 pixels), and be sufficiently brighter than the background (signal-to-noise ratio ≥ 3×) as shown (Fig. 3.3).

3.5   Experimental Methods For SWNT Ensembles

Raw HiPco samples were prepared and characterized using procedures described in Chapter 2, Experimental Section 2.4.

3.6   Results and Discussion for Individual (6,5) Tubes

3.6.1   SWNT Intensity and Spectrum

We first compared the intensity and spectral width of the luminescence emitted by individual (6,5) SWNTs from two different HiPco batches (164.4, in red and 187.4,
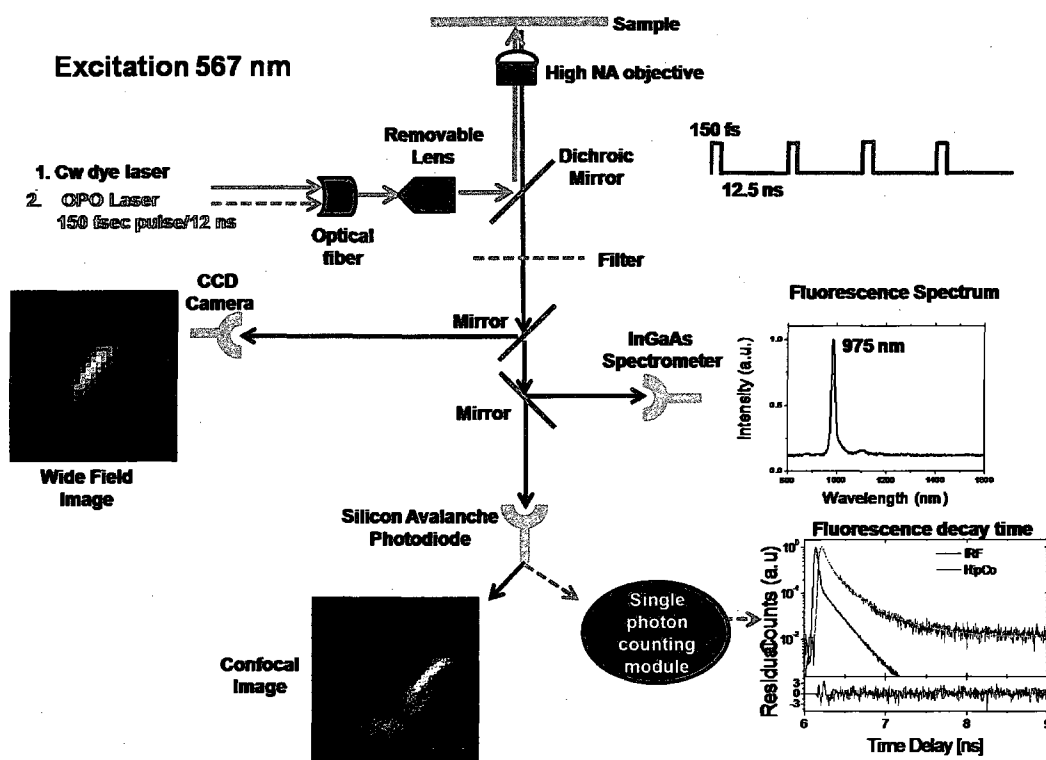
Figure 3.2 : Instrumental setup for spectroscopy study

in black) and one CoMoCat lot (RCU-A013, in blue) dispersed in aqueous suspensions as describe in Section 3.4.1. This procedure produces suspensions of relatively long tubes with very high luminescence properties as evidenced by the photothermal [Berciaud et al., 2004, 2006] and near-IR images [Cognet et al., 2008b; Tsyboulski et al., 2005] in Figure 3.1. For accurate observations, the SWNTs were then immobilized by mixing the suspensions in agarose gels (5 wt%). The preparation was sandwiched between a glass cover slip and a glass slide and mounted on an inverted microscope for examination. Transferring of the aqueous suspension into the gels did not generate significant statistical error on the luminescence intensity of the tubes as shown in section 3.9.2. In all measurements, we selected the (6,5) SWNT species (peak emission at 975 nm) by exciting them resonantly at their second order excitonic

Image Selection

Good Tube

• **Long**
• **Brighter than background**

Bad Tubes

• **Long**
• **NOT Brighter than background**

• **Not Long**
• **Brighter than background**
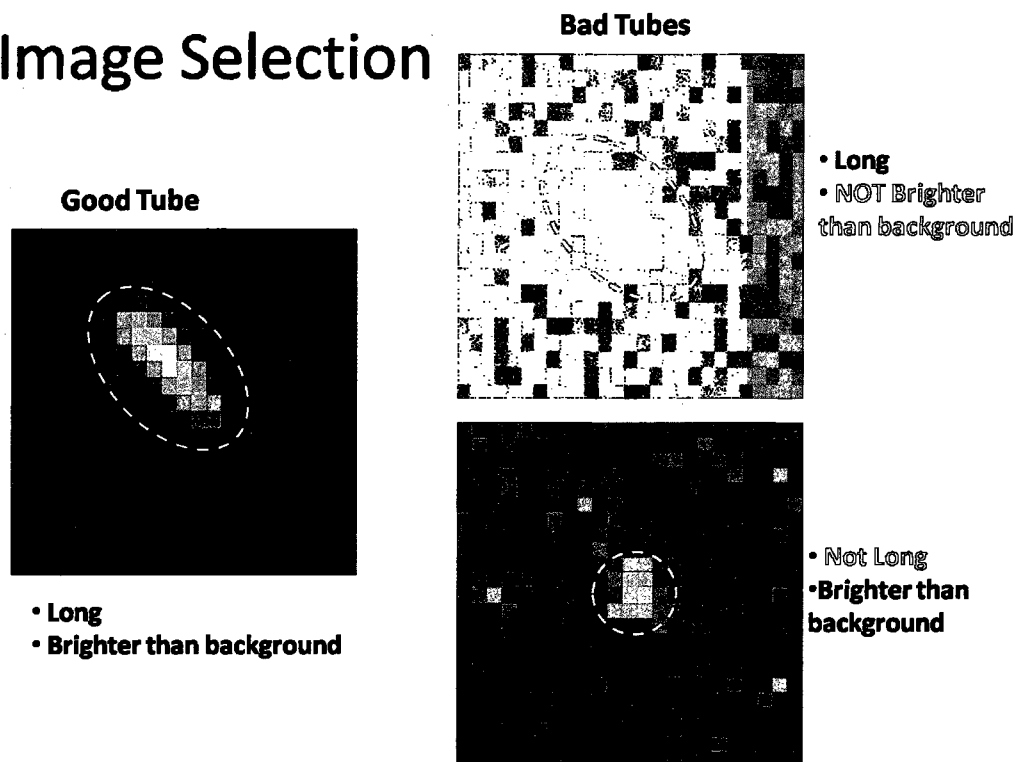
Figure 3.3 : Criteria for choosing best tubes

resonance (E_{22} = 567 nm). We first worked in a wide-field configuration by focusing the beam of a dye laser into the back aperture of a high NA objective, yielding excitation intensities below 1 kW/cm^2 of circularly polarized light on several tens μm^2. Experiments were carried out at room temperature. The fluorescence was collected with the same objective and first imaged on a low noise CCD camera (Micromax, Roper Scientific). The initial SWNT concentration was adjusted such that bright individual nanotubes could be optically resolved (Fig. 3.4a). The fluorescence of these bright tubes was then sent to a cryogenically cooled 1-D InGaAs detector (OmaV, Roper) placed at the output of a spectrometer to ensure that individual (6,5) nanotubes were imaged by monitoring the narrow spectral width of the emission ($\sim$22 $\pm$ 1 meV) (Fig.3.4b).
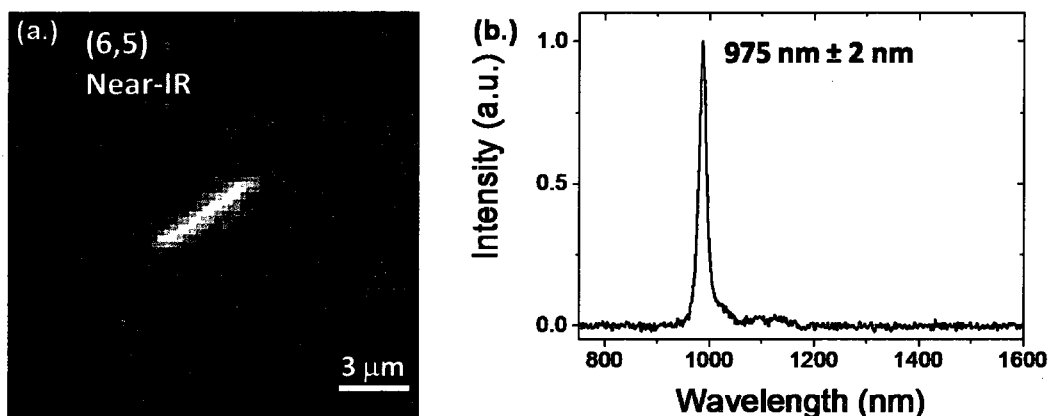
Figure 3.4 : Spectroscopy of individual (6,5) SWNTs. (a.) near-IR image. (b.) Fluorescence spectrum.

3.6.2 Statistical Results

Figure 3.5 shows the histograms of the signal intensity (mean intensity was obtained by measuring the average mean intensity of 2 consecutive pixels of 10 images minus the background) and full-width at half maximum (FWHM) of the spectra collected from individual (6,5) SWNTs processed using the HiPco (batch 164.4 and 187.4) or CoMoCat methods and dispersed in DOC. HiPco SWNTs systematically displayed approximately twice the brightness of the near-IR luminescence than CoMoCat nanotubes. Interestingly, this difference was associated with narrower and less dispersed emission linewidths for HiPco nanotubes than for CoMoCat ones. Identical results were observed for nanotubes dispersed in SDBS with the only difference that HiPco SWNTs of batch 164.4 displayed intermediate fluorescence intensities (Fig. 3.6). No difference was observed between the histograms of the peak luminescence emissions of the different nanotube batches (538 ± 10 nm, 548 ± 14 nm, and 229 ± 16 nm for the HiPco batch 164.4, 187.4, and CoMoCat samples, respectively, in DOC and 311

± 20 nm, 509 ± 18 nm, and 210 ± 14 nm for the same samples in SDBS). SWNT suspensions prepared with DOC thus appeared redshifted by approximately 10 ± 1 nm in the emission profile (985 ± 2 nm), consistent with previous observations [Arnold et al., 2006]. However, the emission properties of the SWNTs remained identical if excitation was performed at 567 or 571 nm (peak absorption for (6,5) nanotubes dispersed in DOC, see section 3.9.1); therefore, the excitation wavelength used was 567 nm for all samples to eliminate further experimental variables.
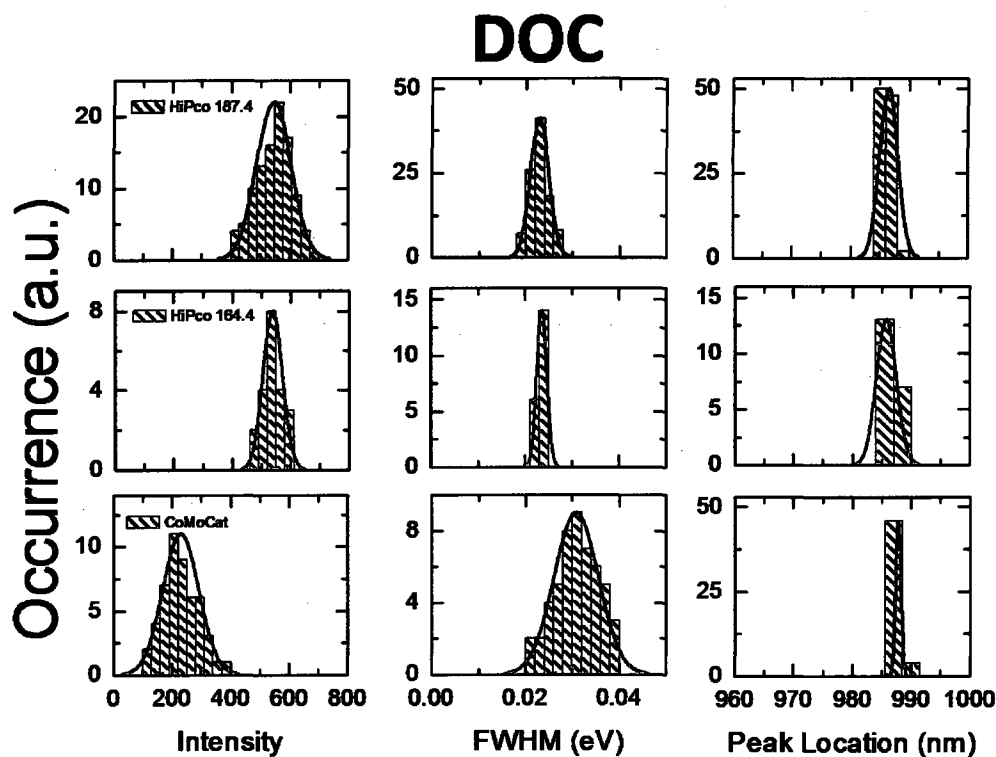
Figure 3.5 : Statistical study of individual (6,5) in DOC: intensity, full-width at half maximum, and peak location

The observed differences in luminescence intensities and linewidths are most likely due to extrinsic effects such as the local environments of the nanotubes or defects
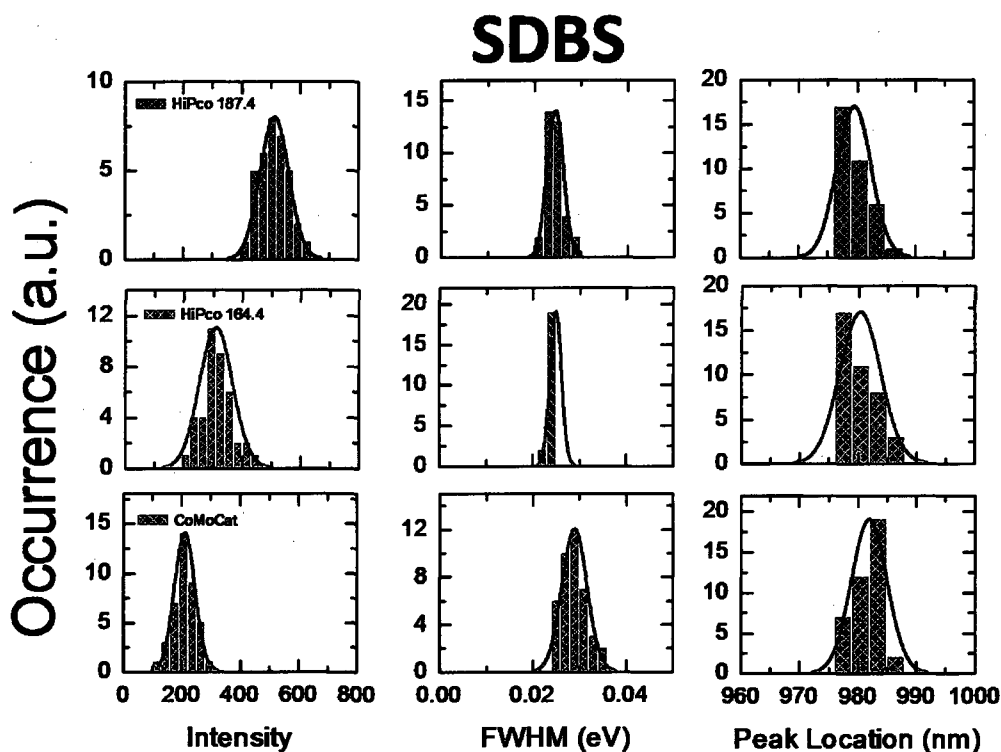
Figure 3.6 : Statistical study of individual (6,5) in SDBS: intensity, full-width at half maximum, and peak location

introduced during the synthesis and processing steps. The same statistical difference was also found between the two HiPco batches in SDBS which illustrates the strong sensitivity of the SWNT suspension quality on the synthesis conditions, and thus the sensitivity of their luminescence properties to the immediate environment. To illustrate this point further, we studied the luminescence intensity and linewidth of HiPco nanotubes suspended in DOC directly spincoated onto bare glass slides or glass slides previously coated by a positively charged polymer substrate (i.e., polylysine as in [Hogele et al., 2008]). In contrast to nanotubes immobilized in agarose gels, the resulting luminescence of the tubes onto bare or polylysine covered glass slides was subject to substantial blinking, which was associated with lower emission intensities

and broader emission linewidth in comparison to SWNTs in gels (Fig. 3.7.a) (near-IR blinking from SWNTs deposited on polylysine can be seen in Fig. 3.19). We observed that increasing the number of aliquots of SWNT suspension spun onto the substrate decreased the degree of blinking. This observation is due to weaker interaction between the substrate and the tubes. Figure 3.7.b shows the dependence of the mean luminescence intensities as a function of the mean spectral linewidth for the different samples measured under the different conditions. A clear trend indicates that narrower emission linewidth is associated with higher emission intensity.
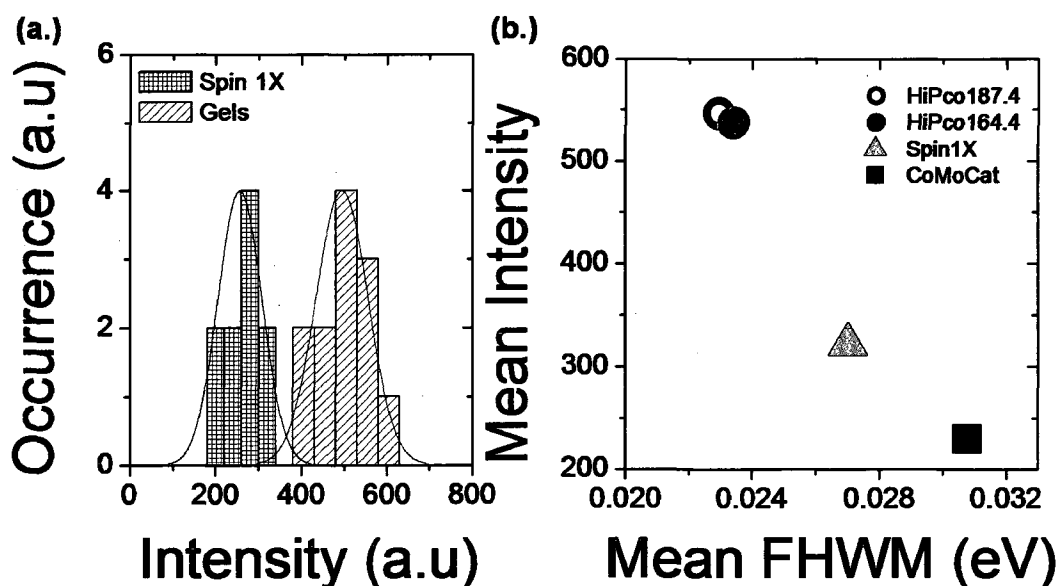
Figure 3.7 : (a.) Fluorescence intensity for HiPco 187.4 tubes in DOC after spinning onto a glass substrate (green) or in gels (blue). (b.) Correlation of the mean luminescence intensities to the mean spectral linewidth.

3.6.3 Time Resolved Spectroscopy

As often discussed in the literature, degraded emission properties of luminescent SWNTs are likely due to the increased role of non-radiative decay mechanisms of

the excitons produced in excited nanotubes; up to now, no direct evidence of these decays has been observed. Berciaud et al recently studied the luminescence decays of individual HiPco SWNTs (batch 162.1) and showed that they systematically exhibited bi-exponential decays due to a weak coupling between a dark exciton lying a few millieV (meV) below the bright one. We performed an analogous study on the different samples mentioned above. For this study, the nanotubes were excited in a confocal setup using either the cw dye laser or an optical parametric oscillator ($\sim$150 fsec pulses, 76 MHz repetition rate). After photon absorption, the ensuing S_{22} excitons decay on a $\sim$40 fsec timescale [Manzoni et al., 2005] essentially into the S_{11} excitonic manifold [Hertel et al., 2008], from which luminescence photons are emitted. After identification by their emission spectrum under cw excitation, the near-IR luminescence of the (6,5) nanotubes was sent to a silicon avalanche photodiode (APD). Luminescence decays were recorded under pulsed excitation using a conventional time resolved single photon counting scheme.

Figure 3.8.a shows a representative bi-exponential decay of a (6,5) SWNT obtained with excitation intensities of 20 nW for HiPco (red trace) and CoMoCat (black trace) tube ($\sim$10^{12} photons/pulse/cm^2). Given resonant (567 nm) absorption cross section per (6,5) nanotube unit of length of $\sim$10^{12} cm^2/μm, this translates to less than one photon absorbed per pulse and per nanotube segment of 90 nm ensuring the absence of multiexcitonic interactions (gold trace represents the instrument response function (IRF)). We ensured that the emission intensity remained constant during the 10 min acquisition time needed to record accurate decays. A representative confocal image of tube intensity and its emission peak can be seen in Figure 3.8.b and c, respectively. For the majority of the nanotubes, we observed biexponential behavior with short times (τ_{short}) ranging between 10 – 65 psec and long times (τ_{long}) between 100 – 350 psec (Fig. 3.9.a) consistent with previous observations [Berciaud et al., 2008]. Moreover, CoMoCat tubes (black squares, 3.9.a) showed the shortest

lifetimes with narrow distributions around 15 psec for the short time and 200 psec for the longest component. Conversely, HiPco tubes (red dots, 3.9.a) displayed the longest decays (τ_{long} = 200 – 800 psec and τ_{short} = 45 – 65 psec). No correlation was found between the decay times and the peak emission wavelengths, and/or between τ_{short} and the weight of the fast decay, defined as $Y_{short} = A_{short}\tau_{short}/(A_{short}\tau_{short} + A_{Long}\tau_{Long})$, where A is the pre-exponential constant (mean 85 ± 5%) (Figure 3.8.d), consistent with previous observations [Berciaud et al., 2008].
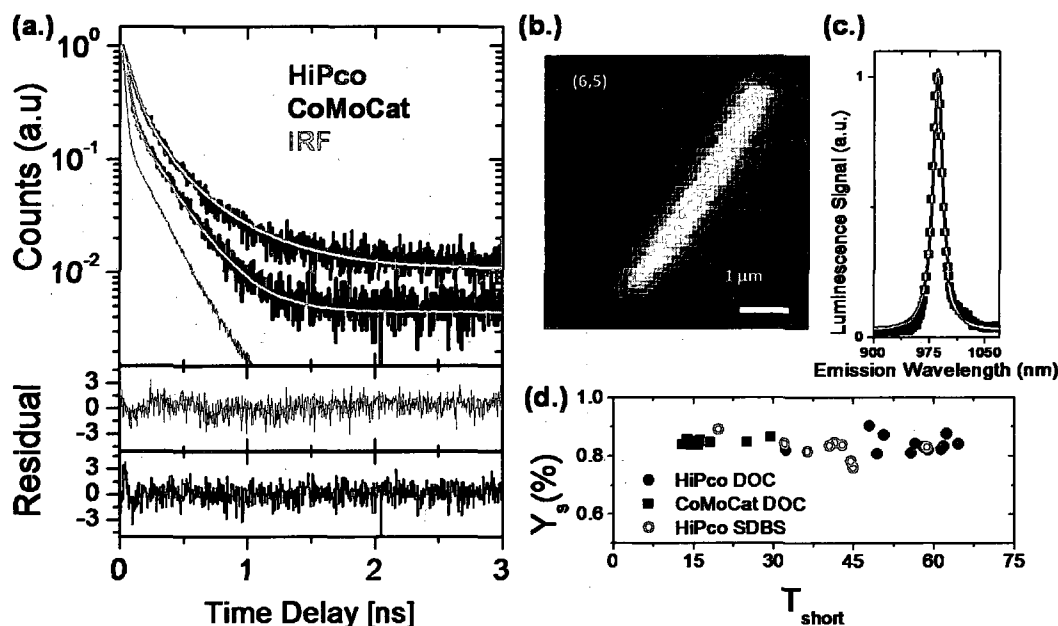
Figure 3.8 : Time Resolved Spectroscopy. (a.) Representative excitonic lifetime. (b.) Representative confocal image of a (6,5) tube. (c.) Emission peak. (d.) Correlation between the decay times and peak emission wavelengths.

We further studied the influence of the immediate environment of HiPco 187.4 nanotubes on their luminescence decays by comparing DOC suspended nanotubes in gels or deposited on surface and SDBS suspended nanotubes in gels, Figure 3.9.b. Whereas DOC suspended nanotubes studied in aqueous gels displayed the longest

decay times (red dots, Fig. 3.9.b), the same nanotubes spincoated on surfaces (blue triangles, Fig. 3.9.b) or SDBS suspended nanotubes studied in gels (black dots, Fig. 3.9.b) displayed a broad decay time distribution centered on shorter values than DOC nanotubes in gels. Interestingly, while high values of τ_{long} are only observed for DOC suspended HiPco nanotubes studied in aqueous gel environments, τ_{short} is greatly affected by synthesis methods and environmental conditions. Berciaud et al previously modeled the origin of the two decay times from a weak coupling between a dark exciton lying a few meV below the bright one. In the frame of this model, the shortening of the decay times —which almost exclusively affects the short component —suggests that additional fast non-radiative relaxation pathways induced by defects or environmental interactions couple predominantly to the bright state (Fig. 3.9).
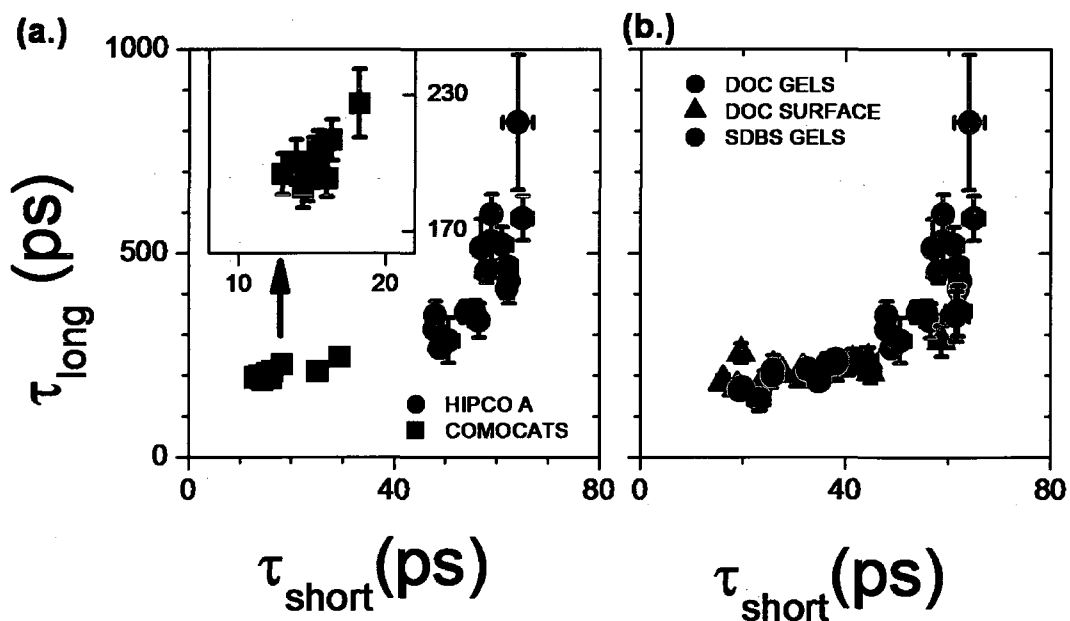
Figure 3.9 : Time Resolved Spectroscopy. (a.) Representative excitonic lifetime. (b.) Influence of the immediate environment of HiPco 187.4 nanotubes on their luminescence decays.

3.6.4 Correlations

To evaluate further the luminescence of the SWNTs, we examined the short component of the bioexponential decay (τ_{short}) as a function of intensity and FWHM, because τ_{short} is known to be the main radiative level which is primarily affected by synthesis methods and environmental conditions [Berciaud et al., 2008; Hirori et al., 2006]. Figure 3.10.a shows that τ_{short} increases as the emission intensity increases, while τ_{short} decreases as FWHM increases (Fig. 3.10.b), clearly indicating that τ_{short} is the radiative level most affected by intrinsic and extrinsic factors. Importantly, SDBS tubes exhibited a broader distribution across all tube types and techniques (studied in this report) compared with DOC. This can be as result of more homogeneous surface coverage with DOC than SDBS, effectively isolating the tubes from its local environment and thus minimizing interactions. This observation was also corroborated in our excitonic time resolved experiments, which showed longer lifetimes for samples in DOC than in SDBS.
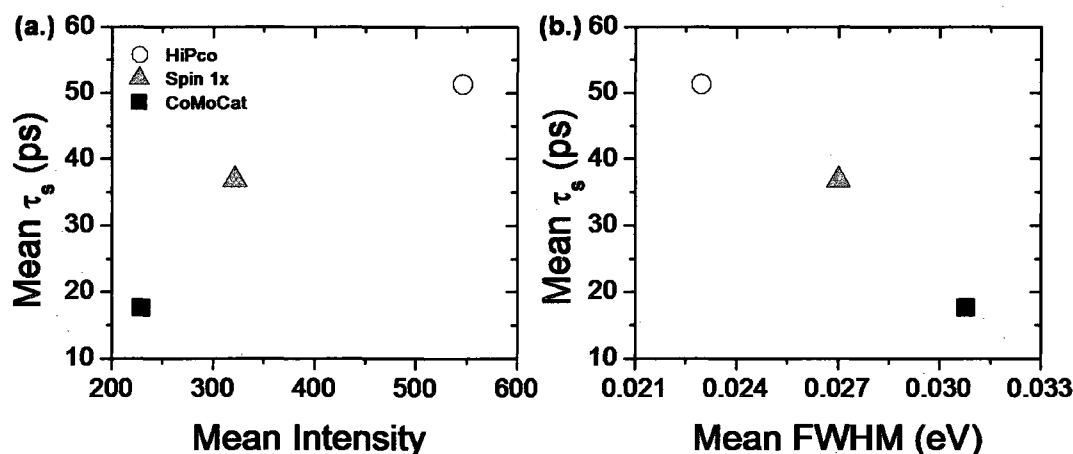
Figure 3.10 : Correlations. (a.) Mean τ_{short} as a function of mean intensity. (b.) Mean τ_{short} as a function of mean FWHM.

3.7 Results and Discussion for Ensembles of HiPco SWNTs

3.7.1 Bulk Spectroscopy Characterization of Different HiPco SWNT Batches

Substantial spectroscopic evidence was found with individual (6,5) SWNTs to support our initial hypothesis that the synthesis method (HiPco, CoMoCat) and other environmental conditions have a profound effect on the optical properties of individual SWNTs. Moreover, we observed that the optical properties of the tubes can vary within different batches from the same process (HiPco batches 187.4 and 164.4). Here we present bulk spectroscopy characterization of individually suspended HiPco SWNTs from batches 113.1, 164.4 and 187.4 after homogenization, ultra-tip sonication, and ultracentrifugation (as described in Experimental Section 2.4). Characterization was conducted using Raman spectroscopy, absorbance and fluorescence; these techniques will give us a complete picture of the distribution of tube chiralities and diameters present in the samples.

Absorbance, Fluorescence and 2D-Contour Plots

Figure 3.11.a shows the absorbance of batches 187.4 (black trace), 164.4 (red trace), and 113.1 (blue trace) normalized to concentration with well defined and narrow peaks, representative of well dispersed suspensions of individual tubes. The peaks associated with small diameter tubes in the E_{11} region ($\sim$900 to 1100 nm) (see Sec. 1.2.2) are enhanced for the 187.4 batch (black trace) in comparison with the other two batches indicating that the concentration of small diameter tubes in this batch is higher. Conversely, batch 113.1 exhibits less intense and broader peaks in this region. Fluorescence spectroscopy with 785 nm excitation wavelength (Fig. 3.11.b) shows high luminescence intensity for small diameter tubes (900 – 1100 nm) in batch 187.4 as shown in the absorbance spectrum. In contrast, batch 113.1 exhibits higher luminescence intensity in the large diameter tube region ($\sim$1200 – 1400 nm) as de-

picted by the blue arrow, while batch 164.4 showed fluorescence peaks with intensity in between the other two batches. These two sets of results indicate that the HiPco process can indeed produce different amounts of large and small diameter tubes than previously thought. It is important to note that the overall fluorescence intensity of batch 187.4 was ~4× more intense than 164.4 and ~6× more than 113.1 at the same concentration indicating brighter and possibly better dispersed SWNTs in batch 187.4.
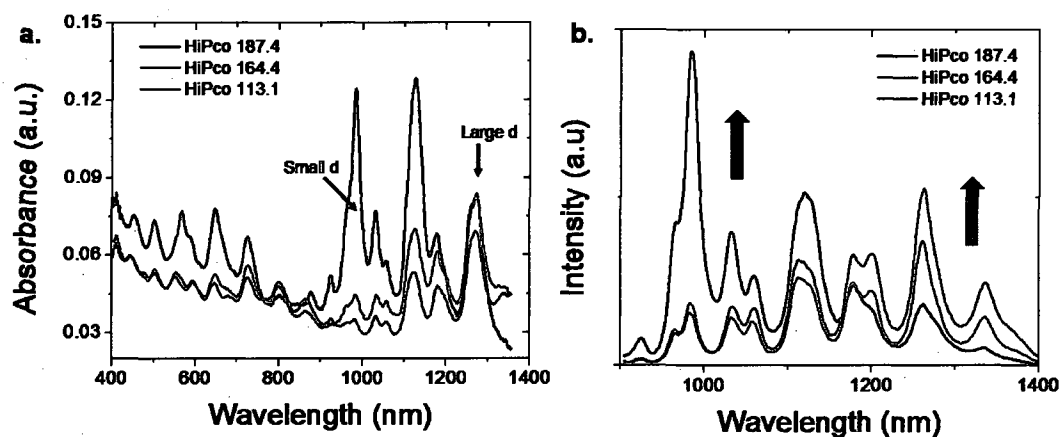
Figure 3.11 : Absorbance (a.) and fluorescence (b.) spectra of different HiPco batches. Black trace, batch 187.4; red trace, batch 164.4; blue trace, batch 113.1.

In order to examine further the distribution of semiconducting SWNTs in the different batches, we constructed 2D-contour plots of the fluorescence intensity vs. excitation and emission wavelength of the different batches (Fig. 3.12). This analysis shows a complete picture of the distribution of semiconducting tubes in each of the batches, with a broader distribution of tube types observed in batch 113.1 than in 187.4. Batch 187.4 shows high intensity for small diameter tubes and very low signal for large diameter tubes; in contrast large diameter tubes are the predominant species in batch 113.1. Batch 164.4 higher luminescence intensities for smaller diameter SWNTs, –especially (6,5), than 113.1; yet, multiple species of SWNTs are present

in both batches. To quantify relative abundance, a histogram of the diameter distribution obtained from fluorescence measurements was prepared (Fig. 3.12). Batch 187.4 has the narrowest diameter distribution with a small mean diameter, i.e., 0.747 nm, which is very close to the theoretical diameter of a (6,5) SWNT (0.757 nm). Batches 164.4 and 113.1 have a broader distribution with larger mean diameters of 0.83 and 1.03 nm, respectively. These 2D-contour plots and diameter distributions unambiguously confirm the different distribution of semiconducting tubes in each of the batches and corroborate the observations made with absorbance and fluorescence (Fig. 3.11).
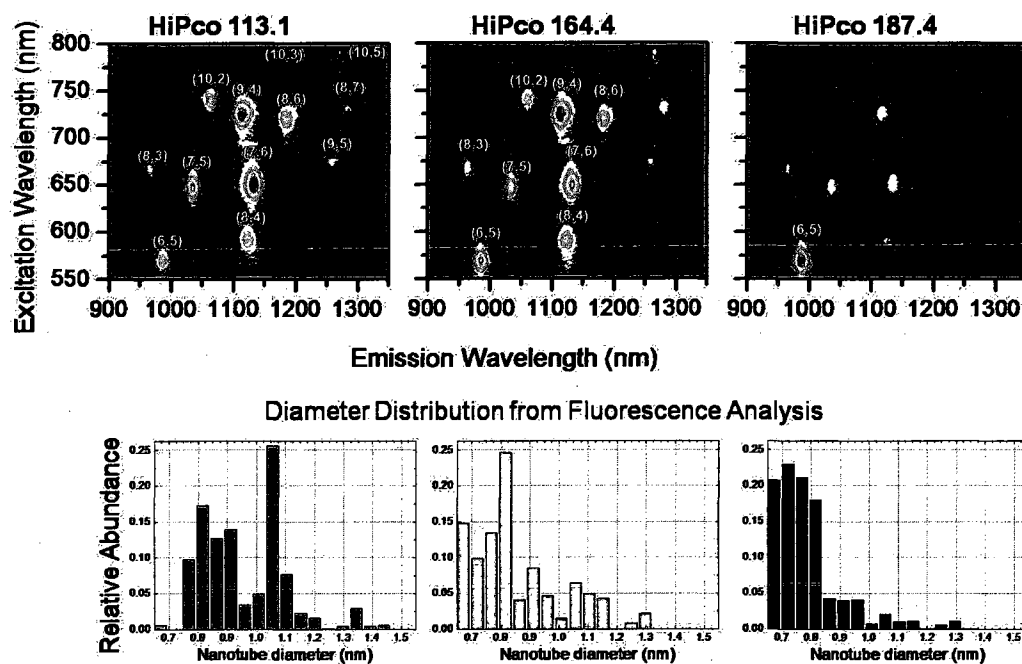
Figure 3.12 : 2D-contour plots of the fluorescence intensity vs. excitation and emission wavelength and histograms of the diameter distribution as a function of nanotube diameter obtained from fluorescence.

Raman Spectroscopy

Because fluorescence spectroscopy only gives information about semiconducting SWNTs, Raman spectroscopy is used to gain insight to other tube chiralities. Different excitation wavelengths are in resonance with different populations and tube types, and thus can be used to better understand the exact identity of SWNTs in a given batch. Figure 3.13 shows the Raman spectra of the 3 batches using 785 nm excitation wavelength, which is known to be in resonance with large diameter semiconducting tubes [Dresselhaus et al., 2007a; Doorn et al., 2004; Duque et al., 2008a]. A limitation to using this wavelength is that the fluorescence peaks of some of the tubes are so intense that they can mask the presence of other important peaks; therefore a very low excitation power was required to prevent detector saturation ($\sim$5 % overall power). Nevertheless, we can identify the different fluorescence peaks of the tubes assigned to (7,5), (6,5), (8,3) and (9,1) [Moore et al., 2003], the G-band, and the radial breathing modes (RBM). Interestingly, the fluorescence signal obtained for HiPco batch 187.4 with 785 nm excitation was $\sim$2$\times$ more intense than batch 164.4, which was $\sim$4$\times$ more intense than batch 113.1, consistent with the 2D-contour plots and fluorescence observations. Moreover, the RBM peaks between 180 and 300 cm^{-1}, which correspond to large diameter semiconducting tubes, are less intense in batch 187.4 than in the other two batches; however the RBM intensities at 380 cm^{-1} (small diameter semiconducting (5,4) tube, $d = 0.62$ nm) show the opposite trend.

Raman using 633 nm excitation wavelength showed several important characteristics (Fig. 3.14). The G-band for the 3 batches is constant with no shifting, and no prominent D-band was observed. The RBM, on the other hand, exhibited a very different and opposite behavior.

The peak at $\sim$195 cm^{-1} was almost nonexistent for batch 187.4, very pronounced in batch 113.1, and displayed intermediate intensity for 164.4 (187.4 < 164.4 < 113.1). Either a higher concentration of metallic tubes or a greater number of large
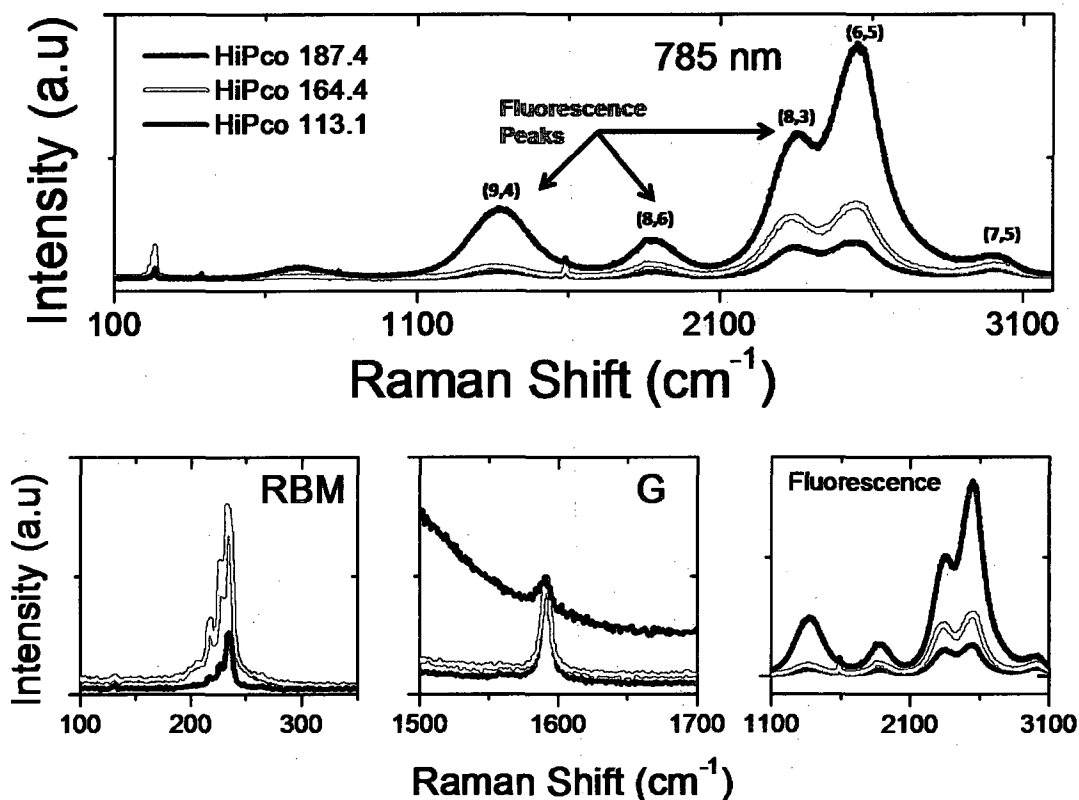
Figure 3.13 : Raman spectra with 785 nm excitation wavelength of different HiPco batches.

diameter semiconducting tubes are present in 113.1 than in 187.4; based on the $\sim$15 cm^{-1} cm^{-1} positive shift of the G'-band (2500 – 2700 cm^{-1}) in 113.1, we conjecture that this batch contains a higher number of large diameter tubes. Moreover, the peaks between 220 and 320 cm^{-1}, associated with semiconducting SWNTs, showed an opposite behavior: higher intensity for 187.4 than for 164.4 and 113.1 (187.4 > 164.4 > 113.1), consistent with all the above observations. However, whether or not the concentration of metallic tubes is higher in batch 113.1 still remains to be determined.

Raman spectroscopy at 514 nm excitation wavelength is known to come into resonance with metallic SWNTs and the E$_{33}$ transition of large diameter semicon-
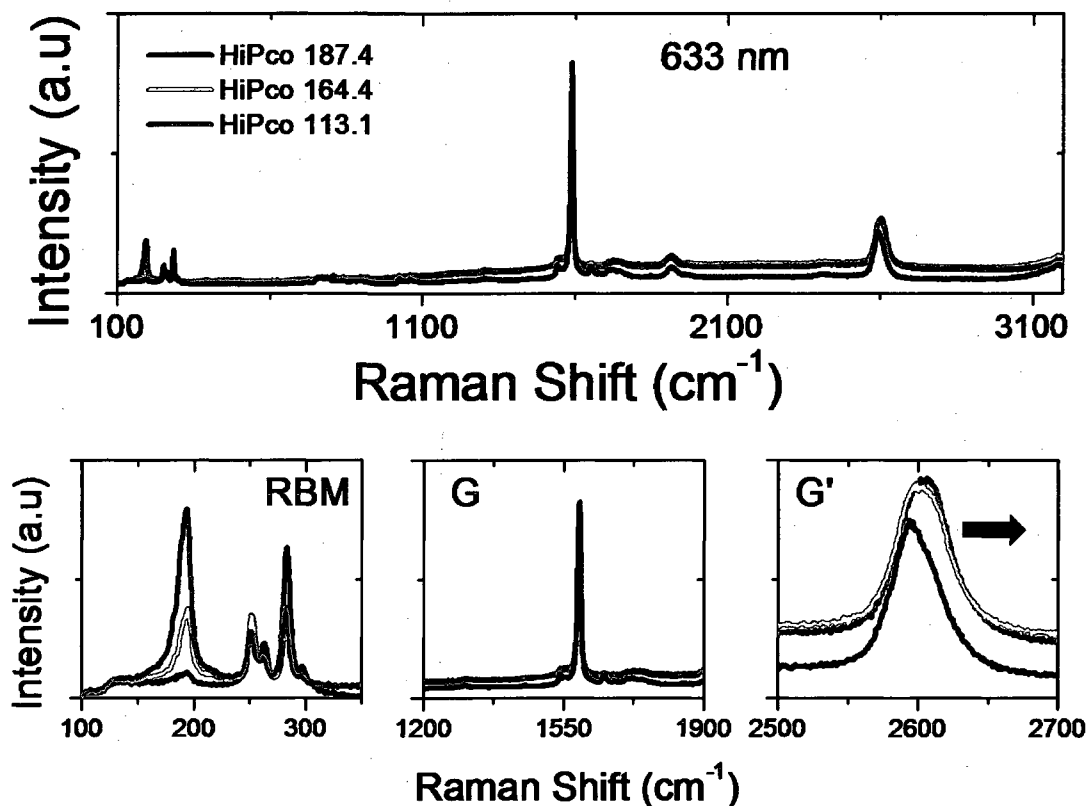
Figure 3.14 : Raman spectra with 633 nm excitation wavelength of different HiPco batches.

ducting SWNTs. Therefore, this technique can be used to gain insight to the metallic population of the HiPco batches and definitely determine if 113.1 contains a greater concentration of metallic tubes. Figure 3.15 shows the Raman spectra obtained for the 3 different batches. At $\sim$190 cm^{-1} a new peak appears for 113.1 while the peak assigned to metallic SWNTs (250 – 300cm^{-1}) remains roughly constant. The new peak at $\sim$190 cm^{-1} originates from resonance with large diameter semiconducting SWNTs. This observation was corroborated by comparing the RBM signal of HiPco SWNTs with laser oven SWNTs (Fig. 3.16, green trace), which are known to have a greater diameter distribution, in the range of 1.1 – 1.8 nm [Thess et al., 1996; Maruyama et al., 2003].

Moreover, the G'-band for 113.1 shifts $\sim$15 cm^{-1} in the positive direction compared to batch 187.4, which was also observed with 633 nm excitation. The Breit-Wigner-Fano peak (1550 cm^{-1}) is known to arise from conduction of electrons in metallic SWNTs. In batch 113.1, the intensity of this peak lies between that observed for 164.4 and 187.4, indicating that batch 113.1 does not have a higher population of metallic SWNTs, but a greater distribution towards large diameter tubes. This also suggests that the intensity enhancement observed for the RBM metallic peak at 633 nm excitation is due to the presence of large diameter semiconducting SWNTs. Overall, this set of results demonstrates that batch 113.1 has a distribution of SWNTs favoring large diameter semiconductors compared with the other two batches.

Figure 3.16 shows the RBMs of each HiPco batch and one laser oven sample using 3 different excitation wavelengths. The first column shows the RBMs with 514 nm excitation, in resonance with metallic tubes in HiPco samples and the E_{33} transition of large diameter semiconductors (diameter $>$ 1.3 nm) in laser oven SWNTs. The metallic peak (yellow region) has nearly the same intensity in all of the batches, indicating comparable fraction of metallic species in all batches. The peak at $\sim$190 cm^{-1} (green region) arises from the E_{33} resonance of large diameter semiconducting SWNTs. This peak is most intense for batch 113.1 and laser oven SWNTs. The RBMs observed with 633 nm excitation show the metallic peak (orange region) and large diameter semiconductors (purple region). The metallic peak in batch 187.4 is small in comparison with batch 113.1 where this peak is the most intense. In contrast, the semiconducting peaks are more intense in 187.4 than 113.1. Interestingly, both the metallic and semiconducting peaks have roughly the same intensity and integrated area in batch 164.4. RBM using 785 nm excitation (in resonance with large diameter semiconducting SWNTs) showed a much lower intensity in batch 187.4 than 164.4 or 113.1 (gray region) but higher intensity at $\sim$380 cm^{-1} which corresponds to the small diameter semiconducting SWNT (5,4), d = 0.62 nm (magenta section), further
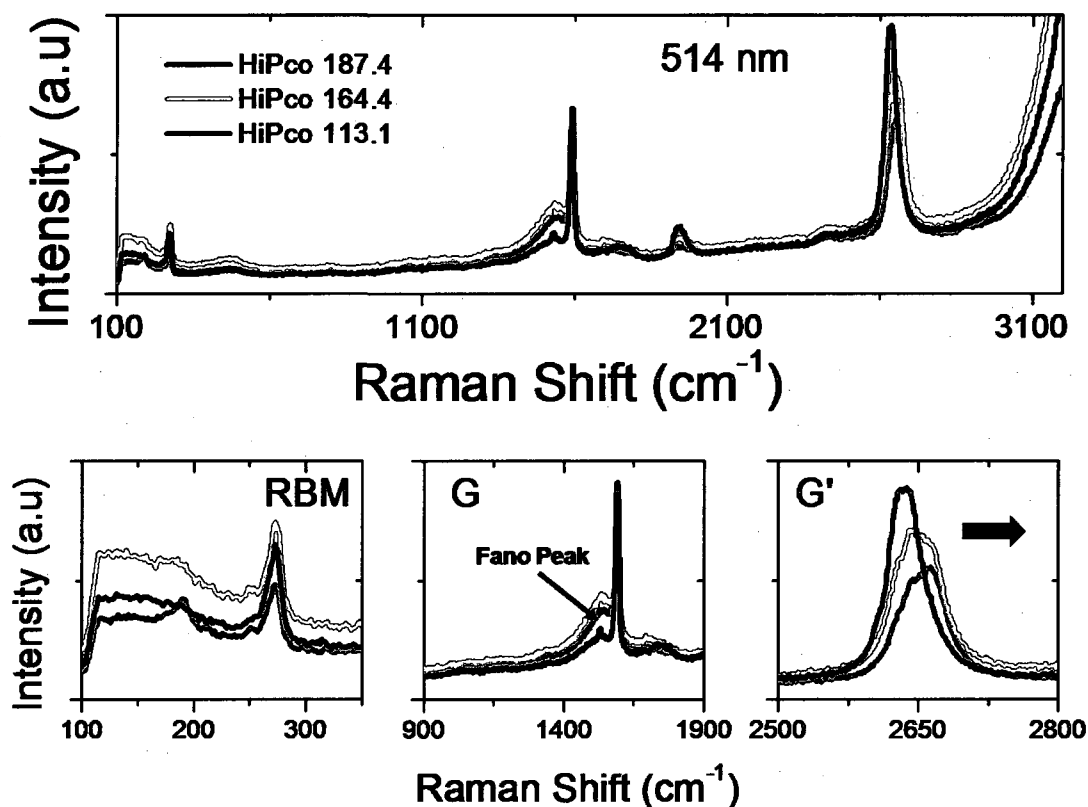
Figure 3.15 : Raman spectra with 514 nm excitation wavelength of different HiPco batches.

indicating the differences in the tube population. Importantly, similar Raman observations were obtained with all batches before ultracentrifugation, indicating that this step does not deplete selectively any specific type or diameter. We can conclude from this set of RBMs that batch 187.4 is highly enriched in small diameter semiconducting tubes —especially the (6,5) — with approximately the same population of metallic tubes than the other samples studied. Batch 113.1 has a fewer small diameter tubes and a higher population of larger diameter. To corroborate these observations, we obtained Raman spectra of laser oven carbon nanotubes, which have a diameter distribution toward large diameter SWNTs, ~1.5 nm. Figure 3.16 shows the RBM of the laser oven tubes (green trace), displaying peaks in the lower RBM frequencies

($\leq$ 200 cm^{-1}), as with HiPco batch 113.1. Importantly, we did not observe any fluorescence signal coming from the laser oven tubes in the near-IR region using 660 or 785 nm excitation wavelength, confirming the absence of small diameter semiconducting SWNTs. This set of results confirms the observation that the HiPco processes produces different diameter distributions of SWNTs, and underlines the necessity to better characterize the produced samples and understand the parameters that control the growing mechanism. In addition, some of the contradictory reports in the literature regarding the quantum yield of SWNTs and/or the excitonic dynamics (see Sec. 3.2) can be the result of differences in tube population and/or quality or synthesis procedure.

Analysis at the single molecular level using Raman, absorbance, and luminescence techniques should be employed to better characterize the tube populations.

3.8 Conclusions

We observed that individual (6,5) SWNTs in DOC have a narrower and more homogeneous luminescence spectra than SWNTs dispersed in SDBS. Statistically, we found that HiPco SWNTs systematically displayed approximately twice the brightness of the near-IR luminescence than CoMoCat nanotubes with narrower and less dispersed emission linewidths. These differences in luminescence intensities and linewidths are most likely due to extrinsic effects of the local environments of the nanotubes or defects introduced during the synthesis and processing steps. We believe that the SDBS samples gave more heterogeneous results because the surfactant micelle is bound less tight around the SWNTs, allowing vacancies to form which in turn lead to variations in results.

Time resolved luminescence decays showed bi-exponential behavior with short times (τ_{short}) ranging between 10 − 65 psec and long times (τ_{long}) between 100 − 350 psec, consistent with previous observations. Moreover, CoMoCat tubes showed the
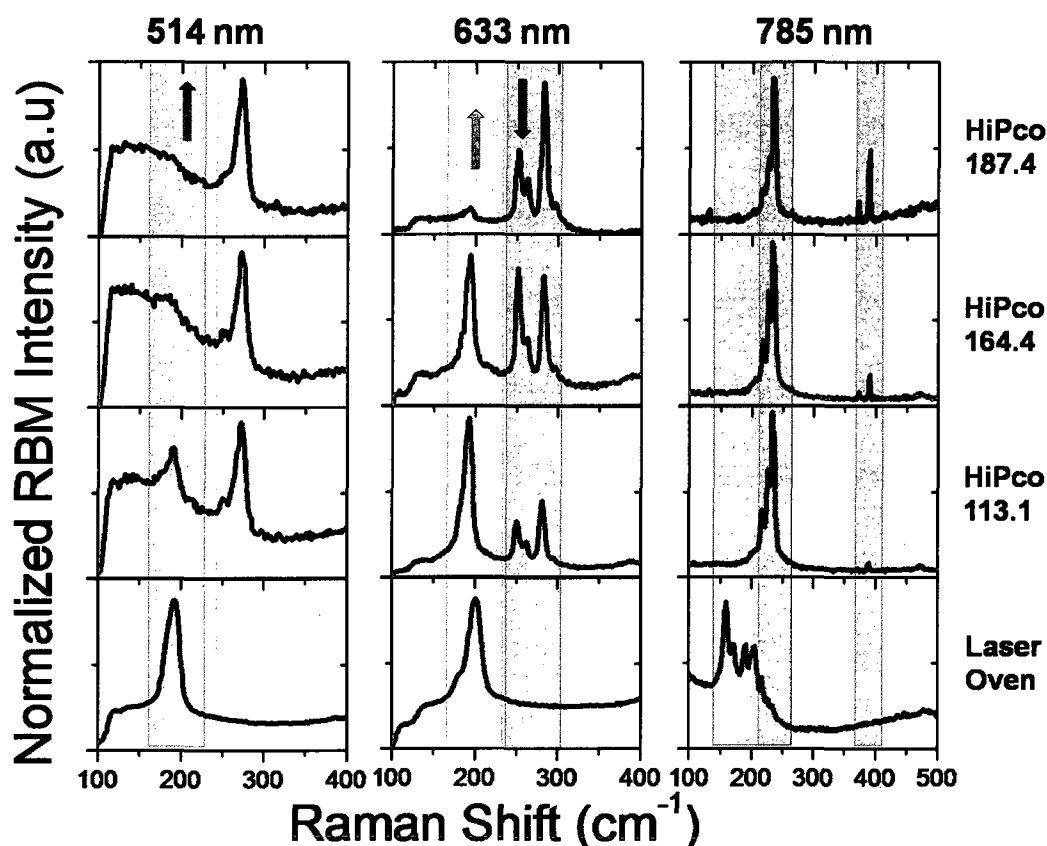
Figure 3.16 : RBM of HiPco batches 187.4 (black trace), 164.4 (red trace), and 113.1 (blue trace) and laser oven (green trace) SWNTs with 514, 633, and 785 nm excitation wavelength. Green region indicates large diameter semiconducting SWNTs, yellow region indicates metallic SWNTs, orange region indicates metallic SWNTs, purple region region indicates semiconducting SWNTs, blue and brown regions indicate large diameter semiconductors, and magenta region indicates small diameter semiconducting SWNTs.

shortest lifetimes with narrow distributions around 15 psec for the short time and 200 psec for the longest component. Conversely, HiPco tubes displayed the longest decays between 200 – 800 psec and shorter decays between 45 – 65 psec.

We found that the immediate environment of nanotubes affects their luminescence decays; DOC suspended nanotubes in aqueous gels displayed the longest decay times, but the same nanotubes spincoated on surfaces or SDBS suspended nanotubes

studied in gels displayed a broad decay time distribution centered on shorter values than DOC nanotubes in gels. Interestingly, τ_{short} increases as the emission intensity increases, while τ_{short} decreases as FWHM increases, indicating that τ_{short} is the radiative level most affected by intrinsic and extrinsic factors.

We observed that the optical properties of SWNTs can change within different batches of the same process (HiPco). This underlines the necessity for complete characterization of the produced samples and the need to better understand the parameters that control the growing mechanism of the HiPco process in order to minimize sample heterogeneities.

Overall, substantial spectroscopic evidence was found to support the profound effect that the synthesis method (HiPco, CoMoCat) and environmental conditions have on SWNT optical properties. Moreover, variations of tube types present were highlighted between different batches of the same synthesis process.

3.9 Appendix 3

3.9.1 Excitation with 571 nm Wavelength

SWNT suspensions prepared with DOC are redshifted by 4 ± 1 nm (571 nm) in the absorbance spectra and approximately 10 ± 1 nm in the emission profile (985 ± 2 nm), consistent with previous observations [Arnold et al., 2006]. However, the emission properties of the SWNTs remained unchanged if excitation was performed at 567 or 571 nm (Fig 3.17); therefore, unless otherwise indicated, the excitation wavelength used was 567 nm to reduce the number of experimental variables.

3.9.2 HiPco 187.4 DOC-SWNTs Under Different Conditions

Figure 3.18 shows the intensity statistics of HiPco 187.4 DOC-SWNTs under different conditions: in solution and in a agarose gel. Clearly, the distribution and mean intensity did not change after transferring the SWNTs from the aqueous suspension into agarose gels. This result indicates that immobilizing SWNTs in agarose gels does not affect the optical properties of individual semiconducting SWNTs and will serve as the ideal medium to minimize the environmental interactions (as shown in Figure 3.7.a and described in Section 3.9.3).

Similar results were obtained with individual HiPco and CoMoCat SWNTs suspended in SDBS and after in-situ polymerization of VP (describe in Sec. 2.5.4).

3.9.3 Polylysine Deposition

The deposition of polylysine onto glass slides was performed following Hogele et al. [2008] which reports to have optimal photoluminescence of SWNTs on surfaces. They claimed that the positively charged polylysine reduced the surface–tube interactions and enabled the tubes to exhibit their optimal optical properties. We examined these claims by depositing DOC-SWNTs onto glass slides previously covered with polyly-

HiPco
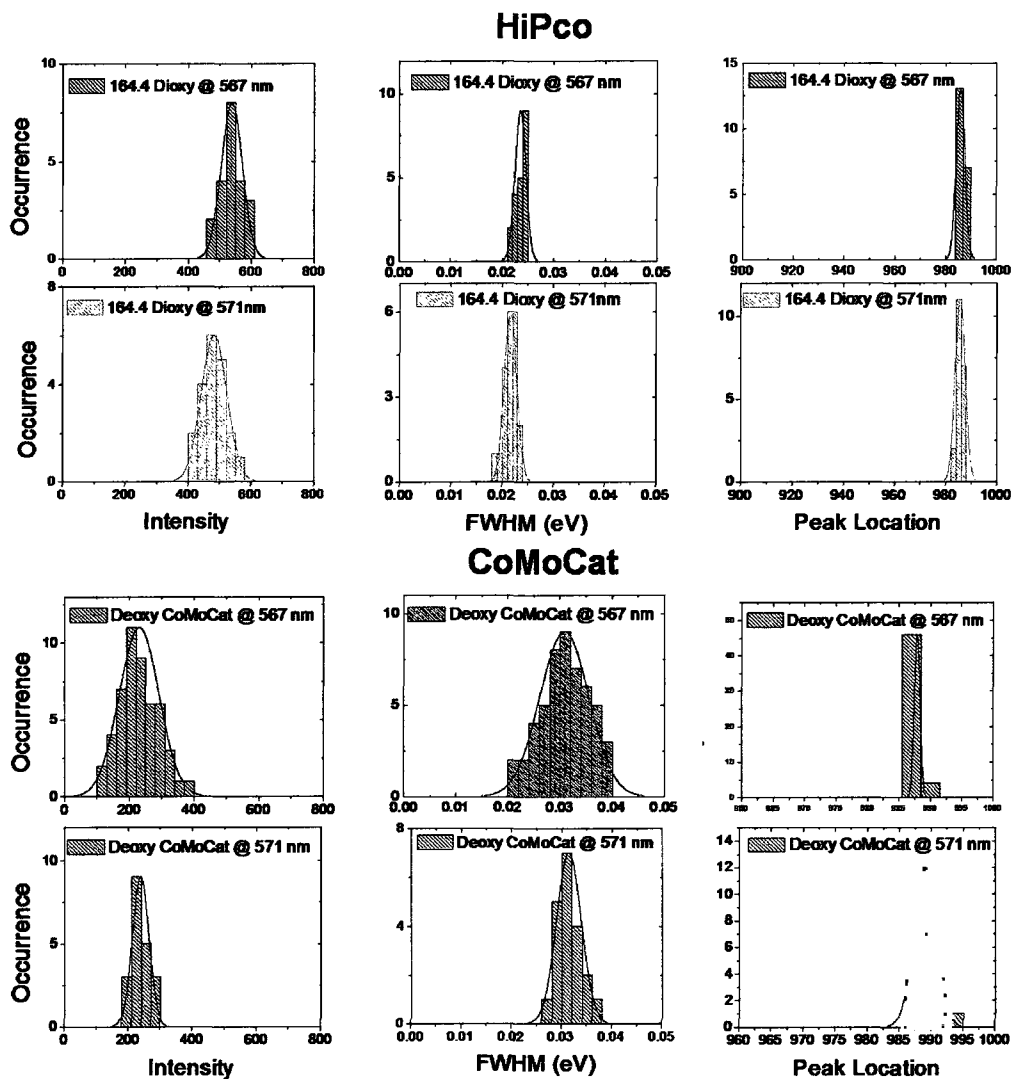
Figure 3.17 : Statistical study using excitation at 571 nm wavelength

sine. We found only partial deposition of tubes in small patches where the polylysine had adhered to the glass slides (Fig.3.19.a). Moreover, we found substantial blinking, with fluorescence intensity fluctuations of more than 80% (from ~210 to ~43 fluorescence oscillation) as shown in the black trace on Figure 3.19.b, compared to the near-IR luminescence in agarose gels, which exhibit a stable luminescence (red dots).
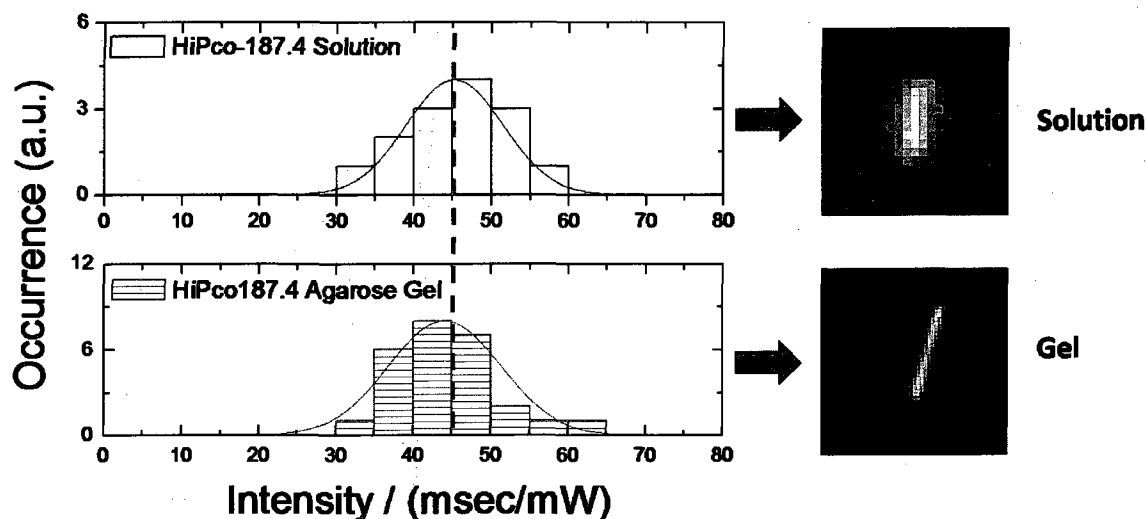
Figure 3.18 : Intensity statistics of HiPco 187.4 DOC-SWNTs in different conditions: solution and gels.

Snapshots of the near-IR luminescence blinking can be seen in Figure 3.19.c. We attribute this to charge transfer and strong interaction between the positively charged surface (polylysine) and the negatively charged SWNTs (DOC). Similar results were obtained with SWNTs dispersed in SDBS. This clearly indicates a strong interaction between the substrate and the SWNTs.

Preparation procedure:

◇ Plasma clean glass slides

◇ Add 100 μL polylysine

◇ Wait for 1 hr

◇ Rinse with DI water and dry

◇ Add 50 μL of tubes, wait 30 min

◇ Rinse again with DI water

◇ Image
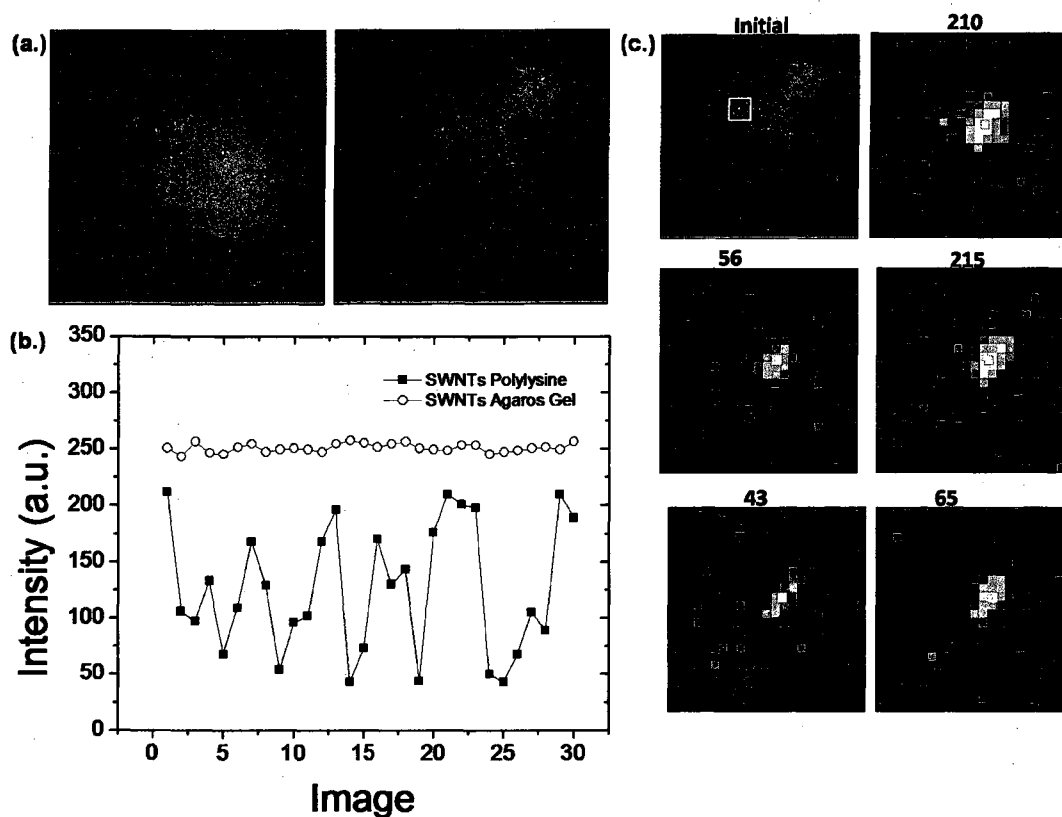
Figure 3.19 : Polylysine Blinking. (a.) SWNTs on polylysine patches. (b.) near-IR stability on gels and polylysine. (c.) Snapshots of the luminescence blinking in polylysine. Near-infrared images of individual SWNTs were obtained on glass surfaces covered with polylysine after spin coating. Numbers above each image indicate the intensity of the selected pixel in yellow.

3.9.4 Photothermal Images of HiPco and CoMoCat Samples

Figure 3.20 shows representative photothermal images of HiPco and CoMoCat samples after the same dispersion procedure (Sec. 3.4.1). On average, HiPco tubes were longer than CoMoCat ones, as shown in Figure 3.20.
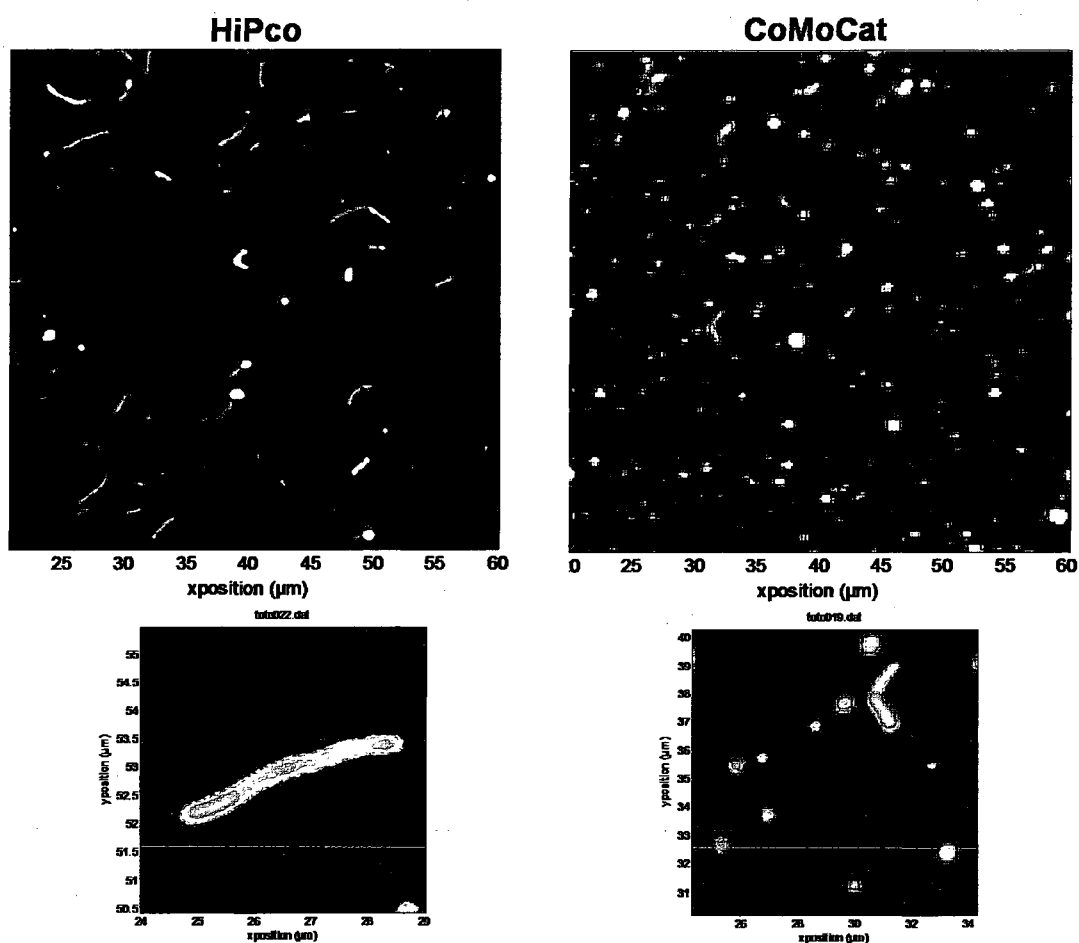
Figure 3.20 : Photothermal images of HiPco and CoMoCat samples

3.9.5 Representative near-IR and Fluorescence Spectra of HiPco and Co-MoCat Samples

Figure 3.21 shows representative near-IR images and fluorescence spectra of HiPco and CoMoCat samples excited at their second order excitonic resonance (E_{22} = 567 nm) with a cw laser. It shows uniform fluorescence intensity with narrow and well-defined fluorescence peaks representative of individual tubes.
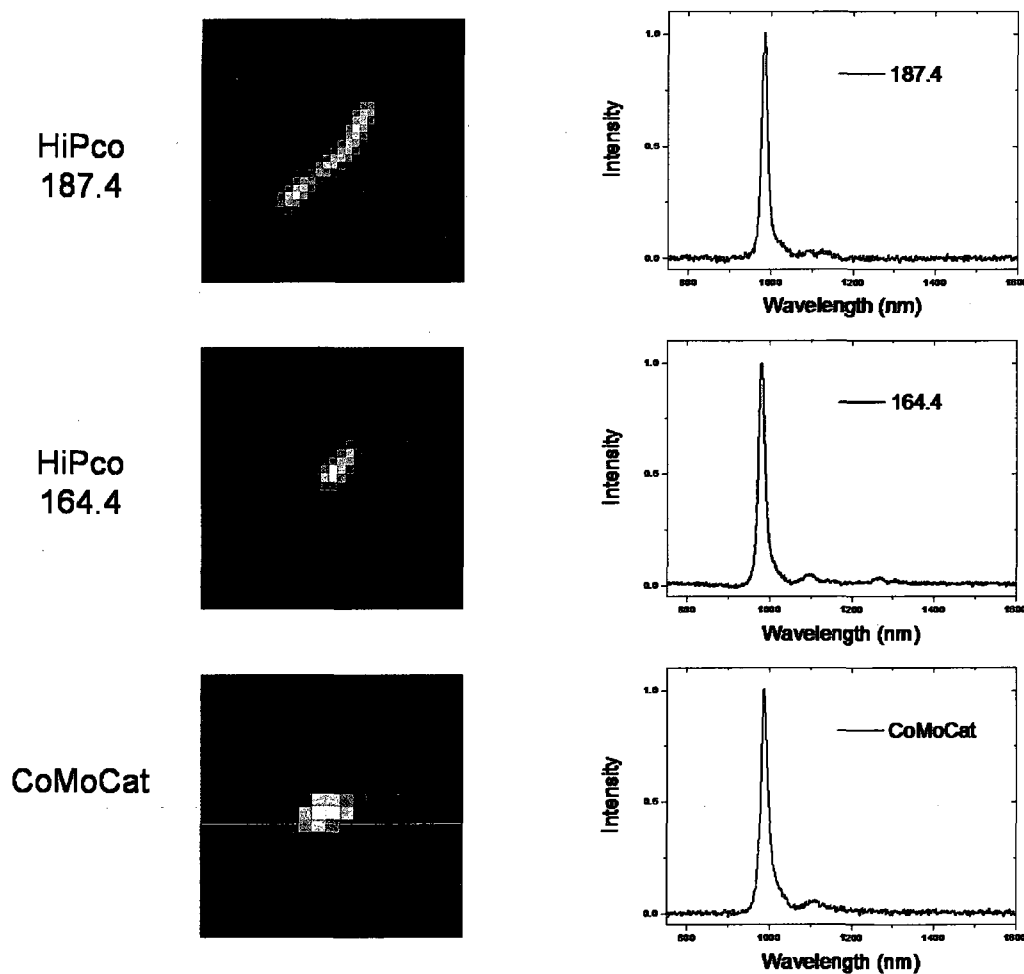
Figure 3.21 : Representative near-IR images and fluorescence spectra of HiPco and CoMoCat tubes.

3.9.6   Multi-Surfactant Streets

Mixtures of SDBS and agarose gels prepared with DOC produce a set of worm like micelles, or long linear paths in which SWNTs moved at a very fast rate maintaining constant luminescence as shown in Figure 3.22.a–b. This set of experiments can potentially be important for measuring 1-D diffusion of nano-objects.

The suspension was prepared by mixing 0.5 g of agarose in 10 mL of 1 wt% SDBS.

(a.)

(b.)

Start

End

Figure 3.22 : Multi-surfactant streets

To obtain was heat up to 80 °C and 200 μL of the agarose-SDBS solutions was mixed with 20 μL of DOC-SWNTs at 1 wt% DOC and 30 mg/L SWNTs. The resulting suspension was examined using procedures describe in Section 3.4.2.

Chapter 4

Antenna Chemistry with Metallic Single-Walled Carbon Nanotubes

4.1 Objective

The objective of this chapter is to explore the interactions between electromagnetic radiation and aqueous suspensions of individual surfactant stabilized SWNTs. We hypothesize that under electromagnetic radiation metallic SWNTs will preferentially polarize creating a localized apparent field enhancement at the tips due to their high aspect ratio and electronic properties —antenna behavior. This field enhancement can generate sufficient current densities which might drive electron transfer reactions preferentially at their tips, potentially reducing transition metal salts into nanoparticles. In order to demonstrate this hypothesis, we study the redox landscape of surfactant-stabilized SWNTs, and how their immediate surrounding affects their Fermi level. We can test the reaction selectivity between SWNTs and transition metal salts under electromagnetic radiation. The selectivity is assessed using microscopic and spectroscopic techniques such as atomic force microscopy, ultraviolet-visible absorbance, and Raman spectroscopy. At the end we expect to obtain a system with tunable reaction conditions where spontaneous particle formations are controlled and selective deposition is obtained to form novel nanostructures.

4.2 Introduction

Single-wall carbon nanotubes (SWNTs) comprise a large family of cylindrical all-carbon polymers with remarkable mechanical and electrical properties; the specific structure of individual SWNT can be uniquely described by an (n,m) vector (type) that defines its diameter and chirality [Saito et al., 1992]. Individual metallic SWNT are essentially ballistic conductors that support high DC current densities [McEuen et al., 2002] with a finite density of states at the Fermi level and have a high axial dielectric constant [Benedict et al., 1995]. As a consequence, metallic SWNT rapidly polarize in response to externally applied electric fields. Therefore, metallic SWNT can be considered nano-scale antennae [Wang et al., 2004a; Dresselhaus, 2004]. Their high aspect ratio, $\beta \equiv L/D \sim 1000$, provides a localized apparent field amplification factor (equal to the aspect ratio) at their tips, which enables substantial field emission currents in vacuo [Bonard et al., 1998]. This polarization–based 'antenna effect' has several interesting and useful manifestations like type separation [O'Connell et al., 2002], conversion of radio frequencies (RF) and optical frequencies into heat [Gannon et al., 2007; Imholt et al., 2003], and electrodeposition on the ends of bundles [Bradley et al., 2005].

Separately, spontaneous reduction-oxidation (redox) processes involving electron transfers to and from individualized SWNT in anionic surfactant suspensions [Moore et al., 2003] have become an active research topic. The ultraviolet-visible (UV-vis) absorption peaks of semiconducting SWNT bleach selectively upon protonation in acidic media [Strano et al., 2003]. Near infrared fluorescence quenching has been used to monitor diameter-selective oxidation of semiconducting SWNT by organic acceptors [O'Connell et al., 2005]. Similarly, aqueous suspensions of acid-oxidized SWNT (bearing anionic carboxylic acid groups) display selective interactions between metallic SWNT and nucleophilic (electron-rich) species like alkyl amines [Chattopadhyay et al., 2003] and bromine [Chen et al., 2003b]. These results are consistent with a

key spectroelectrochemical Raman study that attributes diameter and class-specific redox potential variations to systematic differences in absolute Fermi levels [Okazaki et al., 2003]. Representative redox reactions with transition metal species include electroless deposition of gold and platinum on SiO_2-supported SWNT [Choi et al., 2002], glucose sensors based on SWNT fluorescence quenching by ferricyanide ion [Barone and Strano, 2006], silver nanoparticle production upon illumination of DNA-wrapped SWNT [Zheng and Rostovtsev, 2006], and selective modification of carbon nanotubes with metal salt solution via bipolar electrochemistry [Warakulwit et al., 2008]. Other techniques have been reported to obtain homogeneous and indiscriminate metal nanoparticle coatings around carbon nanotubes (CNTs) [Liu et al., 2003; Jiang et al., 2003b; Ellison, 2007; Rahman et al., 2005].

4.3   Overall Findings

Here, we explore the intersection of SWNT redox chemistry and antenna effects, and demonstrate redox processes initiated by microwave field-induced dipoles in well-dispersed SWNT-surfactant suspensions —nanotube antenna chemistry. We find that microwave frequencies activate preferentially metallic SWNT. The process directly reduces transition metal ions in solution to produce nanoparticles, both free-floating and regio-specifically deposited on nanotube extremities, and shows partial diameter selectivity based on the oxidation potential of the acceptor species involved. We demonstrate a charge transfer mechanism based on Fowler-Nordheim field emission. This process is quite distinct from previous reports using microwave fields to simply heat multi-wall carbon nanotube aggregates in the presence of transition metal ion mixtures, which generates disordered metal deposition on their sidewalls [Chen et al., 2003a, 2004; Luo et al., 2007]. The reactions are activated also by electromagnetic fields in the radio frequency (RF) and optical regimes. Atomic force microscopy (AFM) images show formation of novel SWNT Nanoparticles-Nanotube Structures (nanoPaNTs). The resulting nanoPaNTs include dumbells, SWNTs partially or com-

pletely encapsulated by metal, rings, and straight SWNT "threaded" through rings to form shish-kebab structures. Mixtures of surfactants and polymers apparently disrupt the local environment of polarized SWNT, reducing the energy needed for forming ordered nanostructures, especially rings. We infer that electrodeposition reactions proceed on a significantly faster time scale than ring formation. These processes can potentially be used for self-assembly of complex 3-D structures and for templating the formation of nanorods with high aspect ratio. The reactions reported here yield novel composite nanostructures that could prove useful in applications as varied as radio frequency thermoablation [Gannon et al., 2007], photothermal ablation [Kam et al., 2005], and photoconversion [Kymakis and Amaratunga, 2002].

4.4 Experimental Methods

4.4.1 Reagents

Surfactants employed included Pluronics (F88-Prill, $HO(C_2H_4O)_n$–$(C_3H_7O)_m$–$C_2H_4O)_n$, BASF), sodium dodecyl sulphate (SDS, $C_{12}H_{25}OSO_3Na$, 99+%, Aldrich), dodecyl-benzenesulfonic acid, sodium salt (SDBS, $C_{18}H_{29}O_3SNa$, 99+%, Aldrich), Triton X (TX-100, $C_{14}H_{22}O(C_2H_4O)_n$, 99%, Aldrich), and cetyl-trimethy-ammonium bromide (CTAB, $(C_{16}H_{33})N(CH_3)_3Br$, 99%, Aldrich); all were used as received and employed at 1 weight percent (wt%) in deionized (DI) water. Transition metal salts, all used as received from Aldrich, were used as redox agents, including gold (HAuCl$_4$, 99.999%), silver (AgNO$_3$, 99.999%), palladium (K$_2$PdCl$_4$, 99.99%), platinum (H$_2$PtCl$_6$, 99.995%), copper (CuCl$_2$, 99.999%), tin (SnCl$_2$, 99.99%), and iron (FeCl$_3$, 99.99%). All metal salt solutions were prepared at a concentration of 1 mM in deionized water. Unless otherwise stated, all microwave reactions were performed in a MARS$_X$ (CEM Corporation, Matthews, NC, USA) operating at 2.54 GHz (multimode) with 1000 W for 10 sec. Microwave reactions were performed with 1 mL of SWNT suspension (plus variable amounts of metal salt solution, as noted) in 2 mL glass vials (1 cm diameter × 3 cm tall). The (uncapped) sample vials were placed

over the geometric center of the microwave reactor on an inverted Pyrex dish (80 ×
40 mm); no other accessories were placed inside the reactor.

4.4.2 SWNTs Suspension Preparation

SWNT-microwave (MW) interactions were studied using aqueous surfactant suspen-
sions of individualized raw HiPco SWNT [Carver et al., 2005] (batch number 164.4)
produced in the Carbon Nanotechnology Laboratory at Rice University. The sur-
factant suspensions were prepared using homogenization, ultrasonication, and ultra-
centrifugation following standard literature methods [O'Connell et al., 2002]. Deion-
ized (DI) water (18 MΩ resistivity) obtained from a NanoPure system (Barnstead,
Dubuque, IA USA) was used throughout this work.

Stable suspensions of SWNT solutions were prepared by first homogenizing
250 mg of raw HiPco SWNTs in 200 mL nanopure water that contained 1 wt% sur-
factant at 500 RPM for 2 hrs (Dremel Multi-Pro tool, 35,000 RPM, Racine, WI).
Second, tip sonication (Cole Parmer Ultrasonic Processor, Tip —Model CV26, Ver-
non Hills, IL) was performed in a 20 mL water bath at 20 % power for 2 min followed
by bath sonication (Cole Parmer Ultrasonic Cleaner (Model 08849–00), Vernon Hills,
IL) for 2 min. Third, ultracentrifugation (Sorvall Discovery 100SE (by Hitachi), Ro-
tor —AH629, 36 mL) for 4 hrs at 29K RPM was followed by subsequent removal
of 2/3 volume of the supernatant portion via pipette. Note that our experimental
observations suggests that homogenization, low sonication time/power, and temper-
ature control of the SWNT suspension are the most important steps to obtaining a
suspension of SWNTs suitable for electromagnetic experiments. All reactions were
carried out using surfactant suspended SWNTs at an initial SWNT concentration of
10 mg/L; SWNT concentration in [mg/L] was determined by dividing the absorbance
value at 763 nm by 0.043. This value was used to normalize the fluorescence spectra.

4.4.3 Spectroscopic Measurements

Unless otherwise stated, all spectroscopic measurements were obtained with 1 mL of SWNT-surfactant mixture in a sterile 1.5 mL polymethylmethacrylate (PMMA) cuvette (LPS, L324101). Ultraviolet-visible-near infrared absorbance and fluorescence spectra were obtained with a Nanospectralyzer Model NS1, Version 1.95 (Applied Nanofluorescence, Houston, Texas, USA). Absorbance spectra were obtained in the visible and near infrared regions (400 to 1400 nm) using integration times of 500 ms and 10 accumulations. The SWNT fluorescence was excited at 660 nm and emission spectra were obtained between 900 and 1400 nm using 500 ms integration times and 10 accumulations. Absorbance at 763 nm was used to normalize the fluorescence spectra. Liquid-phase Raman measurements were obtained using 785, 633, and 514 nm laser excitation with an inVia micro-Raman spectrometer (Renishaw, Gloucestershire, UK). Liquid samples were held in a Renishaw Raman Macro Sampling Set in a 2 mL glass vial. Raman spectra were collected from 100 to 3200 cm^{-1} with Wire2 data acquisition software, using 20 sec exposure times and 1 accumulation.

4.4.4 Atomic Force Microscope

Atomic force microscope (AFM) images were obtained with a Nanoscope IIIa (Digital Instruments/Veeco Metrology, Inc., Santa Barbara, CA USA), operating in tapping mode, using 1 – 10 Ohm–cm phosphorus (n) doped Si tips (Veeco, MPP-11100-140) at a scan rate of 2 Hz and 512 × 512 resolution. Samples for AFM analysis were prepared with 20 μL of SWNT suspensions spin coated at 3000 RPM onto a roughly 0.25 cm^2 freshly cleaved mica surfaces (Ted Pella, Inc., Redding, CA USA). To remove the excess of surfactant, immediately after the SWNT suspension was deposited, the substrate was rinsed with 2 mL of 2-isopropanol, followed by 5 μL of N-methyl-pyrrolidone (NMP), and then again 2 mL of 2-isopropanol after which the sample was spun for 10 min. To obtain high quality AFM images, we found that the cleaning

procedure was fundamental, as well as the addition of the SWNT suspension in a continuous flow instead of drop-wise. Drops cause a build-up of SWNT layers that tend to form bundle-like structures.

4.5 Results and Discussion

4.5.1 SWNT Antennae

An antenna transmits and receives electromagnetic waves at wavelengths that are close to the length of the antenna, and it does so by converting electrical current to electromagnetic waves and vice versa. All antennas have two major properties. First, their response varies with orientation of the incoming radiation. Second, their response varies with their length, being strongest when the length is a multiple of half of the wavelength (λ) of the radiation (0.5λ, 1.0λ, 1.5λ, etc) [Wang et al., 2004a; Dresselhaus, 2004]. Carbon nanotubes have been shown to act as antennae in the microwave, radio, optical, and near-infrared frequencies by converting the incident radiation into heat [Gannon et al., 2007; Kam et al., 2005; Kymakis and Amaratunga, 2002].

4.5.2 Electric Field Structure Around a SWNT

Figures 4.1.a shows the polarized electric field structure around individual bare and surfactant-coated metallic SWNT immersed in water. The electric field was obtained using a COMOSOL Multiphysics software, see section 4.7.11. This model serves to visually illustrate our hypothesis that electric fields (e.g. in a microwave reactor) will interact exclusively with suspended metallic SWNT to drive electron transfer reactions, especially at their tips (Fig 4.1.b,c). The nanotubes have length $L = 1$ μm and diameter $D = 1$ nm, and are fully aligned with an electric field E $= 1$ V/m (10^6 V/μm). Good conductors maintain uniform potential by redistribution of charge when subjected to external electric fields; the tubes are set to 0 V, the potential at

their mid-point. The apparent electric field strength at the tip of the bare nanotube is amplified by geometric effects by about $\beta/2$, to yield $E_{tip} \approx 500$ V/m [Buldum and Lu, 2003]. The local field strength decays rapidly with distance r from the SWNT, by r^{-2} away from the hemispherical ends and r^{-1} away from the sidewalls of the SWNT, respectively. The SDBS surfactant layer compresses further the electric field gradient around the SWNT tip, as discussed quantitatively below (Section 4.5.10). In alternating (AC) fields, an induced potential of $\delta U = \pm\ EL/2 \approx \pm\ 0.5$ V is expected between the SWNT tips and the electrolyte bath a few nm away, significantly modulating their normal redox potential(sec). Semiconducting SWNT polarize weakly and are essentially unaffected by such applied fields [Krupke et al., 2003].

4.5.3 Alignment of SWNT Under Applied Field

The alignment of the SWNTs with the applied electromagnetic field, especially for metallic tubes, is an important factor that must be considered. This is crucial because if the SWNTs do not align with the applied field for the duration of the experiment, the electric field gradient around the SWNT tip will not generate, thus no redox reaction will occur. To evaluate the alignment of metallic SWNT with the applied microwave field, we computed the ratio between the electric torque E^T following the work of Mendes et al. [2008]:

$$E^T = \pi r_{NT}^2 l_{NT} \varepsilon_m [K^{\parallel} K^{\perp}][L^{\parallel} L^{\perp}]\frac{E_{MW}^2}{80} \underbrace{(\vec{\mu} \cdot \vec{r})(\vec{\mu} \times \vec{r})}_{Orientation\ Vector} \tag{4.1}$$

and the thermal energy kT, where k is Boltzmann's constant and T is absolute temperature, then:

$$K^{\parallel,\perp} = \frac{(\varepsilon_{NT} - \varepsilon_m)}{(\varepsilon_m + (\varepsilon_{NT} - \varepsilon_m)L^{\parallel,\perp})} \approx \frac{1}{L^{\parallel,\perp}} \tag{4.2}$$
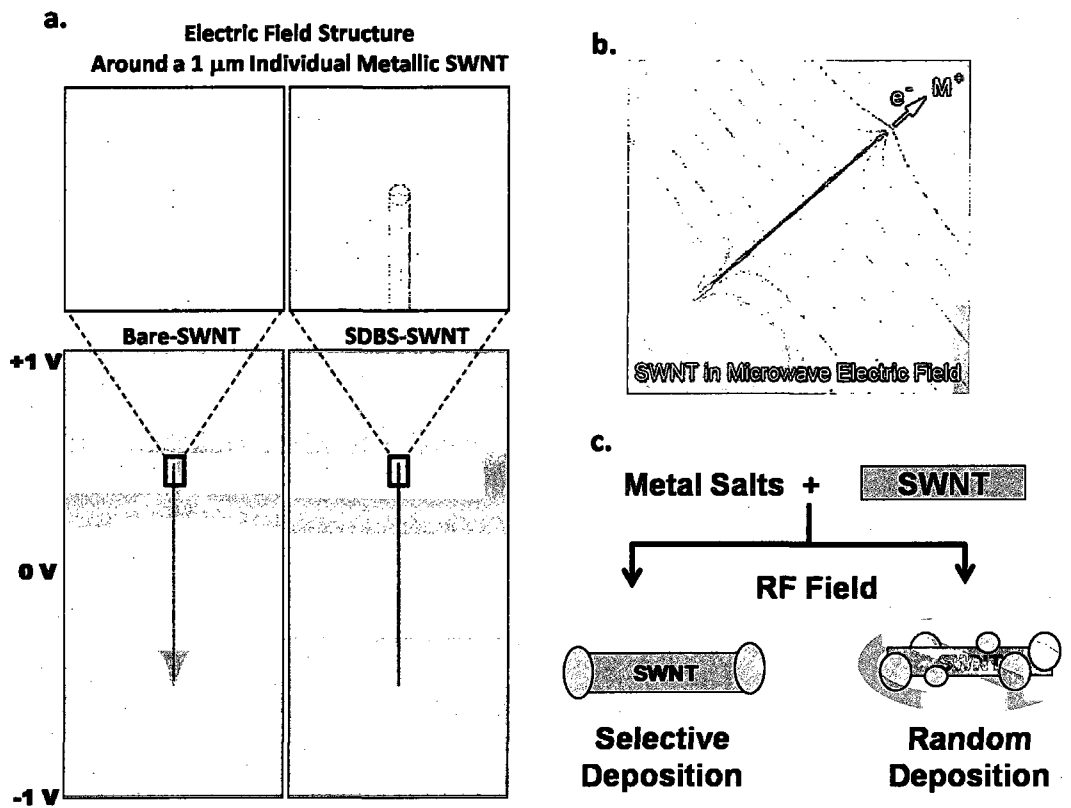
Figure 4.1 : (a–b) Electric field structure around a SWNT (diameter 1 nm, length 1 μm) in a constant 1 V/ m field. (a.) (left) and without (right) 3 nm surfactant layer. (b.) Redox reactions with transition metal salts. (c.) Selective tip deposition of metal particles.

$$L^{\parallel} = \frac{4\pi_{NT}^2}{l_{NT}^2} \left(\log\left[\frac{l_{NT}}{r_{NT}}\right] - 1 \right) \tag{4.3}$$

$$L^{\perp} = \frac{1 - L^{\parallel}}{2} \tag{4.4}$$

We assume that the magnitude of the orientation vector is 1/2 (because we have the magnitude of the product of sine (dot product) and cosines (cross product), whose maximum value is 1/2), the dielectric constant of the SWNTs (ε_{NT}) is much

larger than the medium (ε_m) (which is a valid assumption for metallic tubes) and we account only for its real part (permittivity). A ratio $E^T/(kT) > 1$ indicates that SWNTs will overcome Brownian motion, thus aligning with the applied field. We use an estimated electric field strength in the microwave reactor $E_{MW} \sim 3.45 \times 10^5$ V/m (Sec. 4.7.3), divided by the dielectric constant of water to account for the capacitance of the medium, and we consider a length distribution of HiPco SWNT between 100 – 1000 nm (l_{NT}) with an average radius $r_{NT} \sim 0.5$ nm. In these conditions, metallic SWNT longer than ~ 400 nm will overcome Brownian motion and align with the applied field within the time scale of the experiment, 10 sec (see Sec. 4.5.4 for experimental details), while metallic and semiconducting SWNTs shorter than ~ 400 nm will undergo rotational diffusion (Fig 4.2).

Because the duration of the electromagnetic radiation exposure in our experimental work is ~ 10 sec, which is about three orders of magnitude higher than the characteristic time for dipolar alignment [Jones, 1995] and Brownian rotation [Duggal and Pasquali, 2006] (few ms), and the average experimental field strength is 3.5 × 10^5 V/m, yields a dielectric alignment energy far in excess of the thermal energy kT, indicating that metallic SWNT aligned with the field and polarized.

4.5.4   Spontaneous Reduction of Transition Metal Salts

We performed control experiments with various SWNT-surfactant suspensions and transition metal acceptor species to screen out systems with spontaneous redox reactions and isolate conditions wherein electron transfer reactions could be unambiguously attributed to electric field stimulation. 1 mL surfactant-SWNT samples (1 wt% surfactant, 10 mg/L SWNT) and 30 μL metal salt solution (1 mM), were heated to 55 °C for 2 hours, then characterized with ultraviolet-visible absorbance, near infrared fluorescence, and atomic force microscopy (AFM); no specific reducing agents [Kim et al., 2002] were employed. Results are summarized in Figure 4.3. The
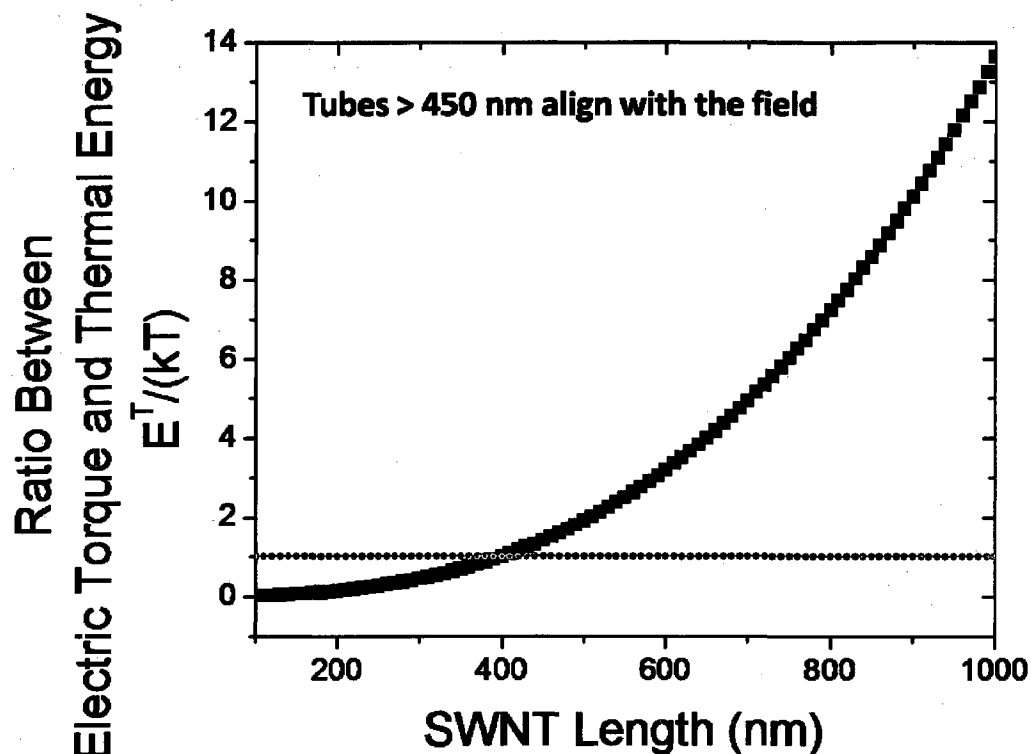
Figure 4.2 : Alignment of metallic SWNT with a microwave field.

non-ionic surfactants Triton X (TX) and Pluronics (F88), and the cationic surfactant cetyltrimethylammonium bromide (CTAB) supported rapid spontaneous reactions with most metal salts tested, qualitatively indicated by producing colored solutions as well as nanoparticles directly observable by AFM. No spontaneous reactions were observed in sodium dodecylbenzene sulfonate (SDBS) suspensions with any of the acceptors listed. The smaller anionic surfactant, sodium dodecyl sulfonate (SDS), supported very slow reactions (taking over 48 hrs) with H_2PtCl_6 or $HAuCl_4$. We also verified that no detectable (by ultraviolet-visible and AFM) nanoparticles were produced when SDBS solutions (without SWNT) were heated with the listed transition metal salts in a multi-mode microwave reactor ($MARS_X$, CEM, 2.54 GHz) at 1000

W for 10 sec (standard microwave protocol used throughout this work). Microwave processing increased their temperature by an average of 35.7 ($\pm$1) $^{\circ}$C, regardless of the metal salt employed.

All further tests of microwave field-induced chemistry were therefore performed with SDBS. Metal salts were reduced to metal nanoparticles in this system exclusively when activated by microwave radiation. SWNT/SDBS + $HAuCl_4$ sample temperatures increased by 36.2 ($\pm$1) $^{\circ}$C during the procedure, just 0.5 $^{\circ}$C more than in the control sample (no SWNTs). This negligible temperature difference eliminates the possibility of significant localized thermal effects via direct microwave heating of these well-dispersed nanotubes. Particle formation in this case is clearly driven by microwave activation and not by a purely thermal process. Examination of the AFM images (discussed below) shows that while a substantial fraction of the SWNTs have attached metal particles, others are devoid of particles. The rightmost column in Fig. 4.3 shows the percentage (std. dev.) of nanotubes with attached nanoparticles as directly observed by AFM. Interestingly, the percentage of SWNT with attached nanoparticles decreases monotonically with the oxidation potential of the transition metal acceptor employed. This fraction also approximates the proportion of metallic SWNT with redox potentials more negative than the acceptor employed (see Fig. 4.3).

4.5.5 SWNT Redox Landscape

The SWNT redox landscape for aqueous suspensions of SWNTs in small-molecule anionic surfactants, including SDS and SDBS is depicted in Figure 4.4.a. It gives a prediction of the Fermi level of the SWNTs as a function of bandgap and their relative reactivity, from which we can design a series of experiments in which different SWNT populations can be accessed. Figure 4.4.a is an extrapolation from spectroelectrochemical Fermi level observations reported by Okazaki et al. [2003],

Spontaneous Particle Formation at 55°C							MW Reaction SWNT-SDBS
Reactant U vs NHE	SDBS	SDS	F88	TX	CTAB	PVP	% SWNT with Particles
$SnCl_2$ 0.1375							0
$CuCl_2$ +0.342							20 ± 9
K_2PdCl_4 +0.591							
$FeCl_3$ +0.771							63 ± 16
$AgNO_3$ +0.799							
$HAuCl_4$ +1.002							85 ± 13
H_2PtCl_6 +1.180							

Figure 4.3 : Summary of spontaneous and microwave-stimulated nanoparticle formation using various combinations of metal salts and surfactants (dark = spontaneous particle formation; light = no particles).

and plotted in the manner introduced by O'Connell et al. [2005] for semiconducting SWNT, who verified the semiconductor valence band levels using organic oxidizers to quench fluorescence in the near infrared (both of these key prior works examined SWNT in conjunction with aqueous SDS). Okazaki monitored the intensity of Raman radial breathing mode (RBM) scattering from individual laser-oven SWNT (with 2 nm mean diameter) captured on a gold electrode as a function of electrode potential versus an electrolyte containing sodium dodecylbenzene sulfonate (SDS). The potentials giving maximum radial breathing mode intensity for given individual SWNT were reported as the absolute Fermi level for metals and the absolute mid-gap level for semiconductors. Metals and semiconductors were found to follow distinct linear trends when plotted against radial breathing mode frequency, respectively, with:

$$V_{f(met)} = 1.120 + 22.2 \text{ mV} \times v_{rbm} \text{ and } V_{f(semi)} = 1.584 + 12.0 \text{ mV} \times v_{rbm}$$

(V in volts below vacuum; v_{rbm} in cm^{-1}).

Landscape

Since the Raman radial breading mode (RBM) frequencies are uniquely related to tube diameter by $v_{rbm} = A/d_t + B$ (with A = 223.5 cm^{-1} and B = 12.5 cm^{-1}) and the bandgap fluorescence wavelength of semiconducting SWNT varies to first order inversely with diameter with $\lambda_{11} = 1167d_t$ (both in nm), we can generate a simple quasi-linear relationship for the Fermi level and redox potentials of semiconducting and metallic SWNT as a function of diameter (for metals) and bandgap emission frequency (for semiconductors) together (Fig. 4.4.a). Normal Hydrogen Electrode (NHE) (VNHE = 0) is usually taken to be 4.5 volts below the vacuum level [Nozik, 1978], allowing one to relate redox potentials to the work function, which is referenced to vacuum (Fig. 4.4.a).

The redox potentials of SWNT in our SDBS suspensions appear to be equivalent to those in SDS, since the pattern and degree of diameter-selective fluorescence quenching by different metal salts with different redox potentials (see Fig. 4.4.b) is similar to that caused by 4-amino-1,1-azobenzene-3,4-disulphonic acid (AB) (~0.65 V vs. NHE) as reported by O'Connell et al. [2005]. The metallic curve in particular is an extrapolation from a fairly small set of tubes (with diameters of 0.85 − 1.15 nm) observed by Murakoshi, so the Fermi levels for smaller tubes like those in our samples (0.8 − 1.4 nm; 1.1 nm average) should be taken as approximate. The redox levels shown in Fig. 4.4.a might not be valid for nanotubes suspended in neutral or cationic surfactants due to charge screening around the tubes as discussed in Section 4.5.5. If the microwave field only activates metallic SWNT via antenna processes, then the reacting-fraction data shown here provide experimental support for the diameter dependence of the redox potential of metallic SWNT indicated in Fig.

4.4.b, and further implies that the fundamental process involves transfer of electrons from metallic SWNT to acceptors with higher oxidation potential. Four important observations can be extracted from Figure 4.4.a.

- The Fermi levels of the SWNTs do not equilibrate with the bath. We attribute this to the surfactant layer which creates an insulator around the SWNTs and a low k value (Fig 4.4.c).

- There is a large offset between the semiconducting and the metallic SWNTs. The surfactant layer creates an energy barrier between the tubes and the bath, which does not allow electron recombination between the bath and the SWNTs and leaves the metallic tubes positively charged with respect to the bath (Fig 4.4.a).

- The Fermi level of the SWNTs has a systematic variation with diameter dependence.

- Different populations of tubes can participate selectively in redox reaction with organic and inorganic acceptor and donor molecules by adjusting the redox potential. For example, different redox level metal salts react preferentially with different tube types and diameters (Fig 4.4.b).

The preferential diameter reactivity can be clearly observed in the selective fluorescence quenching of the SDBS-SWNT suspension exposed to different transition metal salts such as: Cu^{2+}, Fe^{3+}, and Au^{3+} (Fig 4.4b); as the redox potential of the transition metal salt increases from 0.342 to 1.002 V, the fluorescence peaks between 1150 and 1400 nm disappear at a faster rate than those between 900 and 1150 nm (large to small diameter semiconductors). This selective fluorescence quenching is consistent with the prediction obtained in Fig. 4.2.a.
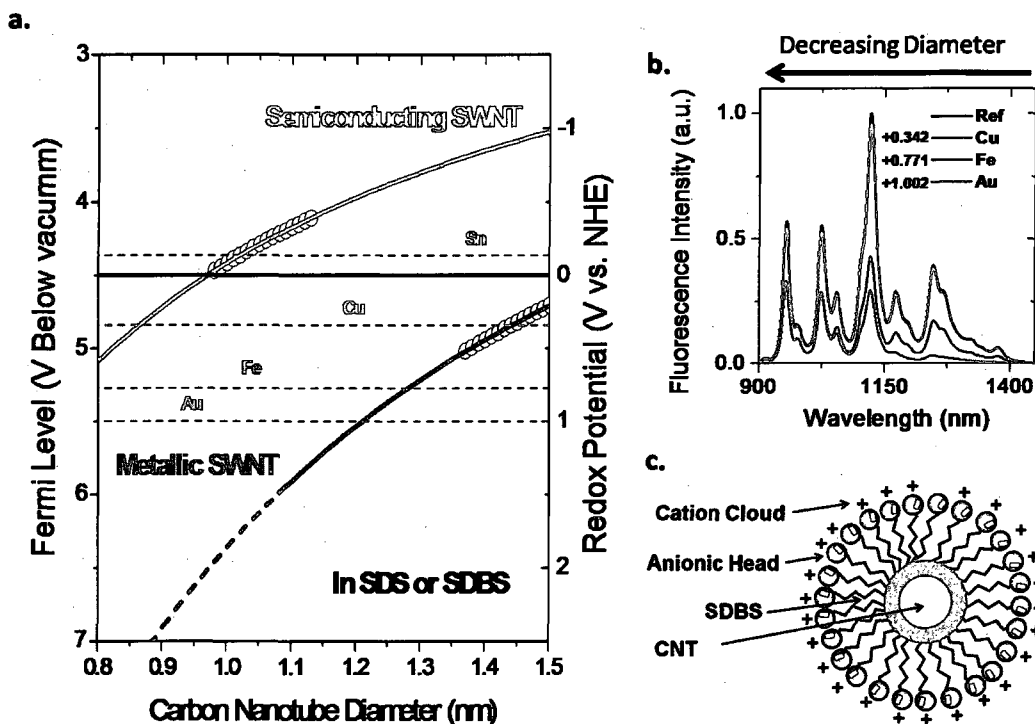
Figure 4.4 : SWNT Redox Landscape. (a.) Fermi level and redox potential of metallic and semiconducting SWNTs (b.) Fluorescence dependence on redox potential of metal salts, 660 nm excitation wavelength. (c.) Surfactant arrangement around SWNTs.

Diameter Dependence

In order to better illustrate the diameter selectivity predicted with the redox landscape (sec. 4.5.5), the fluorescence intensity of SDBS-SWNT was monitored as the concentration of Fe(III) ion salts increase. Figure 4.5 shows that as the concentration of metal ions increased, the fluorescence peaks decreased at different rates with faster rates for larger diameter semiconducting SWNTs. The inset of Figure 4.5 shows the rate constant for 6 different semiconducting SWNTs as a function of tube diameter. We observed that the rate constant increased linearly with diameter, between 6 and

15.
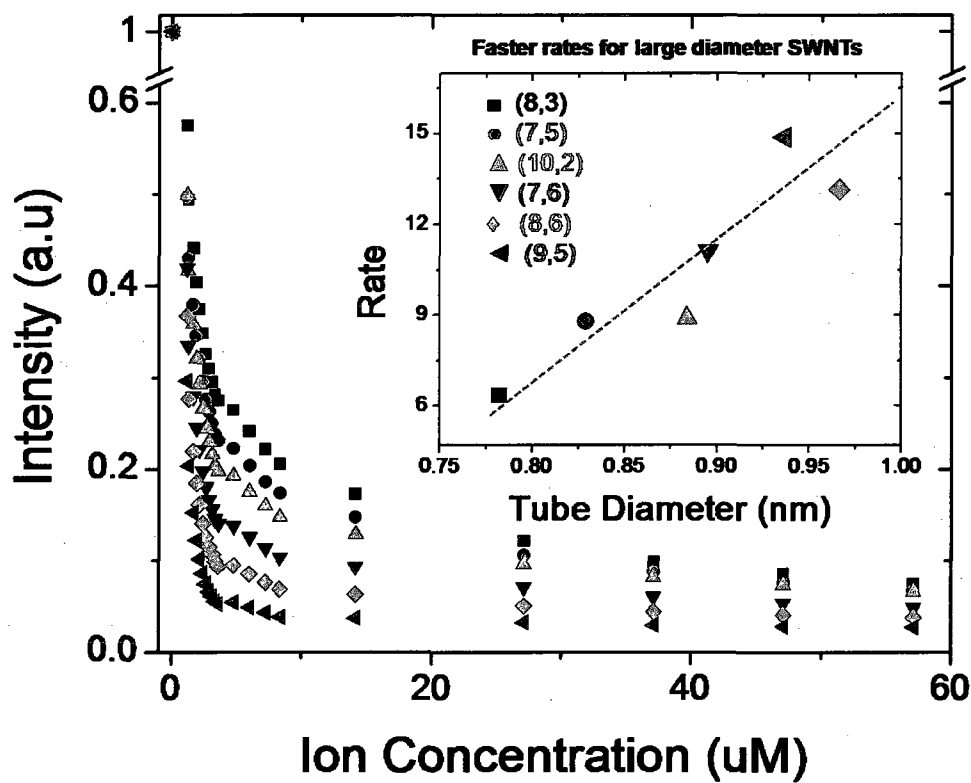
Figure 4.5 : SWNT redox landscape. (a.) Fluorescence intensity decay of SWNTs in SDBS as a function of ion concentration with 660 nm excitation wavelength. Inset shows the rate constant as a function of chirality: (8,3) black square, (7,5) red dot, (10,2) up green triangle, (7,6) down blue triangle, (8,6) light blue diamond, and (9,5) left magenta triangle.

Rates of Reaction

The reactivity of surfactant-suspended SWNTs may be controlled by altering the Fermi level of the tubes via surfactant selection. Charged surfactant monolayers pro-

vide an insulating barrier along the tube as well as a surface dipole which generates a diameter-dependent potential well. The energy value of the potential well can be modified by adjusting the surfactant charges around the tube. This ability is illustrated by comparing the reaction rates of Fe(III) metal ions with SWNTs wrapped in positively charged (CTAB), negatively charged (SDBS, as shown in Figure 4.5), and neutral (Triton X) surfactants. Figure 4.6 shows that the overall reactivity of the SWNTs decreases as the surfactant charge goes from negative to neutral, with no apparent selectivity with positively charged surfactants (inset Fig. 4.6). This indicates that the Fermi level of the suspension has been changed by only altering the surfactant employed. Therefore, for all experiments probing the selectivity of redox reactions between SWNTs and transition metal salts in the presence of incident radiation (microwaves), SDBS suspended SWNTs were used so that the broadest spectrum of SWNT reactivity is available. Interestingly, we also found that using SDS (another anionic surfactant) gives similar diameter dependent reactivity as SDBS, but with reaction rates roughly twice as fast as SDBS. This can be caused by differences in the packing and/or arrangement of the surfactants around the tube.

4.5.6 Deposition Morphology

Figures 4.7.a–b contrast the morphology of nanoparticles generated by spontaneous (thermal) and microwave-driven processes. Atomic force microscopy (AFM) of a representative spontaneous reaction product, HAuCl$_4$ with SWNTs suspended in F88, clearly shows a combination of free metal particles and non-selective sidewall decoration of the SWNTs (Fig. 4.7a). This reaction mixture turned reddish and developed a strong ultraviolet-visible absorption peak at 523 nm within ten minutes of warming in a water bath to 55 °C; both factors are indicative of gold nanoparticle formation [Kim et al., 2002]. In contrast, when SDBS-SWNT suspensions were irradiated in the microwave reactor for only 10 sec at 1000 W in the presence of HAuCl$_4$, the solutions
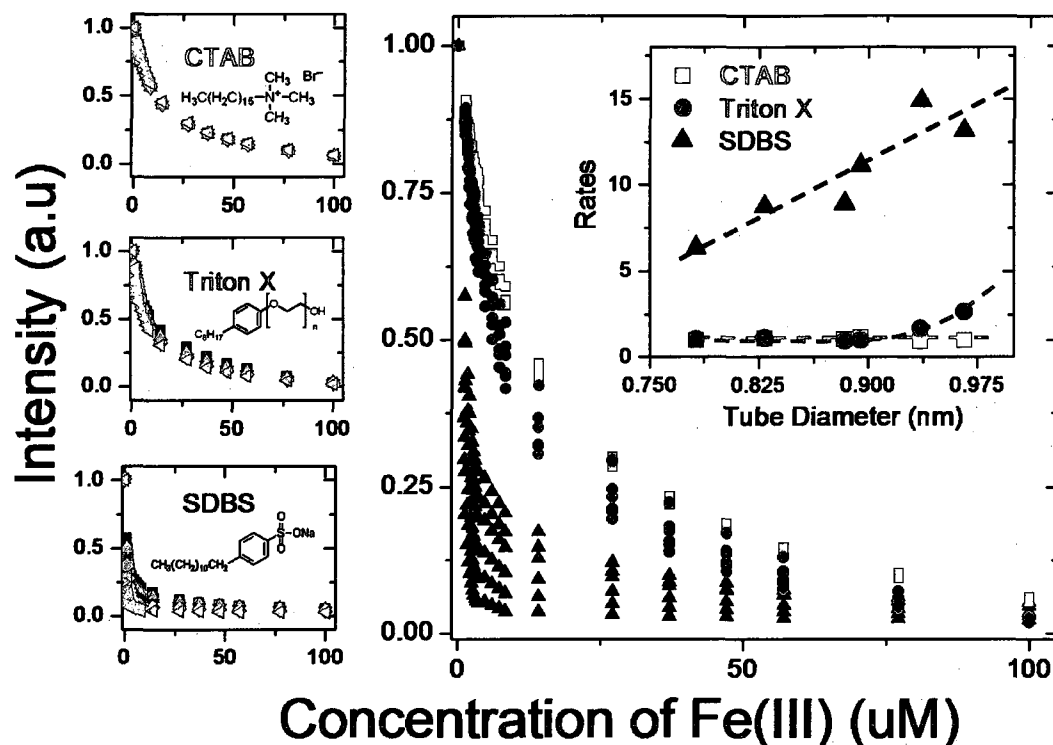
Figure 4.6 : SWNT redox landscape. Fluorescence intensity of SWNTs in different charged surfactants CTAB (cationic), Triton X (nonionic), and SDBS (anionic) using 660 nm excitation wavelength. Inset shows the rate constants as a function of chirality of the SWNTs suspension: black triangle SDBS, red dots Triton X, and red squares CTAB. The SDBS data was previously shown in Figure 4.5.

immediately displayed color changes and ultraviolet-visible absorbance features characteristic of Au nanoparticle formation (Fig. 4.8). The Au reduction produces some residual hydrochloric acid (HCl) which accounts for the small change of pH after the reaction reached completion* and undergoes the following reaction:

a.) $AuCl_4^- + 4e^- \leftrightarrows Au^0 + 4Cl^-$

b.) $2H_2O \leftrightarrows O_2 + 4e^- + 4H^+$

c.) $4Cl^- + 4H^+ \leftrightarrows 4HCl$

---
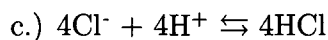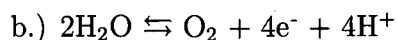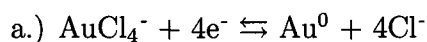
*After Au reduction the pH of the suspension decreased about 0.8 units (6.15 to 5.35). After 3 days the pH returned to almost the starting point (6.03).

Several factors support this reaction scheme: (a.) metallic SWNTs have a substantial positive reduction potential in this system (Fig. 4.6). (b.) modulation by the microwave field will periodically induce at the SWNT tips a potential higher than their quiescent reduction potential, and (c.) after electron ejection, the SWNT will be positively charged and will have even higher oxidizing power. In combination, these factors appear to generate sufficiently high potential to oxidize water and free the protons needed to balance the chloride ion and produce HCl, consistent with the observed pH shift. The amount of oxygen generated is not sufficient to generate bubbles. AFM images of SWNTs treated in this manner show a highly preferential deposition of Au nanoparticles at the tips of the SWNTs (Fig. 4.7.b.3). Raising the initial gold concentration (150 μM Au) resulted in progressive growth of apparently coaxial metal sheaths extending back from the tips of some of the SWNTs (Fig. 4.7.b.(4)). These sheaths have a fairly uniform height of 10 nm, while the tip particles averaged 14 nm in height by AFM. Reactions yielding cylindrical deposits developed a purplish color and the 530 nm feature broadened significantly to the red, entirely consistent with the known spectroscopic characteristics of gold nanorods (Section 4.5.7 and Appendix 4.7.5, Figures 4.7 and 4.21) [Kim et al., 2002]. Overall, these deposition structures accurately reflect the locations of high field gradients around the SWNT tips, in good accord with our model for antenna chemistry with metallic SWNT (additional spectroscopic and microscopic evidence of tip deposition is presented in Section 4.7.5).

4.5.7 Selective Activation of Metallic SWNTs

To directly probe SWNT type selectivity in these reactions, we analyzed the ultraviolet-visible and liquid-phase Raman signatures of SDBS-SWNT-HAuCl$_4$ mixtures after microwave processing. Before the spectroscopic data can be analyzed for the relative abundance of various SWNT types, the strong absorption peak of Au nanoparticles
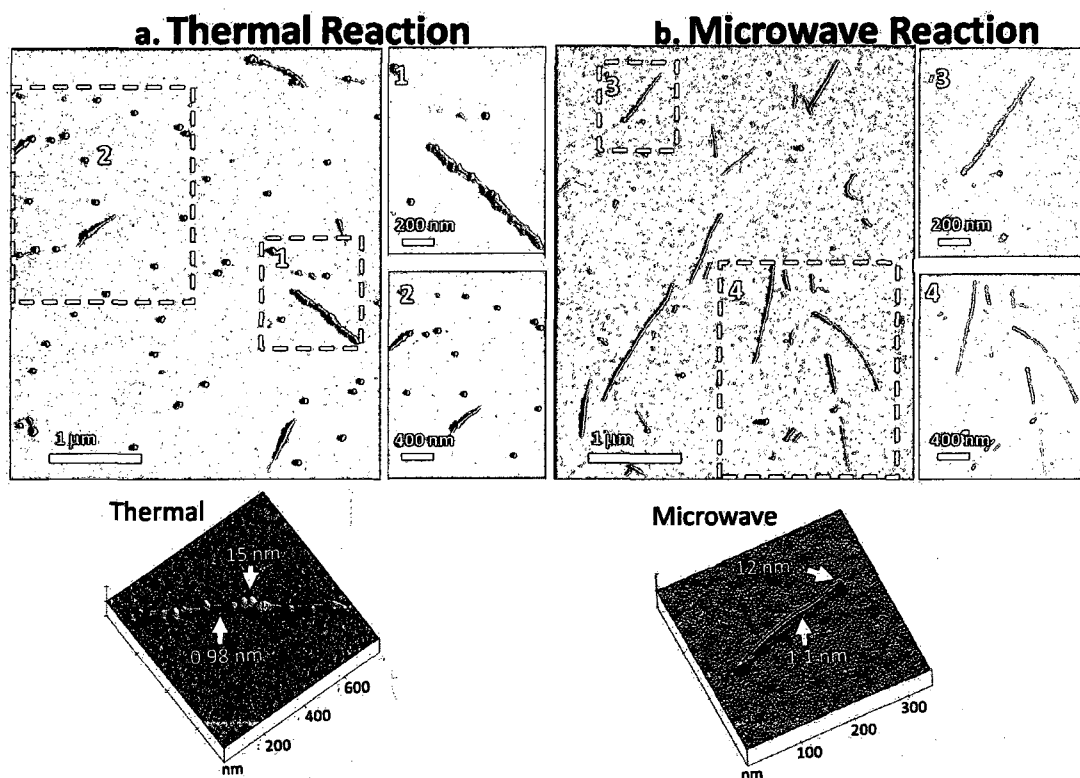
Figure 4.7 : SWNT-Au nanoparticle morphologies. (a–b.) Representative AFM images of spontaneous and indiscriminate sidewall decoration (a) and tip selective (b) reduction of Au metal salts onto SWNTs by thermal (a) and microwave (b) reduction. 3-D thermal and microwave reduction of Au metal particles.

at around 530 nm needs to be removed. We achived this by mild centrifugation (Mi-croD, Fisher Scientific, at 4,500 g for 10 minutes, Fig. 4.8b). Centrifugation quickly removes larger Au particle-containing species from solution due to their high density (Fig. 4.9b). Spectra from the supernatant after centrifugation are shown in Figure 4.9, while Figure 4.11 shows spectra obtained by resuspending the pellets that had precipitated upon mild centrifugation.
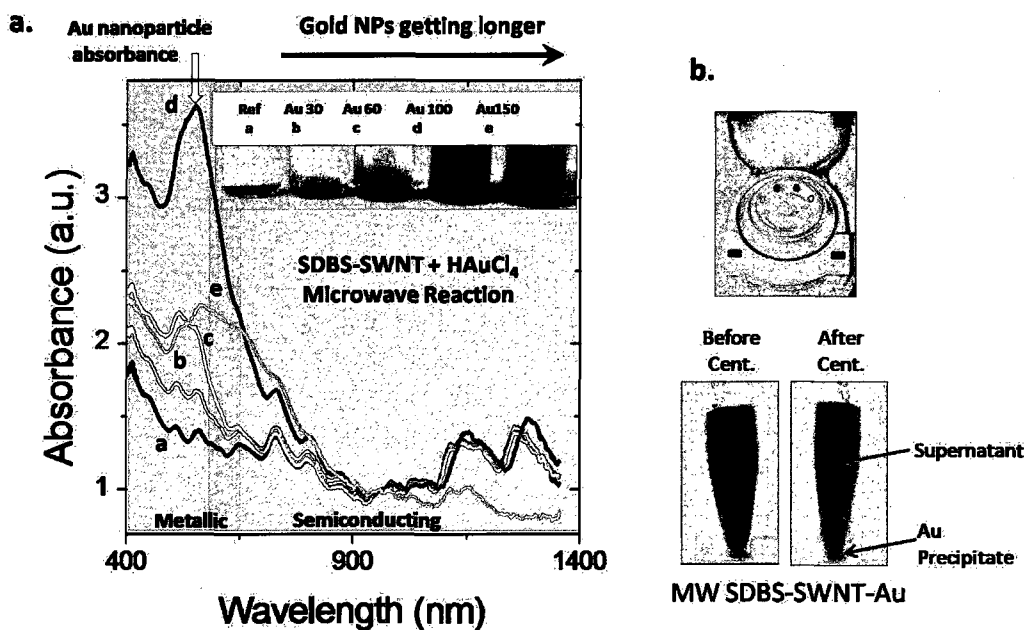
Figure 4.8 : (a.) Absorbance of microwave driven reaction of SDBS-SWNT with different amounts of 1mM $HAuCl_4$ (0 μL reference, black; 30 μL, red; 60 μL, green; 100 μL, blue; and 150 μL, light blue). (b.) Representative Au removal via centrifugation.

Supernatant

Figure 4.9a–d shows the spectral effect of adding three different amounts of 1 μM $HAuCl_4$ solution to the SWNT-SDBS suspension prior to microwave processing compared to the reference suspension without gold (black trace) after mild centrifugation for the supernatant section. A significant and progressive depletion of the metallic peaks (400–650 nm) (inset, Fig. 4.9a.a) is seen with increasing $HAuCl_4$ concentration, along with eventual bleaching of the E_{11} transitions of the large diameter semiconductors (1100–1400 nm). Further evidence of type selectivity in this process is provided by liquid-phase Raman spectra obtained using three different excitation wavelengths that are in resonance with different populations of HiPco SWNTs (514 nm, in resonance mainly with metallic tubes; 633 nm, which samples a portion of both

metallic and semiconducting SWNT populations; and 785 nm, in resonance mainly with semiconducting tubes) [Kataura et al., 1999; Maultzsch et al., 2005; Telg et al., 2006; Dresselhaus et al., 2007a]. Importantly, liquid-phase Raman avoids morphology-related spectral modifications previously noted with precipitated SWNT [Dyke et al., 2005] and allows quantitative interpretation by integrating the area of radial breathing mode (RBM) peaks for metallic and semiconducting SWNT populations. Figure 4.9.b–d show the RBM peaks of the supernatant solution using the three different excitation wavelengths (b) 633 nm, (c) 785 nm, and (d) 514 nm (see Appendix 4.7.6). Figure 4.9.b shows that when the SWNT suspension is microwave processed with 500 μL of HAuCl$_4$ solution, essentially all of the metallic SWNT species are apparently removed after centrifugation, yielding a supernatant highly enriched in small diameter semiconducting SWNT. We also observed that the integrated area of the metallic SWNT peak using 633 nm excitation decreased exponentially with gold concentration (Figure 4.10). To further confirm the metallic depletion and diameter (d_t) selectivity, we obtained Raman using 514 nm excitation, which brings metallic SWNT in our samples into resonance (Fig. 4.9.d). We observed that after the addition of 500 μL of HAuCl$_4$ and microwave processing (green trace), the RBM features associated with the metallic SWNT were depleted approximately 90% compared to the starting material (black trace). Figure 4.9c shows Raman spectra excited at 785 nm (sensitive to semiconducting SWNT); the shoulders at 215 and 225 cm^{-1} ((9,7), d_t = 1.103 nm and (10,5), d_t = 1.050 nm respectively) decrease somewhat more rapidly than the main peak at 233 cm^{-1}, which is associated with the smaller (11,3) (d_t = 1.014 nm) [Maultzsch et al., 2005; Bachilo et al., 2002]. This modest effect indicates a slight preference for interactions between larger diameter semiconducting SWNT (or bundles containing them [Crochet et al., 2007]) and the gold acceptor species, similar to prior reports employing organic acceptors [O'Connell et al., 2005]. We also carried out microwave activation experiments using CoMoCat SWNT; these have comparable length but significantly smaller average diameter [Alvarez et al., 2002] than HiPco

SWNT (0.89 nm vs. 1.1 nm, respectively), and therefore should reside at higher oxidation potentials according to the redox landscape depicted in Fig. 4.4a. Interestingly, microwave processing of SDBS-suspended CoMoCat SWNT with $HAuCl_4$ failed to generate gold nanoparticles. This could indicate that the native redox potential of the metallic SWNT strongly influences the rate of the microwave reaction. Complete spectrums are reported in Appendix 4.7.6.

Pellet

The SWNT+Au pellets generated by centrifugation were resuspended in 100 μL of DI water in order to obtain liquid-phase Raman using 633 nm excitation. The reference SWNT suspension displayed no color change after microwave processing, nor was a pellet formed during centrifugation. SWNT are present in both the supernatant and pellet, as shown by their key spectroscopic features (Figure 4.11.a–c). The supernatant solution (red trace) is enriched in small diameter semiconducting SWNT, while the pellet (orange trace) exhibits an enrichment of metallic tubes. The Raman spectrum of the pellet has a significantly higher baseline, likely due to lossy scattering from the gold nanostructures. Interestingly, the G peak from the pellet displays a -12 cm^{-1} shift, while the intensity of the D-band is higher than in the reference spectrum (Fig. 4.11.c). We attribute the change in the D feature to gold nanoparticle attachment, while the G peak shift suggests charge injection from the gold nanoparticles; similar shifts have been reported upon alkali intercalation of SWNT bundles [Claye et al., 2001, 2000]. Moreover, the Breit-Wigner-Fano peak at 1550 cm^{-1} that arises from conduction electrons in metallic SWNT [Kataura et al., 1999] disappears from the semiconductor-enriched supernatant solution, but is prominent in the resuspended pellet, again indicating a strong enrichment in metallic SWNT. Figure 4.11.d is a representative image of the SDBS-SWNT-Au suspension before and after centrifugation; note that the red coloration from gold nanostructures is removed from the
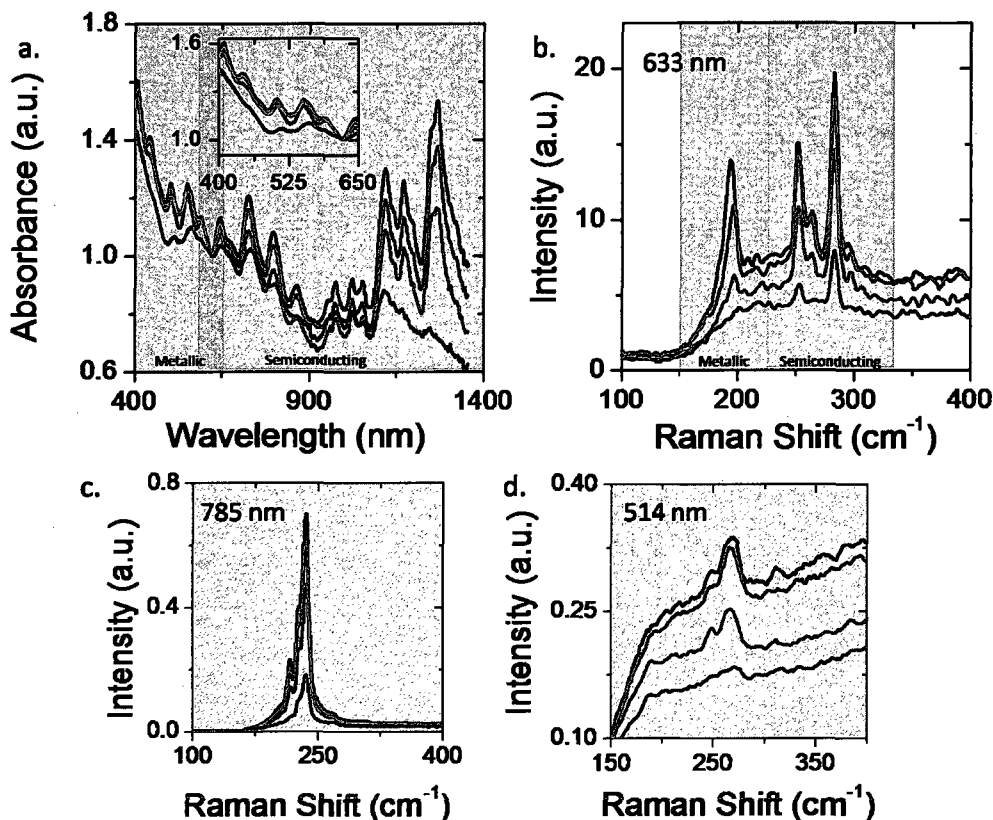
Figure 4.9 : SWNT selectivity in microwave-driven redox reactions, Supernatant. (a–d) Absorbance (a.) and liquid-phase Raman RBM using 660 nm excitation (b.), 785 nm excitation (c.) and 514 nm excitation (d.) spectra of SDBS-SWNT-Au suspensions after addition different amounts of 1 mM Au salt solutions (0 μL reference, black; 100 μL, blue; 300 μL, red; and 500 μL, green) and subsequent microwave processing.

centrifuged solution. SWNT bundles comprising both metallic and semiconducting SWNT [Bachilo et al., 2002] are likely activated by the microwave process and then removed from solution during centrifugation, accounting for the decreased concentration of semiconducting SWNT in the final supernatant.
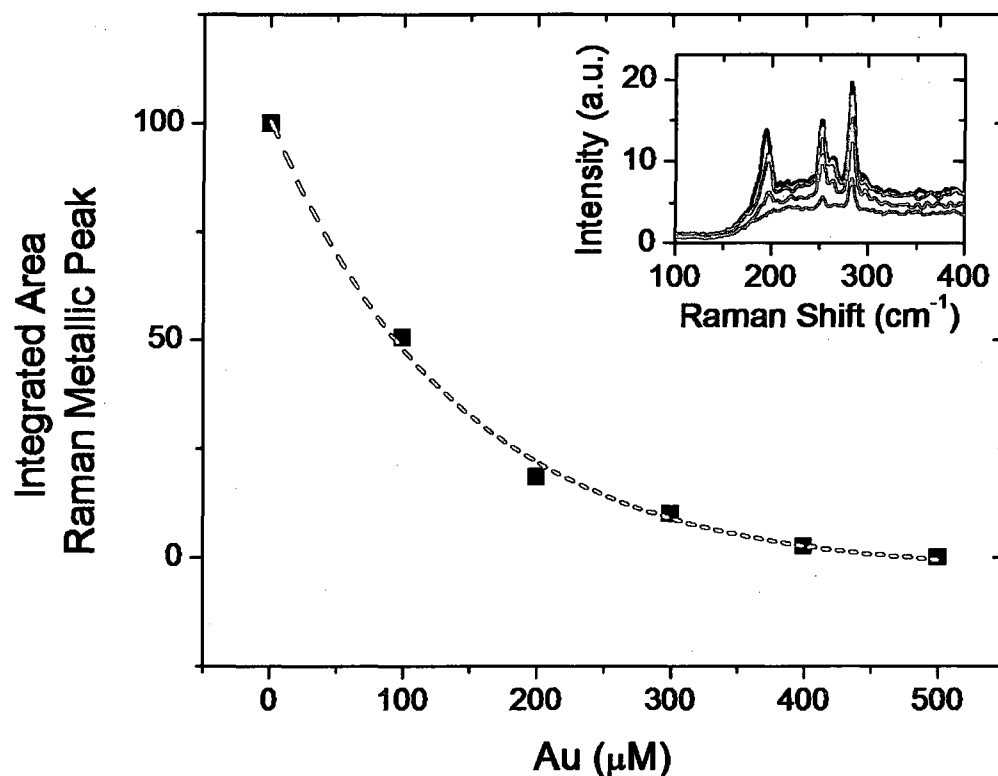
Figure 4.10 : Integrated area of the metallic SWNT peak as a function of metal ion concentration using 633 nm excitation wavelength. Red trace is an exponential fitting to the experimental data (black squares).

4.5.8 Selective Deposition Under Other EM Fields (Radio-Frequencies and Visible Light)

Selective reduction and deposition of particles was achieved not only using microwaves but also with radio frequencies (RF) as well. The RF experiments were carried out on SWNT suspensions between a pair of silicon wafer electrodes with insulating thermal oxide surfaces (Fig 4.12). The electrodes were spaced apart by 150 μm; 2 MHz RF at 150 V peak-to-peak was applied for 3 min using a Huttinger RF power supply. Similar nanoparticle electrodeposition was obtained using Pt, Pd, Fe and Cu salts.
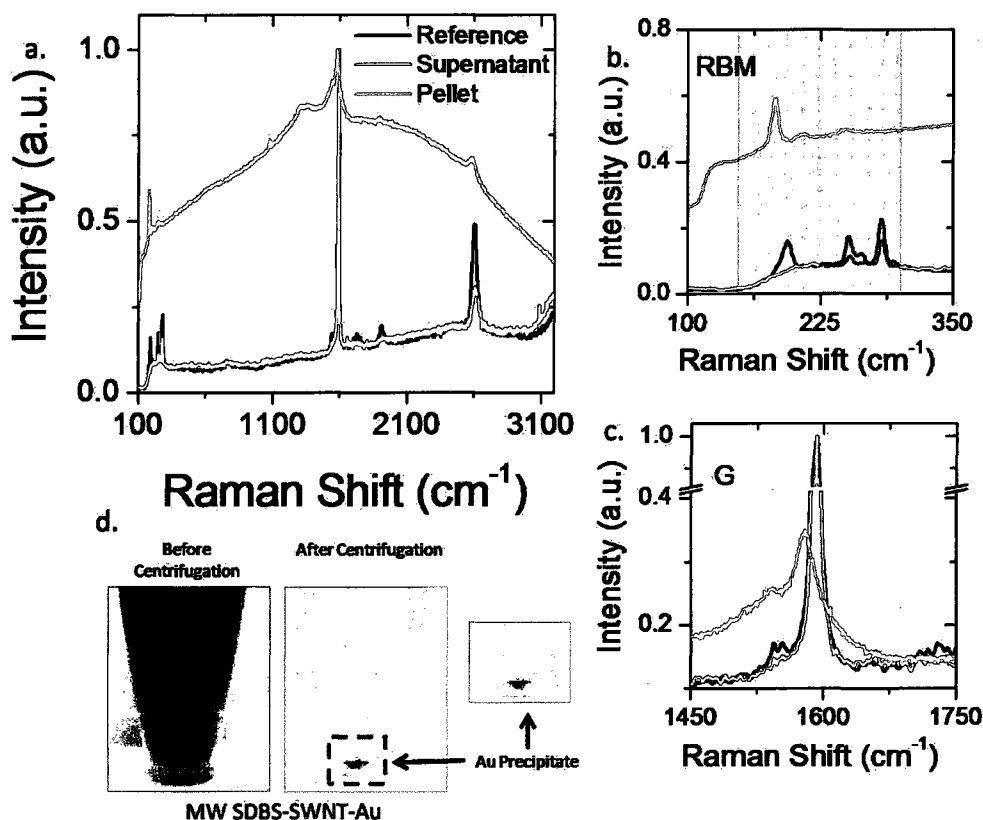
Figure 4.11 : SWNT selectivity in microwave-driven redox reactions. (a-c.) Liquid-phase Raman spectra using 660 nm excitation from SDBS-SWNT-Au precipitate (orange), reference (black), and supernatant (red). (b.) RBM region. (c.) G peak. (d.) Representative image of the SDBS-SWNT-Au suspension before and after centrifugation.

Interestingly, we also found particle formation at the tips of the SWNTs with 5 min exposure to a broad band light source (Near infrared to 220 nm) in the presence of Pt, Au and Ag salts (Fig 4.12.c). Free-floating gold nanoparticles were generated copiously in this reaction; these could result from gold reduction by photoelectrons ejected from SWNT by hard ultraviolet lines in the Hg lamp (254 and 187 nm). A small fraction of nanoparticles was found directly deposited on SWNT. About 10% of the SWNT were decorated. Nanoparticles found on SWNT were concentrated at

or near their tips, less tip-specific than with microwave excitation.

SWNT display optical absorptions due to resonant band-to-band transitions [Bachilo et al., 2002; Dresselhaus et al., 2005] and π-plasmon excitation [Attal et al., 2006; Reed and Sarikaya, 2001; Reed et al., 2001]; however, it is not clear whether they can support antenna-like collective resonances in the optical regime. Optically-driven collective resonances (surface plasmon polaritons) are well known for certain metallic nanoparticles [Wang et al., 2006; Laverdant et al., 2007; Maier, 2006], where they generate strong electric field gradients at asperities and junctions [Jiang et al., 2003a; Redmond and Brus, 2007]. These effects underlie surface enhanced Raman scattering [Kneipp et al., 1997] as well as shape-selective photochemistry [Jiang et al., 2003a; Maillard et al., 2003]. Similar effects have not been reported for SWNT, even though they are excellent conductors with high extinction coefficients. Theoretical studies by Burke [Burke, 2003] indicate that SWNT have exceptionally high kinetic inductance, which decreases their group velocity (and thus their response frequency) to $\sim 10^6$ m/sec (300 times slower than the speed of light $c = 3 \times 10^8$ m/sec). Studies by Hanson [Hao and Hanson, 2006] show that SWNT with lengths in the micrometer range should polarize and display relatively sharp current resonance at low THz frequencies. This model is supported experimentally by a recent observation of ballistic electron resonance of SWNT in the THz regime [Zhong et al., 2008]. Kinetic inductance is diameter —and carrier density dependent; Datta [Salahuddin et al., 2005] has shown that metallic structures over about 10 nm in diameter should have group velocities close to c; this is supported by Ren's experimental observation of resonant scattering by multi-wall carbon nanotubes (MWNTs) in the visible regime [Salahuddin et al., 2005].

Preferential nanoparticle production at the SWNT tips suggests that SWNT polarize axially to some extent even at optical frequencies. Given their low carrier

density, this result would not be expected based on prior theoretical reports [Durkop et al., 2004; Salahuddin et al., 2005]. Further studies are needed in order to clarify the complete mechanism of this reaction and reconcile our experimental observation with theoretical predictions.
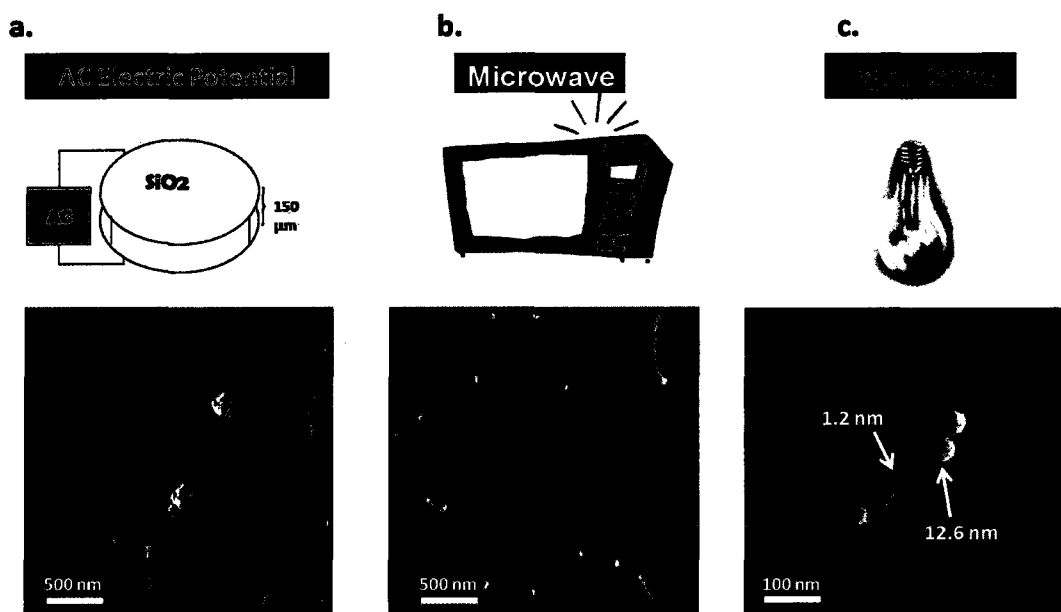
Figure 4.12 : Representative AFM image of tip deposition of metallic nanoparticles by RF (a) microwave (b), and light (c).

4.5.9 Electrodeposition Kinetics

Electrodeposition kinetics were examined in the microwave-driven reaction between SWNT-SDBS suspensions and $FeCl_3$, which generate relatively few free-floating particles. Figure 4.13.a shows AFM images of individual SWNTs with metal particle formation at four different initial metal ion concentrations; particles were again predominantly deposited at the ends of the SWNTs. Figure 4.13.b reveals that the size of the metal particles (95% confidence intervals) increases sub-linearly with $FeCl_3$

concentrations up to 80 μM. Figure 4.13.c shows a representative AFM image of an individual SWNT with attached nanoparticles at its tips and their respective vertical heights. Initial $FeCl_3$ concentrations above 80 μM yields spontaneous sedimentation of SWNT-metal complexes after microwave treatment; this probably accounts for the decrease in observed particle size with the highest iron concentrations. No nanoparticles were detected with starting iron concentrations below 5 μM, which could due to SDBS sequestration of Fe(III) cations at sites inaccessible to reduction by SWNT tips (at SWNT sidewalls or on free SDBS micelles). The kinetics of diffusion-limited electrodeposition on ultramicroelectrodes is well described by [Milchev et al., 2001]:

$$I = \left(\frac{zFD^{1/2}c}{\pi^{(1/2)}t^{1/2}} \right) + \left(\frac{zFDc}{r_o} \right) \tag{4.5}$$

where I is current density, z is ion valence, F is Faraday's constant, D is the diffusion coefficient of Fe(III) ions, c is the molar concentration of Fe(III) ions, r_o is the particle radius and t is time. Neglecting the first term in Eq. 4.5 (unimportant for sub-micrometer diameter electrodes [Milchev et al., 2001]), we can expand the current density term (yielding $q/t = zFDc\pi r_o$), where q is charge and using πr^2 for the cross-sectional area), express the amount of deposited material in moles ($M = q/(zF)$), assume a spherical deposit (of volume V $= 4/3 \ \pi r^3$) expressed as its molar volume (V_m), to obtain an expression for expected particle size as a function of time, diffusion constant, and initial concentration of acceptor species:

$$r^2 = 0.75V_mDct \tag{4.6}$$

Equation 4.6 yields a near-quantitative match to the experimental data using $t = 1$ sec, Fe^0 molar volume $V_m = 7.09 \ cm^3$/mole and Fe(III) diffusion rate $D = 3 \times 10^{-6}cm^2sec^{-1}$ [Bluhm et al., 2000]. This satisfying agreement between experiment and established kinetic theory (Figure 4.13.b, red curve) for electrodeposition at ultra-microelectrodes strongly suggests that formation of iron nanoparticles proceeds at or near diffusion limited rates and implies electrodeposition currents on the order of

10^{-15} A per SWNT tip. We note that if the iron nanoparticles are oxidized (which increases their molar volume, iron basis) then the deposition rate could be as much as a factor of two lower (the molar volumes of FeO, Fe_2O_4, and Fe_2O_3 are 11.97, 14.92, and 15.20 cm^2/mole, respectively). Using the different molar volume values of Fe in Eq. 4.6, we obtained reasonable agreement to our experimental observation (see Appendix 4.7.7, Fig. 4.23).
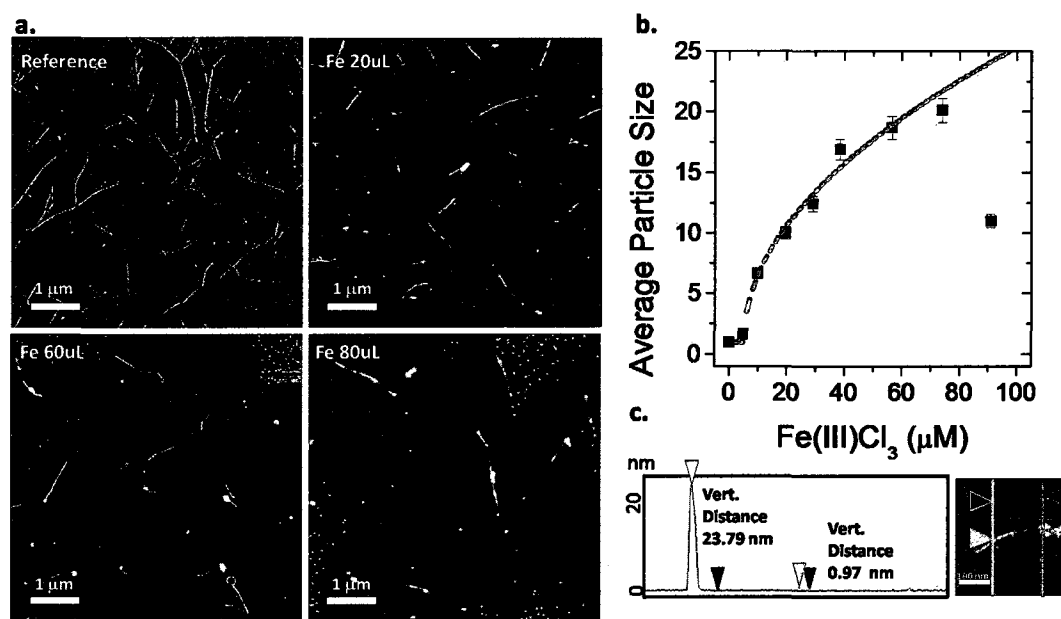
Figure 4.13 : Microwave electrodeposition kinetics of $FeCl_3$ on SWNT. (a.) Representative AFM images of microwave induced reduction of Fe^{3+} metal ions. (b.) Particle size distribution on the tips of individual SWNTs. (c.) Representative AFM image of individual SWNT-metal complex with their respective vertical distance.

4.5.10 Theoretical Calculations of Emission Current

The fundamental mechanism involved in this simple antenna chemistry is an important question to consider. Reactant cations (e.g., $Fe(OH)_2^+$) may associate with the surfactant's sulfonate anions before reduction, while anionic reactants (e.g. $AuCl_3^-$)

must reside outside the surfactant's outer Helmholtz plane [Nozik, 1978]. Therefore, nanoparticle formation likely involves a long-range electron transfer of at least 3 to 5 nm. A similar process was described by Graetzel [Miller et al., 1991], who conclusively demonstrated a long-range tunneling mechanism for redox reactions across self-assembled monolayers of alkane thiols on biased gold electrodes. We estimate that the minimum electron transfer rate needed to generate observable nanoparticles in 10 seconds to be at least 10^{-18} A (assuming an effective duty cycle of 10%, 100 atoms per particle, and 3 e$^-$ per Fe ion, we can estimate a nanoparticle size of around 1.1 nm^3), while the larger particles seen would require currents in the vicinity of 10^{-16} to 10^{-15} A. We quantitatively explored the origin of these rather substantial electrodeposition currents using the Fowler-Nordheim (F-N) equation (Eq. 4.7) [Bonard et al., 1998], which describes the tunneling current density through a potential barrier under high electric field,

$$ J = K_1 \cdot E^2 \exp\left(-\frac{K_2}{E}\right) \tag{4.7} $$

$K_1 = 1.5413 \times 10^{-6} \, \frac{1}{\Phi}$

$K_2 = 6.828 \times 10^{7} \, \Phi^{3/2}$

where J is the current density in amperes per square meter, K_1 and K_2 are constants, Φ is the effective barrier height or the work function in volts, and E is the effective field in volts per meter.

We replace E with βE_{tip} to account for the geometric field amplification generated by the aspect ratio of the nanotubes and assume that the emitter area α is 10^{-18} m^2 (approximate SWNT cross-section). The effective field E_{tip} at the surface of the SWNT tip is also modified (decreased) by the relative dielectric constant k of its local environment. We use $k = 2.3$, the dielectric constant of polyethylene, which should be representative of the alkyl 'tail' of the SDBS surfactant. Inserting the constants, amplification factor, and emitter area yields Eq. 4.8, which is seen by inspection to be very sensitive to both field strength E and barrier height Φ:

$$J = 1.5413 \times 10^{-6} \frac{1}{\Phi} \cdot (\beta E)^2 exp \left(-\frac{6.828 \times 10^7 \Phi^{3/2}}{\beta E} \right) \qquad (4.8)$$

Below, we explore the values of E_{tip} and Φ required to generate current densities consistent with our observed results. Since F-N emission is extremely non-linear in E_{tip}, we use the peak field strength, $1.414/k$ E_{avg}, where $E_{avg} = 3.5 \times 10^5$ V/m (see Appendix 4.7.3).

We first consider the case of a bare metallic SWNT immersed in a hydrocarbon dielectric ($k = 2.3$). For analyzing nanotube field emission measurements in vacuo, Φ is normally set to their work function ~ 4.7 V [Suzuki et al., 2004]. That Φ value generates impossibly low currents under our conditions, however. Figure 4.14.a (green trace) shows the expected emission current (per SWNT tip) for SWNT of various lengths when Φ is set to 1.5 V, the oxidation potential of a 1 nm diameter metallic SWNT. This indicates that only SWNT of several microns in length would generate detectable nanoparticles, which is contrary to our experimental observations —nanoparticles occur commonly on the tips of SWNT down to a few hundred nm in length. Figure 4.14.b. shows the tip currents expected from 500 nm long tubes while varying the effective barrier height Φ; this indicates that Φ must be in the 0.25 – 0.30 V range to generate currents consistent with observations. This range is not impossibly low, but seems unrealistic, even noting that there exist multiple reports of long-range electron transfer reactions at scanning probe (STM) tips wherein effective barriers of less than 1 V have been observed [Halbritter et al., 1995; Kuznetsov and Ulstrup, 2000; Nagy and Wandlowski, 2003].

We next consider the more complex case of SWNT coated with a thin insulator in an aqueous environment, and develop a simple model explaining the gradient compression visualized in the SDBS-SWNT image in Fig. 4.1. Compared to the bare-SWNT case, it appears that essentially all of the field gradient around the tip of the

nanotubes is compressed into the thin surfactant coating. This initially non-intuitive computed result is actually entirely reasonable, considering that the SDBS layer and aqueous electrolyte bath form a capacitive voltage (potential) divider network. When capacitors of dissimilar magnitude are connected in series, most of the applied voltage drops across the smaller capacitance. Here, the smaller capacitor is the 3.5 nm thick concentric spherical section comprised of SDBS between the conducting SWNT and electrolyte (electrodes). The larger-value capacitor is the semi-infinite spherical section of aqueous electrolyte. With a 1 nm diameter nanotube and a 3 nm thick surfactant layer, the resulting capacitances are $C_{electrolite} = 4\pi \, \varepsilon_o \, \kappa_2 r_2 = 1.6 \times 10^{-19}$ F and $C_{surfactant} = [4\pi \, \varepsilon_o \, \kappa_1]/[r_1^{-1} - r_2^{-1}] = 3.1 \times 10^{-17}$ F (using $\kappa_1 = 2.3 \, \varepsilon_0$, $\kappa_2 = 80 \, \varepsilon_o$, $\varepsilon_o = 8.854 \times 10^{-12}$ F/m, $r_1 = 0.5$ nm, $r_2 = 3.5$ nm). Since the capacitance of the surfactant layer is $\sim$100 times smaller, it captures essentially all of the electric potential drop in the system, just as Figure 4.1.a indicates. Notably, this capacitance is sufficiently small that adding one electron to the tip of the nanotube will raise its potential by about one volt.

This gradient compression effect serves to increase the effective electric field strength at the SWNT tips, compounding the geometric amplification factor $\beta = L/2D$. Essentially the entire modulation potential, $\delta U = EL/2$, appears across the 3 nm thickness T of the surfactant layer at the tip of the SWNT. The concentric spherical geometry at the tip of the SWNT/surfactant structure further focuses the electric field at the SWNT tip by yet another geometric factor, $G = (r_2/r_1)^2$, where r_2 and r_1 are the radii of the surfactant shell and SWNT tip, respectively. G varies significantly with nanotube diameter; if T is 3 nm for all SWNT, then in a 1 nm diameter tube $G = 49$ and overall the field amplification is greater than β by a factor of $G/T = 49/3 \sim 16.3$, which we will call ζ (zeta). ζ values are plotted for SWNT of various diameters in Figure 4.14.c, assuming a surfactant layer 3 nm thick.

Returning to the Fowler-Nordheim estimates, but including the potential gradient compression factor ζ, Figure 4.14.a shows the expected emission current assuming barriers of 4.7 V (red trace) and 1.5 V (black trace). If the tunnel barrier is 4.7 V, then the short tubes ($\sim$200 nm long) cannot generate enough current to produce nanoparticles. With a barrier of 1.5 V, however, then the expected emission current is sufficient for short tubes to produce nanoparticles, as observed experimentally. The blue trace in Figure 4.14.b shows emission current for 500 nm long SWNT (1 nm diameter) as a function of barrier height. Interestingly, barriers around 1.7 V produce emission in the 10^{-15} A range, consistent with our experimentally observed deposition rates. Careful additional study is certainly needed, but we consider the experimental results to be consistent with a classic Fowler-Nordheim field emission process through a barrier roughly equal to the SWNT oxidation potential, noting that the apparent field strength is substantially augmented by the nanotubes' geometric factor β as well as the gradient "compression" factor ζ within the surfactant layer.

4.5.11 Self-Assembled Nanoparticle-Nanotube Structures (nanoPaNTs) Based on Antenna Chemistry of Single-Walled Carbon Nanotubes

Encapsulation

By sequentially combining the tip selective deposition and exposure to visible light, we were able to progressively grow metallic Au nanoparticles starting from the SWNT tips, resulting in cylindrical sheaths that ultimately coat SWNTs completely (Fig. 4.15). Progressive growth was accomplished by first depositing metallic particles selectively at the ends of the SWNTs using SDS as the surfactant under microwave irradiation (Fig. 4.7.b) followed by exposure to broadband optical radiation for approximately 2 hrs (Fig. 4.12.c); the color changed from light red (indicative of spherical Au nanoparticles, inset) to blue (elongated Au nanoparticles) [Kim et al., 2002] (see Appendix 4.7.9). In order to maintain a stable SWNT-Au suspension, polyvinyl
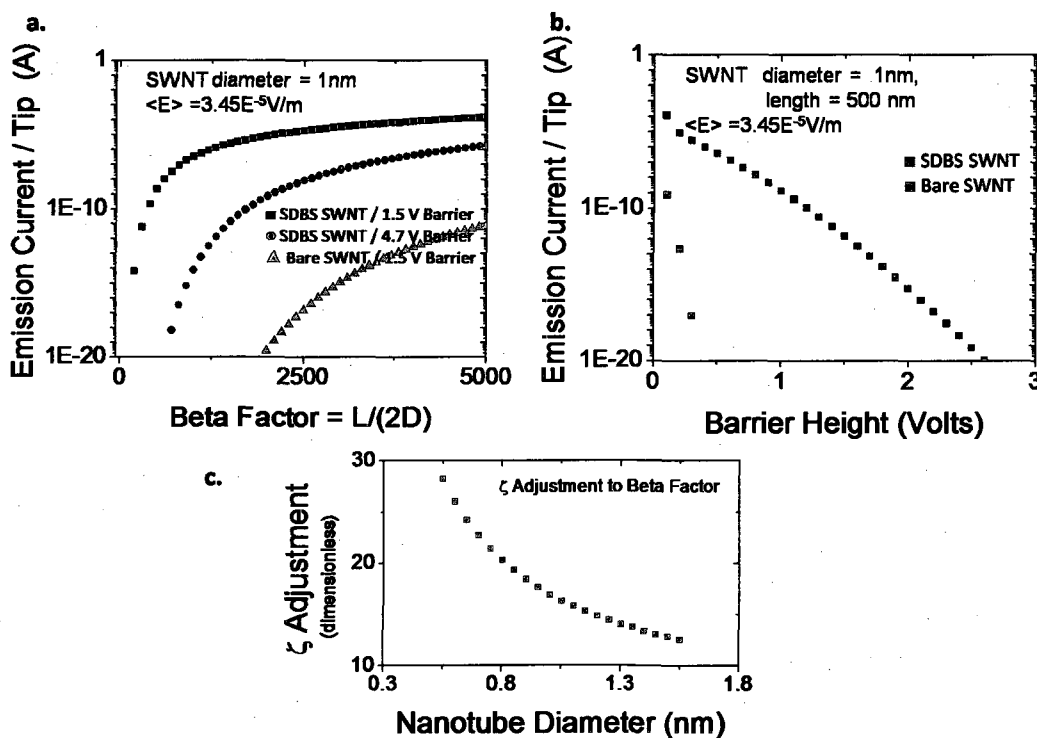
Figure 4.14 : Emission current of a metallic SWNT in microwave fields, $E_{avg} = 3.5 \times 10^5$ V/m . (a.) Emission current as a function of tube length for bare (green), barrier of 1.5 V (black), and 4.5 V (red). (b.) Emission current as a function of compression barrier for bare (purple) and SDBS covered (blue) SWNT. (c.) Enhancement factor as a function of tube diameter.

pyrrolidone (PVP) was added (0.25 wt %) after initial microwave exposure; PVP is a well-known capping agent used to stabilize both SWNTs [O'Connell et al., 2001] and metallic nanoparticles [Sarkar et al., 2008; Tang et al., 2008]. The initial step—tip nucleation and formation of small metal sheaths along the sidewalls of the SWNT— is due to the accumulation of charge at the tips of the SWNT from polarization (Section 4.5.2 and 4.5.10). Likely, the subsequent growth and complete encapsulation of the SWNTs by a metallic sheath is initiated by a plasmonic absorption of incident light by Au. This selective growth resembles previous reports of plasmon photoreduction

of silver spherical seeds into triangles with visible light [Jiang et al., 2003a]. The final structure of these metallic nanoparticles is dependent on the incident wavelength. Figure 4.15.b shows a SWNT with a uniform Au sheath of 4.3 ± 0.3 nm and an aspect ratio of ~140. We also observed that the free floating Au particles maintained their initial size (averaging 12 nm) (green trace in Figure 4.15.b); we believe that the growth of the metal sheath along the tube was directed by the longitudinal Au plasmon. It should be possible to extend this templated synthesis to other types of nanorods, such as Ag and Pt. Extended broadband optical IR radiation without prior tip nucleation in a microwave field led to samples with irregular shaped nanoparticles and big agglomerates on the SWNT ends, with an average size of 35 nm (± 2 nm) and no evidence of SWNTs covered with a metallic sheath (Fig. 4.25). The high aspect ratio of metallic SWNT-nanorods could have potential use in nanomedicine and molecular sensing or delivery. Au nanorod synthesis using SWNT scaffolds seems simpler and more effective than reported procedures for making high aspect ratio metallic nanorods [Gole et al., 2004; Gao et al., 2003].

Rings

A variety of unusual nanostructures were observed after microwave excitation of SWNT suspensions prepared in surfactant mixtures (SDBS+PVP). SWNT rings were formed upon microwave irradiation when the surfactant composition was adjusted to 0.75 wt% SDBS and 0.25 wt% PVP. Figure 4.16 shows single (Fig 4.16.a–f) and bundled (Fig. 4.16.f–h) SWNT rings. Rings were also generated in the presence of reducible transition metal salts (i.e., Au, Ag and Cu) (Fig. 4.16.d). We found that SDS could be substituted for SDBS in the surfactant mixture without affecting the reaction. No rings were obtained in the absence of microwave irradiation or when either surfactant was used alone. Experiments in the presence of metal salts sometimes led to ring-dot structure (Figure 4.16.d), where it appears that first distinct
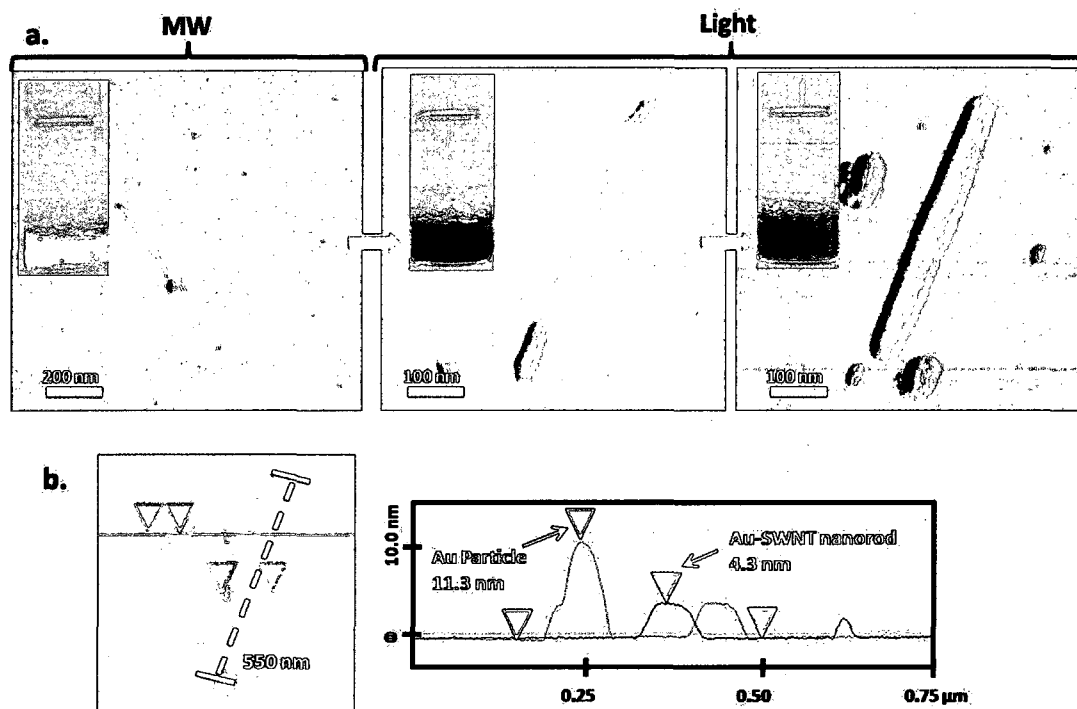
Figure 4.15 : SWNT metal encapsulation. (a.) Representative AFM images and solution color changes with the progressive growth of metallic nanoparticle along a SWNT. (b.) Height measurements of the Au nanorod.

Cu particles originated at the ends of the SWNT, followed by ring formation (also observed with Au and Ag). We infer that particle formation at the SWNT tips and ring formation must occur on distint time scales. If, in fact, the ring had formed first, the tip field enhancement would have disappeared, either eliminating particle production or yielding non-specific side-wall decoration of the SWNT at multiple locations. Ring formation therefore appears to be a slower and more energetic process than nanoparticle deposition, which proceeds with diffusion limited kinetics on sub-second timescales (Section 4.5.9). We note that these SWNT ring-dot structures resemble the "c" shaped resonant structures discussed in the literature concerning negative index materials [Pendry et al., 1999]. This suggests that ring-dot structures with SWNT tips separated by (insulating) metal oxide nanoparticles might have interesting EM

scattering properties. Additional representative AFM images of these products at different magnifications are shown in Figure 4.17.a–d. It can be seen that a high yield of rings was obtained with relatively small diameters. Figure 4.17.e shows the diameter distribution of the SWNT rings ranging between 30 and 75 nm, with a mean diameter of 50 nm. Also shown are remarkable structures that appear to be long, unmodified SWNTs "threaded" through one or more rings in shish kebab fashion. These results may indicate type selectivity in ring formation under microwave irradiation, based on experimental findings of preferential activation of metallic SWNT under similar operating conditions (Section 4.5.7). Although ring formation has been seen and studied in the SWNT/CNT context for several years [Buldum and Lu, 2003; Martel et al., 1999b,a; Liu et al., 1997; Sano et al., 2001; Zhang et al., 2003], this is the first reported incident of ring formation as a result of microwave irradiation.
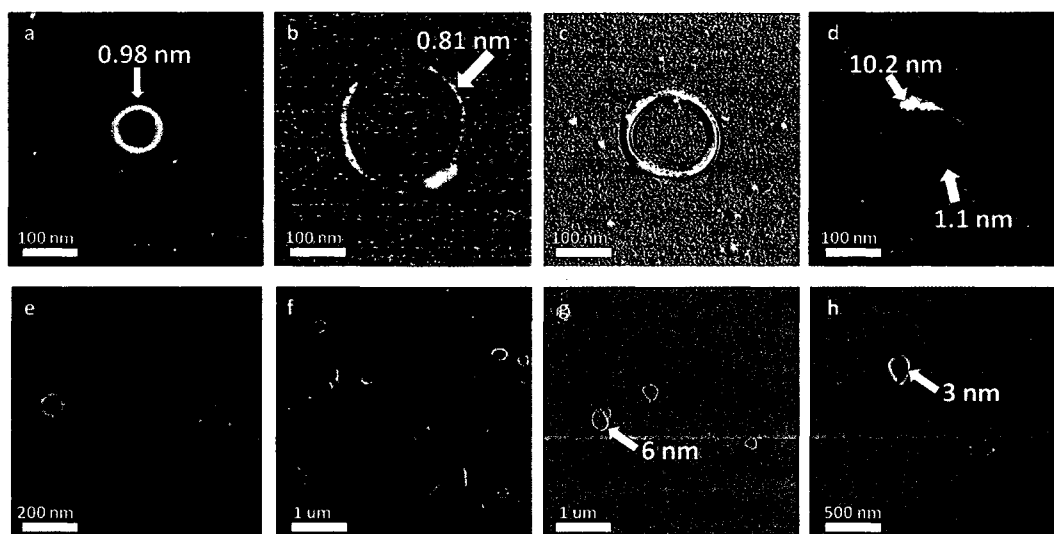
Figure 4.16 : Representative AFM image of SWNT rings. (a–f.) Individual SWNT rings. (f–h.) Rings of SWNT bundles. (b–f.) Rings with overlapping ends. (c–d.) Rings with metallic particles on the side-walls (c.) and at the ends (d.). (f.) Racket-like SWNTs rings.
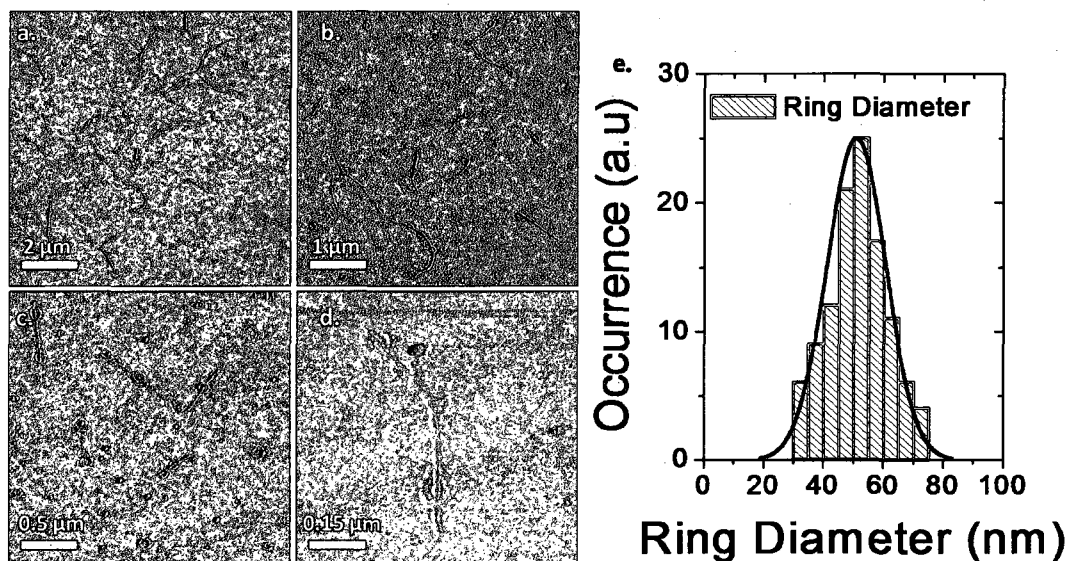
Figure 4.17 : Representative AFM images of SWNT rings on sticks. (a–d.) AFM images at 10 (a), 5 (b), 2.5 (c) and 0.75 (d) μm of SWNT rings on sticks. (e.) Diameter distribution of SWNT rings for several AFM images.

Rings Formation Energetics

Although we cannot yet explain the ring formation mechanism, we suspect that the field-induced accumulation of charges at the SWNT tips is involved, along with resulting electrochemical and/or electrostatic effects. The energetics of SWNT bending dictate that the active mechanism must either reduce their bending stiffness, or generate substantial bending forces.

Ring formation is well known and understood in semi-flexible filaments and molecules like DNA [Bloomfield, 1991; Vasilevskaya et al., 1997; Fang and Hoh, 1998; Schnurr et al., 2000; Montesi et al., 2004]. For example, it has been theoretically shown and observed experimentally that semi-flexible molecules in poor solvents can undergo conformational changes to minimize solvent contact and obtain a more energetically favorable configuration, which can result in partially collapsed shapes, racket

conformations, and tori [Montesi et al., 2004; Schnurr et al., 2000]. These conformations reduce molecule-solvent contact without causing excessive bending penalties and result from the interplay between two opposite forces: the bending force related to the chain stiffness and the self-attraction. However, the metastable (unraveled) configuration is separated from the lower-energy shapes (rackets, tori) by an energy barrier. Essentially, the chain must bend into higher energy conformations before the self-attractive forces take over and drive loop closure. Normally, thermal fluctuations provide the barrier-crossing mechanism; when such thermal fluctuations are too weak compared to the bending stiffness, no conformational changes (ring formation) are observed unless external forces bend the chains causing the crossing of the energy barrier [Montesi et al., 2004]. The simplest model that can effectively capture the competition of bending and self-attraction (see, e.g., Martel et al. [1999a] and Schnurr et al. [2000, 2002]) is based on a semi-flexible filament whose total energy U includes a bending energy U^b dependent on the bending stiffness κ, and a self-attractive energy, U^a dependent on the self-attractive potential per unit length of overlapping u_o

$$U = U^b + U^a = \frac{1}{2}\kappa \int_0^L ds \left(\frac{d\theta}{ds}\right)^2 - \lambda u_o \qquad (4.9)$$

where L is the length of the filament, s is arc length along the filament contour, θ is the angular position, r is the ring radius, and λ is the extent of overlap (Figure 4.18.a). Here we have disregarded the effect of the coordination number in filaments with multiple self-overlaps, which changes quantitatively (but not qualitatively) the energy of tightly wound filaments (see discussion in Schnurr et al. [2002]). Assuming that the filament shape is circular yields $s = \theta r$ and $\lambda = L\text{-}2\pi$ and the final expression of the total energy

$$U = \frac{\kappa L}{2r^2}(L - 2\pi)u_o \qquad (4.10)$$

for

$$2\pi r \leq L \text{ and } U = \kappa L/2r^2 \text{ for } 2\pi r \geq L$$

Equation 4.10 can be used to plot an energy landscape which illustrates the energy of a chain at different stages of ring formation (Fig.4.18.b). Clearly, the energy minimum is in the ring configuration for sufficiently strong self-attraction, as in the case of SWNTs, where the self-attractive potential per unit length of overlap is 500 eV/μm [Thess et al., 1996]. However, in order to fold, the filament must overcome an energy barrier

$$U^{max} = 2\pi^2 \frac{\kappa}{L} = 2\pi^2 k_b T \frac{L_p}{L} \qquad (4.11)$$

where k_b is Boltzmann's constant, T is temperature and $L_p \equiv \kappa/(k_b T)$ is the filament persistence length. Therefore, the energy barrier can be estimated based on the SWNT persistence length. Martel et al. [1999a] and Yakobson et al. [1996] computed L_p by treating SWNTs as continuum elastic cylindrical thin shells, for which $\kappa = \pi C r_3$; Martel et al estimated $C \approx 130$ N/m based on early theoretical modeling by Yakobson et al. [1996]; Kudin et al. [2001] later computed $C \approx 345$ N/m based on ab-initio calculations. Direct measurements of the persistence length of SWNTs in water [Fakhri et al., 2008; Duggal and Pasquali, 2006] show that the persistence length of typical HiPco SWNTs (diameters $\approx$ 0.8 to 1.2 nm) ranges from 25 to 140 μm (i.e., $C \approx 680$ N/m).

A relatively long, thin SWNT with $L_p = 25$ μm and $L = 2$ μm would have to overcome an energy barrier U$^{max} \approx 250 k_b T \approx 6.3$ eV before self-attraction would take over and close the ring; even using the lower theoretical estimate of persistence length of Martel yields a minimum activation energy $U^{max} \approx 50 k_b T \approx 1.3$ eV for ring formation. Importantly, Martel's method, (Equation 4.12 which is based on continuum mechanics theory [Yakobson et al., 1996], is similar to the one proposed by us in Equation 4.11:

$$E^s = \frac{YI}{2r^2} \qquad (4.12)$$

where Y is the Young modulus, r is the ring radius and $I = (\pi/4)[r'^4 - (r'-t)^4]$ is the

geometrical moment of inertia of a tube having external radius r' and wall thickness t ($t = 0.35$ nm). Martel's approach can be cast in terms of in-plane stiffness by expanding and rearranging the geometrical moment of inertia as follows:

$$I = (\pi/4)[r'^4 - (r' - t)^4] = (\pi/4)[r'^4 - (r'^4 - 4r'^3 t + 6r'^2 t^2 - 4r' t^3 + t)] \quad (4.13)$$

replacing Eq. 4.13 into Eq. 4.12 and knowing that $r' = d/2$ we obtain:

$$I = \frac{\frac{Y\pi t}{8}[d^3 - 3d^2 t + 4dt^2 - 2t^3]}{2r^2} \quad (4.14)$$

then Martel's in-plane stiffness is $C_{Martel} = Y\pi t/8$; which gives the implied in-plene value of 130 N/m.

Clearly, the energy barrier to form the rings is too high (on the scale of $k_b T$) for spontaneous activation (in fact, no rings are observed in the absence of EM fields). How the EM field is able to transmit so much energy to bend the SWNTs is not at all clear. The active ring formation mechanism must generate substantial buckling and bending forces; the attractive interactions between SDBS and PVP [Duque et al., 2008a; Atkin et al., 2005; Brackman and Engberts, 1993; Strano et al., 2003; Zanette et al., 1997; Zhai et al., 2004] may assist this mechanism by bridging opposite ends of a bending SWNT and therefore stabilize the intermediate configurations. We suspect that the field-induced accumulation of charge at the SWNT tips is the primary cause of the bending forces, along with corollary electrochemical and electrostatic effects.

Although the minimum energy configuration is that of a tightly wound ring, only a small degree of overlap (tens of nm) is required to stabilize the ring conformation. Figure 4.16) show rings with small overlap (e.g., 20 nm in Figure 4.16.b) as well as racquet shapes with ~50 nm overlap (Figure 4.16.f); these conformations are kinetically trapped states, similar to those observed in SWNT systems [Martel

et al., 1999a,b] and in the condensation of DNA and other semiflexible structures [Vasilevskaya et al., 1997; Fang and Hoh, 1998; Schnurr et al., 2002; Montesi et al., 2004].

Overall, these observations suggest that the electromagnetic field induces unanticipated compressive and bending forces needed to start the process of SWNT ring formation. The PVP chains may contribute to the ensuing of such forces or lower the activation energy by bridging opposite sides of a bending SWNT. Further experimental and theoretical work is needed to explain the formation of rings driven by electromagnetic fields.
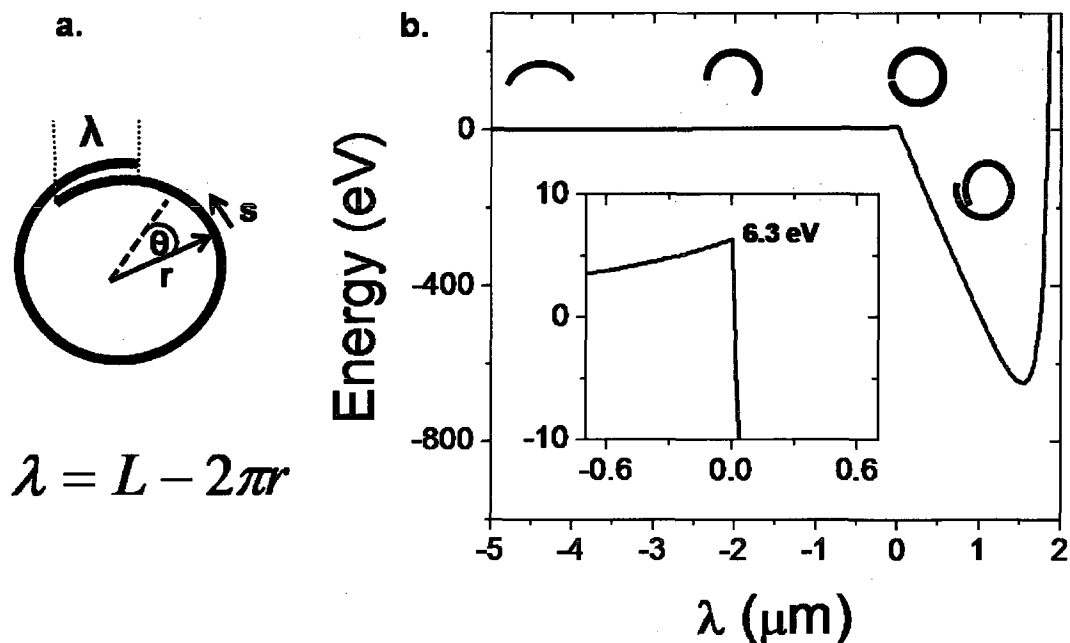
Figure 4.18 : Self-attraction energy to induce ring formation. (a.) Ring overlapping. (b.) Energy barrier to induce ring formation. (L_p = 25 μm, L = 2 μm and u_o = 500 eV/ μm).

4.6 Conclusions

We have found compelling evidence for *antenna chemistry* using highly dispersed SWNT-surfactant suspensions in a variety of electromagnetic fields (radio-frequency, microwave, and light). Electric field-driven redox processes with reducible transition metal salts result in tip-specific deposition of metallic nanoparticles and sheaths, yielding novel nanoparticle-nanotube structures. These nanoPaNTs structures include dumbells, SWNTs partially or completely encapsulated by metal, rings and straight SWNT "threaded" through rings to form shish-kebab structures suggesting routes towards the formation of spontaneous yet complex 3-D structures and high aspect ratio nanorods via template synthesis. We find substantial evidence that metallic nanotubes participate preferentially in these reactions, which suggests a general route for separating and fractionating metallic nanotube species. Reduction of Fe(III) species to produce nanoparticles on the SWNT tips appears to proceed at or near diffusion-limited rates. These redox processes appear to proceed via a long-range electron transfer mechanism involving tunneling or outright field emission into solution. The effective electric field at the tips of metallic SWNT is enhanced by their aspect ratio as well as a gradient "compression" effect caused by the thin, low-κ dielectric shell of surfactant molecules. Reduction of transition metal salts under these conditions to produce nanoparticles further implies strong rectification despite symmetric AC field stimulation. The formation of rings occurs only under microwave irradiation and when negatively charged surfactants (SDS or SDBS) are combined with PVP, which is known to disrupt the surfactant micelles around SWNTs, thus decreasing the energy needed for ring closure. Metal salts are not required for ring formation. Moreover, we observed that ring formation occurs more slowly than oxidation reactions. We anticipate that the novel composite nanostructures (nanoPaNTs) produced by this approach could prove to be useful nanoelectronics and catalysts, while the underlying electron transfer and rectifying processes could eventually lead to interesting applications in energy harvesting, nanomedicine, and chemical synthesis.

4.7 Appendix 4

4.7.1 Near Infrared Fluorescence of SDBS-SWNT with Transition Metal Salts

Figure 4.4.b shows the NIR fluorescence spectrum with 660 nm excitation wavelength of 1 mL SDBS-SWNT solution (10 mg/L) after the addition of 60 μL of 1 mM metal ions (Cu, orange; Fe, magenta; Au, green, and reference solution, black). NIR fluorescence quenching for semiconducting SWNT clearly depends on the oxidation potential of the metal salt added and systematically depends on SWNT diameter. The driving force for oxidative electron transfer increases with tube diameter, so the larger SWNT species are more thoroughly quenched. This result is consistent with the work of Okazaki et al. [2003] and O'Connell et al. [2005] described in the main text. We conclude that the redox model based on these works which employed SDS SWNT suspensions are valid for the present work.

4.7.2 Spontaneously Deposited Nanoparticle Diameter Statistics

Nanoparticles were spontaneously produced in a mixture of 1 mL F88 SWNTs and 30 μL HAuCl$_4$ (1 mM) upon heating to 55 °C for 2 hrs. Ultraviolet-visible spectra and TEM images (not shown) confirm the presence of gold nanoparticles. The heights of 50 such Au nanoparticles were measured by AFM and compiled in a histogram as shown in Figure 4.19. The sample showed an average height of 9.7 nm with a standard deviation of 2 nm. Similar particle distributions were observed with other metal salts and the average particle size increased with higher metal concentration.

4.7.3 Electric Field Strength in Sample Medium

We estimate the effective electric field strength in the microwave reactor using two approaches. The first is based on energy conservation in conjunction with the Poynting vector [Jackson, 2006]. Since the SWNT samples are so small (1 mL), we assume

Mean	SD	Maximum	Minimum	Size
9.702	2.02842	14	5.9	50
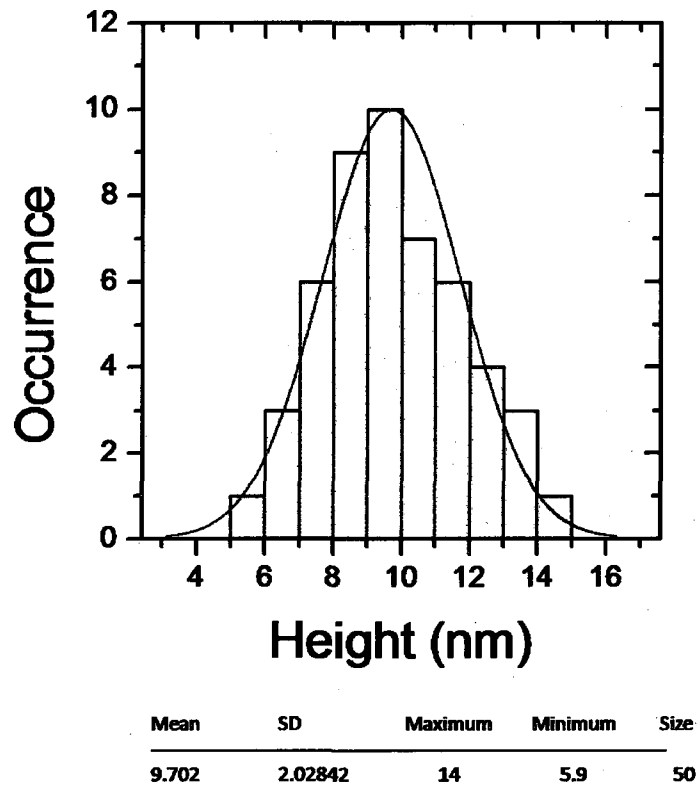
Figure 4.19 : Histogram of particle size.

that the microwave energy coming into the reactor from the magnetron is dissipated uniformly over the interior surface of the working chamber. Given a 1 kW input power and 2.1 m^2 interior surface area, the local power density is ~476 W/m^2. Using this value in conjunction with the Poynting vector [Jackson, 2006] (Eq. 4.15), which relates power flow across a surface to the average electric field strength (Eq. 4.16), we compute the (free space) electric field strength (Eq. 4.20) to be ~3.5 × 10^5 V/m.

$$\vec{S} = \vec{E} \times \vec{H} = \frac{1}{\mu_0 \mu_r} \vec{E} \times \vec{B} \qquad (4.15)$$

Solving for the time average magnitude of the Poynting vector in terms of E

$$< |\vec{S}| > = \frac{\varepsilon_0^2 c}{2} \sqrt{\frac{\varepsilon_0}{\mu_r}} |\vec{E}|^2 \qquad (4.16)$$

And isolating E, we obtain

$$E = \frac{1}{\varepsilon_o} \sqrt[2]{\frac{2 \times <S>}{c \sqrt{\frac{\varepsilon_r}{\mu_r}}}} \qquad (4.17)$$

A second approach for estimating the electric field strength in the reactor is based on observed solution heating rates in conjunction with established dielectric heating theory (Eq. 4.18) and physical constants for water [Piyasena et al., 2003].

$$\Delta T = \frac{2 * \pi t f \varepsilon_o \varepsilon_r' \tan \delta V^2}{C_p \rho} \qquad (4.18)$$

1.0 mL samples of DI water, processed under the standard microwave protocol, heated by 25.0 °C. Using $f = 2.45$ GHz and 12 for the loss factor ($\varepsilon_r' \tan \delta$) and 4.18 J /(g K) for the heat capacity of water, we obtain a field strength of 2.99×10^3 V/m within the sample. Adjusting for the dielectric constant of water, 80, we obtain an estimate for the average electric field in the microwave reactor of 2.39×10^5 V/m (Eq. 4.18). Given that the sample would have lost some heat to the sample vial and cooled somewhat prior to temperature measurement, this is a lower bound on the electric field strength and acceptably close to the first value generated above to serve as an experimental verification. We therefore use the value derived from the Poynting vector, 3.5×10^5 V/m, in the field emission and alignment calculations.

4.7.4 Multipanel Deposition

Figure 4.20 shows representative AFM images of different steps in the metallic deposition onto SWNTs. Shown are the SWNT starting material, sidewall decoration obtained with thermal procedures, tip deposition obtained upon exposure to microwave and metal salts (given are images taken in amplitude and height modes) as
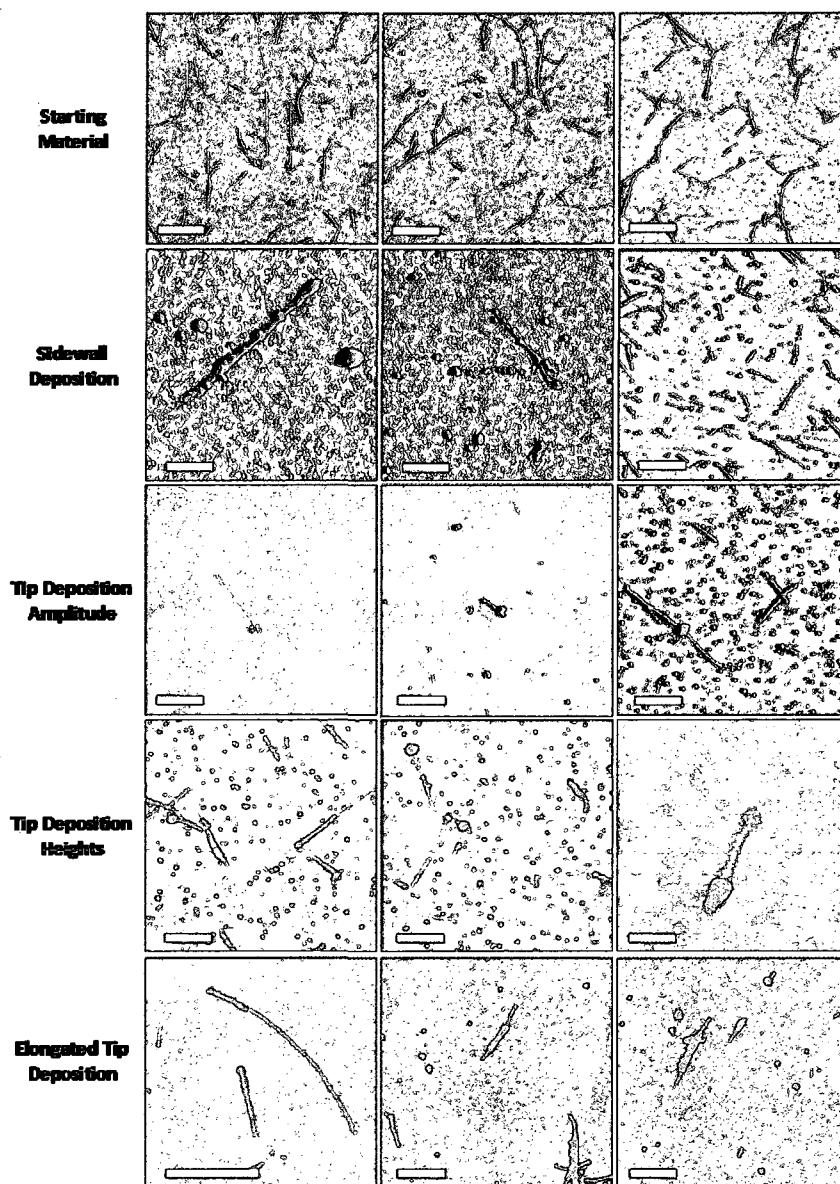
Figure 4.20 : Representative AFM images of metal deposition on SWNTs. Scale bars are all 1 μm.

well as elongated tip deposition. Scale bars are all 1 μm.

4.7.5 Nanoparticle Spectroscopy

Figure 4.21 shows a representative image of solutions containing SWNTs with different types of Au nanoparticle tip deposition and its corresponding absorbance spectrum. The black trace in the spectrum is the starting material; one can see the representative peaks for the SWNTs ($\sim$5 mg/L). Depending on the amount of metal salt added, after microwave reaction we observed that a strong peak at around 523 nm develops for the spherical nanoparticles (in red, 50 μL of Au salt solution). If the concentration of metal salts is increased (120 μL), this feature broadened significantly (blue trace) indicative of large and elongated Au particles.
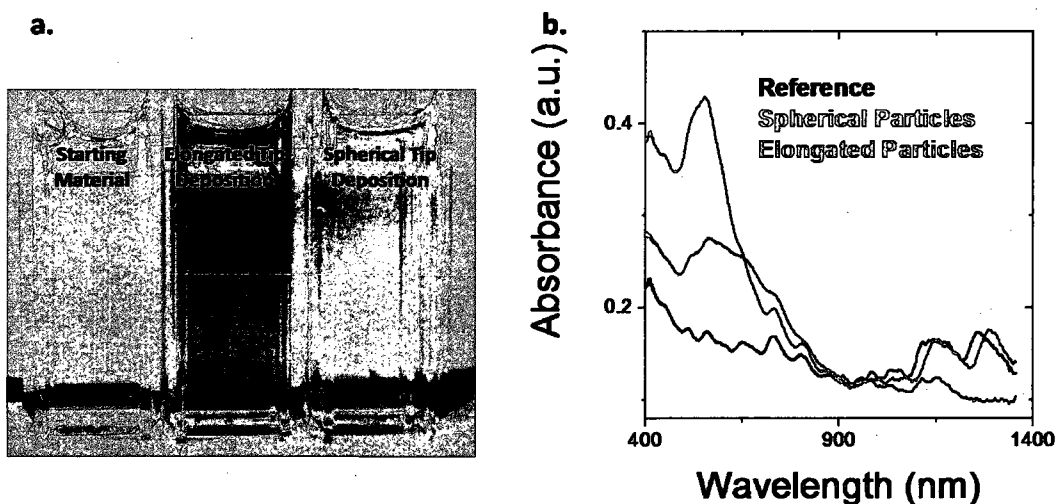
Figure 4.21 : Spectroscopy images of nanoparticles. (a.) Image of the different particle sizes. (b.) Absorbance of different particle size.

4.7.6 Liquid-Phase Raman Spectroscopy

Raman spectra were obtained using three different excitation wavelengths 785, 633, and 514 nm of SDBS-SWNT-Au suspensions after addition of different amounts of 1

mM Au salt solutions (0 μL reference, black; 100 μL, blue; 300 μL, red; and 500 μL, green) and subsequent microwave processing (Fig. 4.22). Since 785 nm excitation wavelength is mostly in resonance with small diameter (d_t) semiconductive HiPco SWNTs, fluorescence signals (1100 – 3200 cm^{-1}, $d_t = 0.69 – 0.88$ nm) can also be obtained for different SWNTs. The integrated area of these peaks decreases at a faster rate for larger diameter semiconductive tubes (2100 – 3200 cm^{-1}, $d_t = 0.78 – 0.88$ nm) than for small diameter SWNTs (1100 – 2100 cm^{-1}, $d_t = 0.69 – 0.75$ nm) [Bachilo et al., 2002; O'Connell et al., 2002; Moore et al., 2003; Jackson, 2006; Strano et al., 2004]. Even though these are small diameter SWNTs, this is yet another spectroscopic indication of our diameter selectivity.

4.7.7 Fe Nanoparticles at SWNT Tips

Figure 4.23 shows the fitting of our experimental observation using Eq. 4.6 for different types of iron particles. We observed that our experimental observations (black squares) are within the theoretical prediction (Eq. 4.6) for metallic or metal-oxide nanoparticles, especially within the lower Fe concentrations where the particles are not precipitating out of solution.

4.7.8 X-ray photoelectron spectroscopy (XPS)

Figure 4.24 shows the XPS spectrum of SWNTs containing Fe with (blue trace) and without (black trace) exposure to microwave field. X-ray photoelectron spectroscopy (XPS) was performed on a PHI Quantera SXM Scanning X-ray Microprobe (Chanhassen, MN USA) with a pass energy of 26.0 eV, 45° takeoff angle and a 100 μm beam size. The samples were collected after inducing flocculation of the SWNT-Fe suspension via acetone addition. XPS Fe signal was only obtained for the suspension that underwent microwave exposure (blue). The integrated area of the peaks indicated that the resulting nanoparticles were composed of 43.5% Fe, 52.8% Fe_2O_3 ($2P_{3/2}$), and 3.7 % Fe_2O_3 ($2P_{1/2}$). It is important to note that the signal was low due to the
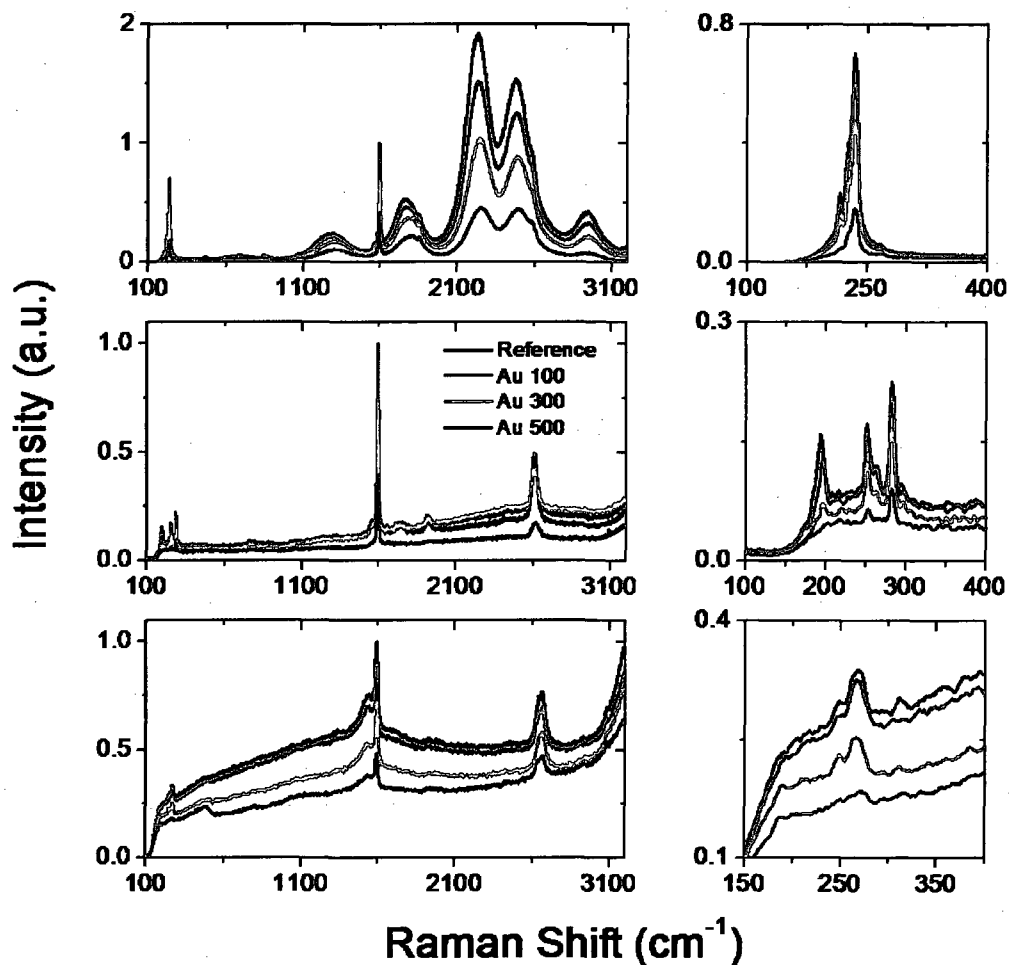
Figure 4.22 : Complete Raman spectra of SWNT-Au solution at 514, 633, and 785 nm excitation.

overall low concentration of metal particles (designed to minimize the flocculation of the SWNT suspension due to the Fe ions).

4.7.9 Formation of nanoPaNTs

nanoPaNTs were obtained using various experimental procedures and electromagnetic radiation. Selective deposition of particles at the ends of the SWNTs (dumbells) were
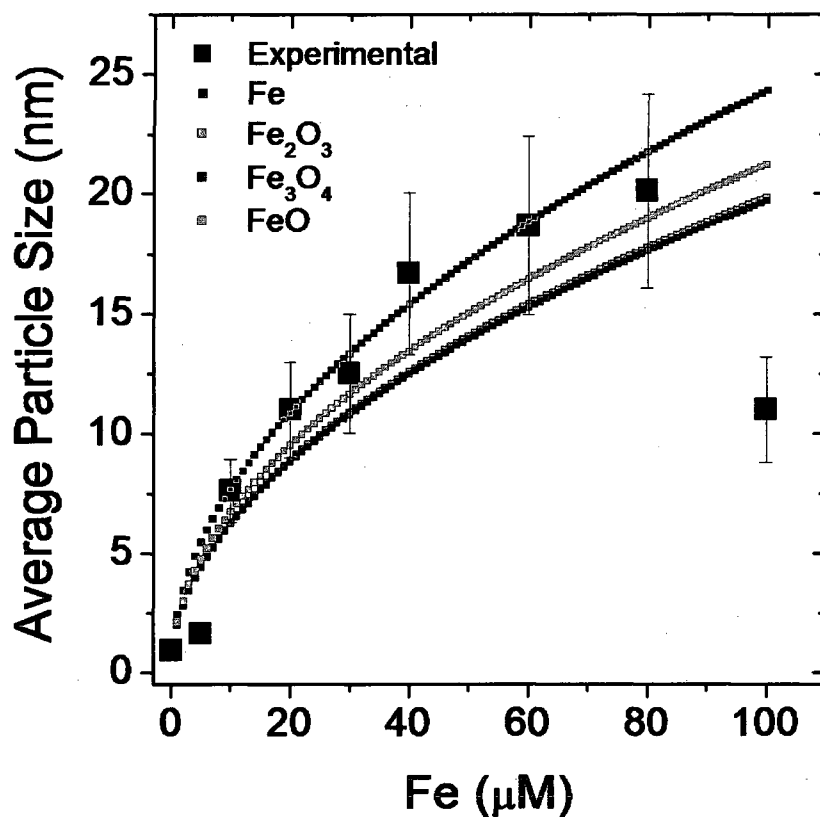
Figure 4.23 : Theoretical fitting to particle size.

obtained using microwaves, radio frequencies, and light irradiation. The microwave radiation source was a multi-mode microwave reactor (MARSX, CEM Corporation, 2.54 GHz. Matthews, NC, USA) programmed at 1000 W. The reactions were carried out in the center of the microwave using 5 mL of SWNT suspensions and 8 sec exposure time. RF low frequency radiation was provided by an AC power supply (Huttinger, 13.56 MHz. Farmington, CT, USA). The 40 μL sample containing SWNTs and Au salts was placed between two silica oxide wafers (n-type arsenic, 3.5μm oxide layer, Wafer World, West Palm Beach, FL USA) spaced 150 μm apart
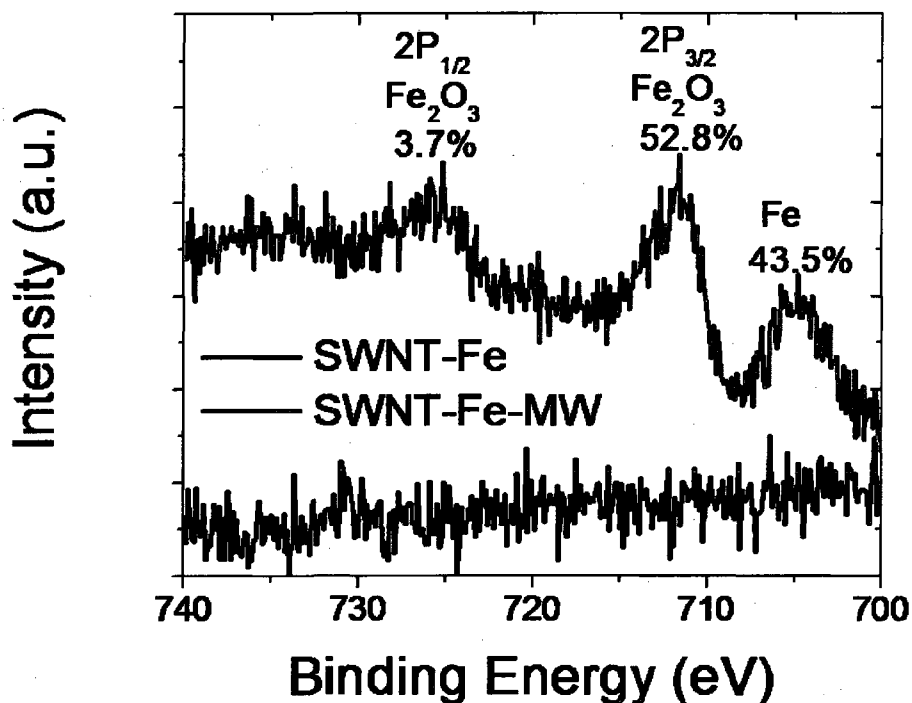
Figure 4.24 : XPS spectra of SWNTs containing Fe nanoparticles.

by a glass cover slip and exposed to 150 V for 3 min. The source of light irradiation was a mercury arc lamp (ACE glass, near infrared to 220 nm ultraviolet at 150 W, Vineland, NJ). Light-irradiated samples were exposed for 5 min. All samples were prepared from suspensions with a SWNT concentration of 5 mg/L to which 50 μL solutions of 1 mM metal ion salts (Au, Pt, Ag or Fe) were added. Progressive growth of nanoparticles and complete metal sheath encapsulation were obtained by first performing selective metal deposition at the SWNT tips via microwave exposure followed by exposure to light irradiation using a mercury arc lamp for 2 hrs. During light irradiation, 10 aliquots (50 μL each) of metal salts (1 mM) were added every 10 min. Ring structures were obtained in separate experiments that utilized a mixture of

surfactants (0.75 wt% SDBS and 0.25 wt% PVP) under microwave irradiation, with and without the presence of metal salts.

4.7.10   Extended Broadband Optical Radiation

Extended irradiation with broadband light source (near infrared to 220 nm ultraviolet at 150 W) gave nanoparticle formation of agglomerates mostly extending from the ends of the tubes. No specific particle size and shape were obtained.
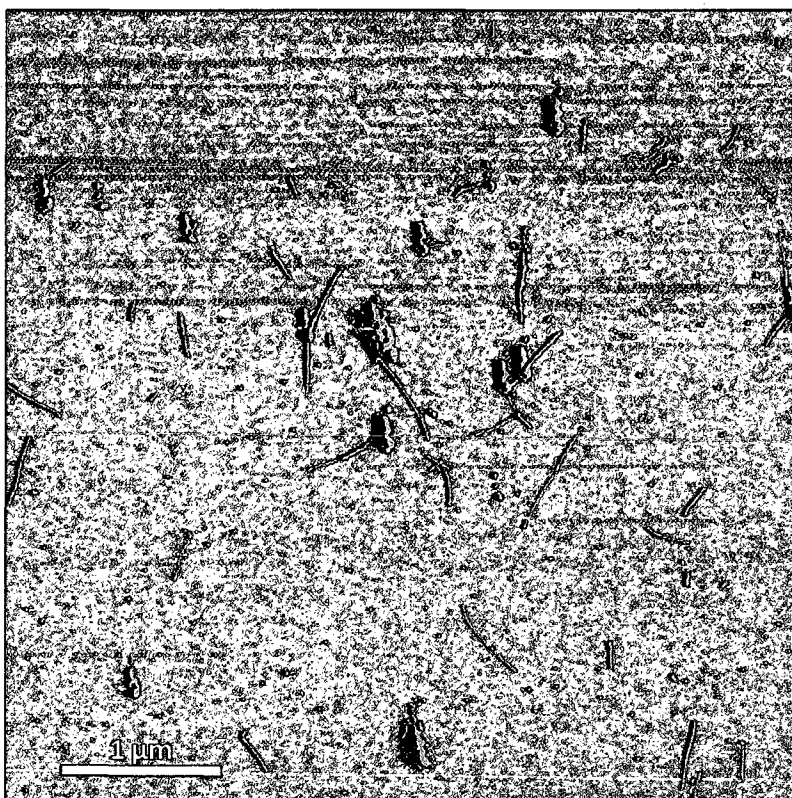
Figure 4.25 : Representative AFM image of extended broadband optical radiation.

4.7.11 Electric Field Structure Around a SWNT Calculation

The electric field model was generated using COMSOL Multiphysics 3.4 software, numerically solving the Maxwell equations in two dimensions with axial symmetry. The field gradient is calculated by setting the applied potential and geometry. Because the electric field is irrotational, it is possible to express the electric field as the gradient of a scalar function, called the electrostatic potential or voltage. An electric field, E, can be expresed as points from regions of high potential, to regions of low potential, φ, as:

$$E = -\vec{\nabla}\varphi \qquad (4.19)$$

since there is no charge distribution, the electric field becomes:

$$\nabla^2 \phi = 0 \qquad (4.20)$$

which is Laplace's equation. The model assumes that the SWNT is a metallic rod with uniform potential of 0 V located half-way between a pair of boundaries set respectively at $+ 1$ V/μm and -1 V/μm. The nanotube is modeled as a hemispherically-capped cylinder and has a length of 1 μm and aspect ratio of 1000:1. The nanotube is aligned with the electric field generated by the fixed potential boundaries. The dielectric constant of the medium is set at 80 ε_o, to mimic the aqueous environment used in the experiments. The surfactant shell was modelled as a hemispherically-capped cylinder extending three units (nanotube diameter $\equiv$ 1 nm $\equiv$ 1 unit) with dielectric constant of 3 ε_o (appropriate for hydrocarbons), to mimic the hydrophobic tails of SDBS and assuming field continuity at the hydrocarbon/water interface.

Chapter 5

Carbon Nanotube Electrochemical Photocathodes with Optical Rectenna Behavior

5.1 Objective

The aim of this chapter is to develop a photovoltaic (PV) that converts incident light into current. We are using the antenna like behavior from carbon nanomaterials with a current rectifying diode to inject electrons in solution. These electrons can be collected in the form of current or used to drive redox reactions.

5.2 Introduction

Energy deficiency is one of the most important challenges that affect humanity [Smalley, 2005; Lewis, 2007]. Due to rapidly rising global energy costs and demand, energy security issues and solar energy harvesting technologies have become increasingly important. The projected world energy consumption is approaching a deficit of a terawatt (TW) [Smalley, 2005] making renewable energy sources a topic of high interest. Solar energy is the most abundant renewable source of energy, with an estimated flux of 165,000 terawatts (TW) hitting the earth continuously. Effective conversion (only 0.1 percent) of the incident solar energy into electricity could solve a major part of humanity's energy problems [Lewis, 2007], and photovoltaic (PV) technologies are one the most promising approaches to capture sunlight and generate electricity [Lewis, 2007]. PV devices generate electricity from an incident wavelength source by utilizing a photodiode array that allows electrical current to flow in only one direction [Shah

et al., 1999]. Despite the multiple efforts, limited efficiency and expensive single crystal materials hinder its applicability [Lewis, 2007]. In recent years through material engineering and device innovation, several improvements have been made; however, multi-gap PVs which are affordable and easily made are still lacking [Oregan and Gratzel, 1991; Kamat, 2007].

One type of optical multi-gap device that converts incident radiation to electricity with high efficiency (90% overall) [Brown, 1984] and feasible economics is an optical rectifying antenna (rectenna). Optical rectennas consist of two key elements: an optical antenna that absorbs the incident light and a diode that rectifies the transient alternating current (AC) signal [Brown, 1984]. Rectifying barriers have been constructed from self-assembled monolayers (SAM) in non-linear rectifying devices [Reed et al., 1997; Tour, 2000]. The development of photovoltaic devices made of carbon nanotubes (CNTs) [Dresselhaus, 2004] or metallic nanowires [Fletcher, 1973; Lin et al., 1996] which behave as optical antennae have proven to be of great importance across multiple disciplines. CNTs are excellent candidates for optical antennas due to their size and electronic and optical properties [Saito et al., 1992]. Single walled carbon nanotube (SWNT) networks have been shown to efficiently absorb and thermalize electromagnetic radiation across the RF [Gannon et al., 2007], microwave (MW) [Imholt et al., 2003], and optical [Ajayan et al., 2002] regimes. Therefore, SWNTs can be considered nano-scale antennae [Wang et al., 2004b]. Recently, it was shown that sparse arrays of vertically aligned multi-walled carbon nanotubes (MWNTs) do indeed act as optical antennae and resonantly scatter visible light in a length dependant manner [Kempa et al., 2007]. Moreover, we recently showed that metallic HiPco SWNTs individually suspended in surfactants behave as nano-antennae under microwave irradiation. The surfactant layer around the tube creates a low-κ dielectric shell which enables sufficient current densities such that electrons injected in solution drive redox reactions with transition metal salts [Duque et al.,

2008c]. It should be noted that an experimental CNT-PV that exhibits rectenna behavior has not yet been conceived.

5.3 Overall Findings

In this work, we present a novel optical rectenna that combines a sparse array of CNT antennae (photocathodes) with physisorbed surfactant molecules which behave as a rectifying barrier (diode). This system is made into a liquid electrolyte Graetzel cell when placed in a current collecting conductive medium [Gratzel, 2003]. More precisely, we use two types of photocathode CNTs electrodes: MWNT and vertically grown SWNT carpet. MWNT were used as proof of principle, while SWNT carpets, with a higher number of available antennae, provide a means to explore the wavelength dependence of different kinds (diameter and/or chirality) of tubes. Moreover, we not only demonstrate rectification of the AC signal but also charge separation in the optical regime that generates measurable electrical current. We then utilize the charge separation to induce reduction of transition metal salts in single-walled carbon nanotube (SWNT) suspensions.

5.4 Experimental Methods

5.4.1 Photocathode Preparation

We fabricated two different types of photocathode cells; the first type was prepared by affixing a small mass (< 0.5 mg) of Mitsui MWNTs (~50 nm diameter and 1 – 5 μm long) (Fig. 5.1.a) onto a 3 mm diameter patch of conductive carbon tape. The second type utilized carpets of individual carbon nanotubes fabricated in a hot filament chemical vapor deposition apparatus [Pint et al., 2008] which were flipped by pressing a piece of adhesive material onto the top of the carpet and removing it

in order to obtain SWNT antennae. The different photocathodes were then mounted on an indium tin oxide (ITO) coated glass substrate or a copper puck (Fig. 5.1.a). A poly-dimethylsiloxane (PDMS) cylinder was glued around the photocathode to hold electrolyte fluid, and a gold wire or a small piece of ITO was inserted into the electrolyte as the current collecting anode (counter electrode) (Fig. 5.1.b).

The cell was illuminated with broadband light generated by a 30 W quartz tungsten halogen (QTH) lamp and delivered to the sample through a glass fiber optic bundle or with a 150 W xenon arc lamp equipped with a ultraviolet-visible-near Infrared monochromator (100 to 1800 nm). The current was measured with a computer controlled (Labview), Keithley 485 picoammeter.
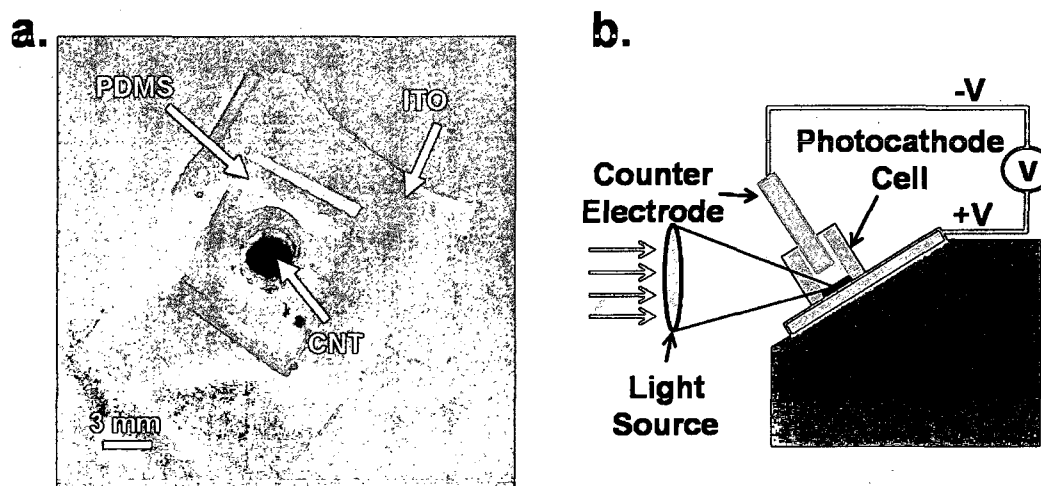
Figure 5.1 : Photocathode cells.

5.4.2 Photocathode Schematics

Figure 5.2 is a schematic representation of the photovoltaic cell with the most important components. The substrate used was a conductive surface (either ITO or Cu)

and the electrode was a piece of conductive carbon tape. Two types of CNT were used: MWNTs or flipped carpets, the electrolyte solution consisted of SDBS (1 wt %) doped with Fe(EDTA). A piece of glass with an ITO layer, serves as a counter electrode to collect the photocurrent generated.
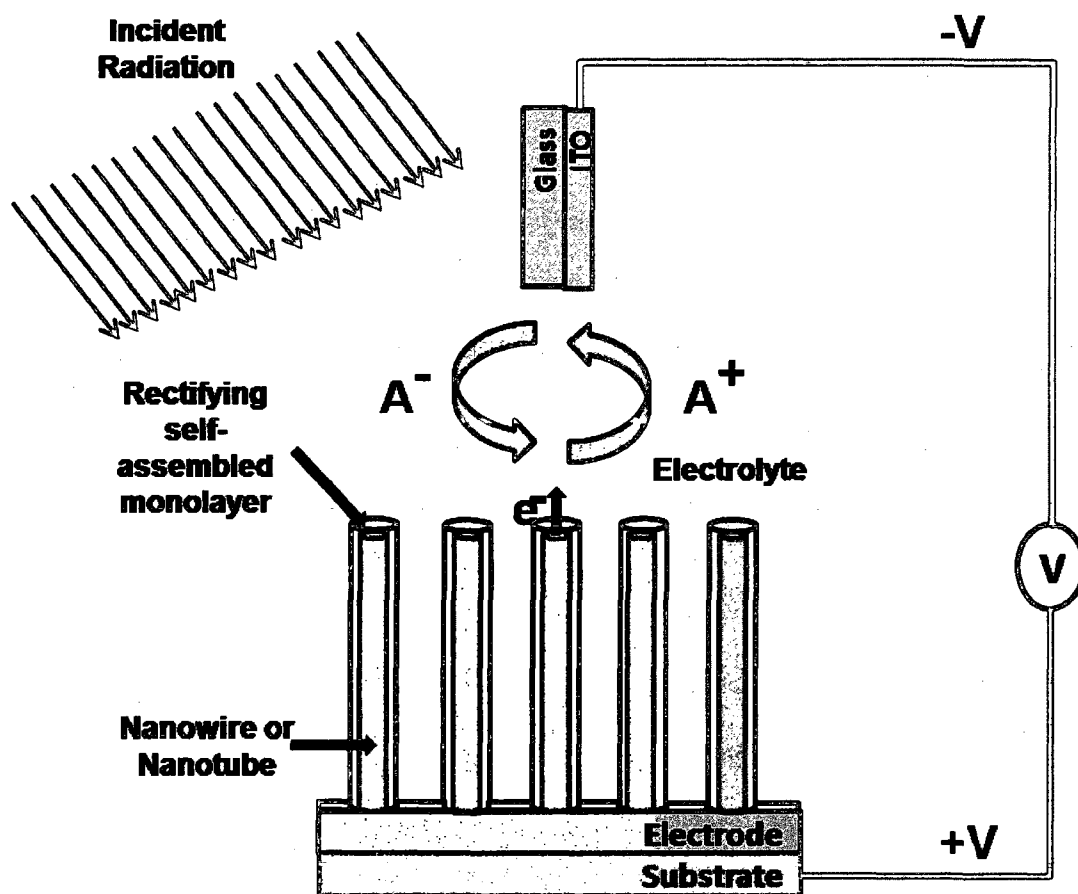
Figure 5.2 : Photocathode schematics.

5.4.3 Flipped Carpet

The inset of Figure 5.3.a shows a flipped carpet on a 2 mm diameter piece of carbon tape adhered to a copper puck. Figure 5.3 also shows scanning electron microscope images (SEM) of a flipped SWNT carpet taken with a JEOL 5300 at 20 kV. This image shows bundles of individual SWNTs after the flipping procedure at five different magnifications (41×, 150×, 1500×, 15000×, and 50000×). The bundles are the SWNT antennae responsible for the current generation.
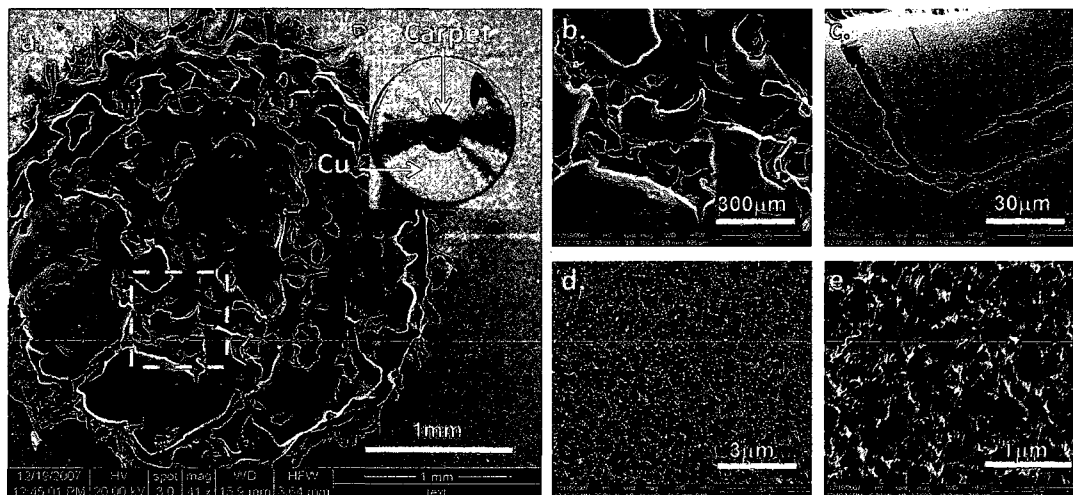
Figure 5.3 : SEM image of a flipped carpet.

5.4.4 Electrolyte

The electrolyte was prepared by mixing 1 wt % sodium dodecylbenzene sulfonate (SDBS) doped with 100 μM iron ethylenediaminetetracetic acid ((Fe-(EDTA)) in deionized water (DI). SDBS served as the rectifying layer and Fe-EDTA as an electron carrier. For experiments with gold covered CNT, the electrolyte was also doped with the long chain alkyl thiol 12-mercaptododecanoic acid.

5.5 Results and Discussion

5.5.1 Optical Rectenna

Optical rectennas are based on the idea of capturing photons with resonant $\lambda/2$ or $\lambda/4$ dipole antennas and converting their energy into an electrical standing wave. Energy is extracted by rectifying the fast AC signal. A simple rectenna can be constructed from a Schottky diode placed between antenna dipoles; the diode rectifies the current induced in the antenna by incident electromagnetic radiation. Schottky diodes are used because they have the lowest voltage drop and highest speed and therefore waste the least amount of power due to conduction and switching. Microwave rectennas operate at ~ 1010 Hz with over 90% efficiency [Reed et al., 1997]; however, fabricating a device that can rectify an AC signal at ~ 1015 Hz is very difficult. The performance-limiting factor at rectification in the optical regime is the cutoff frequency of the rectifying structure. The idea of an optical rectenna was proposed as early as 1972 [Fletcher, 1973], but has never been demonstrated.

5.5.2 Photocurrent as a Function of Rectifying Barrier

We fabricated a photocathode with optical rectenna behavior by mounting a small amount of CNT and creating a surrounding diode with physisorbed anionic surfactant molecules. To illustrate that the role of the surfactat layer on the tubes was in fact the rectifying barrier, photocurrents were recorded as the QTH lamp was switched on and off (~ 100 sec per cycle) (Fig. 1.d) with various electrolytes as follows: deionized water (green in Fig. 5.4.c), 1 wt % sodium dodecylbenzene sulfonate (SDBS) aqueous solution (red in Fig. 5.4.c), and 1 wt % SDBS aqueous solution doped with 100 μM iron ethylenediaminetetracetic acid ((Fe-(EDTA)) (electron carrier, blue in Fig.

5.4.c). A control without MWNT containing 1 wt % SDBS aqueous solution doped with 100 μM Fe-(EDTA) is shown (black, in Fig. 5.4.c). Photocurrent response was observed in all cases when the carbon tape was coated with MWNT, with distinctive spikes appearing immediately after turning the light on and off. We believe that the positive and negative spikes in this case are caused by two factors; the charging and discharging of the CNT mass (bulk CNT have been shown to have very high electrolytic capacitance and are therefore used in super-capacitors) [Frackowiak and Beguin, 2001] as well as the incomplete surface coverage of the surfactant around the large diameter MWNTs [Richard et al., 2003]. It has been shown that SDS micelles form structures such as rolled-up half-cylinders around the nanotube that are dependent on the tube diameter. These structures leave vacancies on the sidewall of the tubes which allow for partial recombination of electrons, ultimately causing a drop in the photocurrent produced.

Even though current response was observed with DI water alone, the current decreased rapidly to the baseline (green in Fig. 5.4.c). Conversely, upon addition of SDBS, the current remained constant while the light was on, only returning to the baseline after the light was turned off (red in Fig. 5.4.c). This response is an indication that the physisorbed anionic surfactant molecules (SDBS) around the CNTs behave as a diode (rectifying barrier) by creating an insulating layer around the tube which does not allow the Fermi level of the tubes to equilibrate with the electrolyte solution [Duque et al., 2008c], thus creating a voltage offset (Fig. 5.4.d). This voltage offset results in a barrier to both electron and hole flow between the nanotubes and the electrolyte solution and is responsible for the stabilization of the photocurrent generated. Upon addition of an electron carrier (Fe-(EDTA)) the current increased slightly (blue in Fig. 5.4.c), as the electron transport in the electrolyte was improved. Moreover, a strong dependence on the intensity of the incident light exposed to the system was also found; the photocurrent generated was proportional to the inten-

sity of the light (blue squares, Fig. 5.4.b). These results indisputably show that photocurrent can be generated and directed using CNTs as optical antennae and surfactant layers as the rectifying barrier. Although the current generated was small, TEM images (Fig. 5.4.a) show that only a very small fraction of MWNTs are able to behave as optical antennae by protruding from the mass. Similar qualitative current generation trends were obtained using SWNT mounted on Cu pucks.
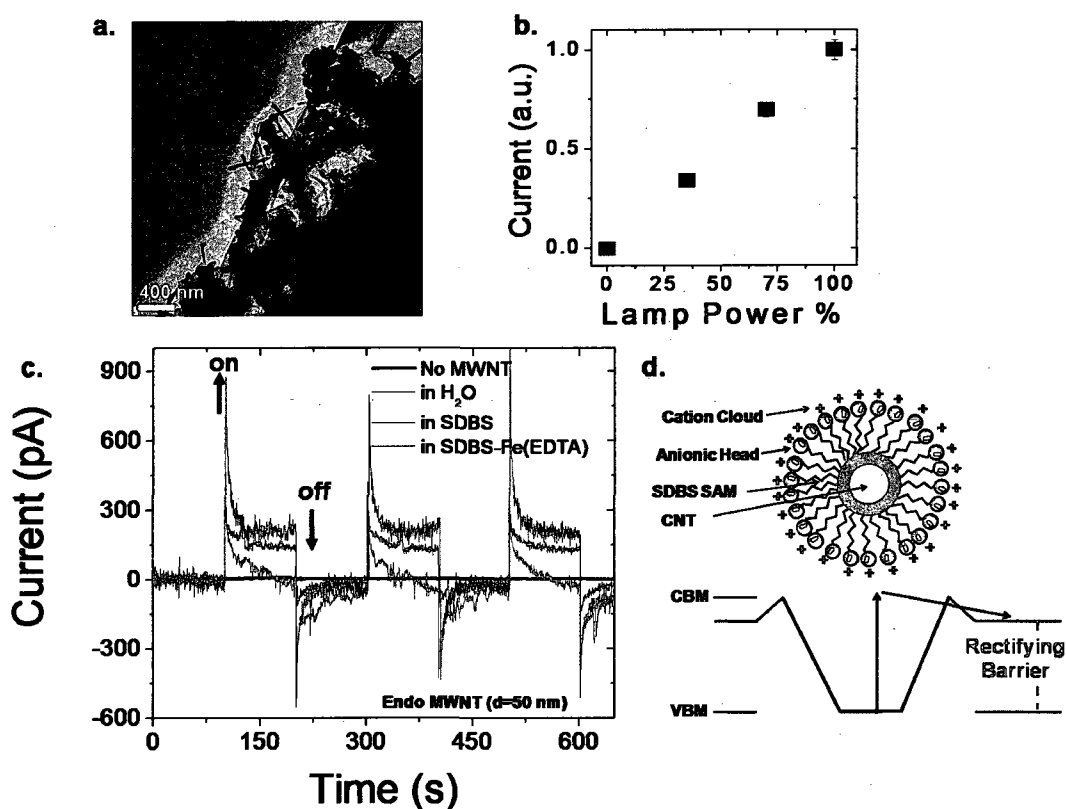
Figure 5.4 : Endo MWNT current generation and photocathode cell. (a) Representative TEM image of Endo MWNT. (b) Photocurrent dependence on incident light power (c) Optical rectenna photocurrent generation. (d) Energy barrier produced by surfactant layer.

5.5.3 Current Emission as a Function of Wavelength and Tube Type

To provide additional insight to the operative mechanism of the photocurrent response and further support the optical rectenna hypothesis, we explored photocurrent response upon exposure to specific wavelengths. Flipped carpets (fCNTs) of individual SWNT were mounted on a copper substrate and exposed to a xenon arc lamp equipped with a ultraviolet-visible-near-infrared monochromator (see Sec. 5.4). For wavelength dependent experiments, SWNT substrates were chosen over MWNTs because the low percentage of MWNTs protruding from the bulk creates fewer available active antennae, as shown in Figure 5.4.a. Vertically grown SWNT carpets will give a higher number of antennae whose smaller diameter allows for better surfactant coverage (diode) that will ultimately provide higher current density (Fig. 5.3). In addition, the use of SWNT allows for the possibility to explore the wavelength dependence of different kinds (diameter and/or chirality) of tubes. We found a strong photocurrent peak around 300 nm (green box, Fig. 5.5.a) and a small secondary peak which occurs between $\sim$900 and 1700 nm (gray box, Fig. 5.5.a). We tentatively assigned the 300 nm feature to excitations of graphitic π-plasmons [Kuzuo et al., 1992; Lu et al., 2005; Seepujak et al., 2006] (red-shifted due to $\kappa = 80$ in water). Our π-plasmons observation was demonstrated by studying a broad range of carbon materials which generate photocurrents in SDBS electrolytes including MWNTs, SWNT arrays, graphite nanoplatelets, and carbon tape (Fig. 5.5.b). The second photocurrent peak in the NIR was unique to MWNTs and SWNTs. Figure 5.5.d shows the photocurrent generation of carpets produced under different conditions which result in different distributions of diameter and types of tubes (small diameter single walls (i) or large diameter single walls that may also contain few MWNT (iii)) [Pint et al., 2008]. The fCNTs were inverted onto a conductive substrate to expose the vertically aligned and sparsely dispersed CNTs. All types of fCNT samples exhibit the same peak at around 310 nm as shown with the MWNT sample (Fig. 5.5.c), corroborating that this peak is due to the graphitic π-plasmon. The photocurrent in the NIR, on the

other hand, shows a different behavior. Three distinct peaks appear (yellow, blue, and red boxes, Figure 5.5.b); we found these to be dependent on the distribution of tube types (or diameter) in the sample. The sample with a high ratio of small diameter tubes (red trace) shows two peaks, one at ~800 nm and the other at approximately 1050 nm (this peak was visible in all samples). As the diameter of the tubes was increased, a distinct peak started to emerge at ~1250 nm; this continued until the fCNTs were composed of mostly MWNT and large diameter SWNTs (green trace). At this point the signal matched that of the Mitsui MWNT (blue trace) and the 800 nm peak was attenuated.

Figure 5.6.a shows representative TEM images of the different diameter distributions of the fCNT samples used. Moreover, fluorescence and absorbance spectra were obtained from these samples corroborating the different diameter distribution of such samples (Fig. 5.6.b–c).

5.6   Comparison Between SDS and SDBS

Because SDBS has a strong absorption around 300 nm due to the presence of the benzene ring, we replaced SDBS with sodium dodecyl sulfate (SDS) to ensure that the nanotubes are the absorbing species at 310 nm. The current generated with SDS was qualitatively the same as SDBS with strong current generation at 310 nm and roughly no current at other wavelengths (Fig. 5.7.a, SDBS-blue and SDS-red). Figure 5.7.b shows the photocurrent generated using different incident light radiation. We can see that the maximum current generated was obtained with 310 nm incident light while no current was obtained with 500 nm using both surfactants. Also, using the QTH lamp we only obtained < 40 % of the photocurrent generated.

5.6.1   Current Generation with Gold Covered Carpets

In an attempt to obtain a more efficient photocathode cell with a broader absorbance in the visible region, we evaporated roughly 10 nm of gold (Au) onto fCNTs. Au is well
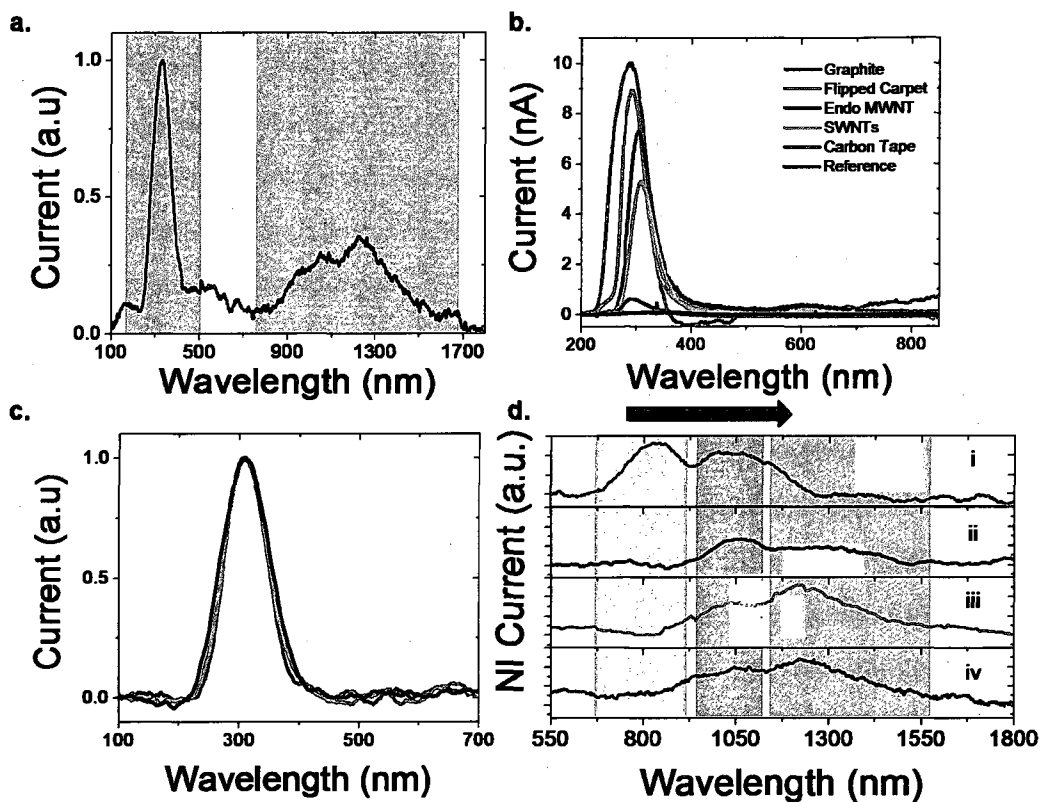
Figure 5.5 : Wavelength specific response. (a.) Current generation of fCNTs as a function of wavelength. (b.) Photocurrent for multiple carbon sources. (c.) Photocurrent at 310 nm for different fCNT; Red, mostly small diameter SWNTs. Black, small and large diameter SWNTs. Green, large diameter SWNTs and few MWNTs. (d.) Photocurrent generation of different CNT samples i.) Mostly small diameter SWNTs. ii.) Small and large diameter SWNTs. iii.) Large diameter SWNTs and few MWNTs. iv.) Endo MWNTs.

known to possess very strong absorption in the visible region, and the size and shape of the Au nanoparticles can be deduced from to the absorption spectrum [Kim et al., 2002]. Figure 5.8.a shows field emission scanning electron microscope (SEM) images and backscattered electron detection (BSE) of flipped carpets with and without Au. These images show bundles of individual SWNTs between 10 – 50 nm in diameter (50,000×). BSE images confirm that Au was deposited onto the CNTs without sig-
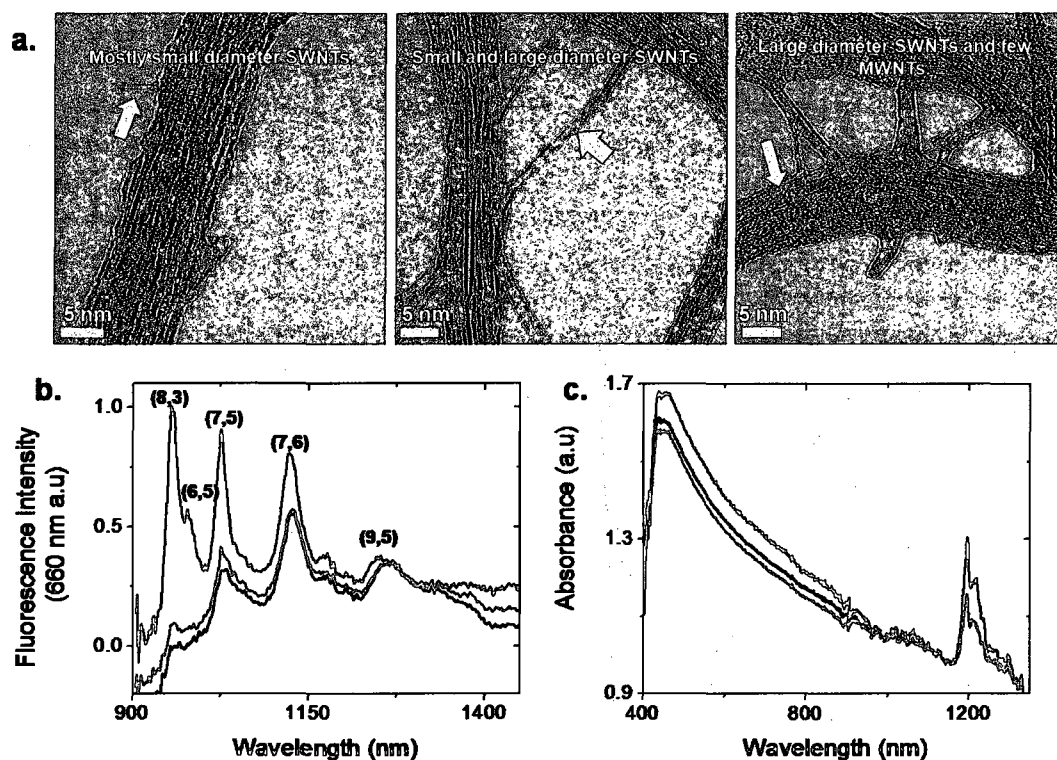
Figure 5.6 : (a.) Representative TEM images of CNT samples. Fluorescence (b) and absorbance (c) spectra of different carpets; red, mostly small diameter SWNTs; black, small and large diameter SWNTs; green, large diameter SWNTs and few MWNTs.

nificantly changing the tube spacing and/or orientation. Photocurrent measurements were obtained using a mixture of SDBS and Fe-(EDTA) doped with the long chain alkyl thiol 12-mercaptododecanoic acid. Since only partial coverage of the tubes was obtained with Au evaporation, the long-chain thiol serves as the rectifying diode for the fCNT-Au [Reed et al., 1997; Tour, 2000] and the SDBS for the uncovered portions of the CNTs. Photocurrent generation as a function of wavelength with fCNTs after Au deposition displayed a red-shift of the maximum current peak by roughly 100 nm (red trace in Fig.5.8.b) in contrast to fCNTs without Au (blue trace in 5.8.b). More-over, fCNTs-Au has a more intense and broader current profile than fCNT without Au, indicating that the photoabsorption can be adjusted by changing metal coverage
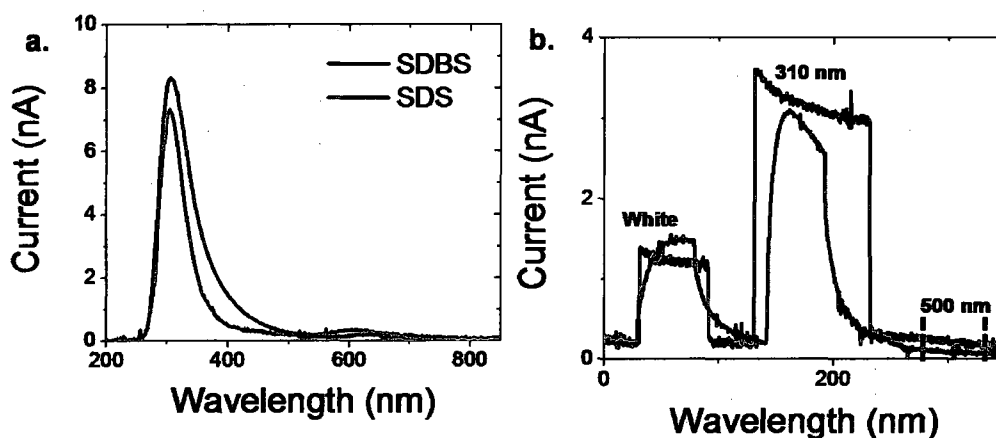
Figure 5.7 : (a.) Photocurrent as a function of wavelength. (b.) Photocurrent with different incident radiation wavelengths.

and/or thickness [Kim et al., 2002]. No appreciable current generation was observed in the NIR after Au evaporation. Photocurrent generation was also measured by cycling the light on and off (400 nm wavelength) as a function of time (Fig. 5.8.c). We observed the same fast response to light as with the other types of fCNTs. When the light was turned on or off we observed an exponential increase and decay in current, respectively, indicating that after exposure to light the CNTs charge and discharge. Moreover, the charge and discharge time constants are consistent in every cycle, as shown in the insert of Figure 5.8.c, with faster rates observed for increasing current than decreasing (by a factor of $\sim 2\times$, $\tau = 10.1$ and $\tau = 23.8$ sec). No current was obtained when experiments were performed in the absence of fCNTs as a function of wavelength (orange trace, Fig. 5.8.c). Importantly, we increased our current generation by 3 orders of magnitude from measurements in pico amps (pA) with MWNTs to nano amps (nA) with carpets, corroborating our observation for the need for more protruding antennae. We envision that with better engineering of the photocathode, we can increase the current collection by several orders of magnitude and get even closer to an efficient device that can play an important role in solving our energy needs.
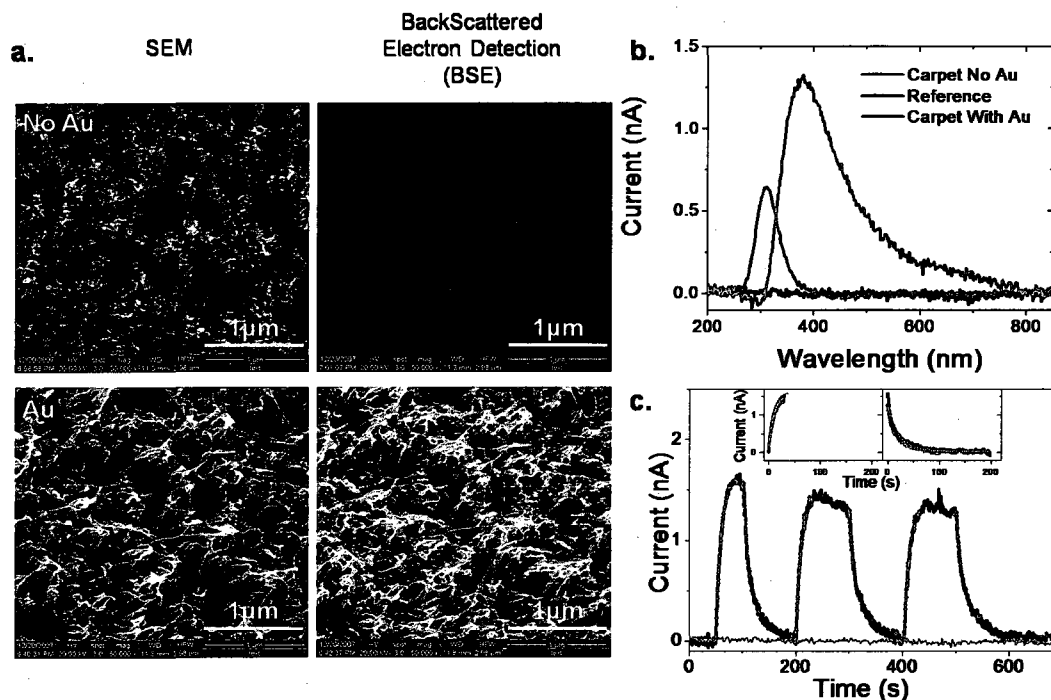
Figure 5.8 : Photocurrent with fCNTs with and without Au. (a) SEM images of fCNTs with and without Au. (b) Current as a function of wavelength for fCNTs with (red) and without (blue) Au and no CNT as reference (carbon tape, black). (c) Cyclic current generation after turning light on and off at 400 nm. Inset is the current charge and discharge at each cycle.

5.6.2 Redox Reactions Utilizing Charge Separation with 310 nm Incident Light

To further illustrate that the current generation is a direct consequence of the incident light being exposed to the CNTs, we use the inherent charge separation that is generated to reduce metal transition salts ($HAuCl_4$) that were added to individually suspended surfactant stabilized HiPco SWNTs [O'Connell et al., 2002]. We hypothesized that if the CNTs are injecting electrons into the solution, the Au^{3+} salts will

undergo redox reactions, become reduced with the excess electrons that are present, and form metallic nanoparticles. The metal particle formation was monitored using absorbance. SDBS is the ideal surfactant for this test because SDBS does not spontaneously reduce Au^{3+} metal salts [Duque et al., 2008c]. 100 μL of $AuCl_3$ (1 mM) was added to 2 mL of SDBS-SWNTs suspension (5.5 mg/L) and exposed to three different light conditions: no light, ambient light, and 310 nm light source (1.2 mW) for 2 hrs. Figure 5.9.a shows that SDBS-SWNT-Au solutions in the dark (red trace, B) do not show any significant changes in absorbance compared to the reference solution (black trace, A), while the solution exposed to ambient light (green trace, C) displays a small change in the absorbance. Although only a small change in the absorbance was observed, the changes that occurred were in the region that Au metal particles are known to absorb light ($\sim$530 nm) [Kim et al., 2002], indicating a small fraction of the metal ion salts were reduced into particles. In contrast, when the SDBS-SWNT-Au solution was exposed to 310 nm light source, a significant absorbance peak was developed (Fig. 5.9.a, blue trace, D). Moreover, the solution itself began to turn red within the first 10 min (Fig. 5.9.d), while the other solutions did not significantly change color after 2 h. This color change is a visual indication that Au metallic nanoparticles were formed [Kim et al., 2002]. A SDBS-Au solution in the absence of SWNTs was also exposed to the 310 nm light source and served as a control (Fig. 5.9.a, light blue, E); no metal particle formation was observed.

Fluorescence spectroscopy is commonly used to monitor diameter-selective oxidation of semiconducting SWNT with faster reaction rates for large diameter tubes (small bandgap) than small diameter tubes [O'Connell et al., 2005] due to its strong sensitivity to the local environment [Duque et al., 2008a]. We recently proposed a redox landscape model for SWNTs suspended in SDBS and showed that the Fermi level of the tubes systematically change with diameter. Moreover, high oxidation potential species like transition metal salts can selectively access different populations

of tubes [Duque et al., 2008c] (Chap. 4). Figure 5.9.b shows a diameter dependent fluorescence quenching after addition of Au^{3+} ion salts, especially for the solution kept in the dark (red trace, B). In contrast, the suspension exposed to 310 nm light (blue trace, D) has approximately the same fluorescence intensity across all diameters as the reference solution (black trace, A). The selective fluorescence quenching of solution B is due to the presence of free floating Au^{3+} ion salts which disrupt the luminescence of the large diameter semiconductors to a larger degree than small diameters, as predicted by the redox landscape (see Section 4.5.5 for more details) [Duque et al., 2008c]. However, after reduction and subsequent particle formation as a consequence of the excess electrons present in solution from the light-SWNT interaction, the fluorescence is able to recover to that of the reference solution due to a decrease in Au^{3+} ions salts available in solution to interact with the tubes and disrupt the luminescence. AFM images of the solution exposed to the 310 nm light source (Fig. 5.9.c) show a vast number of free particles with a height range between 4 and 10 nm. Interestingly, we also observed a large number of tubes forming into ring structures. The heights of these rings are between 1.2 and 5 nm with an average inner diameter of 245 nm, indicating that the rings are formed by individuals or bundles of 2 − 4 SWNTs. At this time, we do not have a clear explanation for the mechanism of ring formation, but we can infer that the accumulation of charges at the end of the tubes can potentially be the source as described in our previous work [Duque et al., 2008b] (Sec. 4.5.11). In contrast, the solutions exposed to ambient light or kept in the dark neither exhibited particle nor SWNT ring formation.

5.7 Conclusions

We show that spatial arrays of CNT can form an optical rectenna that responds to an incident light source and generates a current offset that can be rectified by a self-assembled monolayer of anionic surfactant. Moreover, we show that the current
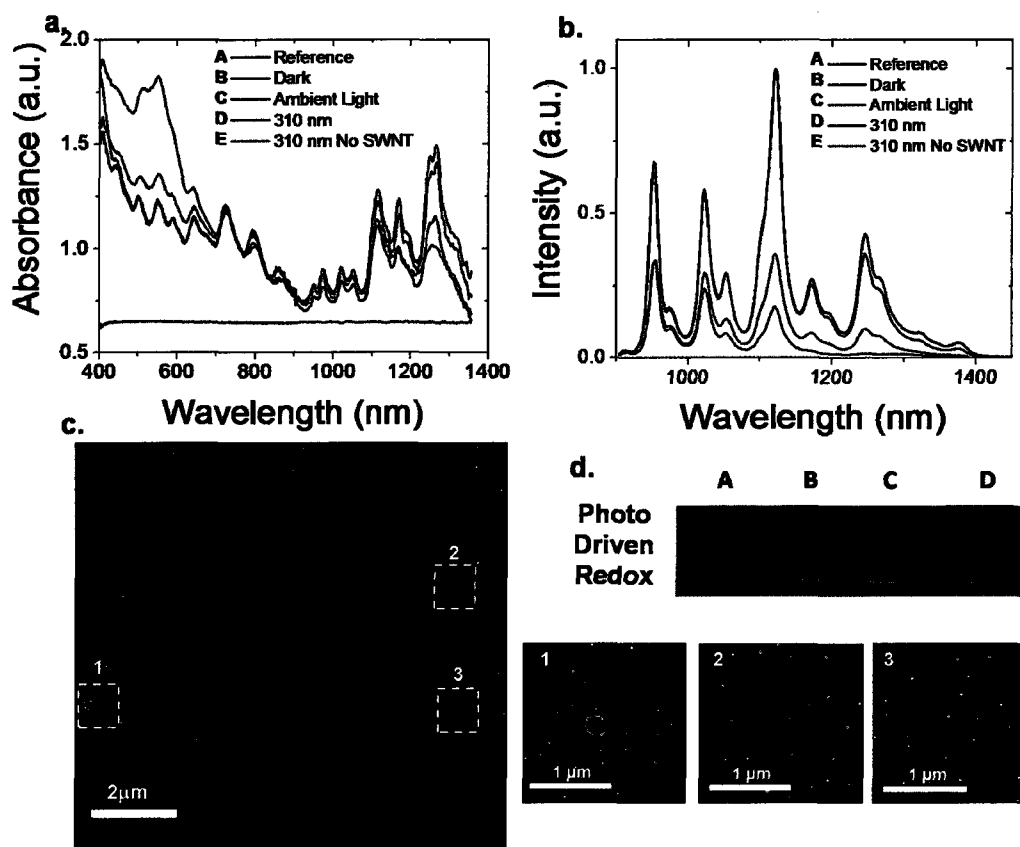
Figure 5.9 : Photochemical reduction of Au^{3+} ions in SDBS-SWNT suspensions under different light conditions. (a.) Absorbance spectra. (b.) Fluorescence spectra. (c.) Representative AFM image of SDBS-SWNT-Au exposed to 310 nm light source. (d.) Image of SDBS-SWNT-Au suspension after light irradiation.

generated has a wavelength dependence that can be adjusted by the evaporation of metal on the CNT substrate. We foresee an extensive use of these optical rectennas as photovoltaic devices, as well as a wide interest in diverse fundamental research and applied technologies.

5.8 Appendix 5

5.8.1 Xenon Lamp Spectra

Figure 5.10 shows the spectrum of the 150 W xenon arc lamp equipped with a ultraviolet-visible-near Infrared monochromator used in the experiments. Red trace is the ultraviolet-visible spectrum and the black trace is the near infrared.
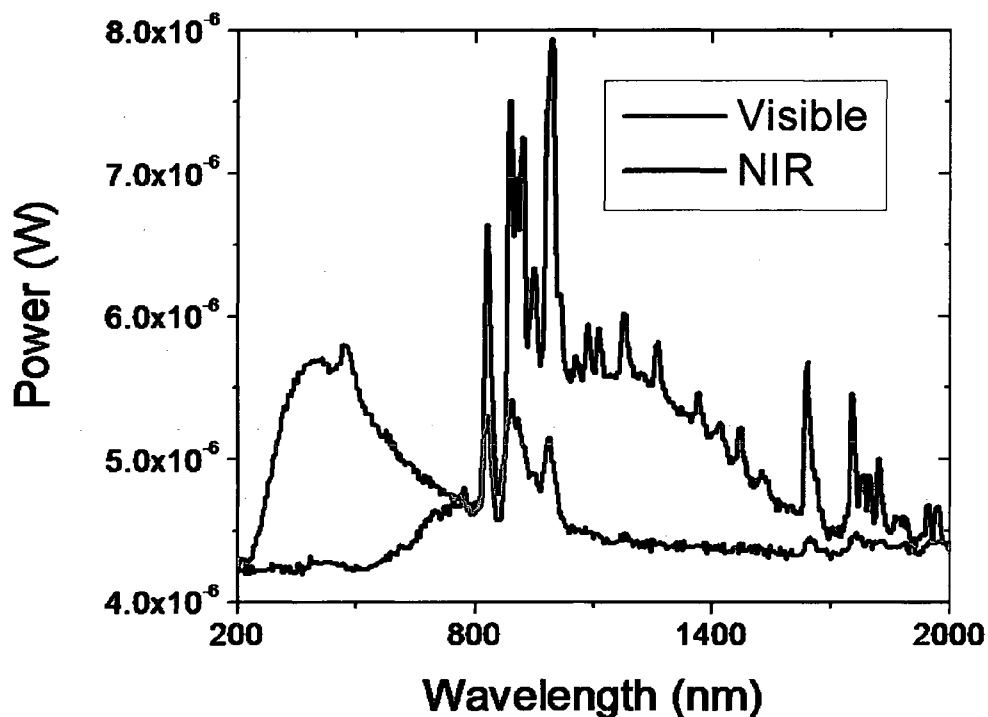
Figure 5.10 : Incident light power.

5.8.2 Spontaneous Particle Formation

In contrast to the finding in Sec. 5.6.2, if the SDBS-SWNT suspension is doped with PVP, which is known to spontaneously reduce metal salts (Chap. 4), we detect particle formation via absorbance and change of color in all instances even in the absence

of SWNTs (Fig. 5.11). This indiscriminate and uncontrolled Au particle formation is due to the presence of PVP and not the incident light, further underscoring the importance of the SWNT antenna behavior in the Au particle formation.
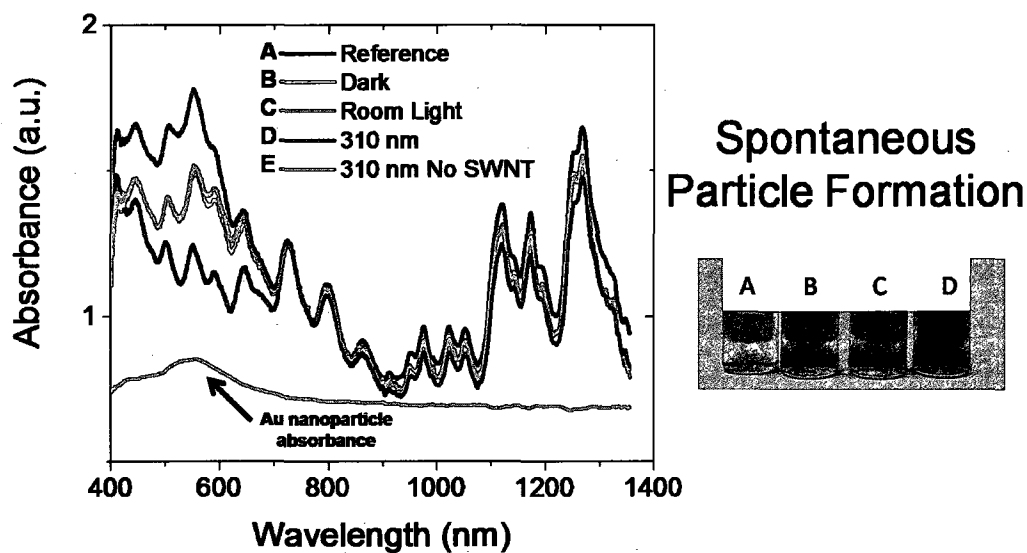
Figure 5.11 : Spontaneous Au nanoparticle formation in PVP-SDBS-SWNT suspensions.

5.8.3   Other AFM Images of Rings

Figure 5.12 shows additional AFM images of ring formation due to incident light at 310 nm from Sec. 5.6.2.
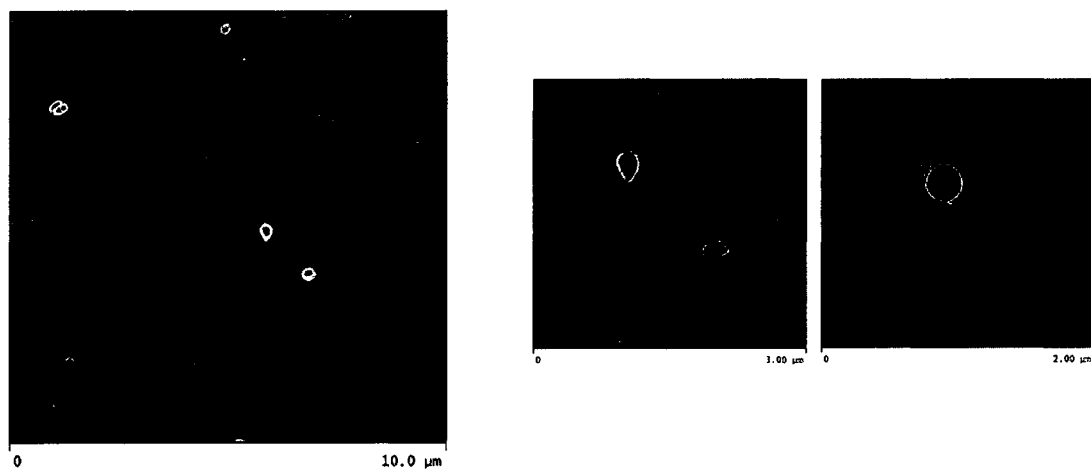
Figure 5.12 : AFM images of SWNT rings via 310 nm light source.

Chapter 6

Other Experiments

6.1 Photoluminescence of SWNTs in Deoxycholate Gels

The objective of this experiment was to study the optical properties of individual SWNT suspended in sodium deoxycholate (DOC) using procedures described in Chapter 2, Experimental Section 2.4 after the addition of acid (HCl) (Fig. 6.1). SWNT at a concentration of ~12 mg/L in DOC (1 wt% DOC per weight) were exposed to HCl, 1 N, resulting in a gel-like structure. All of the spectroscopy characteristics of the tubes after acidification remained relatively constant with a small drop in the luminescence intensity but no shifting in the peaks. Raman signatures were constant without any major changes in the RBM or G-band (Fig. 6.2). Figure 6.3 shows snap shots at different time frames of an individual (6,5) tube in a DOC gel-like structures. Its luminescence remains high and stable. Additionally, the tubes appear to move around the gel-like structure with a motion resembling "reptation". Importantly, the DOC gel-like structures can be obtained in the absence of SWNTs.

6.2 AB Fluorescence

Previous studies have used near infrared fluorescence quenching to monitor diameter-selective oxidation of semiconducting SWNT by organic acceptors [O'Connell et al., 2005]. The reactions were conducted using SWNTs dispersed in sodium dodecyl sulfate (SDS) surfactant to which organic charge-transfer molecules like 4-amino-1,1-azobenzene-3,4-disulphonic acid (AB) were added. It was found that large diameter
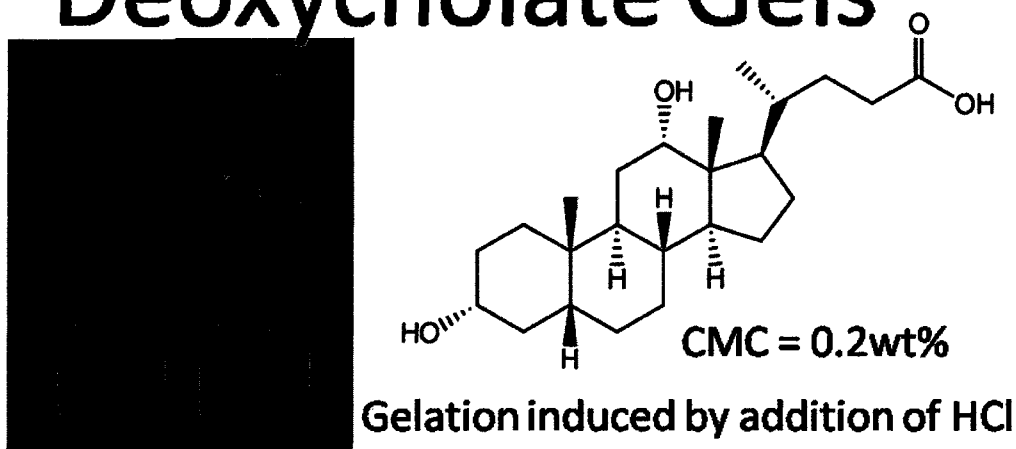
Figure 6.1 : DOC gels.

semiconducting SWNTs react at faster rates than small diameter SWNTs [O'Connell et al., 2005]. My additional findings to this topic were that their observations depend on the pH of the starting solution. If the reaction is induced at neutral pH (6 – 7), it is preferential toward large diameter semiconducting tubes; if the reaction is instead carried out under basic conditions (pH $\geq$ 9), then the reactivity is reversed and small diameter tubes undergo a faster rate of reaction. Figure 6.4 shows the fluorescence intensity of the different fluorescence peaks (at 660 and 785 nm excitation wavelength) as a function of time. One can clearly see that at pH 6 the large diameter tubes such as (9,5) with 660 nm excitation (yellow stars) or (9,7) for 785 nm excitation wavelength (red stars) have the faster reaction rates, while at pH 9, (8,3) (blue dots) at both excitation wavelengths have the fastest reaction rates. Figure 6.5 shows the different fluorescent peaks of SDBS-SWNT suspensions with their corresponding assigned (n,m) vector at both excitation wavelengths (660 and 785 nm) before the reaction.
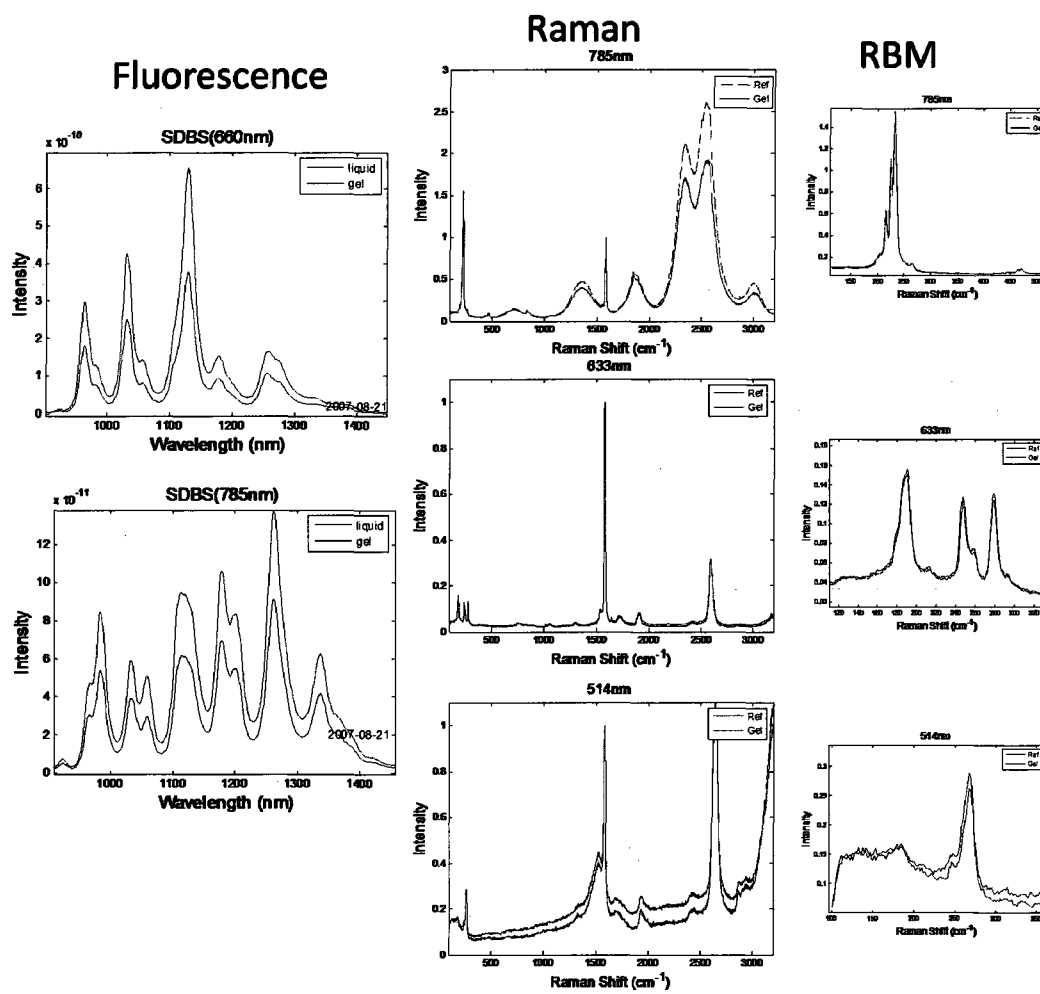
Figure 6.2 : DOC gel spectroscopy.
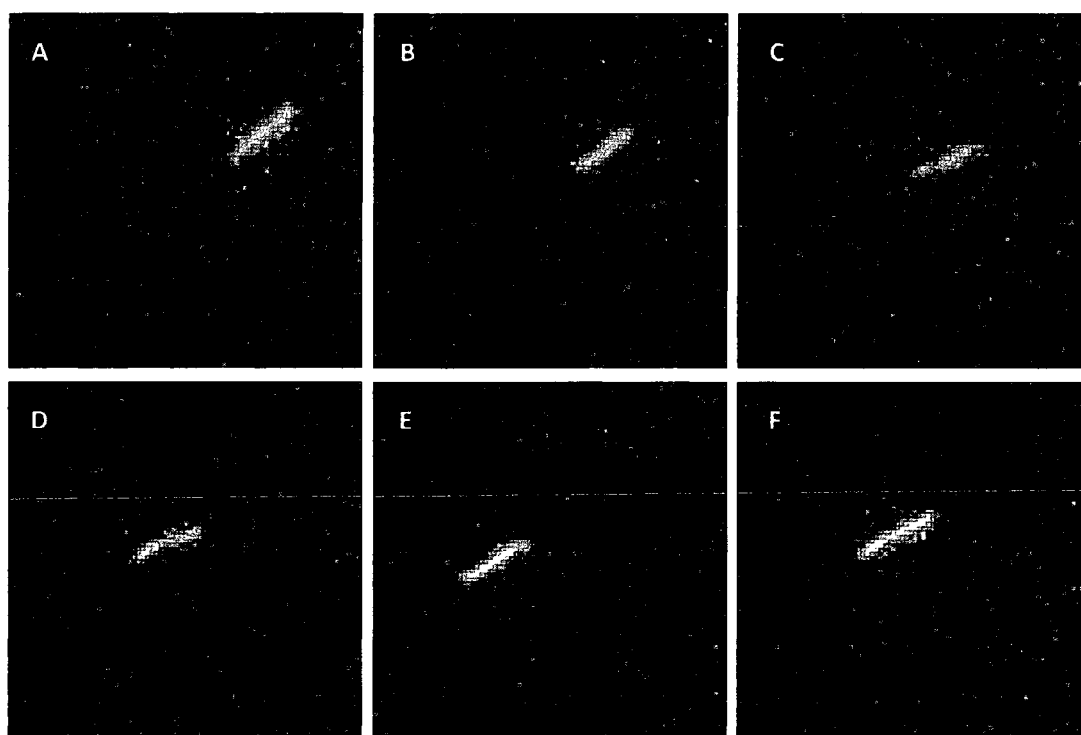
Figure 6.3 : Individual DOC-SWNT in a DOC gel.
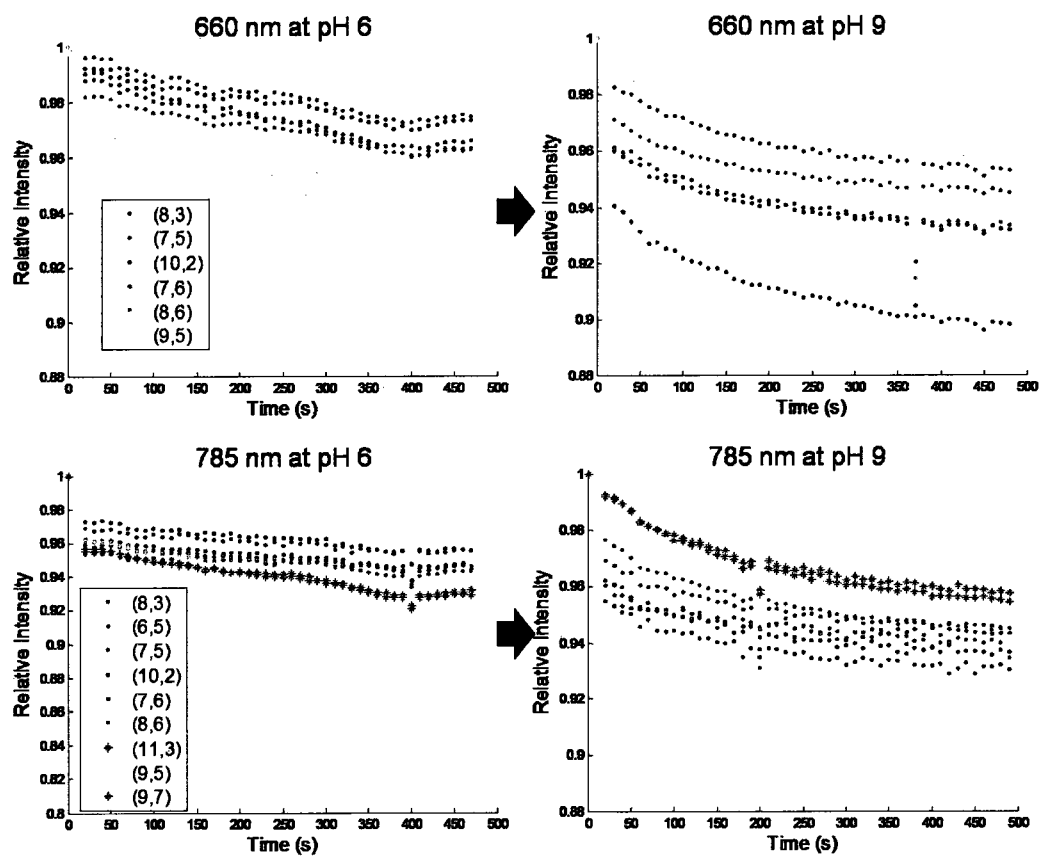
Figure 6.4 : AB reaction rates.
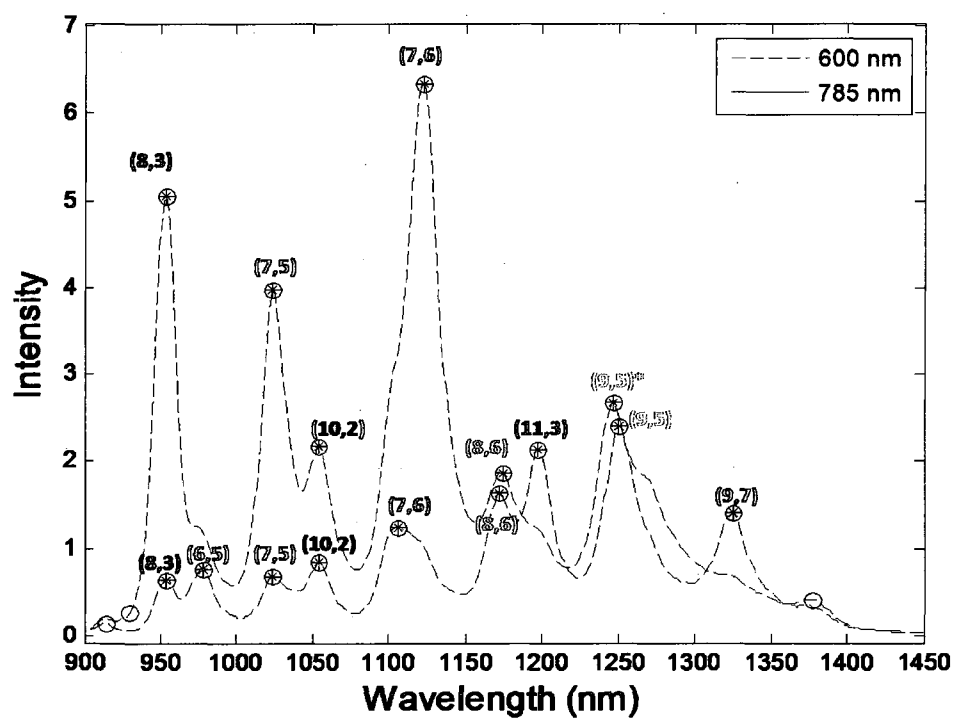
Figure 6.5 : Fluorescence peaks of SDBS-SWNT suspensions.

Chapter 7

Overall Conclusions

- By studying the spectroscopic and structural behavior of mixtures of anionic surfactant and PVP polymers at various pH, we have identified a mixture (ISPVP-SDBS) that could serve as a universal wrapping agent of individual SWNTs. Due to its effectiveness at all pH, in highly saline environments as well as in physiological media, we foresee an extensive use of ISPVP-SDBS-SWNTs in fields as varied as chemistry, physics and biology for fundamental research as well as more applied technologies.

- We observed that DOC-SWNTs have a narrower and more homogeneous luminescence distribution with longer lifetimes and brighter tubes than SDBS-SWNTs. The increased heterogeneity of results obtained with SDBS-SWNT suspensions can be due to a less-tight surfactant micelle around the tubes that allows vacancies to form which in turn lead to inconsistent results. Moreover, we found that the synthesis process (HiPco or CoMoCat) has a profound effect on the luminescence properties of the tubes; even larger spectroscopic inconsistencies were observed in different batches from the HiPco process.

- We have found compelling evidence for *antenna chemistry* using highly dispersed SWNT-surfactant suspensions in a variety of electromagnetic fields (radiofrequencies, microwaves, and light). Electric field-driven redox processes with reducible transition metal salts result in tip-specific deposition of metallic nanoparticles and sheaths, yielding novel nanoparticle-nanotube structures (nanoPaNTs)

such as dumbells, SWNTs partially or completely encapsulated by metal, rings and straight SWNT "threaded" through rings to form shish-kebab structures. We find substantial evidence that metallic nanotubes participate preferentially in these reactions, with diffusion-limited rates. The effective electric field at the tips of metallic SWNT is enhanced by their aspect ratio as well as a gradient "compression" effect caused by the thin shell of surfactant molecules. We anticipate that the novel composite nanostructures (nanoPaNTs) produced by this approach could prove to be useful nanoelectronics and catalysts, while the underlying electron transfer and rectifying processes could eventually lead to interesting applications in energy harvesting, nanomedicine and chemical synthesis.

- We show that spatial arrays of CNT can form an optical rectenna that responds to an incident light source and generates a current offset that can be rectified by a self-assembled monolayer of anionic surfactant. Moreover, we show that the current generated has a wavelength dependence that can be adjusted by the evaporation of metal on the CNT substrate. We foresee an extensive use of these optical rectennas as photovoltaic devices, as well as a wide interest in diverse fundamental research and applied technologies.

Bibliography

P. M. Ajayan, M. Terrones, A. de la Guardia, V. Huc, N. Grobert, B. Q. Wei, H. Lezec, G. Ramanath, and T. W. Ebbesen. Nanotubes in a flash - ignition and reconstruction. *Science*, 296(5568):705–705, 2002. [Cited twice on page 2 and 139.]

W. E. Alvarez, F. Pompeo, J. E. Herrera, L. Balzano, and D. E. Resasco. Characterization of single-walled carbon nanotubes (SWNTs) produced by CO disproportionation on Co-Mo catalysts. *Chemistry of Materials*, 14(4):1853–1858, 2002. [Cited once on page 104.]

M. S. Arnold, A. A. Green, J. F. Hulvat, S. I. Stupp, and M. C. Hersam. Sorting carbon nanotubes by electronic structure using density differentiation. *Nature Nanotechnology*, 1(1):60–65, 2006. [Cited twice on page 57 and 75.]

R. Atkin, M. Bradley, and B. Vincent. Core-shell particles having silica cores and pH-responsive poly(vinylpyridine) shells. *Soft Matter*, 1(2):160–165, 2005. [Cited 3 times on pages 18, 28, and 124.]

S. Attal, R. Thiruvengadathan, and O. Regev. Determination of the concentration of single-walled carbon nanotubes in aqueous dispersions using UV-visible absorption spectroscopy. *Analytical Chemistry*, 78(23):8098–8104, 2006. [Cited twice on page 7 and 109.]

S. M. Bachilo, M. S. Strano, C. Kittrell, R. H. Hauge, R. E. Smalley, and R. B. Weisman. Structure-assigned optical spectra of single-walled carbon nanotubes. *Science*, 298(5602):2361–2366, 2002. [Cited 8 times on pages 6, 11, 18, 104, 106, 109, and 132.]

M. G. Banks. An extension of the Hirsch index: Indexing scientific topics and compounds. *Scientometrics*, 69(1):161–168, 2006. [Cited once on page 18.]

P. W. Barone and M. S. Strano. Reversible control of carbon nanotube aggregation for a glucose affinity sensor. *Angewandte Chemie-International Edition*, 45(48): 8138–8141, 2006. [Cited once on page 84.]

R. H. Baughman, A. A. Zakhidov, and W. A. de Heer. Carbon nanotubes - the route toward applications. *Science*, 297(5582):787–792, 2002. [Cited once on page 18.]

L. X. Benedict, S. G. Louie, and M. L. Cohen. Static polarizabilities of single-wall carbon nanotubes. *Physical Review B*, 52(11):8541–8549, 1995. [Cited twice on page 2 and 83.]

S. Berciaud, L. Cognet, G. A. Blab, and B. Lounis. Photothermal heterodyne imaging of individual nonfluorescent nanoclusters and nanocrystals. *Physical Review Letters*, 93(25):257402, 2004. [Cited twice on page 13 and 54.]

S. Berciaud, D. Lasne, G. A. Blab, L. Cognet, and B. Lounis. Photothermal heterodyne imaging of individual metallic nanoparticles: Theory versus experiment. *Physical Review B*, 73(4):045424, 2006. [Cited twice on page 13 and 54.]

S. Berciaud, L. Cognet, P. Poulin, R. B. Weisman, and B. Lounis. Absorption spectroscopy of individual single-walled carbon nanotubes. *Nano Letters*, 7(5):1203–1207, 2007. [Cited twice on page 13.]

S. Berciaud, L. Cognet, and B. Lounis. Luminescence decay and the absorption cross section of individual single-walled carbon nanotubes. *Physical Review Letters*, 101 (7):077402, 2008. [Cited 5 times on pages 50, 60, 61, and 63.]

S. Berger, C. Voisin, G. Cassabois, C. Delalande, P. Roussignol, and X. Marie. Temperature dependence of exciton recombination in semiconducting single-wall carbon nanotubes. *Nano Letters*, 7(2):398–402, 2007. [Cited once on page 50.]

V. A. Bloomfield. Condensation of DNA by multivalent cations - considerations on mechanism. *Biopolymers*, 31(13):1471–1481, 1991. [Cited once on page 121.]

E. A. Bluhm, N. C. Schroeder, E. Bauer, J. N. Fife, R. M. Chamberlin, K. D. Abney, J. S. Young, and G. D. Jarvinen. Surface effects on metal ion transport across porous alumina membranes. 2. Trivalent cations: Am, Tb, Eu, and Fe. *Langmuir*, 16(17):7056–7060, 2000. [Cited once on page 111.]

J. M. Bonard, J. P. Salvetat, T. Stockli, W. A. de Heer, L. Forro, and A. Chatelain. Field emission from single-wall carbon nanotube films. *Applied Physics Letters*, 73 (7):918–920, 1998. [Cited 3 times on pages 2, 83, and 113.]

J. C. Brackman and J. Engberts. Polymer micelle interactions - Physical organic aspects. *Chemical Society Reviews*, 22(2):85–92, 1993. [Cited twice on page 18 and 124.]

J. C. Bradley, S. Babu, and P. Ndungu. Contactless tip-selective electrodeposition of palladium onto carbon nanotubes and nanotibers. *Fullerenes Nanotubes and Carbon Nanostructures*, 13(3):227–237, 2005. [Cited twice on page 2 and 83.]

W. C. Brown. The history of power transmission by radio-waves. *IEEE Transactions on Microwave Theory and Techniques*, 32(9):1230–1242, 1984. [Cited twice on page 139.]

A. Buldum and J. P. Lu. Electron field emission properties of closed carbon nanotubes. *Physical Review Letters*, 91(23):236801, 2003. [Cited twice on page 89 and 120.]

P. J. Burke. An RF circuit model for carbon nanotubes. *IEEE Transactions on Nanotechnology*, 2(1):55–58, 2003. [Cited once on page 109.]

L. J. Carlson, S. E. Maccagnano, M. Zheng, J. Silcox, and T. D. Krauss. Fluorescence efficiency of individual carbon nanotubes. *Nano Letters*, 7(12):3698–3703, 2007. [Cited once on page 50.]

R. L. Carver, H. Q. Peng, A. K. Sadana, P. Nikolaev, S. Arepalli, C. D. Scott, W. E. Billups, R. H. Hauge, and R. E. Smalley. A model for nucleation and growth of single wall carbon nanotubes via the HiPco process: A catalyst concentration study. *Journal of Nanoscience and Nanotechnology*, 5:1035–1040, 2005. [Cited once on page 86.]

D. Chattopadhyay, L. Galeska, and F. Papadimitrakopoulos. A route for bulk separation of semiconducting from metallic single-wall carbon nanotubes. *Journal of the American Chemical Society*, 125(11):3370–3375, 2003. [Cited once on page 83.]

W. X. Chen, H. Gui, J. Y. Lee, and Z. L. Liu. Rapid synthesis of Pt/carbon nanometer catalyst by microwave irradiation and its electrocatalytic activity for electrooxidation of methanol. *Chemical Journal of Chinese Universities-Chinese*, 24(12): 2285–2287, 2003a. [Cited once on page 84.]

W.-X. Chen, J. Y. Lee, and Z. Liu. Preparation of Pt and PtRu nanoparticles supported on carbon nanotubes by microwave-assisted heating polyol process. *Materials Letters*, 58(25):3166–3169, 2004. [Cited once on page 84.]

Z. H. Chen, X. Du, M. H. Du, C. D. Rancken, H. P. Cheng, and A. G. Rinzler. Bulk separative enrichment in metallic or semiconducting single-walled carbon nanotubes. *Nano Letters*, 3(9):1245–1249, 2003b. [Cited once on page 83.]

P. Cherukuri, C. J. Gannon, T. K. Leeuw, H. K. Schmidt, R. E. Smalley, S. A. Curley, and B. Weisman. Mammalian pharmacokinetics of carbon nanotubes using intrinsic near-infrared fluorescence. *Proceedings of the National Academy of Sciences of the United States of America*, 103(50):18882–18886, 2006. [Cited once on page 19.]

I. W. Chiang, B. E. Brinson, R. E. Smalley, J. L. Margrave, and R. H. Hauge. Purification and characterization of single-wall carbon nanotubes. *Journal of Physical Chemistry B*, 105(6):1157–1161, 2001. [Cited once on page 5.]

H. Choi, M. Shim, S. Bangsaruntip, and H. Dai. Spontaneous reduction of metal ions on the sidewalls of carbon nanotubes. *Journal of the American Chemical Society*, 124(31):9058–9059, 2002. [Cited once on page 84.]

A. Claye, S. Rahman, J. E. Fischer, A. Sirenko, G. U. Sumanasekera, and P. C. Eklund. In situ Raman scattering studies of alkali-doped single wall carbon nanotubes. *Chemical Physics Letters*, 333(1-2):16–22, 2001. [Cited once on page 105.]

A. S. Claye, N. M. Nemes, A. Janossy, and J. E. Fischer. Structure and electronic properties of potassium-doped single-wall carbon nanotubes. *Physical Review B*, 62(8):R4845–R4848, 2000. [Cited once on page 105.]

L. Cognet, D. A. Tsyboulski, J.-D. R. Rocha, C. D. Doyle, J. M. Tour, and R. B. Weisman. Stepwise quenching of exciton fluorescence in carbon nanotubes by single-molecule reactions. *Science*, 316(5830):1465–1468, 2007. [Cited 4 times on pages 1, 18, 37, and 50.]

L. Cognet, S. Berciaud, D. Lasne, and B. Lounis. Photothermal methods for single nonluminescent nano-objects. *Analytical Chemistry*, 80(7):2288–2294, 2008a. [Cited once on page 13.]

L. Cognet, D. A. Tsyboulski, and R. B. Weisman. Subdiffraction far-field imaging of luminescent single-walled carbon nanotubes. *Nano Letters*, 8(2):749–753, 2008b. [Cited once on page 54.]

J. Crochet, M. Clemens, and T. Hertel. Quantum yield heterogeneities of aqueous single-wall carbon nanotube suspensions. *Journal of the American Chemical Society*, 129(26):8058–8059, 2007. [Cited twice on page 50 and 104.]

H. J. Dai. Carbon nanotubes: Opportunities and challenges. *Surface Science*, 500 (1-3):218–241, 2002. [Cited twice on page 2 and 18.]

G. Decher. Fuzzy nanoassemblies: Toward layered polymeric multicomposites. *Science*, 277(5330):1232–1237, 1997. [Cited once on page 27.]

S. K. Doorn, D. A. Heller, P. W. Barone, M. L. Usrey, and M. S. Strano. Resonant Raman excitation profiles of individually dispersed single walled carbon nanotubes in solution. *Applied Physics A-Materials Science and Processing*, 78(8):1147–1155, 2004. [Cited 3 times on pages 8, 23, and 67.]

M. Dresselhaus, G. Dresselhaus, R. Saito, and A. Jorio. Raman spectroscopy of carbon nanotubes. *Physics Reports*, 409(2):47–99, 2005. [Cited 3 times on pages 8, 18, and 109.]

M. Dresselhaus, G. Dresselhaus, and M. Hofmann. The big picture of Raman scattering in carbon nanotubes. *Vibrational Spectroscopy*, 45(2):71 – 81, 2007a. [Cited 5 times on pages 6, 8, 23, 67, and 104.]

M. S. Dresselhaus. Applied physics - Nanotube antennas. *Nature*, 432(7020):959–960, 2004. [Cited 4 times on pages 2, 83, 88, and 139.]

M. S. Dresselhaus, G. Dresselhaus, R. Saito, and A. Jorio. Exciton photophysics of carbon nanotubes. *Annual Review of Physical Chemistry*, 58:719–747, 2007b. [Cited twice on page 6 and 50.]

R. Duggal and M. Pasquali. Dynamics of individual single-walled carbon nanotubes in water by real-time visualization. *Physical Review Letters*, 96(24):246104, 2006. [Cited twice on page 91 and 123.]

G. Dukovic, B. E. White, Z. Y. Zhou, F. Wang, S. Jockusch, M. L. Steigerwald, T. F. Heinz, R. A. Friesner, N. J. Turro, and L. E. Brus. Reversible surface oxidation and efficient luminescence quenching in semiconductor single-wall carbon nanotubes. *Journal of the American Chemical Society*, 126(46):15269–15276, 2004. [Cited once on page 26.]

J. G. Duque, L. Cognet, A. N. G. Parra-Vasquez, N. Nicholas, H. K. Schmidt, and M. Pasquali. Stable luminescence from individual carbon nanotubes in acidic, basic, and biological environments. *Journal of the American Chemical Society*, 130(8): 2626–2633, 2008a. [Cited 5 times on pages 42, 51, 67, 124, and 153.]

J. G. Duque, J. A. Eukel, M. Pasquali, and H. K. Schmidt. Self-assembled nanoparticle-nanotube structures (nanoPaNTs) based on antenna chemistry of single-walled carbon nanotubes. *ACS Nano*, Submitted, 2008b. [Cited once on page 154.]

J. G. Duque, M. Pasquali, and H. K. Schmidt. Antenna chemistry with metallic single-wall carbon nanotubes. *Journal of the American Chemical Society*, 130: 15340–15347, 2008c. [Cited 5 times on pages 139, 145, 153, and 154.]

T. Durkop, S. A. Getty, E. Cobas, and M. S. Fuhrer. Extraordinary mobility in semiconducting carbon nanotubes. *Nano Letters*, 4(1):35–39, 2004. [Cited once on page 110.]

C. A. Dyke, M. P. Stewart, and J. M. Tour. Separation of single-walled carbon nanotubes on silica gel. Materials morphology and Raman excitation wavelength affect data interpretation. *Journal of the American Chemical Society*, 127(12): 4497–4509, 2005. [Cited twice on page 23 and 104.]

W. J. Ellison. Permittivity of pure water, at standard atmospheric pressure, over the frequency range 0–25 THz and the temperature range 0–100 degrees C. *Journal of Physical and Chemical Reference Data*, 36(1):1–18, 2007. [Cited once on page 84.]

N. Fakhri, D. A. Tsyboulski, L. Cognet, B. Weisman, and M. Pasquali. Bending dynamics of single-walled carbon nanotubes in water: The archetypal semiflexible filaments. *Submitted Physical Review Letters*, 2008. [Cited once on page 123.]

Y. Fang and J. H. Hoh. Surface-directed DNA condensation in the absence of soluble

multivalent cations. *Nucleic Acids Research*, 26(2):588–593, 1998. [Cited twice on page 121 and 125.]

J. C. Fletcher. Electromagnetic wave energy converter. United States Patent 3760257, 1973. [Cited twice on page 139 and 144.]

E. Frackowiak and F. Beguin. Carbon materials for the electrochemical storage of energy in capacitors. *Carbon*, 39(6):937–950, 2001. [Cited once on page 145.]

C. J. Gannon, P. Cherukuri, B. I. Yakobson, L. Cognet, J. S. Kanzius, C. Kittrell, R. B. Weisman, M. Pasquali, H. K. Schmidt, R. E. Smalley, and S. A. Curley. Carbon nanotube-enhanced thermal destruction of cancer cells in a noninvasive radiofrequency field. *Cancer*, 110(12):2654–2665, 2007. [Cited 5 times on pages 2, 83, 85, 88, and 139.]

J. Gao, C. M. Bender, and C. J. Murphy. Dependence of the gold nanorod aspect ratio on the nature of the directing surfactant in aqueous solution. *Langmuir*, 19 (21):9065–9070, 2003. [Cited once on page 118.]

T. Gokus, A. Hartschuh, H. Harutyunyan, M. Allegrini, F. Hennrich, M. Kappes, A. A. Green, M. C. Hersam, P. T. Araujo, and A. Jorio. Exciton decay dynamics in individual carbon nanotubes at room temperature. *Applied Physics Letters*, 92 (15):3, 2008. [Cited once on page 50.]

A. Gole, C. Orendorff, and C. Murphy. Immobilization of gold nanorods onto acid-terminated self-assembled monolayers via electrostatic interactions. *Langmuir*, 20 (17):7117–7122, 2004. [Cited once on page 118.]

M. Gratzel. Dye-sensitized solar cells. *Journal of Photochemistry and Photobiology C-Photochemistry Reviews*, 4(2):145–153, 2003. [Cited once on page 140.]

D. Guowei, K. Adriane, X. Chen, C. Jie, and L. Yinfeng. PVP magnetic nanospheres:

Biocompatibility, in vitro and in vivo bleomycin release. *International Journal of Pharmaceutics*, 328(1):78–85, 2007. [Cited once on page 41.]

A. Hagen, M. Steiner, M. B. Raschke, C. Lienau, T. Hertel, H. H. Qian, A. J. Meixner, and A. Hartschuh. Exponential decay lifetimes of excitons in individual single-walled carbon nanotubes. *Physical Review Letters*, 95(19):197401, 2005. [Cited once on page 50.]

J. Halbritter, G. Repphun, S. Vinzelberg, G. Staikov, and W. J. Lorenz. Tunneling mechanisms in electrochemical STM - distance and voltage tunneling spectroscopy. *Electrochimica Acta*, 40(10):1385–1394, 1995. [Cited once on page 114.]

J. Hao and G. W. Hanson. Infrared and optical properties of carbon nanotube dipole antennas. *IEEE Transactions on Nanotechnology*, 5(6):766–775, 2006. [Cited twice on page 2 and 109.]

D. A. Heller, P. W. Barone, J. P. Swanson, R. M. Mayrhofer, and M. S. Strano. Using Raman spectroscopy to elucidate the aggregation state of single-walled carbon nanotubes. *Journal of Physical Chemistry B*, 108(22):6905–6909, 2004. [Cited twice on page 23.]

T. Hertel, V. Perebeinos, J. Crochet, K. Arnold, M. Kappes, and P. Avouris. Inter-subband decay of 1-D exciton resonances in carbon nanotubes. *Nano Letters*, 8(1): 87–91, 2008. [Cited once on page 60.]

H. Hirori, K. Matsuda, Y. Miyauchi, S. Maruyama, and Y. Kanemitsu. Exciton localization of single-walled carbon nanotubes revealed by femtosecond excitation correlation spectroscopy. *Physical Review Letters*, 97(25):257401, 2006. [Cited twice on page 50 and 63.]

A. Hogele, C. Galland, M. Winger, and A. Imamoglu. Photon antibunching in the photoluminescence spectra of a single carbon nanotube. *Physical Review Letters*, 100(21):217401, 2008. [Cited 3 times on pages 50, 58, and 75.]

L. B. Huang, H. N. Pedrosa, and T. D. Krauss. Ultrafast ground-state recovery of single-walled carbon nanotubes. *Physical Review Letters*, 93(1):017403, 2004. [Cited 3 times on pages 50.]

T. J. Imholt, C. A. Dyke, B. Hasslacher, J. M. Perez, D. W. Price, J. A. Roberts, J. B. Scott, A. Wadhawan, Z. Ye, and J. M. Tour. Nanotubes in microwave fields: Light emission, intense heat, outgassing, and reconstruction. *Chemistry of Materials*, 15 (21):3969–3970, 2003. [Cited 3 times on pages 2, 83, and 139.]

M. F. Islam, E. Rojas, D. M. Bergey, A. T. Johnson, and A. G. Yodh. High weight fraction surfactant solubilization of single-wall carbon nanotubes in water. *Nano Letters*, 3(2):269–273, 2003. [Cited once on page 3.]

J. D. Jackson. How an antenna launches its input power into radiation: The pattern of the Poynting vector at and near an antenna. *American Journal of Physics*, 74 (4):280–288, 2006. [Cited 3 times on pages 127, 128, and 132.]

J. Jiang, K. Bosnick, M. Maillard, and L. Brus. Single molecule Raman spectroscopy at the junctions of large Ag nanocrystals. *Journal of Physical Chemistry B*, 107 (37):9964–9972, 2003a. [Cited 3 times on pages 109 and 118.]

K. Jiang, A. Eitan, L. S. Schadler, P. M. Ajayan, R. W. Siegel, N. Grobert, M. Mayne, M. Reyes-Reyes, H. Terrones, and M. Terrones. Selective attachment of gold nanoparticles to nitrogen-doped carbon nanotubes. *Nano Letters*, 3(3):275–277, 2003b. [Cited once on page 84.]

T. Jones. *Electromechanics of Particles*. Cambridge University Press, NY, 1995. [Cited once on page 91.]

N. W. S. Kam, M. O'Connell, J. A. Wisdom, and H. J. Dai. Carbon nanotubes as multifunctional biological transporters and near-infrared agents for selective cancer cell destruction. *Proceedings of the National Academy of Sciences of the United States of America*, 102(33):11600–11605, 2005. [Cited twice on page 85 and 88.]

P. V. Kamat. Meeting the clean energy demand: Nanostructure architectures for solar energy conversion. *Journal of Physical Chemistry C*, 111(7):2834–2860, 2007. [Cited once on page 139.]

Y. J. Kang and T. A. Taton. Micelle-encapsulated carbon nanotubes: A route to nanotube composites. *Journal of the American Chemical Society*, 125(19):5650–5651, 2003. [Cited once on page 33.]

H. Kataura, Y. Kumazawa, Y. Maniwa, I. Umezu, S. Suzuki, Y. Ohtsuka, and Y. Achiba. Optical properties of single-wall carbon nanotubes. *Synthetic Metals*, 103(1-3):2555–2558, 1999. [Cited twice on page 104 and 105.]

K. Kempa, J. Rybczynski, Z. P. Huang, K. Gregorczyk, A. Vidan, B. Kimball, J. Carlson, G. Benham, Y. Wang, A. Herczynski, and Z. F. Ren. Carbon nanotubes as optical antennae. *Advanced Materials*, 19(3):421–426, 2007. [Cited once on page 139.]

Z. H. Khan and B. Husain. Carbon nanotube and its possible applications. *Indian Journal of Engineering and Materials Sciences*, 12(6):529–551, 2005. [Cited once on page 18.]

A. Khanal, Y. Li, N. Takisawa, N. Kawasaki, Y. Oishi, and K. Nakashima. Morphological change of the micelle of poly(styrene)-b-poly(2-vinylpyridine)-b-poly(ethylene oxide) induced by binding of sodium dodecyl sulfate. *Langmuir*, 20(12):4809–4812, 2004. [Cited once on page 27.]

F. Kim, J. H. Song, and P. D. Yang. Photochemical synthesis of gold nanorods. *Journal of the American Chemical Society*, 124(48):14316–14317, 2002. [Cited 8 times on pages 91, 99, 101, 116, 149, 151, and 153.]

K. Kneipp, Y. Wang, H. Kneipp, L. T. Perelman, I. Itzkan, R. Dasari, and M. S. Feld. Single molecule detection using surface-enhanced Raman scattering (SERS). *Physical Review Letters*, 78(9):1667–1670, 1997. [Cited once on page 109.]

A. G. Krivenko, N. S. Komarova, E. V. Stenina, L. N. Sviridova, V. A. Kurmaz, A. S. Kotkin, and V. E. Muradyan. Electrochemical behavior of electrodes containing nanostructured carbon of various morphology in the cathodic region of potentials. *Russian Journal of Electrochemistry*, 42(10):1047–1054, 2006. [Cited once on page 2.]

R. Krupke, F. Hennrich, H. von Lohneysen, and M. M. Kappes. Separation of metallic from semiconducting single-walled carbon nanotubes. *Science*, 301(5631):344–347, 2003. [Cited twice on page 2 and 89.]

K. N. Kudin, G. E. Scuseria, and B. I. Yakobson. C2F, BN, and C nanoshell elasticity from ab initio computations. *Physical Review B*, 64(23):235406, 2001. [Cited once on page 123.]

A. M. Kuznetsov and J. Ulstrup. Theory of electron transfer at electrified interfaces. *Electrochimica Acta*, 45(15-16):2339–2361, 2000. [Cited once on page 114.]

R. Kuzuo, M. Terauchi, and M. Tanaka. Electron energy-loss spectra of carbon nanotubes. *Japanese Journal of Applied Physics Part 2-Letters*, 31(10B):L1484–L1487, 1992. [Cited once on page 147.]

E. Kymakis and G. A. J. Amaratunga. Single-wall carbon nanotube/conjugated polymer photovoltaic devices. *Applied Physics Letters*, 80(1):112–114, 2002. [Cited twice on page 85 and 88.]

J. Laverdant, S. Buil, and X. Quelin. Local field enhancements on gold and silver nanostructures for aperture near field spectroscopy. *Journal of Luminescence*, 127 (1):176–180, 2007. [Cited once on page 109.]

C. Y. Lee, S. Baik, J. Q. Zhang, R. I. Masel, and M. S. Strano. Charge transfer from metallic single-walled carbon nanotube sensor arrays. *Journal of Physical Chemistry B*, 110(23):11055–11061, 2006. [Cited once on page 1.]

J. Lefebvre, D. G. Austing, J. Bond, and P. Finnie. Photoluminescence imaging of suspended single-walled carbon nanotubes. *Nano Letters*, 6(8):1603–1608, 2006. [Cited once on page 50.]

N. S. Lewis. Toward cost-effective solar energy use. *Science*, 315(5813):798–801, 2007. [Cited 4 times on pages 138 and 139.]

G. H. Lin, R. Abdu, and J. O. Bockris. Investigation of resonance light absorption and rectification by subnanostructures. *Journal of Applied Physics*, 80(1):565–568, 1996. [Cited once on page 139.]

J. Liu, H. J. Dai, J. H. Hafner, D. T. Colbert, R. E. Smalley, S. J. Tans, and C. Dekker. Fullerene 'crop circles'. *Nature*, 385(6619):780–781, 1997. [Cited once on page 120.]

Y. J. Liu, Z. H. Zhang, L. H. Nie, and S. Z. Yao. Study on the influence of anionic and cationic surfactant on Au-colloid modified electrode function by cyclic voltammetry and electrochemical impedance techniques. *Electrochimica Acta*, 48(19):2823–2830, 2003. [Cited once on page 84.]

Q. Lu, R. Rao, B. Sadanadan, W. Que, A. M. Rao, and P. C. Ke. Coupling of photon energy via a multiwalled carbon nanotube array. *Applied Physics Letters*, 87(17): 173102, 2005. [Cited once on page 147.]

Y. S. Luo, S. Q. Li, Q. F. Ren, J. P. Liu, L. L. Xing, Y. Wang, Y. Yu, Z. J. Jia, and J. L. Li. Facile synthesis of flowerlike Cu2O nanoarchitectures by a solution phase route. *Crystal Growth and Design*, 7(1):87–92, 2007. [Cited once on page 84.]

S. A. Maier. Plasmonics: Metal nanostructures for subwavelength photonic devices. *IEEE Journal of Selected Topics in Quantum Electronics*, 12:1214–1220, 2006. [Cited once on page 109.]

M. Maillard, P. R. Huang, and L. Brus. Silver nanodisk growth by surface plasmon

enhanced photoreduction of adsorbed Ag+. *Nano Letters*, 3(11):1611–1615, 2003. [Cited once on page 109.]

A. A. Mamedov, N. A. Kotov, M. Prato, D. M. Guldi, J. P. Wicksted, and A. Hirsch. Molecular design of strong single-wall carbon nanotube/polyelectrolyte multilayer composites. *Nature Materials*, 1(3):190–194, 2002. [Cited once on page 27.]

C. Manzoni, A. Gambetta, E. Menna, M. Meneghetti, G. Lanzani, and G. Cerullo. Intersubband exciton relaxation dynamics in single-walled carbon nanotubes. *Physical Review Letters*, 94:207401, 2005. [Cited once on page 60.]

R. Martel, H. R. Shea, and P. Avouris. Ring formation in single-wall carbon nanotubes. *Journal of Physical Chemistry B*, 103(36):7551–7556, 1999a. [Cited 4 times on pages 120, 122, 123, and 124.]

R. Martel, H. R. Shea, and P. Avouris. Rings of single-walled carbon nanotubes. *Nature*, 398(6725):299–299, 1999b. [Cited twice on page 120 and 125.]

S. Maruyama, Y. Miyauchi, Y. Murakami, and S. Chiashi. Optical characterization of single-walled carbon nanotubes synthesized by catalytic decomposition of alcohol. *New Journal of Physics*, 5:149, Oct. 2003. [Cited once on page 69.]

J. Maultzsch, H. Telg, S. Reich, and C. Thomsen. Radial breathing mode of single-walled carbon nanotubes: Optical transition energies and chiral-index assignment. *Physical Review B*, 72:205438, 2005. [Cited twice on page 104.]

T. J. McDonald, C. Engtrakul, M. Jones, G. Rumbles, and M. J. Heben. Kinetics of PL quenching during single-walled carbon nanotube rebundling and diameter-dependent surfactant interactions. *Journal of Physical Chemistry B*, 110(50):25339–25346, 2006. [Cited once on page 18.]

P. L. McEuen, M. S. Fuhrer, and H. K. Park. Single-walled carbon nanotube elec-

tronics. *IEEE Transactions on Nanotechnology*, 1(1):78–85, 2002. [Cited twice on page 2 and 83.]

M. J. Mendes, H. K. Schmidt, and M. Pasquali. Brownian dynamics simulations of single-wall carbon nanotube separation by type using dielectrophoresis. *Journal of Physical Chemistry B*, 112(25):7467–7477, 2008. [Cited once on page 89.]

A. Milchev, D. Stoychev, V. Lazarov, A. Papoutsis, and G. Kokkinidis. Electrocrystallisation of metal catalysts: nucleation and growth of platinum on a titanium electrode. *Journal of Crystal Growth*, 226(1):138–147, 2001. [Cited twice on page 111.]

C. Miller, P. Cuendet, and M. Gratzel. Adsorbed omega-hydroxy thiol monolayers on gold electrodes : Evidence for electron tunneling to redox species in solution. *Journal of Physical Chemistry*, 95(2):877–886, 1991. [Cited once on page 113.]

M. Miyazaki, H. Onose, N. Iida, and H. Kazama. Determination of residual double bonds in resin-dentin interface by Raman spectroscopy. *Dental Materials*, 19(3): 245–251, 2003. [Cited once on page 35.]

A. Montesi, M. Pasquali, and F. C. MacKintosh. Collapse of a semiflexible polymer in poor solvent. *Physical Review E*, 69(2):021916, 2004. [Cited 4 times on pages 121, 122, and 125.]

V. C. Moore, M. S. Strano, E. H. Haroz, R. H. Hauge, R. E. Smalley, J. Schmidt, and Y. Talmon. Individually suspended single-walled carbon nanotubes in various surfactants. *Nano Letters*, 3(10):1379–1382, 2003. [Cited 3 times on pages 67, 83, and 132.]

G. Nagy and T. Wandlowski. Double layer properties of Au(111)/H2SO4 (Cl)+Cu2+ from distance tunneling spectroscopy. *Langmuir*, 19(24):10271–10280, 2003. [Cited once on page 114.]

A. Nish and R. J. Nicholas. Temperature induced restoration of fluorescence from oxidised single-walled carbon nanotubes in aqueous sodium dodecylsulfate solution. *Physical Chemistry Chemical Physics*, 8(30):3547–3551, 2006. [Cited once on page 2.]

S. Niyogi, S. Boukhalfa, S. B. Chikkannanavar, T. J. McDonald, M. J. Heben, and S. K. Doorn. Selective aggregation of single-walled carbon nanotubes via salt addition. *Journal of the American Chemical Society*, 129(7):1898–1899, 2007. [Cited once on page 2.]

A. J. Nozik. Photoelectrochemistry - Applications to solar-energy conversion. *Annual Review of Physical Chemistry*, 29:189–222, 1978. [Cited twice on page 95 and 113.]

M. O'Connell, S. M. Bachilo, C. Huffman, V. C. Moore, M. S. Strano, E. Haroz, K. L. Rialon, P. Boul, W. H. Noon, C. Kittrell, J. Ma, R. H. Hauge, R. B. Weisman, and R. Smalley. Band gap fluorescence from individual single-walled carbon nanotubes. *Science*, 297:593–596, 2002. [Cited 14 times on pages 1, 2, 6, 8, 11, 18, 20, 24, 50, 83, 86, 132, and 152.]

M. J. O'Connell, P. Boul, L. M. Ericson, C. Huffman, Y. H. Wang, E. Haroz, C. Kuper, J. Tour, K. D. Ausman, and R. E. Smalley. Reversible water-solubilization of single-walled carbon nanotubes by polymer wrapping. *Chemical Physics Letters*, 342(3-4): 265–271, 2001. [Cited once on page 117.]

M. J. O'Connell, E. E. Eibergen, and S. K. Doorn. Chiral selectivity in the charge-transfer bleaching of single-walled carbon-nanotube spectra. *Nature Materials*, 4 (5):412–418, 2005. [Cited 10 times on pages 1, 37, 83, 94, 95, 104, 127, 153, 159, and 160.]

Y. Ohno, S. Iwasaki, Y. Murakami, S. Kishimoto, S. Maruyama, and T. Mizutani. Chirality-dependent environmental effects in photoluminescence of single-walled

carbon nanotubes. *Physical Review B*, 73(23):235427, 2006. [Cited twice on page 1 and 11.]

K. Okazaki, Y. Nakato, and K. Murakoshi. Absolute potential of the Fermi level of isolated single-walled carbon nanotubes. *Physical Review B*, 68(3):35434, 2003. [Cited 3 times on pages 84, 93, and 127.]

B. Oregan and M. Gratzel. A low-cost, high-efficiency solar-cell based on dye-sensitized colloidal TiO2 films. *Nature*, 353(6346):737–740, 1991. [Cited once on page 139.]

N. R. Palwai, D. E. Martyn, L. F. F. Neves, Y. Tan, D. E. Resasco, and R. G. Harrison. Retention of biological activity and near-infrared absorbance upon adsorption of horseradish peroxidase on single-walled carbon nanotubes. *Nanotechnology*, 18 (235601):235601, 2007. [Cited once on page 2.]

J. B. Pendry, A. J. Holden, D. J. Robbins, and W. J. Stewart. Magnetism from conductors and enhanced nonlinear phenomena. *IEEE Transactions on Microwave Theory and Techniques*, 47(11):2075–2084, 1999. [Cited once on page 119.]

V. Perebeinos, J. Tersoff, and P. Avouris. Scaling of excitons in carbon nanotubes. *Physical Review Letters*, 92(25):257402, 2004. [Cited once on page 50.]

C. L. Pint, N. Nicholas, S. T. Pheasant, J. G. Duque, A. N. G. Parra-Vasquez, G. Eres, M. Pasquali, and R. H. Hauge. Temperature and gas pressure effects in vertically aligned carbon nanotube growth from Fe-Mo catalyst. *Journal of Physical Chemistry C*, 112(36):14041–14051, 2008. [Cited twice on page 140 and 147.]

P. Piyasena, C. Dussault, T. Koutchma, H. S. Ramaswamy, and G. B. Awuah. Radio frequency heating of foods: Principles, applications and related properties - A Review. *Critical Reviews in Food Science and Nutrition*, 43(6):587–606, 2003. [Cited once on page 129.]

G. Rahman, D. Guldi, E. Zambon, L. Pasquato, N. Tagmatarchis, and M. Prato. Dispersable carbon nanotube/gold nanohybrids: Evidence for strong electronic interactions. *Small*, 1(5):527–530, 2005. [Cited once on page 84.]

P. K. Rai, R. A. Pinnick, A. N. G. Parra-Vasquez, V. A. Davis, H. K. Schmidt, R. H. Hauge, R. E. Smalley, and M. Pasquali. Isotropic-nematic phase transition of single-walled carbon nanotubes in strong acids. *Journal of the American Chemical Society*, 128(2):591–595, 2006. [Cited once on page 7.]

P. L. Redmond and L. E. Brus. "hot electron" photo-charging and electrochemical discharge kinetics of silver nanocrystals. *Journal of Physical Chemistry C*, 111: 14849–14854, 2007. [Cited once on page 109.]

B. W. Reed and M. Sarikaya. Electronic properties of carbon nanotubes by transmission electron energy-loss spectroscopy. *Physical Review B*, 64(19):195404, 2001. [Cited once on page 109.]

B. W. Reed, M. Sarikaya, L. R. Dalton, and G. F. Bertsch. Transmission electron energy-loss spectroscopy study of carbon nanotubes upon high temperature treatment. *Applied Physics Letters*, 78(21):3358–3360, 2001. [Cited once on page 109.]

M. A. Reed, C. Zhou, C. J. Muller, T. P. Burgin, and J. M. Tour. Conductance of a molecular junction. *Science*, 278(5336):252–254, 1997. [Cited 3 times on pages 139, 144, and 150.]

C. Richard, F. Balavoine, P. Schultz, T. W. Ebbesen, and C. Mioskowski. Supramolecular self-assembly of lipid derivatives on carbon nanotubes. *Science*, 300(5620): 775–778, May 2003. [Cited once on page 145.]

R. Saito, M. Fujita, G. Dresselhaus, and M. S. Dresselhaus. Electronic-structure of chiral graphene tubules. *Applied Physics Letters*, 60(18):2204–2206, 1992. [Cited 3 times on pages 1, 83, and 139.]

S. Salahuddin, M. Lundstrom, and S. Datta. Transport effects on signal propagation in quantum wires. *IEEE Transactions on Electron Devices*, 52(8):1734–1742, 2005. [Cited 3 times on pages 109 and 110.]

M. Sano, A. Kamino, J. Okamura, and S. Shinkai. Ring closure of carbon nanotubes. *Science*, 293(5533):1299–1301, 2001. [Cited once on page 120.]

A. Sarkar, T. Mukherjee, and S. Kapoor. PVP-stabilized copper nanoparticles: A reusable catalyst for "click" reaction between terminal alkynes and azides in non-aqueous solvents. *Journal of Physical Chemistry C*, 112(9):3334–3340, 2008. [Cited once on page 117.]

T. Schmidt, G. J. Schutz, W. Baumgartner, H. J. Gruber, and H. Schindler. Characterization of photophysics and mobility of single molecules in a fluid lipid-membrane. *Journal of Physical Chemistry*, 99(49):17662–17668, 1995. [Cited once on page 30.]

T. Schmidt, G. J. Schutz, W. Baumgartner, H. J. Gruber, and H. Schindler. Imaging of single molecule diffusion. *Proceedings of the National Academy of Sciences of the United States of America*, 93(7):2926–2929, 1996. [Cited once on page 30.]

B. Schnurr, F. C. MacKintosh, and D. R. M. Williams. Dynamical intermediates in the collapse of semiflexible polymers in poor solvents. *Europhysics Letters*, 51(3): 279–285, 2000. [Cited 3 times on pages 121 and 122.]

B. Schnurr, F. Gittes, and F. C. MacKintosh. Metastable intermediates in the condensation of semiflexible polymers. *Physical Review E*, 65(6):061904, 2002. [Cited 3 times on pages 122 and 125.]

A. Seepujak, U. Bangert, A. J. Harvey, P. Costa, and M. L. H. Green. Redshift and optical anisotropy of collective pi-volume modes in multiwalled carbon nanotubes. *Physical Review B*, 74(7):075402, 2006. [Cited once on page 147.]

R. Setton. Carbon nanotubes .1. geometrical considerations. *Carbon*, 33(2):135–140, 1995. [Cited once on page 18.]

A. Shah, P. Torres, R. Tscharner, N. Wyrsch, and H. Keppner. Photovoltaic technology: The case for thin-film solar cells. *Science*, 285(5428):692–698, 1999. [Cited once on page 138.]

J. Shaver, J. Kono, O. Portugall, V. Krstic, G. Rikken, Y. Miyauchi, S. Maruyama, and V. Perebeinos. Magnetic brightening of carbon nanotube photoluminescence through symmetry breaking. *Nano Letters*, 7(7):1851–1855, 2007. [Cited once on page 50.]

S. B. Sinnott and R. Andrews. Carbon nanotubes: Synthesis, properties, and applications. Review. *Critical Reviews in Solid State and Materials Sciences*, 26(3): 145–249, 2001. [Cited twice on page 2 and 18.]

J. Sloan, R. E. Dunin-Borkowski, J. L. Hutchison, K. S. Coleman, V. C. Williams, J. B. Claridge, A. P. E. York, C. G. Xu, S. R. Bailey, G. Brown, S. Friedrichs, and M. L. H. Green. The size distribution, imaging and obstructing properties of C-60 and higher fullerenes formed within arc-grown single walled carbon nanotubes. *Chemical Physics Letters*, 316(3-4):191–198, 2000. [Cited once on page 5.]

R. E. Smalley. Future global energy prosperity: The terawatt challenge. *MRS Bulletin*, 30(6):412–417, 2005. [Cited twice on page 138.]

M. P. Stevens. *Polymer Chemistry an Introduction*. Oxford University Press, New York, Oxford, third edition edition, 1999. [Cited twice on page 32 and 33.]

M. Strano, C. Huffman, V. Moore, M. O'Connell, E. Haroz, J. Hubbard, M. Miller, K. Rialon, C. Kittrell, S. Ramesh, R. Hauge, and R. E. Smalley. Reversible, bandgap selective protonation of single-walled carbon nanotubes in solution. *Journal of Physical Chemistry B*, 107:6979–6985, 2003. [Cited 13 times on pages 1, 2, 18, 19, 23, 24, 26, 27, 83, and 124.]

M. S. Strano, M. Zheng, A. Jagota, G. B. Onoa, D. A. Heller, P. W. Barone, and M. L. Usrey. Understanding the nature of the DNA-assisted separation of single-walled carbon nanotubes using fluorescence and Raman spectroscopy. *Nano Letters*, 4(4): 543–550, 2004. [Cited once on page 132.]

S. Suzuki, Y. Watanabe, Y. Homma, S. Fukuba, S. Heun, and A. Locatelli. Work functions of individual single-walled carbon nanotubes. *Applied Physics Letters*, 85 (1):127–129, 2004. [Cited once on page 114.]

X. L. Tang, P. Jiang, G. L. Ge, M. Tsuji, S. S. Xie, and Y. J. Guo. Poly(N-vinyl-2-pyrrolidone) (PVP)-capped dendritic gold nanoparticles by a one-step hydrothermal route and their high SERS effect. *Langmuir*, 24(5):1763–1768, 2008. [Cited once on page 117.]

H. Telg, J. Maultzsch, S. Reich, and C. Thomsen. Resonant-Raman intensities and transition energies of the E-11 transition in carbon nanotubes. *Physical Review B*, 74:115415, 2006. [Cited once on page 104.]

A. Thess, R. Lee, P. Nikolaev, H. J. Dai, P. Petit, J. Robert, C. H. Xu, Y. H. Lee, S. G. Kim, A. G. Rinzler, D. T. Colbert, G. E. Scuseria, D. Tomanek, J. E. Fischer, and R. E. Smalley. Crystalline ropes of metallic carbon nanotubes. *Science*, 273 (5274):483–487, 1996. [Cited twice on page 69 and 123.]

J. M. Tour. Molecular electronics. Synthesis and testing of components. *Accounts of Chemical Research*, 33(11):791–804, 2000. [Cited twice on page 139 and 150.]

D. A. Tsyboulski, S. M. Bachilo, and R. B. Weisman. Versatile visualization of individual single-walled carbon nanotubes with near-infrared fluorescence microscopy. *Nano Letters*, 5(5):975–979, 2005. [Cited 6 times on pages 21, 30, 41, and 54.]

D. A. Tsyboulski, J. D. R. Rocha, S. M. Bachilo, L. Cognet, and R. B. Weisman. Structure-dependent fluorescence efficiencies of individual single-walled cardon nanotubes. *Nano Letters*, 7(10):3080–3085, 2007. [Cited once on page 51.]

V. V. Vasilevskaya, A. R. Khokhlov, S. Kidoaki, and K. Yoshikawa. Structure of collapsed persistent macromolecule: Toroid vs. spherical globule. *Biopolymers*, 41 (1):51–60, 1997. [Cited twice on page 121 and 125.]

D. Wang and L. Chen. Temperature and pH-responsive single-walled carbon nanotube dispersions. *Nano Letters*, 7(6):1480–1484, 2007. [Cited once on page 18.]

F. Wang, G. Dukovic, L. E. Brus, and T. F. Heinz. Time-resolved fluorescence of carbon nanotubes and its implication for radiative lifetimes. *Physical Review Letters*, 92(17):177401, 2004a. [Cited 4 times on pages 2, 50, 83, and 88.]

F. Wang, G. Dukovic, L. E. Brus, and T. F. Heinz. The optical resonances in carbon nanotubes arise from excitons. *Science*, 308(5723):838–841, 2005. [Cited once on page 50.]

R. Wang, P. Cherukuri, J. G. Duque, T. K. Leeuw, M. K. Lackey, C. H. Moran, V. C. Moore, J. L. Conyers, R. E. Smalley, H. K. Schmidt, B. R. Weisman, and P. S. Engel. SWCNT PEG-eggs: Single-walled carbon nanotubes in biocompatible shell-crosslinked micelles. *Carbon*, 45(12):2388–2393, 2007. [Cited once on page 33.]

Y. Wang, K. Kempa, B. Kimball, J. B. Carlson, G. Benham, W. Z. Li, T. Kempa, J. Rybczynski, A. Herczynski, and Z. F. Ren. Receiving and transmitting light-like radio waves: Antenna effect in arrays of aligned carbon nanotubes. *Applied Physics Letters*, 85(13):2607–2609, 2004b. [Cited once on page 139.]

Y. Wang, R. Islam, and G. V. Eleftheriades. An ultra-short contra-directional coupler utilizing surface plasmon-polaritons at optical frequencies. *Optics Express*, 14(16): 7279–7290, 2006. [Cited once on page 109.]

C. Warakulwit, T. Nguyen, J. Majimel, M. H. Delville, V. Lapeyre, P. Garrigue, V. Ravaine, J. Limtrakul, and A. Kuhn. Dissymmetric carbon nanotubes by bipolar electrochemistry. *Nano Letters*, 8(2):500–504, 2008. [Cited once on page 84.]

R. B. Weisman, S. M. Bachilo, and D. Tsyboulski. Fluorescence spectroscopy of single-walled carbon nanotubes in aqueous suspension. *Applied Physics A-Materials Science and Processing*, 78(8):1111–1116, 2004. [Cited twice on page 6 and 23.]

B. I. Yakobson, C. J. Brabec, and J. Bernholc. Nanomechanics of carbon tubes: Instabilities beyond linear response. *Physical Review Letters*, 76(14):2511–2514, 1996. [Cited 3 times on pages 123.]

D. Zanette, S. J. Froehner, E. Minatti, and A. A. Ruzza. Effects of polymer and salt concentrations on ketal acid hydrolysis in solutions of sodium dodecyl sulfate and poly(vinyl pyrrolidone) or poly(ethylene oxide). *Langmuir*, 13(4):659–665, 1997. [Cited twice on page 18 and 124.]

S. Zaric, G. N. Ostojic, J. Kono, J. Shaver, V. C. Moore, R. H. Hauge, R. E. Smalley, and W. Xing. Estimation of magnetic susceptibility anisotropy of carbon nanotubes using magnetophotoluminescence. *Nano Letters*, 4(11):2219–2221, 2004. [Cited once on page 3.]

L. M. Zhai, X. H. Lu, W. J. Chen, C. B. Hu, and L. Zheng. Interaction between spontaneously formed SDBS/CTAB vesicles and polymer studied by fluorescence method. *Colloids and Surfaces A-Physicochemical and Engineering Aspects*, 236 (1-3):1–5, 2004. [Cited 4 times on pages 18, 27, and 124.]

M. Zhang, M. Yudasaka, Y. Miyauchi, S. Maruyama, and S. Iijima. Changes in the fluorescence spectrum of individual single-wall carbon nanotubes induced by light-assisted oxidation with hydroperoxide. *Journal of Physical Chemistry B*, 110(18): 8935–8940, 2006. [Cited 3 times on pages 1 and 11.]

S. L. Zhang, S. M. Zhao, M. G. Xia, E. H. Zhang, and T. Xu. Ring formation of single-walled carbon nanotubes: Competition between conformation energy and entropy. *Physical Review B*, 68(24):245419, 2003. [Cited once on page 120.]

H. B. Zhao and S. Mazumdar. Electron-electron interaction effects on the optical excitations of semiconducting single-walled carbon nanotubes. *Physical Review Letters*, 93(15):157402, 2004. [Cited once on page 50.]

M. Zheng and V. V. Rostovtsev. Photoinduced charge transfer mediated by DNA-wrapped carbon nanotubes. *Journal of the American Chemical Society*, 128(24): 7702–7703, 2006. [Cited once on page 84.]

Z. H. Zhong, N. M. Gabor, J. E. Sharping, A. L. Gaeta, and P. L. McEuen. Terahertz time-domain measurement of ballistic electron resonance in a single-walled carbon nanotube. *Nature Nanotechnology*, 3(4):201–205, 2008. [Cited once on page 109.]